PE&RS
February 2016 Volume 82, Number 2

El Nino 20 Years Ago, and Today—

Continuity is Key to Monitoring Global Changes Over Time

PHOTOGRAMMETRIC ENGINEERING & REMOTE SENSING
The official journal for imaging and geospatial information science and technology

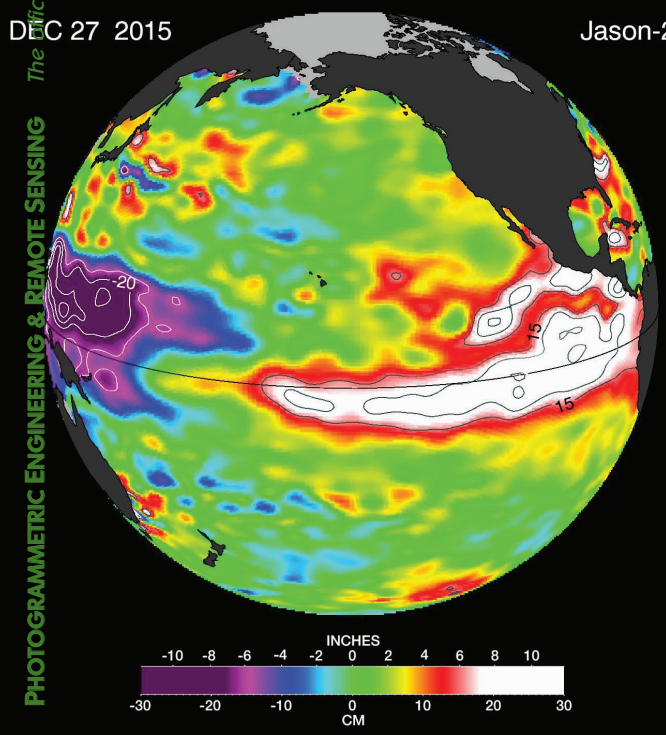

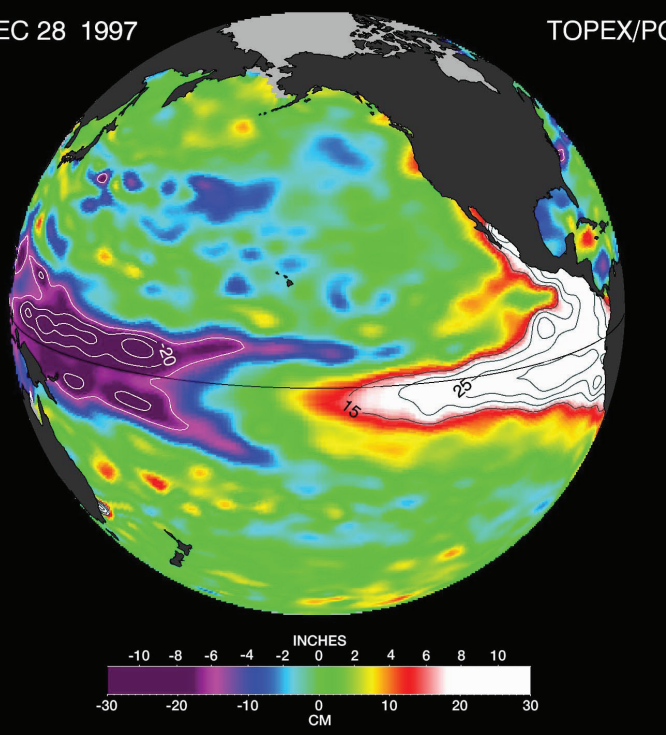

IGTF 2016

ASPRS Annual Conference &
co-located JACIE Workshop

Fort Worth, TX
April 11-15, 2016

HTTP://CONFERENCES.ASPRS.ORG/FORT-WORTH-2016

#IGTF16

#ASPRSorg

ASPRS.ORG

IGTF 2016

ASPRS Annual Conference & co-located JACIE Workshop

Fort Worth, TX | April 11–15, 2016

HTTP://CONFERENCES.ASPRS.ORG/FORT-WORTH-2016/REGISTER

The ASPRS Imaging and Geospatial Technology Forum (IGTF) is the premier scientific and engineering forum in the United States (and one of the top internationally) for geospatial professionals from industry, government, and academia. ASPRS invites your participation.

Register today! Four hours of workshop time is included in the Full and Monday-only registration fees!

The 2016 meeting will add an outreach component called "Frontier Day". Each day of the traditional program will focus on particular application areas, while each session will address the applications from a different technical perspective (e.g. Lidar, Photogrammetry, etc.). Outreach will target new and potential beneficiaries of geospatial technology and services that do not traditionally attend the ASPRS meetings (business development for the benefit of our members), and STEM educators and/or students (youth development for the benefit of society). Keynote presentations will come from representatives of government, academic, and business sectors. The high-level program for the annual meeting looks like this:

As you can see, each day is packed with relevant technical activities, and the evenings have been mostly left open for networking and business.

We are excited to welcome back the JACIE Workshop to again co-locate with our conference.

The intent of the JACIE workshop is to exchange information regarding the characterization and application of the commercial imagery used by the government. This workshop is focused on the synergy of high, medium and low resolution imagery and remote sensing technologies used by the Government. This workshop is sponsored by the Joint Agency Commercial Imagery Evaluation (JACIE) team, a collaborative group of representatives from NASA, NOAA, USDA, and USGS.

Day	Monday, 4/11	Tuesday, 4/12	Wednesday, 4/13	Thursday, 4/14	Friday, 4/15
Program	Various Technical and Society Business Meetings & Classified Session	Applications: Agriculture, Water, & Environment Day	Transportation, Infrastructure, & Energy Day	Technology, Analytics, & Innovation Day	Frontier Day • STEM Outreach • Business Outreach
Learning Activities	Professional Development Workshops	Town Hall: The Future of ASPRS	Exhibits (all day)	Exhibits (all day)	Exhibits & Outreach Seminars
Co-located	JACIE workshop	JACIE workshop	JACIE workshop		
Evening Activities	Board Meeting	SAC/EPC Meetup	Awards Desert Reception	Evening Exhibits (outreach) and Arts Festival	Main Street Fort Worth Arts Festival

IGTF 2016 Website **conferences.asprs.org/Fort-Worth-2016**

Main Street Fort Worth Arts Festival **mainstreetartsfest.org**

ANNOUNCEMENTS

Huntsville, Alabama-based **GeoCue Group** announced the latest release of LP360. Available both as an add-in to ArcGIS® and as a standalone 64 bit application. This release (2015.1.76) includes many feature updates as well as new tools aimed at improving our users' ability to derive value from point clouds. This is one of the important releases in the history of LP360. Geocue fixed more than 380 issues and added significant new features to LP360 product.

Feature updates for this release include: updated attribute class flags and filters to ensure robust compliance with the LAS 1.4 specification, new modes and units for volume outputs as well as improved digitizing tools in standalone for creating 3D stockpile toes.

Significant new features for this release include the new Live View interface for dynamically updating class/flag/return filters, a planar surface statistics point cloud task for testing point cloud precision, a ground cleaner point cloud task for cleanup of unclassified ground patches and a Coordinate Reference System (CRS) Utility for inserting CRS information into LAS file headers. A new feature is an automated stockpile toe extractor for defining the base for volumetric computations. Several new features aimed at engineering applications, such as volumetric analysis, include a feature edit tool for selecting and deleting features as well as an attribute and schema editor for the direct viewing and editing of feature attributes.

Each copy of LP360 includes both a Windows standalone and an ArcGIS extension license. Everyone who has LP360 on current maintenance will be able to update to the new release by using the "LP360 – Check for updates" feature in LP360. To renew maintenance, please contact sales@lp360.com.

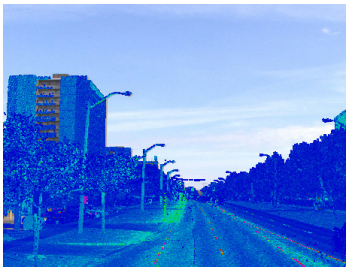

Teledyne Optech introduced the latest model of its Lynx mobile lidar system, the survey-grade Optech Lynx SG-S at the 95th Annual Meeting of the Transportation Research Board (TRB) in Washington, D.C.

The Lynx SG-S pairs Teledyne Optech's powerful lidar technology with a best-in-class position and orientation system to produce 3D data with survey-grade precision from a vehicle moving at highway speeds. With the lidar sensor, 360° Ladybug camera and GNSS antenna all placed on a single, compact platform, field operators can remove and reinstall the system quickly without affecting boresight parameters. The Lynx SG-S joins the rest of the Lynx family of mobile lidar systems, which includes the dual-sensor Lynx SG for high-density surveys and the mapping-grade Lynx MG for asset management and utilities.

Find out more at www.teledyneoptech.com.

SPECTRAL EVOLUTION—Measuring moisture in soil with a field spectroradiometer. Measuring the moisture content in soil can provide critical information on soil and vegetation health – especially useful in applications like crop irrigation management. Proximal soil analysis using a field spectrometer or spectroradiometer, like Spectral Evolution's PSR+, provides a window into soil and vegetation conditions. By taking *in situ* measurements rapidly and without preparing or affecting the sample, spectral information related to the main water features found at 1450-1460nm and 1920-1930nm can provide information on soil water content and be used to derive data on canopy and leaf health.

The PSR+ can measure different soil properties in a single scan, including organic and inorganic content, salinity, soil mineralogy, and moisture content:

- Fast, full spectrum 350-2500nm measurement with just one scan
- High resolution and high sensitivity for clean and accurate spectra
- Autoshutter, autoexposure, and auto-dark correction before each new scan for easy, one-touch operation
- Small and lightweight with rechargeable Li-ion batteries for field operation – half the weight of competitive instruments
- Reliable field performance with an all photodiode array platform and no moving optical parts to fail
- Single user operation with optional rugged handheld GETAC microcomputer that provides a sunlight readable screen plus the ability to tag spectra with GPS, digital camera images, and audio notes
- Standalone operation with 1,000 scan storage

The PSR+ is equipped with the exclusive DARWin SP Data Analysis software package so you can take advantage of the following analysis features:

- Automatically saves data as an ASCII file for easy use with 3rd party software – no pre-processing is necessary
- Collect reference or target data with a single click
- Display reflectance/transmittance data (percentage) or absorbance (logarithmic) versus wavelength
- Access 19 vegetation indices through the DARWin SP software – including water-related indices
- Optional EZ-ID software compares a target sample against a library of known samples
- Custom library module allows you to build your own spectral database as you scan

For more information, visit: http://www.spectralevolution.com/applications_moisture_soil.html.

PE&RS
PHOTOGRAMMETRIC ENGINEERING & REMOTE SENSING
The official journal for imaging and geospatial information science and technology
February 2016 Volume 82 Number 2

FEATURES

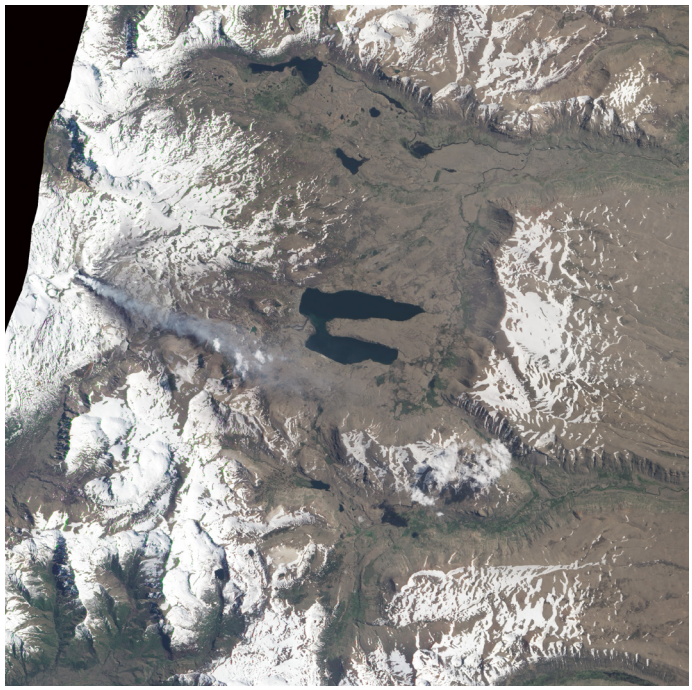

.com

SUBMIT YOUR COMMENTS!

COLUMNS

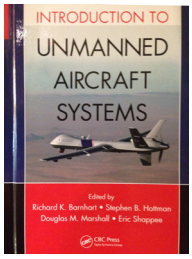

ANNOUNCEMENTS

Is your contact information current?
Contact us at members@asprs.org
or log on to
https://eserv.asprs.org
to update your information.
We value your membership.

DEPARTMENTS

Be a part of ASPRS Social Media:

facebook.com/ASPRS.org

twitter.com/ASPRSorg

pinterest.com/asprs

youtube.com/user/ASPRS

PEER-REVIEWED ARTICLES

See the Cover Description on Page 78

asprs student advisory council
THE IMAGING & GEOSPATIAL INFORMATION SOCIETY STUDENTCOUNCIL@ASPRS.ORG

ASPRS GeoLeague Challenge 2016

To be held at the 2016 Annual Conference in Fort Worth, Texas April 11-15, 2016

This year's challenge celebrates the 100 year anniversary of the National Park Service!

The ASPRS SAC is challenging you and your team to use freely available imagery to produce an innovative visualization product featuring the national park of your choice. Examples include: Time series animation, GIS fly through, Online story map, Image based structure from motion, or a 3D model. Check out FindYourPark.com for more inspiration!

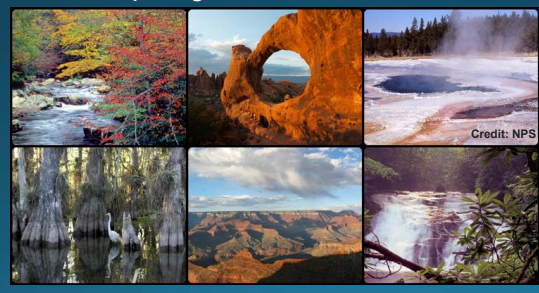

Stay tuned for more details about the challenge and prizes on the ASPRS website!

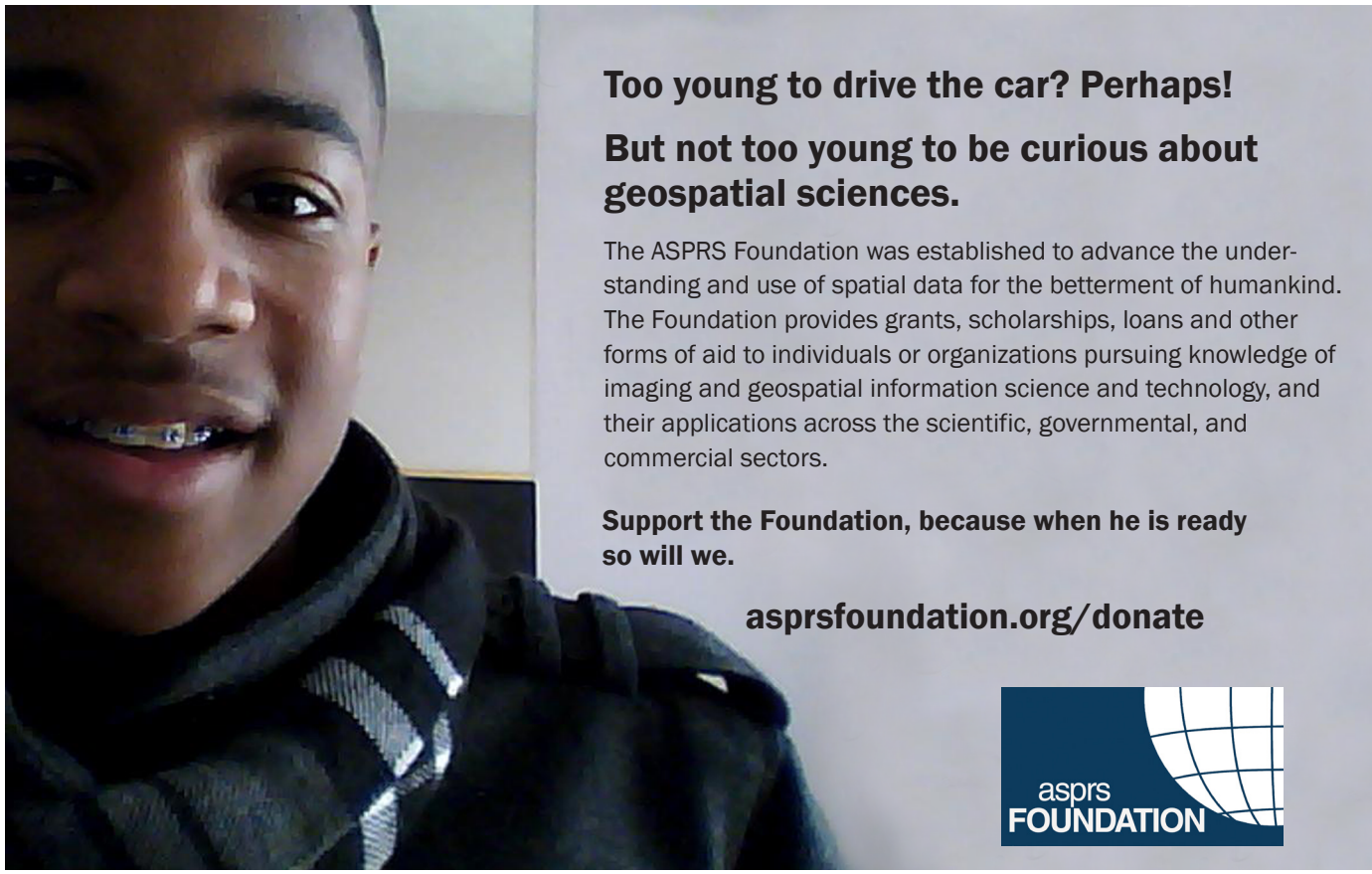

COVER DESCRIPTION

20 years ago a NASA press release announced, "El Nino is Back and Strong. According to NASA, the five years of global ocean topography observations made by TOPEX/Poseidon have been a boon for El Nino researchers, who have been able to track three El Nino events since the satellite's launch in August 1992."

Fast forward to January 17, 2016, Jason-3, a U.S.-European satellite mission, lifted off from Vandenberg Air Force Base in California today at 10:42 a.m. PST aboard a SpaceX Falcon 9 rocket, to become the latest spacecraft to track the rate of global sea-level rise. Jason-3 will also help NOAA's National Weather Service more accurately forecast the strength of tropical cyclones that threaten America's coasts.

Jason-3 continues the legacy of the Topex/Poseidon and earlier Jason satellites. According to Stephen Volz, Ph.D., assistant administrator for NOAA's Satellite and Information Service, "Jason-3 will tell us about the heat of the ocean, vital data if a tropical storm or hurricane is tracking into that location. Having up-to-date sea surface temperatures will help NOAA forecasters better determine if a storm may intensify."

"Jason-3 is a prime example of how our nation leverages NASA expertise in space and scientific exploration to help address critical global challenges in collaboration with NOAA and our international partners," said John Grunsfeld, associate administrator for science at NASA Headquarters.

Coordinating orbits and combining measurements from Jason-2 and Jason-3 should allow even more frequent coverage of the global oceans. Together, the two spacecraft will double global data coverage. This tandem mission will improve our knowledge of tides in coastal and shallow seas and internal tides in the open ocean, while improving our understanding of ocean currents and eddies.

Measurements of sea-surface height, or ocean-surface topography, reveal the speed and direction of ocean currents and tell scientists how much of the sun's energy is stored by the ocean. Combining ocean current and heat storage data is key to understanding global climate changes.

The SpaceX Falcon 9 rocket is seen at Vandenberg Air Force Base Space Launch Complex 4 East with the Jason-3 spacecraft onboard, Saturday, Jan. 16, 2016, in California. Jason-3, an international mission led by the National Oceanic and Atmospheric Administration (NOAA), will help continue U.S.-European satellite measurements of global ocean height changes. Jason-3 was successfully launched the next day. Credits: NASA/Bill Ingalls

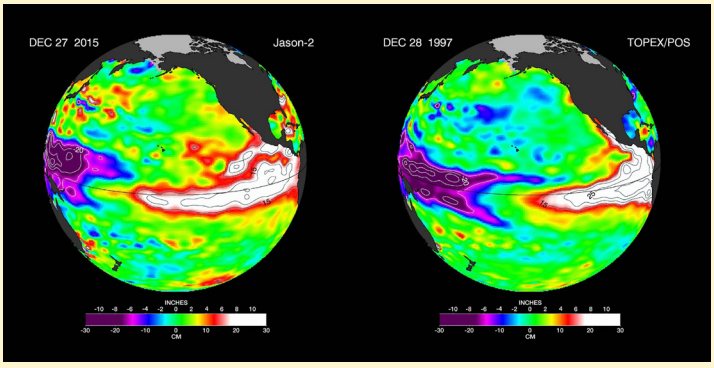

A side by side comparisons of Pacific Ocean sea surface height (SSH) anomalies of what is presently happening in 2015 with the Pacific Ocean signal during the famous 1997 El Niño. Data are from the TOPEX/Poseidon (1997) and the successor OSTM/Jason-2 (2015) satellites. Credits: NASA's Jet Propulsion Laboratory

PHOTOGRAMMETRIC ENGINEERING & REMOTE SENSING

asprs THE IMAGING & GEOSPATIAL INFORMATION SOCIETY

JOURNAL STAFF

Publisher Dr. Michael Hauck
Editor Russell G. Congalton
Technical Editor Michael S. Renslow
Assistant Editor Jie Shan
Assistant Director — Publications Rae Kelley
Electronic Publications Manager/Graphic Artist Matthew Austin

Photogrammetric Engineering & Remote Sensing is the official journal of the American Society for Photogrammetry and Remote Sensing. It is devoted to the exchange of ideas and information about the applications of photogrammetry, remote sensing, and geographic information systems. The technical activities of the Society are conducted through the following Technical Divisions: Geographic Information Systems, Photogrammetric Applications, Lidar, Primary Data Acquisition, Professional Practice, and Remote Sensing Applications. Additional information on the functioning of the Technical Divisions and the Society can be found in the Yearbook issue of *PE&RS*.

Correspondence relating to all business and editorial matters pertaining to this and other Society publications should be directed to the American Society for Photogrammetry and Remote Sensing, 5410 Grosvenor Lane, Suite 210, Bethesda, Maryland 20814-2144, including inquiries, memberships, subscriptions, changes in address, manuscripts for publication, advertising, back issues, and publications. The telephone number of the Society Headquarters is 301-493-0290; the fax number is 301-493-0208; web address is www.asprs.org.

PE&RS. *PE&RS* (ISSN0099-1112) is published monthly by the American Society for Photogrammetry and Remote Sensing, 5410 Grosvenor Lane, Suite 210, Bethesda, Maryland 20814-2144. Periodicals postage paid at Bethesda, Maryland and at additional mailing offices.

SUBSCRIPTION. For the 2016 subscription year, ASPRS is offering two options to our *PE&RS* subscribers -- an e-Subscription and the print edition. E-subscribers can plus-up their subscriptions with printed copies for a small additional charge. Print subscriptions are on a calendar-year basis that runs from January through December. Electronic subscriptions run for twelve months on an anniversary basis. We recommend that customers who choose both e-Subscription and print (e-Subscription + Print) renew on a calendar-year basis. The new electronic subscription includes access to ten years' of digital back issues of *PE&RS* for online subscribers through the same portal at no additional charge. Please see the Frequently Asked Questions about our journal subscriptions.

The rate of the e-Subscription (digital) Site License Only for USA and Foreign: $899.00; e-Subscription (digital) Site License Only for Canada*: $944.00; **Special Offers:** e-Subscription (digital) Plus Print for the USA: $1,160.00; e-Subscription (digital) Plus Print Canada*: $1,224.00; e-Subscription (digital) Plus Print Outside of the USA: $1,175.00; Printed-Subscription Only for USA: $959.00; Printed-Subscription Only for Canada*: $1,013.00; Printed-Subscription Only for Other Foreign: $974.00. *Note: e-Subscription/Printed-Subscription Only/e-Subscription Plus Print for Canada include 5% of the total amount for Canada's Goods and Services Tax (GST #135123065).

POSTMASTER. Send address changes to *PE&RS*, ASPRS Headquarters, 5410 Grosvenor Lane, Suite 210, Bethesda, Maryland 20814-2144. CDN CPM #(40020812)

MEMBERSHIP. Membership is open to any person actively engaged in the practice of photogrammetry, photointerpretation, remote sensing and geographic information systems; or who by means of education or profession is interested in the application or development of these arts and sciences. Membership is for one year, with renewal based on the anniversary date of the month joined. Membership Dues include a 12-month subscription to *PE&RS*. Subscription is part of membership benefits and cannot be deducted from annual dues. Beginning with the January 2016 issue of *PE&RS*, all members outside of the USA will receive access to the full digital edition of the journal rather than the printed copy. Dues for ASPRS Members outside of the U.S. will now be the same as for members residing in the U.S. Annual dues for Regular members (Active Member) is $150; for Student members it is $50 for USA and Canada; $60 for Other Foreign (E-Journal – No hard copy for all Students); for Associate Members it is $100 (member must be under the age of 35, see description on application in the back of this Journal). A tax of 5% for Canada's Goods and Service Tax (GST #135123065) is applied to all members residing in Canada

A GEOSS Architecture Implementation Pilot Project for Disasters in Chile

By Lucia Lovison, Luciano Parodi, Alvaro Monett, Pablo Dueñas, Stuart Frye, Stefano Nativi, and Mattia Santoro

Introduction

On May 22, 1960, a 9.5-magnitude earthquake, the largest ever recorded, occurred off the coast of Chile. On September 16, 2015 Chile was again struck by a 8.3-moment magnitude earthquake. In 2013, 22 million people worldwide were displaced due to natural disaster events (IDMC, 2014). These disasters have a tremendous impact on the lives of the poorest of the poor, who often are not prepared to cope with natural hazards. For them, a hurricane, an earthquake, a tornado, or a drought, may involve the deepening of their already precarious situation. Figure 1 (UN SPIDER, 2013), documents how loss of life and property due to disasters is increasing globally. Figure 2 (German Indonesian Tsunami Early Warning System or GITEWS, 2015) shows how a framework of Earth observations and information derived from both space and *in-situ* networks can support national and local first responders and provide effective tools to rapidly map injuries, damages and identify possible safe areas.

Photogrammetric Engineering & Remote Sensing
Vol. 82, No. 2, February 2016, pp. 79–85.
0099-1112/16/79–85

doi: 10.14358/PERS.83.2.79

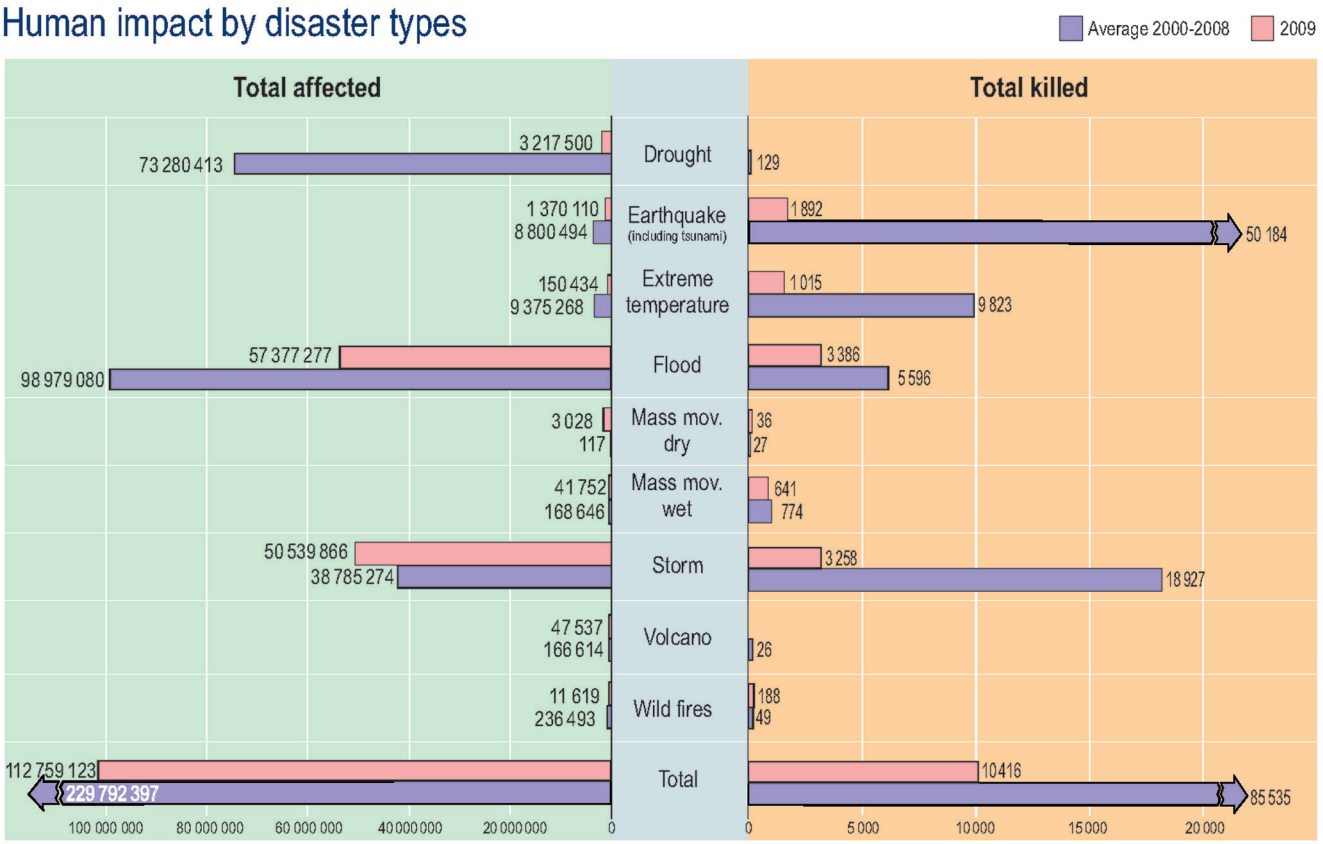

Figure 1. Human Impact by Disaster Type, UN SPIDER, 2013.

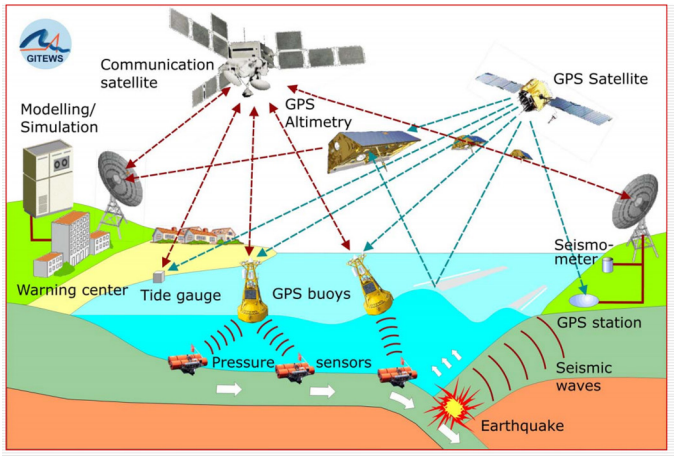

Figure 2. Sensors activated during an earthquake. Source: http://www.gitews.org.

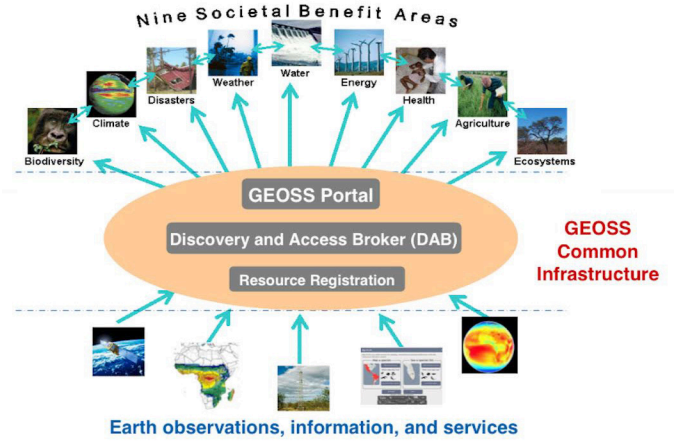

Figure 3. High level GEOSS architecture and GEOSS Common Infrastructure (GCI-GEO, 2014).

The Group on Earth Observations (GEO) was created in Johannesburg, South Africa (UN, 2002; UNISDR, 2005; RIO+20, 2012), and represents a worldwide intergovernmental initiative promoting and collaboratively international disaster mitigation and management activities for disaster risk reduction and increased resilience. GEO is defined as "a voluntary organization and depends on the interest and energy of the international Earth observations and geospatial communities to reach its goals" (GEO, 2015). GEO aims at the creation of a technological infrastructure (called Global Earth Observation System of Systems or GEOSS) to be able to connect different types of information. GEO fosters collaboration between governments, public, and private organizations, for mutual sharing of applications, tools, and Earth observation data. Figure 3 shows that GEOSS activities have been structured within nine Social Benefit Areas (SBAs): agriculture, biodiversity, climate, disasters, ecosystems, energy, health, water, and weather.

GEOSS is a global geospatial information framework where data from users and sensors can be exchanged. This exchange of data is possible by converting and integrating the different data types through interoperable interfaces and standards defined by Service-Oriented Architecture (SOA) on the Internet. The GEOSS Common Infrastructure (GCI) is in charge of connecting Data provider systems and the applications of the GEOSS SBA users (Nativi et al., 2013).

The Architecture Implementation Pilot (AIP), a GEOSS Capacity Building Working Group, was formed by representatives of different national agencies in Chile along with international experts. Chile established its own GEO Group, led by the Ministry of Foreign Affairs, which involves Chilean national agencies and services related to Earth observations. Presently, the agencies includes Centro Sismológico Nacional de la Universidad de Chile (CNS, 2015); Infraestructura de Datos Geospatiales de Chile—Sistema Nacional de Información Territorial (IDE-SNIT, 2015), Ministerio de Bienes Nacionales; Oficina Nacional de Emergencias de Ministerio del Interior y Seguridad Pública de Chile (ONEMI, 2015); Servicio Aerofotogramétrico de la Fuerza (SAF, 2015) Aera de Chile; Servicio Nacional de Geologia y Mineraria de Chile (SERNAGEOMIN, 2015); and Servicio Hydrográfico Oceanográfico de la Armada (SHOA, 2015) de Chile. Each agency contributes to the development and implementation of the Architecture Implementation Pilot (AIP) project for disaster management in Chile.

A high-level architecture of GEOSS and the GCI is depicted in Figure 3. The GEOSS portal is the single Internet gateway to the comprehensive data produced by the GEOSS community. Developed by the European Space Agency (ESA), this portal makes it easier and faster to discover, preview, and download GEOSS resources. The GEOSS portal is powered by the GEO Discovery and Access Broker (DAB) developed by the National Research Council of Italy (CNR). This component stems from the work done in the EuroGEOSS project (Vaccari et al., 2012; Craglia et al., 2011), and applies the brokering approach for multidisciplinary interoperability (Nativi et al., 2013; Nativi et al., 2012; Nativi et al., 2011). This software architecture design implements a "System of Systems" solution based on a brokered architecture to solve interoperability issues. The GEO DAB presently provides broker components for discovery (Nativi and Bigagli, 2009), access (Boldrini et al., 2013), and semantics-enabled search (Santoro et al., 2012) functionalities. The GEOSS Resource Registration tool, a component of GCI, enables both data providers and GEOSS users to register their resources and share their knowledge and experiences. GCI mostly uses geospatial standards such as Open Geospatial Consortium (OGC, 2015, Table 1), ISO-Technical Committee 211 (ISOTC211, 2015) and International Hydrographic Organization (IHO, 2015) standards, but other information technology as well as web and cloud standards are also applied, including the ones promoted by W3C, OASIS (Advancing Open Standards for Information Society) and other organizations.

Table 1. Geospatial Standards from Open Geospatial Consortium, as of June 2015. Some standards were adopted by the International Standardization Organization, Technical Committee--ISO TC 211 and used to exchange different types of data through interfaces according to an interoperable approach. For a complete list, please see: http//www.opengeospatial.org/standards and http://www.isotc211.org

OGC Standards Services	ISO TC211
Web Mapping Service (WMS)	Accepted
Web Feature Service (WFS)/GML	Accepted
Web Coverage Service (WCS)	Accepted
Catalog Service for the Web (CSW)	Accepted
Web Processing Service (WPS)	Accepted
Web Map Tiling Service (WMTS)	not currently
Sensor Web Enablement (SWE)	Accepted
Open GeoSMS	not currently
KML	accepted
GeoSparql	not currently

Objectives

Collaboration amongst people from different countries determines the advancement of skills and scientific knowledge. Technological progress and information science, with the use of interoperable standards, have facilitated the exchange of data silos and associated metadata and fostered global opportunities. While natural disasters are inevitable, the role of GEOSS and its infrastructure is going to mitigate personal and socio-economic effects. Countries can count on increasing resilience capabilities to disasters through more effective prevention, response, and recovery. Here, we show how Chile, within GEOSS, reduces its vulnerability to disasters by undertaking a pilot project for integration of data and metadata.

Data and Study Area

As shown in Figure 4, we concentrated on three testing areas: Talcahuano, Copahue in the Bio Bio Region of Central Chile, and Iquique in northern Chile. On February 27, 2010, the Talcahuano coastal area was devastated by a 8.8-magnitude earthquake and subsequent tsunami. The death toll was 500 and the estimated economic damages totaled about 30 billion US dollars (Prensa Antartica Chilena, 2014). We used data and metadata from the Talcahuano tsunami stations, managed by SHOA (SHOA, 2015) to monitor the occurrence of tsunamis.

One of our testing areas, Copahue, located at the border between Chile and Argentina, has an elevation of about 2,997m above sea level and is the location of a stratovolcano. The caldera extends approximately 6.5km by 8.5km and contains several craters that are aligned in an ENE-WSW direction. The eastern most crater contains a 300m acid lake called El Agrio. In 2013, an increase in volcanic activity and subsequent eruption caused the evacuation of nearly 3,000 people within a

Figure 4. Testing Areas of AIP (Architecture Implementation Pilot) project in Chile.

25km radius from the Chile-Argentina Copahue Region. Other alerts were observed in October and December 2014. The data included in the IDE-SNIT catalog came from a local seismic network managed by SernaGeomin. On March 20, 2014, SernaGeomin raised the alert level of the volcano after observing an increase in the level of the seismic activity.

Most of the image data came from the EO-1 ALI multispectral sensor, usually used to validate Landsat 8 imagery and the Hyperion hyperspectral instrument through a pilot web sensor enablement interface. Both sensors collected data for Copahue at a 30m spatial resolution (Table 2) under a satellite tasking service managed by NASA (2015) Goddard Space Flight Center for EO-1.

On April 1, 2014, the Iquique Region in northern Chile was struck by a 8.2-magnitude earthquake. However, the 8.2 quake does not seem to have completely ruptured the seismogenic active fault that ruptured completely in 1877 (Hayes et al., 2014). The data and metadata came from CSN and from the Incorporated Research Institution for Seismology (IRIS, 2015).

Table 2. Characteristics of sensors ALI and Hyperion on EO-1 Satellite. The 7.7-km Hyperion swath falls on the western edge of the 37-km wide ALI swath. ALI data were used both at level L1T and L1G, respectively with and without geometrically corrected terrain, and where possible, the same level of accuracy was also adopted for Hyperion data.

Bands	ALI (μm)	HYPERION (μm)
Pan	0.480-0.690	Continuous spectra 0.4-2.4
B	0.433-0.453	with 242 Bands.
B	0.450-0.515	
G	0.525-0.605	
R	0.633-0.690	
NIR	0.775-0.805	
NIR	0.845-0.890	
SWIR (8)	1.2-1.3	
SWIR (9)	1.55-1.75	
SWIR (10)	2.08-2.35	
Spatial resolution	Pan: 10m; MS: 30m	30m
Swath width	37km	7.7km

Methods

A simple view of the Chilean Architecture Implementation Pilot (AIP) project developed by the Chile Capacity Building Working Group is shown in Figure 5. Chilean resources were integrated by IDE-SNIT. Later, they were registered to the GCI and make available to any GEOSS user through the geoportal http://earthobservations.org. Presently, any GEOSS user can search, discover, and access the Chilean IDE-SNIT Catalog through the geoportal.

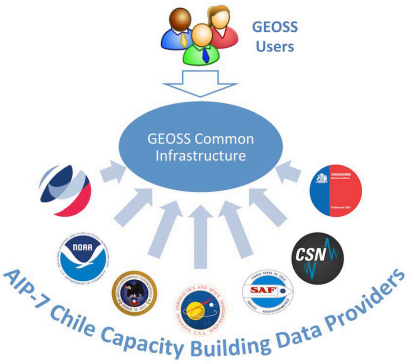

Figure 5. Architecture Implementation Pilot (AIP) Project Agencies – Chile Capacity Building Working Group, as of 2014.

Typical web services architecture was adopted, where data and metadata are converted through geospatial standards and integrated into web services. When metadata services related to different sensors are available or built, they are indexed through the Catalog Service for the Web (CSW) by IDE-SNIT and then registered to the GCI through the GEO DAB brokering service. Once the connection is in place, all metadata and catalog services are searchable and discoverable. When the triggered criteria or policies are established, the Chilean emergency agency, ONEMI, may broadcast alert warnings on natural disasters to different types of users and web clients.

Figures 5 also considers the data from multiple sensors, such as through terrestrial stations, space, sea, and air sensors, as well as data made available through the GCI by the communities of experts, researchers, specialized NGOs, and social networks. Any authorized GEOSS user can access and discover the national and international GEOSS resources during a disaster. GEOSS users can also perform other operations, such as a pre- and post-seismic analysis of the imageries supplied by both SAF and NASA.

The National Catalog of the Chilean Spatial Data Infrastructure (SDI) by IDE-SNIT is shown in Figure 6. The web site allows for the search and discovery of geospatial products generated by State agencies, such as digital maps published on websites and other formats that contain geospatial information, including studies, reports, statistical tables, and charts. The work of the IDE-SNIT focuses on ensuring the enrichment of the contents of the National Catalog tool in close collaboration with regional, national, international stakeholders and users. It is possible to access the National Catalog and all its search capabilities from the Chilean SDI website. Thanks to the OGC standard named "Catalog Service for the Web (CSW)," the National Catalog of Geospatial Information from Chile is interoperable with other metadata catalogues. The IDE-SNIT catalog is, for example, interoperable with the metadata cat-

alog of SERNAGEOMIN, which is so far only available to authorized institutions within Chile. The IDE-SNIT catalog can harvest more than 6,500 metadata records, relative to analog, digital information, and web services related to geological charts, volcanic hazard maps, and mineral deposits. For example, when performing a search using the keyword "Copahue," a metadata record under ISO 19115/19139 standard is deployed, and it is possible to review its contents as it relates to the metadata published by SERNAGEOMIN. The Chilean IDE-SNIT catalog services are then brokered by the GEODAB service for an easier search, discovery, and access to national and international resources through the GEOSS geoportal.

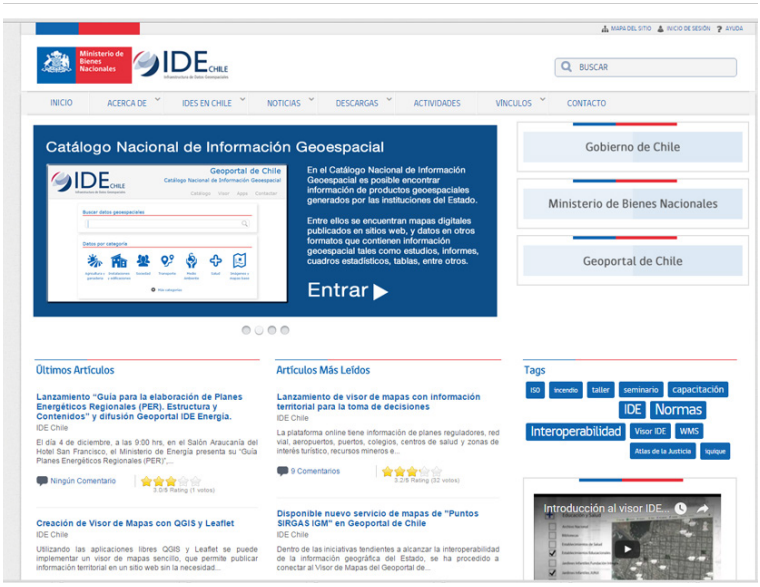

Figure 6. National Catalog of the Chilean Spatial Data Infrastructure (SDI) web site, IDE-SNIT.

The result of a pilot web processing service for Copahue, where a pan-sharpening algorithm was developed by NASA, is shown in Figure 7a. Similarly, Figure 7b displays an image of Copahue from the EO-1 ALI satellite sensor that contributes to the high-resolution imagery on Chile's Sistema Satelital para Observación de la Tierra (SSOT), also known as FASat-Charlie. The EO-1 tasking service pilot capability to execute observation acquisitions by EO-1 satellite allows one to optimize the viewing opportunities of disaster areas and provide improved situational awareness, as events unfold, within a spatial resolution of 10 m. Figure 8 shows a mashup formed by overlaying Google Earth imagery with the raster layer resulting from the Web Coverage Processing Service (WCPS) SWIR composite image of October 8, 2014. The optical image was collected through the pilot satellite tasking service established on EO-1 and a pilot web coverage processing service (WCPS) that used a SWIR algorithm (Table 2) of L1G images taken by EO-1 ALI. The resulting product was overlaid onto Google Earth in order to monitor hot areas of volcanic activity in the Copahue region.

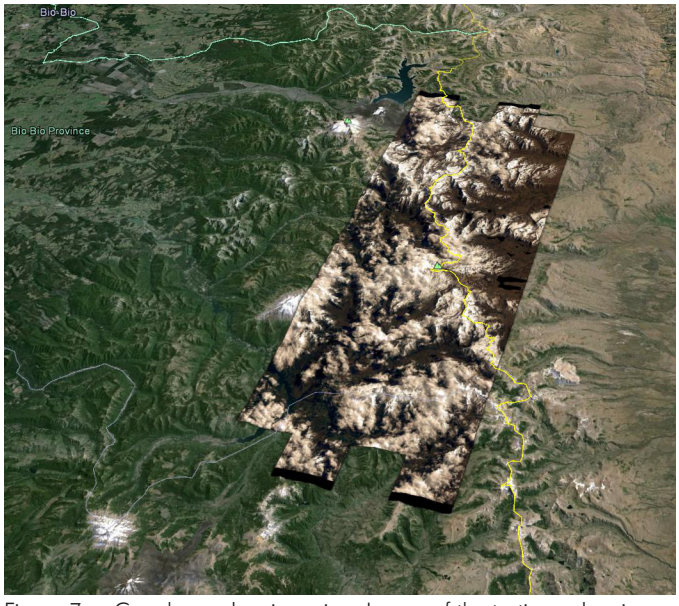

Figure 7a. Copahue volcanic region. Image of the testing volcanic area Copahue from the EO-1 ALI of 8 October, 2014, overlaid on Google Earth. Pan-sharpening algorithm - Testing - Copahue volcanic region. EO-1 image provided courtesy of NASA. Processing done by Lucia Lovison.

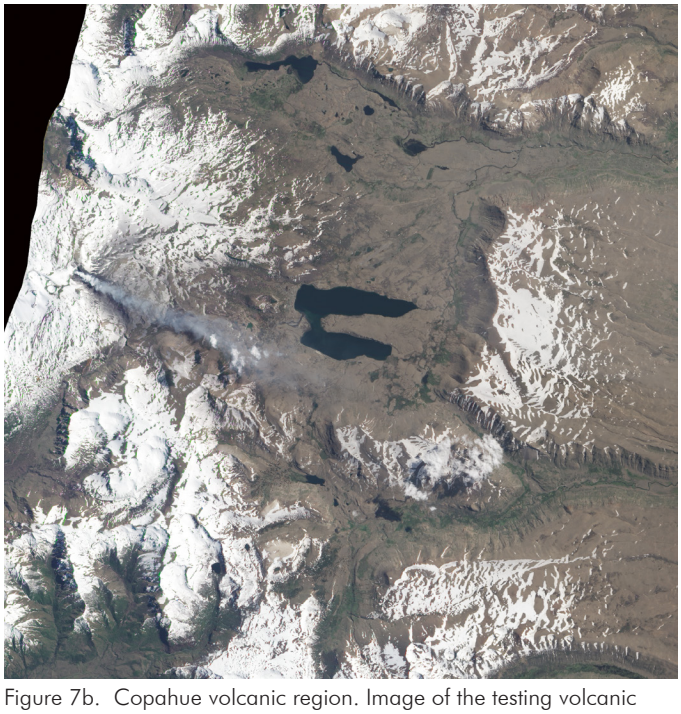

Figure 7b. Copahue volcanic region. Image of the testing volcanic area Copahue from EO-1 ALI on 21 October, 2014. It is a natural color image obtained by combining ALI visible spectral bands 1, 2, and 3 (30m resolution Red-Green-Blue channels) in selected proportions and overlaying the resulting color image on the 10m panchromatic band for high resolution "feathering" then cropping to show only the zoom-in to the volcano Copahue site with annotations added. EO-1 image provided courtesy of NASA. Processing done by Stuart Frye.

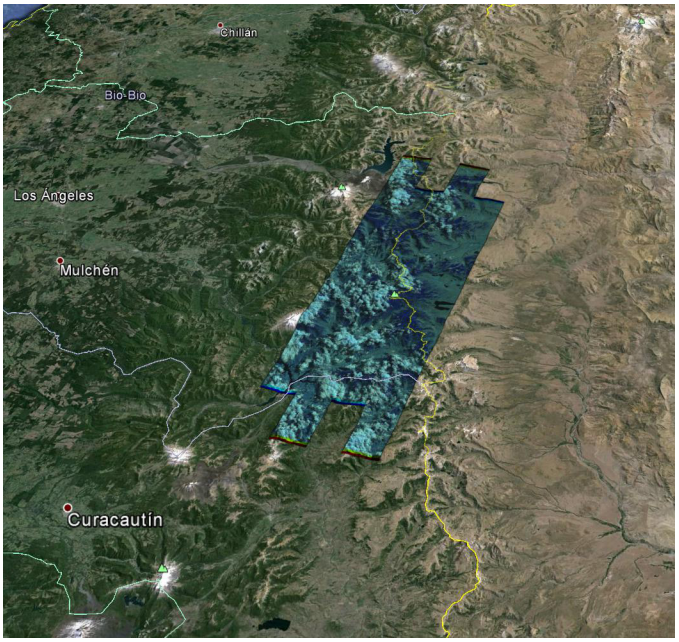

Figure 8. Copahue volcanic region. Mashup of Google Earth with Web Coverage Processing Service testing that used a SWIR image (band 8,9,10, ALI sensor on EO-1 satellite) and pan-sharpening image of Copahue volcanic region. EO-1 Image of 8 October, 2014 provided courtesy of NASA. Processing done by Lucia Lovison.

Pilot Results and Discussion

Thanks to the GCI framework, authorized users may access Web Map Service (WMS), Web Feature Service (WFS), and Sensor Observation Service (SOS) from either any Chile agency or GEOSS organization through the geoportal. At present, we are achieving the following goals in the AIP- Chile Capacity Building Working Group for disasters:

- develop a working relationship within each participant organization despite linguistic, technical and other differences;
- access to and integrate the observational data;
- develop and propose policies and strategies to improve actions by the emergency agency in Chile;
- increase communication and coordination between the national, regional, and international communities in support of reducing risk and better manage disasters.

The use of multiple types of geospatial data from national and international sources greatly expands the capabilities and decreases the cost of managing risks at different scales and stages related to a disaster.

In the development of the testing cases, we are building the requirements and relationship of data, models, and services that can be used during the occurrence of a disaster. Our belief is such that, given the technological advances in digital information, the management of disaster events can be further aided by technology and science.

Thanks to the social network and the big data analysis, professionals from different branches (scientists, geographers, cartographers, and computer system experts) are combining new and sophisticated initiatives to monitor phenomena, describe models and scenarios, and simulate future challenges. Presently, experts forecast that each person will consume data on a mobile device for 1 GB per day by 2020 (Atri, 2015). Furthermore, by 2020 experts believe that 90 percent of the world will be mobile (Lonergan, 2015). In this context, there are growing opportunities to involve citizens through social networks in the process of monitoring and generating information (crowdsourcing and citizen observatory within GEOSS).

GEO works to support risk modeling through the implementation of the Global Earthquake Model initiative (GEM, 2015). GEOSS also helps the scientific community to better understand the causes and dynamics of geological threats through the GEO Geohazard Supersites and Natural Laboratories initiative.

Conclusions

This is a report on a multi-year project aimed at reducing Chile's vulnerability to disasters. Thanks to interoperable geospatial standards through which we convert data and metadata coming from a variety of sources, we register them to the GCI and make them accessible, searchable, discoverable and integrate them through the geoportal. As described in the report by the US President's Council of Advisors of Science & Technology (Holdren, 2014), some data are "born digital," meaning that it is created specifically for digital use by a computer or satellite. Other data are "born analog," meaning that it emanates from the physical world, but can be converted into digital format, such as information captured by phones. Thanks to GEOSS and its model of service-oriented architecture, we can bring together big, disperse, and disparate sources of socially-based data, as well as achieve remarkable results in the mitigation of the vulnerability of societies to natural disasters.

The declining cost of collection, storage, and processing of data, combined with new sources of data like sensors, cameras and other observational technologies, means that we live in a world of near-ubiquitous data collection. This explosion of data will drive demand for high-performance computing and push the capabilities of even the most sophisticated data management technologies in a distributed environment.

Our Chile Capacity Building AIP Working Group future goals are to continue working in order to facilitate alert, preparation, response and recovery from disasters to increase communication and coordination between the national, regional and global communities, and to improve the national response to disasters, so that GEOSS complements other initiatives.

Acknowledgements

The authors are indebted to the Chilean agencies for the data supplied, to NASA and ESA for the facilities and services they have provided.

References

Atri, K. (2015). http://www.teleinfotoday.com/knowledge-center/articles/400-10-x-10-x-10-the-formula-for-beyond-4g (Last date accessed on 06 January 2015).

Boldrini, E., Santoro, M., Papeschi, F., & Nativi, S. (2013). Data Access Services interoperability in the Geosciences by means of the GI-axe Brokering Framework, *EGU General Assembly Conference Abstracts*, Vol. 15, EGU2013-7777.

CSN. (2015). http://www.sismologia.cl/ (Last date accessed on 06 January 2015).

Craglia, M., Nativi, S., Santoro, M., Vaccari, L., & Fugazza, C. (2011). Inter-disciplinary interoperability for global sustainability research. *Proceedings of Geos 2011 Conference, Lecture Notes in Computer Science*. Springer edition.

GEM. (2015). http://www.globalquakemodel.org (Last date accessed on 03 August 2015).

GEO. (2015). http://www.earthobservations.org/ (Last date accessed on 06 January 2015).

GITEWS. (2015). http://www.gitews.org/homepage/ (Last date accessed on 06 January 2015).

Hayes, G.P, Herman, M.W., Barnhart, W.D., Furlong, K.P., Riquelme, S., Benz, H.M., Bergman, E., Barrientos, S., Earle, P.S., & Samsonov, S. (2014). Warning signs of the Iquique earthquake. *Nature*, 512, 295-298.

Holdren, J.P. (2014). Big data and privacy, report to the president. *Executive Office to the President*, 1-76.

IDE-SNIT. (2015). http://www.ide.cl (Last date accessed on 06 January 2015).

IDMC. (2014). Global estimates 2014: People displaced by disasters, *Internal Displacement Monitoring Centre* (IDMC), 67.

ICSMD. (2014). https://www.disasterscharter.org/web/guest/home;jsessionid=5A3B2B7A4E729655066D2C-3187B845E5.intlcharter-prod4040 (Last date accessed on 06 January 2015).

International Hydrographic Organization, IHO. (2015). http://www.iho.int/srv1/index.php?lang=en (Last date accessed on 03 August 2015).

IRIS. (2015) http://www.iris.edu/hq/ (Last date accessed on 03 August 2015).

ISOTC211. (2015). http://www.isotc211.org/ (Last date accessed on 03 August 2015).

Lonergan, D. (2014). http://maps.yankeegroup.com/ygapp/content/2e7a402ed6d34b3bace2da6a3ffd0c4e/68/DAILY-INSIGHT/0 (Last date accessed on 06 January 2015).

NASA. (2015). http://www.nasa.gov/ (Last date accessed on 03 August 2015).

Nativi, S., & Bigagli, L. (2009). Discovery, mediation, and access services for earth observation data. *IEEE Journal on Selected Topics in Applied Earth Observations and Remote Sensing, 2*(4), 233-240.

Nativi, S., Khalsa, S.J., Domenico, B., Craglia, M., Pearlman, J., Mazzetti, P., & Rew, R. (2011). The brokering approach for Earth science cyberinfrastructure. *NSF EarthCube White Paper*. https://rdalliance.org/system/files/filedepot/97/earthcube(BrokeringApproach)_v3.3.pdf (Last date accessed on 06 January 2015).

Nativi, S., Craglia, M., & Pearlman, J. (2012). The brokering approach for multidisciplinary interoperability: A position paper. *International Journal of Spatial Data Infrastructures Research,* 7, 1-15.

Nativi, S., Craglia, M., & Pearlman, J. (2013). Earth science infrastructures interoperability: The brokering approach. *IEEE JSTARS, 6*(3), 118–1129.

Open Geospatial Standards. (2014). http://www.opengeospatial.org/standards (Last date accessed on 06 January 2015).

ONEMI. (2015). http://www.onemi.cl/cat/ (Last date accessed on 06 January 2015).

Prensa Antartica Chilena. (2014). http://prensaantartica.wordpress.com/ (Last date accessed on 06 January 2015).

RIO+20. (2012). http://sustainabledevelopment.un.org/rio20.html (accessed on October, 2014).

SAF. (2015). http://www.saf.cl/ (Last date accessed on 06 January 2015).

Santoro, M. Mazzetti, P., Nativi, S., Fugazza, C., Granell, C., & Diaz, L. (2012). Methodologies for augmented discovery of geospatial resources. *Discovery of Geospatial Resources: Methodologies, Technologies, and Emergent Applications*, Laura Diaz, Carlos Granell, & Joaquin Huerta, eds.172-203. Hershey, PA: Information Science Reference.

SERNAGEOMIN. (2015). http://www.sernageomin.cl/volcanes.php (Last date accessed on 06 January 2015).

SHOA. (2015). http://www.shoa.cl/index.htm (Last date accessed on 06 January 2015).

UN. (2002). http://www.un-documents.net/jburgdec.htm (Last date accessed on 06 January 2015).

UNISDR. (2005). http://www.unisdr.org/2005/wcdr/intergover/official-doc/L-docs/Hyogo-framework-for-action-english.pdf (Last date accessed on 06 January 2015).

UN SPIDER. (2013). http://unstats.un.org/unsd/geoinfo/RCC/docs/rcca10/E%20Conf_103_44_UN-SPIDER_RCCA-Aug2013_v3.pdf (Last date accessed on 06 January 2015).

Vaccari, L., Craglia, M., Fugazza, C., Nativi, S., & Santoro, M. (2012). Integrative research: The EuroGEOSS experience. *IEEE Journal of Selected Topics in Applied Earth Observations and Remote Sensing, 5*(6), 1603-1611.

About the Authors

Lucia C. Lovison is a GEOSS-AIP Capacity Building Leader of GEOSS and part-time Geospatial Director and Librarian of Afriterra Foundation. **Luciano Parodi** is the leader of Chile GEO and a Foreign Service Diplomat of the Ministry of Foreign Affairs. **Alvaro Monett** is the Executive Secretary of IDE-SNIT. **Pablo Dueñas** is a Supervisor and Program Manager, SAF. **Stuart Frye** is a satellite systems engineer at the NASA Goddard Space Flight Center (GSFC). **Stefano Nativi** coordinates the Florence division of the Institute of Atmospheric Pollution Research of the National Research Council of Italy (CNR-IIA). **Mattia Santoro** is a researcher at the Earth and Space Science Informatics Laboratory (ESSI-lab) of the National Research Council of Italy, Institute of Atmospheric Pollution Research (CNR-IIA).

THE ASPRS STUDENT COMMUNITY WELCOMES THE NEW YEAR AND ALL STUDENT MEMBERS!

The Student Advisory Council (SAC) will continue working with the ASPRS Executive Committee to improve the ASPRS student experience.

This year the SAC will continue its role in voicing students' opinions and discuss ways the Society can better serve its student members. Currently, SAC is collaborating with the Early Career Professional Council (ECPC) liaison team to build its identity. Introduced in 2015, the SAC ECPC liaison team is a vital part of students transitioning into the workplace and is encouraged to create initiatives to increase student and professional retention and satisfaction within ASPRS. Students are welcome to provide suggestions and comments on as well as join this liaison team.

Student activities are an important part of the ASPRS community and we want to ensure that student members can benefit their educational/professional careers by interactively communicating with their fellow members in the nationally and regionally organized ASPRS activities. SAC would like to draw your attention to the following changes and opportunities that you may be interested in.

Geoleague Competition—Be prepared for the return of the Geoleague competition. This is the sixth year the GeoLeague Challenge to be held at IGTF, the ASPRS Annual Conference, held in April. To celebrate the 100th Anniversary of the National Park Service, this year's challenge is to use freely available imagery to produce an innovative visualization product featuring the national park of your choice.

SAC Sessions and Topics—This year we plan to arrange two educational track sessions at IGTF, the ASPRS Annual Conference and invite a student/employer speaker especially for students. We would like to have new submissions of abstracts related to educational topics. Students are also encouraged to participate in the SAC sessions to get professional experiences from our previous student members.

Social Media Follow-up—Now our SAC social media, including youtube, twitter, facebook, and *PE&RS* page are now active. Keep yourself updated with the latest news by following us on these social media. Also, submit your educatinal or professional stories for posting on our social media pages.

ASPRS Annual Conference—Do not miss this great opportunity to meet and talk with your fellow members and to share your own research/professional experience! It will be a great opportunity for all to enjoy.

Student Internship—This will be a great chance for members to participate in IGTF, the ASPRS Annual Conference. Interns will receive complimentary conference registration, lodging, and a stipend. Fill out your application by February 12 to get reviewed.

ISPRS 2016 Conference Prague, July 12 to19 2016—ISPRS is an international sister organization to ASPRS. Members of ISPRS have had the opportunity to attend and present at ASPRS Conferences. While several members of ASPRS plan to attend the 2016 ISPRS Conference, the Student Advisory Council is calling for a student presence this year. As a result of this, a few ASPRS student chapters have begun the fundraising process. The SAC is hereby proposing that student members who are interested in attending this conference coordinate efforts with fellow students. This year the conference will take place in Prague Cz and will be an excellent opportunity for students to interact with some of the finest PRS minds on the globe. Students who are interested can contact the SAC directly at studentcouncil@asprs.org. For more information about the conference please visit this page; www.isprs2016-Prague.com.

MAPPINGMATTERS

YOUR QUESTIONS ANSWERED

The layman's perspective on technical theory and practical applications of mapping and GIS

BY Qassim A. Abdullah, PH.D., PLS, CP**

QUESTION:

Q: What are the situations that require us to redo the boresighting of the aerial camera/inertial measurement unit (IMU) misalignment angels? We understand that a new boresight determination is needed, only if, the IMU is removed from the camera and re-attached again. However, we recently encountered a group of experts on the subject who suggested doing boresight calibration for every mission in the project area to increase the accuracy. This poses a great burden to our operations and budget. If we have to fly eight different blocks with eight different missions, we will have to do eight boresight calibrations. Does it really increase accuracy if we boresight the IMU for every mission?

Mulualem Yeshitila, Ethiopia

Dr. Abdullah: Before I address the issues raised in the question, I would like to elaborate on IMU and the need for its boresight calibration for readers who are not familiar with the subject. The IMU, which was introduced to the mapping industry in the late 90s, is a system that uses integrated GPS and inertial technology to measure camera attitude to accuracy sufficient to a certain degree to support photogrammetric mapping. The IMU measures three axes rotational angles in space for object that is rigidly attached to it. The IMU senses gravity and measures acceleration using sets of gyros and accelerometers. Therefore, it has its own reference frame that is different from the camera body frame, the mapping frame, and the mapping coordinates system. For the rotational angles measured by the IMU to be translated to rotation angles referenced in the camera frame and subsequently in the mapping frame, the rotational angles between the camera body frame and the inertial body frame need to be determined accurately. The process of determining such rotation is what we refer to as "boresighting", "IMU misalignment calibration", or "IMU boresighting". In addition, the GPS unit and the IMU are physically separate from the perspective center of the camera lens, and a constant displacement exists between their positions. The extent of this displacement also needs to be determined using conventional surveying techniques prior to the flight missions. The latter displacement is usually referred to as the "lever arm." On the other hand, the rotational IMU misalignment is determined by performing an aerial triangulation process on a small controlled block of imagery usually referred to as the "boresight area." The exterior orientation parameters computed from the aerial triangulation of the boresight area are then used by the IMU processing software to determine the offset values and export the rotational angles (omega, phi, kappa) for every image of the block according the photogrammetric or mapping frame. As for the question on whether an IMU boresighting is needed with every block or mission, my direct answer is no you do not always need to. The importance of the IMU boresighting quality and frequency depend on how the IMU data is used in the mapping process. IMU can be used in two ways during a mapping process. Those are:

1. Direct Sensor Orientation: Here, the IMU-derived exterior orientation angles (omega, phi, kappa) of the camera are fed directly into the photogrammetric plotter or software to set up the stereo models or to perform ortho-rectification. In other words, there is no aerial triangulation in the workflow. In this scenario, the quality and the accuracy of the boresight angles are very critical for obtaining parallax-free stereo geometry. The need and the frequency of the IMU boresighting are widely disputable as IMU manufacturers believe that their systems are stable enough and do not require a boresight determination with every mission. However, users' experiences defeated manufacturers' claims. In many cases, users found boresight determination was needed more frequently than the manufacturers claimed. I do not believe that too many mapping businesses—if any—produce mapping products

"The importance of the IMU boresighting quality and frequency depend on how the IMU data is used in the mapping process."

Photogrammetric Engineering & Remote Sensing
Vol. 82, No. 2, February 2016, pp. 87–88.
0099-1112/16/87–88

doi: 10.14358/PERS.83.2.87

"You do not need to do a new IMU boresighting with each mission as long as you use the IMU-derived exterior orientation within the aerial triangulation and not for direct sensor orientation"

that are regularly meeting a certain map accuracy standard using the direct sensor orientation method.

2. IMU to Aid Aerial Triangulation: This is the most common use of IMU in photogrammetric mapping. Like Airborne GPS, IMU can be used in the aerial triangulation process to provide better estimation for the initial values of the input parameters and to reduce the number of unknowns, therefore decreasing the reliance on ground control points. Since the GPS-derived camera positions, the IMU-derived orientations, ground controls points, and all other measurements and parameters are considered as observations with certain errors budgets, i.e. weighted, in the mathematical model of the aerial triangulation, the need for perfect boresight misalignment diminishes as such less-than-perfect values will be refined and adjusted in the aerial triangulation process anyway. Based on the last statement, you do not need to do a new IMU boresighting with each mission as long as you use the IMU-derived exterior orientation within the aerial triangulation and not for direct sensor orientation. As for how often you need to redo the IMU boresighting, I can safely say that you do not need to redo it if you did it right the first time and if the IMU was not physically disturbed during operations or removed from the camera.

Again, if you are using the IMU-derived orientations to aid aerial triangulation, then you can relax or ignore the experts' advice, as you do not need a new IMU boresighting for each mission. In fact, you can achieve excellent results from frame-based aerial triangulation using only airborne GPS and ground controls, i.e. without data from IMU. That is not the case if you are using a push broom type of camera, where the IMU input is integral for processing the imagery. However, even if you are using a push broom sensor, the IMU-derived orientation is always updated during the aerial triangulation adjustment. Therefore, a slight problem in the boresight values is not going to cause a catastrophe.

Finally, even if you are using the IMU-derived orientations for direct sensor orientation, performing a new IMU boresighting does not always guarantee parallax-free stereo models setup. Experience taught us that you may experience severe parallax on some stereo pairs in the block despite the fact that you performed new IMU boresighting for that mission. Such behavior could be caused by different system components other than the IMU. High-end IMU is great technology and has excellent performance and accuracy. To be fair to the IMU manufacturers, less-than perfect IMU-derived exterior orientation performance does not always mean that the IMU was not accurate. The aerial camera of today is a complex system that contains imaging sensor or camera, GPS, IMU, complicated wiring and cables, many electronic signals and signals synchronization, and IMU-to-camera mount. The IMU could perform perfectly, but other problems could be happening during flight due to one or more of the following:

- Faulty design or fabrication of the camera housing that holds the lens cone
- Defect in the IMU-to-camera mount or in its performance in accurately transferring the motion dynamics of the lens to the IMU box, especially in severe turbulence or vibration caused by a weather front
- Excessive thermal and mechanical stresses that the imaging system is subjected to during rough aerial operations and/or vast change between the temperature on the ground at the hanger and the atmospheric temperature at a flying altitude of 4,000 meter or higher
- Signals synchronization or timing problems between GPS, IMU, and the camera shutter opening signals

"You can achieve excellent results from frame-based aerial triangulation using only airborne GPS and ground controls, i.e. without data from IMU"

All these sources of errors could result in less accurate performance of the IMU-derived exterior orientation despite the high accuracy of the IMU itself. I hope this addresses your concerns and contributes to a more efficient production mapping process.

***Dr. Abdullah is Senior Geospatial Scientist and Associate at Woolpert, Inc. He is the 2010 recipient of the ASPRS Photogrammetric (Fairchild) Award.*

The book comprises a total of 12 chapters, contributed by 13 top experts in the fields of aviation, aeronautics, control and information systems, and engineering.

The editors of the book are professors of Aviation and Unmanned Aircraft Systems research at the Kansas State and the New Mexico State Universities.

In a highly dynamic and constantly evolving as the UAS industry, the book aims at identifying and surveying the basic fundamentals of UAS operations, and as such, it can serve as textbook for introductory collegiate courses in UASs.

Written from a non-engineering civilian operational perspective, the book starts with the history of UASs and continues with the presentation of current technology and what to be expected in the future. Covering all facets of UAS elements and operation, as well as the safety procedures and human factors, it gives the reader a practical understanding of what it takes to safely operate UASs.

Chapter 1 "History" details the history of UAS, especially from a point of view of military applications.

Chapter 2 "Unmanned Aircraft System Elements" describes the UAS elements: Command and Control, Communication, Payload, Launch, Human element. The aim is to quickly introduce the reader to the operational issues of UAS use.

Chapter 3 "U.S. Aviation Regulatory System" focuses on a hot issue, which is quite essential for the industry to grow and evolve in an orderly fashion. It describes in detail the existing aviation regulatory systems in U.S. and internationally. It describes the standards and regulations and identifies the existing gaps with respect to UAS.

Chapter 4 "Certificate of Authorization Process" and Chapter 5 "Unmanned Aircraft System Operations" continue on the previous chapter and studies the certification procedure for authorization in UAS operation. FAA administration procedures and airworthiness certification is presented, since the integration of UAS into the national airspaces seems to be a critical factor for the growth of the UAS industry.

Chapter 6 "Unmanned Aircraft Systems for Geospatial Data" provides a brief summary of sensors used on board a variety of UAS and for different applications. Subsequently, applications of UAS in environmental monitoring and management (precision agriculture, rangeland, ocean and coastal research, contaminant spills and pollution), traffic sensing and disaster response (fires, floods, hurricanes, tornados) are reviewed.

Chapter 7 "Automation and Autonomy in Unmanned Aircraft Systems" is a comprehensive review of human-centric and techno-centric taxonomies and types and levels of automation and introduces the reader to the concepts of design and functional issues of UAS automation. In a highly theoretical manner, it reviews issues like trade-off between operator workload and operator situation awareness, the importance of system-operator communication, and the system reliability on operator trust.

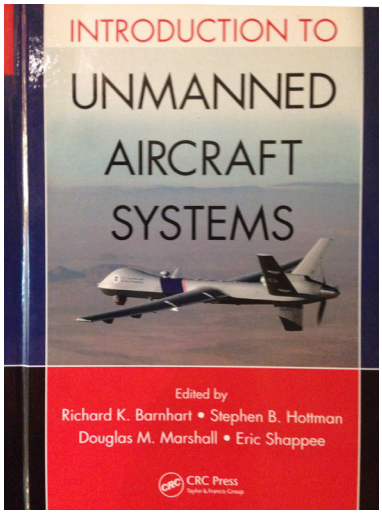

Introduction to Unmanned Aircraft Systems

Edited by R. Barnhart, S. Hottman, D. Marshall, E. Shappee, CRC Press, Taylor and Francis

2012, 215 pp., ISBN 978-1-4398-3520-3 (hardcover), $67.96

Reviewed by Petros Patias, Professor, School of Rural & Surveying Engineering, Faculty of Engineering, The Aristotle University, Thessaloniki, Greece.

Chapter 8 "Safety Assessments" examines several safety tools and techniques, such as hazard analysis and its various forms. It also covers the risk assessment process and provides some guidance on developing a risk assessment tool. Finally, it looks at safety evaluations and provides some thoughts on UAS accident investigation considerations.

To safely operate UAS in the National Airspace System, traffic alert and collision avoidance is mandatory, at least to a level of a manned aircraft. Chapter 9 "Detect, Sense and Avoid" addresses the issue by analyzing the existing technology in both cooperative and non-cooperative aircrafts. Cooperative technologies include the Traffic Alert and Collision Avoidance System (TCAS) and

continued on page 92

Photogrammetric Engineering & Remote Sensing
Vol. 82, No. 2, February 2016, pp. 89–92.
0099-1112/16/89–92

doi: 10.14358/PERS.83.2.89

Michael Zoltek, Senior Project Manager, Woolpert

Licensing, Certification and New Technologies

It is a challenge in the current environment of fast-paced technological advancement to ensure those providing products and services are both capable and qualified to fulfill the needs of clients and customers. How do users of current and future technologies choose providers? How do they know that the product or service they are receiving will have a reasonable expectation for correctness and completeness? Licensure and certification have provided traditional paths for demonstrating knowledge and technical proficiency. "Certification" has historically been utilized to evaluate and ensure technical competence, while "licensure" has traditionally been the mandate of legislation (at both the state and federal level) premised by the need to "***protect the public health, safety and welfare***." Traditional requirements to become licensed include a combination of a defined level of formal education, experience (e.g., time), demonstrated competency in practice (e.g., examples of past work), references from other licensed persons and validation by testing.

Licensing has long been a requirement for doctors, lawyers, engineers and land surveyors. As technologies have advanced, many states have realized the need to license photogrammetrists, providers of a variety of geospatial information (e.g., geographic information systems professionals, or GISPs) and recently those operating unmanned aerial systems (UAS), such as pilots and/or flight planners. As more states enact legislation relating to existing and new geospatial products and services, it is difficult for practicing professionals, state and national organizations, and the public to keep up with changes to existing rules and regulations and the addition of new rules and regulations. The American Society for Photogrammetry and Remote Sensing (ASPRS), as the leading scientific organization representing the photogrammetry and remote sensing profession, provides a resource to readily access this new and changing information through its published maps and variety of geospatial mapping products and services[1]. The "Licensure Maps and Regulations" website[1] shown in Figure 1 gives meta data on State Surveying Regulations; State Licensure Map for GIS Services, Lidar and Topographic Products, Georeferenced Imagery and Authoritative Imagery, respectively, with each state's metadata on existence of State Regulations, Board Website, Individual State Regulations and Composite State Regulation Document. Currently there are twenty-one (21) states that have existing regulations relating to georeferenced imagery products and services, thirty-three (33) that have existing regulations relating to authoritative imagery products and services, forty-seven (47) states with regulations relating to topographic mapping-related products and services, and fifteen (15) states with existing regulations relating to GIS-related products and services.

State Licensure Map - Authoritative Imagery

Disclaimer: This map represents the ASPRS best effort at determining where the specific referenced product or service (Georeferenced Imagery, Authoritative Imagery, or Topographic Mapping) is addressed by individual state regulations relating to Surveying & Mapping. This map is not meant to be an interpretation of said regulations. Before providing geospatial mapping services in any State, practitioners should perform the appropriate research necessary to make a proper determination of which licensing requirements apply to the specific type of work that will be performed.

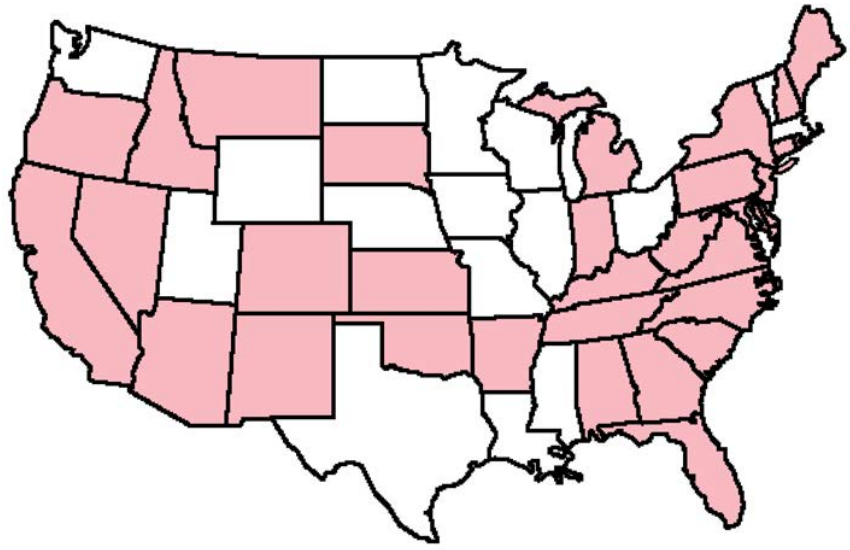

Figure 1: From the "Licensure Maps and Regulations" in ASPRS Profession Practice Division: The State Licensure Map—Authoritative Imagery

Having a list of the current regulations is just the first step. Every provider of a potentially regulated product or service should be aware of and understand how specific state regulations impact their practice because each state regulates geospatial products and services differently. Products or services that are regulated in one state may not be regulated the same way (or at all) in another state. For the practicing geospatial professional (whether it be an engineer, surveyor, photogrammetrist, GISP or UAS pilot), knowledge of an individual area of practice is essential. Knowledge of state, local and possibly even federal regulations are required to properly perform services, provide products and fulfill contractual requirements for clients.

As mentioned earlier, the geospatial industry is going through rapid changes as advancements are made in measurement technologies and capture platforms. The miniaturization of measurement technologies (e.g. imagery and lidar systems) combined with the new and readily available low-cost UAS have allowed for an unprecedented opportunity for both individuals and firms to get into the business of collecting data to support an ever-expanding variety of geospatial products and services. The field-to-finish (e.g., black box) software solutions supporting these new advancements allow for anyone to provide products that appear to be the same as those that have historically been created utilizing validated photogrammetric methods.

At almost every major geospatial conference in the last few years, the "big" giveaway is a UAS. Does this mean that anyone can use this technology to create and provide services to the public? Various states have proposed or enacted legislation that clearly states otherwise. Over the last few years, there have been regulations enacted by over twenty (20) states regarding UAS use[2]. The 2012 FAA enacted its Section 333 exemption policies[3], and in November 2015 published its report, *Unmanned Aircraft Systems (UAS) Registration Task Force (RTF) Aviation Rulemaking Committee (ARC) Task Force Recommendations Final Report*[4], in which it recommended that all UAS flying within U.S. airspace that have a mass of more than 25 grams (~0.55 pounds) be registered with the FAA.

The new legislation and rules are examples of how the landscape of certification and licensure is being affected by new technologies. These rapid changes beg the questions as to which geospatial products and services should require certification and which should require licensure. How will the current and future practice of certified and/or licensed professional practice be affected by these changes? The answers to these questions will define the future of all practicing geospatial professionals, whether they are engineers, surveyors, photogrammetrists, GISPs or UAS pilots.

To help facilitate appropriate regulations regarding certification and licensure, the ASPRS Professional Practice Division (PPD)[5] proactively engages states to discuss potential legislative changes, and assists states by reviewing current and proposed state licensure laws related to geospatial products and services. ASPRS PPD works with individual states to ensure that there is an available licensure path for appropriately educated and experienced professionals. ASPRS PPD also actively engages other national geospatial organizations (URISA, NSPS, MAPPS, etc.) to coordinate efforts of regulation review and interpretation, with the goal of appropriately advising legislative bodies on legislation relating to existing and future geospatial products and services. Additionally, ASPRS has formed its Unmanned Aerial Systems Division whose "objectives include outreach and education, liaising with UAS-interested parties outside the Society, development and promotion of standards and best practices, establishment of calibration and validation sites, and credentialing and certification activities…"[6]

While it is in the best interest of every practicing professional to be active in his or her individual national organizations, it is incumbent upon every practicing geospatial professional to stay up to date on the specific rules affecting his or her practice. The combination of these two items is the only way to ensure the appropriate implementation of certification and licensing requirements, while also ensuring the protection of the health, safety and welfare of the public in our fast-paced geospatial world.

References

[1] http://www.asprs.org/PPD-Division/Licensure-Maps-and-Regulations.html

[2] *Current Unmanned Aircraft State Law Landscape*, by National Conference of State Legislators, November 25, 2015: *http://www.ncsl.org/research/transportation/current-unmanned-aircraft-state-law-landscape.aspx*

[3] *FAA Modernization and Reform Act, of 2012, HR 658*, by Federal Aviation Administration (FAA): https://www.faa.gov/uas/media/Sec_331_336_UAS.pdf and https://www.faa.gov/uas/legislative_programs/section_333/

[4] *Unmanned Aircraft Systems (UAS) Registration Task Force (RTF) Aviation Rulemaking Committee (ARC) Task Force Recommendations Final Report* November 21, 2015: *https://www.faa.gov/uas/publications/media/RTFARC-FinalReport_11-21-15.pdf*

[5] http://www.asprs.org/Divisions/Professional-Practice-Division.html

[6] http://www.asprs.org/Divisions/Unmanned-Autonomous-Systems-Division.html

Author

Michael Zoltek, mike.zoltek@woolpert.com, is Senior Project Manger at Woolpert; Director of the Professional Practice Division (PPD) of ASPRS; ASPRS Certified Photogrammetrist; State Licensed Surveyor/Photogrammetrist* - AL, AZ, CA, CO, CT, FL, GA, ID, LA, MS, NC, ND, NM, NV, NY, OR*, PA, SC, SD, TN, TX, WA, WI, WV, US Virgin Islands; Certified Federal Surveyor (CFedS); Geographic Information Systems Professional (GISP), Nevada State Water-Right Surveyor.

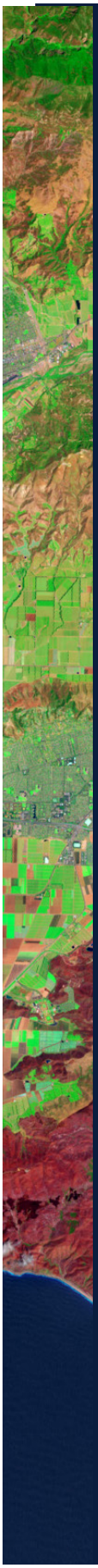

GeoBytes!

ASPRS GIS Division — Free Online Seminars

The ASPRS GIS Division, in cooperation with CaGIS and GLIS, is sponsoring free online live seminars throughout the year.

February 26th
Beyond NDVI ... 2016
Jack Paris

March 25th
A Geospatial Approach to Mapping Environmental Sound Levels Across the United States
Dan Mennitt, NPS
Kurt Fristrup, NPS

April 29th
Designing National Park Service Visitor Maps
Tom Patterson, NPS

May 27th
CyberGIS: Foundations and Principles
Eric Shook, Kent University

July 22th
Getting More From Remote Sensing Data Using OGC Standards
George Percivall, OGC

August 5th
Aqueduct Global Flood Analyzer – A Web Tool To Estimate Global Flood Risks For Current and Future Scenarios
Tianyi Luo, WRI

Attention those seeking ASPRS Certification: ASPRS Online Seminars are a great way to gain Professional Development Hours!

http://www.asprs.org/GISD-Division/Online-Seminars.html

Book Review— Introduction to Unmanned Aircraft Systems
continued from page 89

the Automatic Dependent Surveillance-Broadcast (ADS-B), while the non-cooperative technologies include Active systems (Radar, Laser), Passive systems (Motion detection, Insect model, Electro-Optical, Infrared, Acoustic), Passive systems and Ranging (). Finally, adapting technologies and other alternative approaches to visibility are discussed.

Chapter 10 "Sensors and Payloads" correlates the previously discussed issues of regulations, sense-and-avoid dynamics and technological limitations with issues pertaining to sensors and payloads (ie. data collection characteristics, size, weight, power burden). The aim is to alert the user that the steps to be followed are: termination of what information is to be gathered, identification of the most appropriate suite of sensors, selection of the platform best suited to carry out the mission, calculation of the costs and evaluate the ability to integrate to NAS.

Chapter 11 "Human Factors in Unmanned Aircraft Systems" analyzes the important issues of human factor analysis and user-centered design. More than a decade of research has resulted in a large collection of potential human factors that could influence UAS performance. Issues discussed include: Operational context, Human-Systems integration, System automation, Crew size-Composition-Training.

Chapter 12 "The Future of Unmanned Aircraft Systems" discusses an outlook of UAS development. Issues addressed include the anticipated market growth, the changes in infrastructure, technological advancements in miniaturization, power sources, and the jobs creation in both military and civilian areas.

The form of the book (theoretical analysis, information provision, end-of-chapter discussion questions) and the extent of its contents (system presentation, applications, operational issues, technology) provides a useful textbook for introductory UAS courses and a concise reference for scientists and engineers. A big congratulation to all prominent contributors and the editors!

& GRIDS & DATUMS

REPUBLIC OF COLOMBIA

BY Clifford J. Mugnier, CP, CMS

The City of Santa Fé de Bogotá was founded in 1538, the region Gran Colombia (modern Panamá, Colombia, Venezuela, and Ecuador) achieved independence from Spain in 1819 and reorganized as a republic in 1886. The Instituto Geográfico Militar was founded in 1935 and later renamed in 1950 as the Instituto Geográfico "Agustín Codazzi" - IGAC, the national mapping agency of Colombia that is responsible for all civilian and military mapping. The cartographer, Agustín Codazzi, produced early nineteenth century maps of Gran Colombia. In fact, these famous maps have even appeared on Venezuelan postage stamps. Furthermore, IGAC provides training services in the mapping sciences for many Latin American countries, a service previously provided solely by the U.S. Inter American Geodetic Survey (IAGS).

The first classical geodetic datum established in Colombia is the Bogotá Datum of 1941. The defining parameters are referenced to the International ellipsoid (also called the Hayford 1909 and the Madrid 1924) where a = 6,378,388 meters, $^1/_f$ = 297, with an origin of φ_o = 4° 35′ 56.57″ N, λ_o = 74° 04′ 51.30″W, and h_o = 2,633.6 meters, corresponding to the National Astronomic Observatory in Bogotá as of 1935. The azimuth to station Suba, α_o = 359° 30′ 10.0″, and the initial defining adjustment of the datum included 5 invar baselines, 133 geodetic stations, 12 astro stations, and "the ellipsoid normal is coincident with the direction of the plumb line."

In 1946, the country was divided into four tangent meridian belts, each belt three degrees wide as measured from the observatory. For each belt, the False Eastings and False Northings are equal to 1,000 kilometers each at the intersections of the central meridians (λ_o) and the latitude of the observatory. The belts are lettered as "B" (Bogotá), "Ec" (East central or Este central), "E" (East or Este), and "O" (West or Oeste). There may be a new belt "OO" (Western West or Oeste Occidente) to cover *Isla del Malpelo* in the Pacific Ocean and *Isla de San Andrés* in the Caribbean Sea. The projection system used in Colombia by definition is the Gauss Conform Transverse Mercator, a particular truncation of the Gauss Schreiber which was used in the U.S. for the North American Datum of 1927.

The boundary treaty between Colombia and Panamá was ratified and mutually exchanged on 31 January 1925. There is no indication of the geodetic datum used to provide the geodetic coordinates listed to a tenth of an arc second. Fortunately, the fourteen boundary points are physically marked and are presumably recoverable.

The boundary history between Colombia and Brazil is considerably older, dating back to 1494. The latest treaty with Brazil was signed in 1928, but the coordinates of the boundary markers were not published until 1946, presumably on the Bogotá Datum of 1941.

The land boundary with Venezuela is apparently stable; it is straddled largely by a continuous chain of quadrilaterals. However, the territorial limits of the sea seem to be in dispute, particularly with respect to fishing rights.

Other datums that exist in Colombia (at least theoretically) include the Provisional South American Datum of 1956 (PSAD 56) and the South American Datum of 1969 (SAD 69). Both

Photogrammetric Engineering & Remote Sensing
Vol. 82, No. 2, February 2016, pp. 93–94.
0099-1112/16/93–94

doi: 10.14358/PERS.83.2.93

PSAD 56 and SAD 69 seem to be largely ignored by Colombia although both datums are extended into other countries through Colombia and are extensively used elsewhere. The majority network of Colombia, which had consisted of 21 fixed stations and 679 adjustable stations, was adjusted to the SAD 69 in 1972. However, a free adjustment was also done in 1972 to the total network, which consisted of 1 fixed station and 950 adjustable stations. This free adjustment appears to be the system currently in use under the original name of the Bogotá Datum of 1941. The World Geodetic System of 1984 datum is used extensively in Colombia, albeit just a tool to extend the classical datum.

In 1980, IGAC established a special "city grid" projection for the City of Santa Marta, the oldest city in Colombia (1525). This special system was similar in philosophy to the systems developed for counties in Wisconsin and Minnesota for the convenience of the local surveyors and GIS applications. Specifically, this "city grid" was established at a particular elevation that corresponded to the average elevation of the city. Local surveyors could then ignore the reduction to sea level correction when transferring measured field distances to the city maps. The system was still based on the Gauss Conform Transverse Mercator, but the False Eastings and False Northings were modified by truncating to only five digits from the observatory at Bogotá.

The reference ellipsoid (International) was modified to have its semi-major axis increased by 29 meters, corresponding to the average elevation of the city above mean sea level determined at Buenaventura. Curiously, the system was reversed back to the standard national coordinate system in 1994, while other cities were published with their own special plane coordinate systems such as Villavicencio 1994 (450 meters), Leticia 1994 (100 meters), and Armenia 1995 (1,470 meters).

Although the Colombian definition uses the Gauss Conform Transverse Mercator for these systems, the Local Space Rectangular sometimes used in analytical photogrammetric calculations could just as easily be used with identical results. We commonly use such systems for analytical rectification projects if the project area is free of relief such as a plateau or a flood plain.

Note that these new city systems were orthophoto projects and not just rectified photos. Grids used in Colombia without special modifications to the ellipsoid include the Ciudad de Bogotá (City) Grid and the Ciudad de Medellín (City) Grid. The Grid System used for the Ciudad de Cartagena is the standard "B" belt of the National System.

The contents of this column reflect the views of the author, who is responsible for the facts and accuracy of the data presented herein. The contents do not necessarily reflect the official views or policies of the American Society for Photogrammetry and Remote Sensing and/or the Louisiana State University Center for GeoInformatics (C^{4}G).

This column was previously published in *PE&RS*.

PRUDENT CHANGES NOW FOR A BRIGHT FUTURE

The Imaging and Geospatial Information Society is in a state of transition with a new membership structure, new governance model, and new approach to the business of ASPRS including conferences, publications, and member services. With these measures fully implemented we anticipate a bright, resilient and sustainable future. We are acting responsibly and managing a new reality of lower total membership in a prudent manner with a keen eye on appropriate budget levels and member program execution. The glass is over half full and rising.

Changes now being implemented are the result of several years of work led by my predecessors during their terms as ASPRS presidents. Those changes result from many years of preparatory work that began with President Gary Florence authorizing President-elect Bobbi Lenczowski's task force on Branding. Building on the Branding task force recommendations, President Lenczowski the following year charged Steve DeGloria to convene the Restructuring Task Force. Steve redefined the Mission and Vision statements for the Society as well as developing a new Strategic Plan, all of which were adopted by the ASPRS Board, and recommending changes in the governance model. As President-elect and President, Stewart Walker followed Steve's recommendations and chaired the Streamlining Task Force, which offered guidelines for a new governance structure for the Society. The results and recommendations of the five years of work by these task forces, particularly the recommendations of the Streamlining Task Force, were approved and accepted for implementation by the ASPRS Board of Directors in Tampa, Florida in April 2015. Since that time, it has been my job as President of ASPRS to begin the implementation of the Board approved recommendations and restructuring. These are the changes currently being implemented. Below I briefly summarize the changes.

The first major recommendation being implemented is a change in membership categories. Approved by the Board, the new membership model includes only three membership categories, Individual, Corporate, and Friend. This will help ASPRS focus on the member value proposition, which is distinct for individuals vs. organizations. This change requires a change to the bylaws, which were just approved by the Board after considering important member comment.

The Board decision to restructure membership resulted in the elimination of some membership categories including Honorary Member, Fellow Member, and Emeritus Member. To ease transition to the revised Membership Article, existing Honorary, Fellow, and Emeritus members will retain their honors, titles, and benefits. There will be no new Honorary, Fellow, and Emeritus members, as distinct categories of members. However, the Awards Committee has instituted an appropriate way to recognize the professional contributions of outstanding members. ASPRS will continue to bestow Honorary and Fellow Awards, as the Honorary Lifetime Achievement Award and the ASPRS Fellow Award. These are new designations of our most distinguished awards for members, deserving the Honorary and Fellow distinction. They are true honorifics for our individual members who are carefully selected for the award. In the view of many, this essentially elevates these awards to a higher status, comparable to awards given by other professional societies. There is also a proposal to create an Emeritus

Award for those members who have contributed to the Society throughout their careers.

The Emeritus member category itself is eliminated with no replacement since there is no funding source to pay for the member benefits, previously granted under this membership class. ASPRS had not created an investment model to bank some portion of a member's dues to use in future years, when one might be eligible for Emeritus consideration. New member growth cannot provide sufficient revenue to cover the emeritus members cost. Consequently, ASPRS now has approximately 600 Emeritus members with no source of funds to pay their expenses, which contributes to the withdrawal of Reserve funds. To avoid this problem escalating, the Emeritus membership category will be eliminated. On a personal note, I became eligible for Emeritus status in 2013, but did not take it since I was and am still working and I know ASPRS needs my membership fees. Now with the Board decision, I will never be an Emeritus member of ASPRS, but ASPRS will be better without me as an Emeritus, since I will continue my membership and continue to pay dues. I may, however, receive an Emeritus Award.

Additional functional streamlining changes include modifying the governance structure to eliminate the current 11 member Executive Committee and 27-member Board and replace them with a single governing Board of Directors of 9 voting and three Ex Officio members. The Board approved changes establish: (1) the Technical Divisions Council consisting of the Directors and Associate Directors of the eight Technical Divisions; (2) a Regions Council consisting of the Region Presidents and Vice-Presidents; existing councils for Sustaining Members, Young Professionals, and Students become the Corporate Members Council, Early-Career Professionals Council, and Student Advisory Council. Each of these five Councils will elect its own Chair, who will likely be a Council's selected member to serve as a Director. Thus, the governing body of the Imaging and Geospatial Information Society will include nine voting members, President, President-Elect, Vice President, Immediate Past President, and five Directors, one each for the Technical Divisions, Regions, Corporate Members, Early-Career Professionals, and Student Advisory Councils. Additionally, the Executive Director, Treasurer, and Secretary are non-voting members of the Board of Directors.

Changes to increase revenue within and services from ASPRS include the membership changes, changes to publications including a new subscription model for *Photogrammetric Engineering & Remote Sensing*, a new approach to advertising, steps to increase our online presence, and more adaptive models for conferences. The conference changes include the redesign of the Annual ASPRS conference into the Imaging and Geospatial Technology Forum (IGTF) and the organization of small topically focused conferences, such as UAS Mapping Reno in 2014 and 2015.

In conclusion, ASPRS is undergoing basic changes that are the product of many years of effort and hard work by the ASPRS leadership and members. I call on the Society membership to support these efforts. The strength of the Society is based on its members and the Society will continue to be the primary American organization for imaging and geospatial information with a new membership model and governance structure.

I hope this brief description and chronology helps explain the actions taken by the ASPRS leadership and provide a better basis for your understanding the current state of the Society. Your comments are a source of information used by the Executive Committee and the Board to help frame the governance and operations of ASPRS. At this time of critical change, we are grateful to all members who provided comments and encourage further debate.

E. Lynn Usery
President
American Society for Photogrammetry and Remote Sensing
Research Geographer and Director
Center of Excellence for Geospatial Information

ASPRS MEMBERSHIP

ASPRS would like to welcome the following new members!

At Large
Bikram Gangwar
Rui Liu
Sahel Mahdavi
Mozhdeh Shahbazi
Fubara Warmate
Zhang Yajie
ChengMing Ye, Ph.D.

Central New York
Robert Stevenson

Columbia River
Matthew Borish

Florida
Audra Ferlan
Alexandra Fredericks
April Gibbs
James Kirkpatrick, IV

Heartland
Kalen Brady
Paul Kim
Jonathan Phillips
Scott Wolf

Mid-South
David G. Anderson
Ciaran Manning
Dorris Scott

North Atlantic
Andrew Sechrist

New England
Anthony Campbell
Eric Lundell

Pacific Southwest
Tajudeen Abdulazeez
Madison Davis
Ryan Jackson

Potomac
Craig Labbe
Stephen McGregor
Jessica Stiff
Joseph Zinger

Rocky Mountain
Lisa Godwin
Benjamin Haugen
Michael Sutherland

FOR MORE INFORMATION ON ASPRS MEMBERSHIP, VISIT
HTTP://WWW.ASPRS.ORG/JOIN-NOW/

Your path to success in the geospatial community

NOTICE OF PROPOSED CHANGE TO THE BYLAWS: MEMBER COMMENT INVITED

ASPRS is undergoing a rebirth, which includes improving its member value proposition and simplifying its governance structure.

To that end, the ASPRS Board of Directors unanimously approved the recommendations of the Streamlining Task Force at the May, 2015 Board of Directors meeting (see: http://www.asprs.org/About-Us/ASPRS-Reorganization.html). To implement the recommendations, new bylaws are required. The Board unanimously approved a change in member categories at its January 15 Special Meeting as a first step. As a second step, the Board also unanimously voted to put completely new bylaws before the membership for comment. The proposed bylaws are printed here in entirety.

If the new Bylaws are adopted they would completely replace the existing bylaws. For comparison, the full text of the current ASPRS Bylaws are posted online at: http://www.asprs.org/a/society/Bylaws.pdf, and the proposed new bylaws are below.

If you have comments for the Board to consider prior to the vote, please email them to Comments@asprs.org or mail them to: ATTN: Board Comments, ASPRS, 5410 Grosvenor Lane, Suite 210, Bethesda, MD 20814. The member comment period will close on Friday, February 19, 2016.

ARTICLE I. NAME AND OFFICE

Section 1. Name and Definition

The name of the Organization shall be the American Society for Photogrammetry and Remote Sensing, (ASPRS), hereinafter in these Bylaws called the Society. Photogrammetry and Remote Sensing is the art, science and technology of obtaining reliable information about physical objects and the environment, through the process of recording, measuring and interpreting imagery and digital representations of energy patterns derived from non-contact sensor systems.

Section 2. Office Location

The principal office of the Society shall be in the Washington, D.C. metropolitan area. The Society may have such other offices as may from time to time be designated by the Board of Directors.

ARTICLE II. VISION, MISSION, AND CORE VALUES

Section 1. Vision

Global development and application of imaging and geospatial information improves decision-making, sustains communities, and enhances quality of life.

Section 2. Mission

To promote and advocate imaging and geospatial science for informed, scientifically valid, and technologically sound observations of Earth conditions and trends that lead to improved and effective decision-making.

Section 3. Core Values

- Adoption and practice of the scientific method advances imaging and geospatial science and technology.
- Development and dissemination of guidelines and standards facilitates accessibility and reliable use of imaging and geospatial information.
- Development of new imaging sensors and platforms improves applications by practitioners.
- Expansion of a diverse community of geospatially literate students and professionals sustains our community.
- Adherence to ethical standards strengthens student learning and professional practice.
- Advocacy of relevant imaging and geospatial policies promotes sustainable development and use of Earth resources.

ARTICLE III. MEMBERSHIP

Section 1. Classes of Membership

Membership in the Society shall be classified in the following categories: Individual, Corporate, and Friend. Members have paid dues for the current year and are eligible to participate in all Society activities.

Section 2. Individual Member

An Individual Member is an individual involved in the science and engineering disciplines associated with imaging and geospatial information and shall be entitled to all rights and privileges of the Society applicable to Individual Members, including the right to vote. An applicant for admission as an Individual Member shall file with the Executive Director a

signed statement of concern for, and involvement in, the vision, mission, and core values of the Society by completing an application form prescribed by the Board of Directors. Completion of the form and payment of the required dues shall constitute fulfillment of admission requirements.

Section 3. Corporate Member

A Corporate Member is an organization involved in the science and engineering disciplines associated with imaging and geospatial information. A Corporate Member shall be entitled to all rights and privileges of the Society applicable to Corporate Members, including the right of representation as a Corporate Member to vote and have its representatives hold office. An applicant for admission as a Corporate Member shall file with the Executive Director a signed statement of concern for, and involvement in, the vision, mission, and core values of the Society by completing an application form prescribed by the Board of Directors. Completion of the form and payment of the required dues shall constitute fulfillment of admission requirements.

Section 4. Friend

A Friend is an individual or organization who wishes to support the mission of the Society and shall be entitled to all the rights and privileges of the Society negotiated and set out in the terms of membership with the Executive Director and set forth in an annual written agreement with the Society approved by the Board of Directors. These rights and privileges may not exceed those of Individual or Corporate Members. Completion of negotiation, signing a written agreement, and fulfilling initial conditions of the agreement shall constitute fulfillment of admission requirements.

Section 5. Membership Termination

Membership may be terminated in any of the following ways:

a. Any member desiring to resign from the Society shall submit their resignation in writing to the Executive Director.

b. Any member who does not maintain his/her qualifications for membership or honor the terms of his/her membership agreement shall be subject to termination.

c. Any member may be separated for cause by a two-thirds vote of the Board of Directors. The member shall be offered the right to appeal the separation decision.

ARTICLE IV. OFFICERS AND BOARD OF DIRECTORS

Section 1. Elective Officers

The Elective Officers of the Society shall be President, President-Elect, Vice President and Immediate Past President.

Section 2. President

The President shall be the principal Elective Officer of the Society, shall preside at Annual and Special Meetings of the Society and at meetings of the Board of Directors, and shall be a member *ex officio*, with the right to vote, of all Society Committees except for the Audit and Governance Committees. The President shall provide guidance for promoting the welfare and effectiveness of the Society, and shall perform such other duties as are necessarily incident to the office of President or as may be prescribed by the Board of Directors.

Section 3. President-Elect

The President-Elect shall perform, as necessary, the duties of the President in the event of disability or other absence of the President, shall oversee the activities of the Technical Divisions and Corporate Members Councils, and shall have such other duties as the President or the Board of Directors may assign.

Section 4. Vice President

The Vice President shall represent the elective officers at meetings of the Region Officers Council, oversee the Treasurer's activity, and have such other duties as the President or the Board of Directors may assign, including those of the President-Elect in the event of disability of that officer.

Section 5. Immediate Past President

The Immediate Past President shall chair the Governance Committee, defined in Article IX, Section 7, and serve as an advisor to the President.

Section 6. Appointed Officers

The Executive Director, the Secretary, and the Treasurer shall be appointed by the President with the consent of the Board of Directors. The Appointer Officers shall be responsible to the Board of Directors. Duties for the Appointed Officers are defined in Article XI of these bylaws.

Section 7. Board of Directors

The Board of Directors shall consist of the Elective Officers, Council Chairs, and Appointed Officers. The Appointed Officers shall be *ex officio* members without voting rights.

Section 8. Councils' Representation on the Board of Directors

Council Chairs shall represent Councils, which are defined in Article VIII, on the Board of Directors. The Corporate Members, Early-Career Professionals, Region Officers, Student Advisory and Technical Division Directors Councils shall have one Chair each for Council representation on the Board of Directors.

Section 9. Nomination and Election Procedures

a. Elective Officers

(1) The office of President shall be filled by automatic succession of the President-Elect, who shall normally

succeed to office from the office of Vice President. The Vice President is elected by a plurality of the members voting at large from a choice of two or more nominees on the ballot.

(2) Nominations for any vacant Elective Officer position of the Society shall be made by the Governance Committee, defined in Article IX, Section 7.

(3) The Governance Committee shall nominate candidates for the office of Vice President on or before a date that is twenty weeks prior to the date of the Annual Meeting. Nominee selections shall normally rotate annually among members representing government, industry, and academia. An announcement of the nominations shall be made in a Society publication received by the members eighteen weeks prior to the Annual Meeting. Additional nominations may be made by a nominating letter signed by no fewer than 250 voting members of the Society to be received by the Executive Director no later than fourteen weeks prior to the Annual Meeting. Each candidate shall submit a biographical sketch and a photograph, to be received by the Executive Director no later than thirteen weeks prior to the Annual Meeting.

(4) The Governance Committee shall certify that all nominees are qualified, willing to serve, and meet the requirements set forth in these Bylaws before the announcement of nominees. Nominees may not be candidates for Vice President and any other Board position simultaneously.

b. Technical Division Directors

The Assistant Technical Division Director shall normally succeed to the office of Technical Division Director. Nominees for Assistant Technical Division Director and/or Technical Division Director (if position has no successor) shall be determined by Technical Division operating procedures, as published in the Society's Operating Procedures. Their names, biographical data and photographs shall be forwarded to the Executive Director no later than thirteen weeks before the Annual Meeting, so that they may be included in the election ballot. An Assistant Technical Division Director and/or Technical Division Director (if position has no successor) shall be elected by a plurality of members voting.

c. Vice President and Technical Division Directors Election Procedures

(1) The Executive Director shall be responsible for transmitting to all qualified voting members at least ten weeks before the Annual Meeting the election ballot accompanied by biographical data, photographs, and clear and complete instructions for the balloting procedure. The ballot shall also contain any proposals requiring a vote by the membership. Ballots may be cast electronically or by mail.

(2) Ballots cast electronically must be submitted before 12:00 p.m. Eastern Time of the twenty-first day prior to the Annual Meeting. Member status is required to vote.

(3) Ballots cast by mail must be received at Society headquarters before 12:00 p.m. Eastern Time of the twenty-first day prior to the Annual Meeting. The completed mail ballot shall be unsigned and sealed in an envelope showing on the outside the member's name, written or printed, to determine eligibility to vote.

(4) Election tellers, appointed and informed of their duties by the President, shall record the ballots cast and submit a report to the President twenty days before the Annual Meeting, so that the President may notify the candidates of the outcome nineteen days prior to the Annual Meeting.

(5) A tie vote shall be decided by a majority vote of the Board of Directors.

d. Councils' Representation on the Board of Directors

The Corporate Members, Early-Career Professionals, Region Officers, Student Advisory and Technical Division Directors Councils each shall elect a Chair who serves on the Board of Directors.

(1) The Councils shall each have an election process for the Chair, published in the Society's Operating Procedures. The Corporate Members Council has members, which are organizations that vote but vest the representative responsibility to an individual who may or may not be an Individual Member of ASPRS. Each Council shall ensure that its Council's membership has an opportunity to nominate candidates. At the time of nomination all candidates shall be individual members or corporate member representatives of the Society.

(2) Elections shall be by ballot. The Council's Chair shall be elected by a plurality of the members of the Council Voting is restricted to members of the Society or Corporate Members' representatives.

(3) The name, biographical data and photograph of the elected Chair shall be submitted to the Executive Director not later than forty days prior to the Annual Meeting of the Society.

Section 10. Terms of Office

a. Each Elective Officer and new Council Chair shall take office during the Annual Meeting of the Society and shall serve until the successor is duly elected and installed at the appropriate Annual Meeting. A Council Chair may not serve two consecutive terms in the same office except as provided for elsewhere in the Bylaws.

b. The term for Assistant Technical Division Directors shall be two years. Assistant Technical Division Directors automatically accede to the Technical Division Director position for another two year term.

c. The term for Council Chair shall be two years, except for the Student Advisory Council, which shall be one year. One year is defined as the time between two annual meetings.

d. Incomplete terms of any Elective or Appointed Officer may be filled for the balance of the term by a Presidential appointee approved by the Board of Directors at any regular or special meeting. Incomplete terms of Technical Division Directors, Assistant Technical Division Directors and Council Chairs shall be filled in accordance with the respective procedures for the Technical Division or Council, as published in the Society's Operating Procedures.

e. On any other occasion when a position cannot be filled by procedures defined within these Bylaws or the Society's Operating Procedures, the President may appoint an individual to the position with the concurrence of the Board of Directors.

ARTICLE V. REGIONS

Section 1. Definition

Regions shall function as administrative sub-elements of the Society and provide a forum for local interaction among members, face-to-face meetings, and interaction with regional companies and organizations in the geospatial industry. All Society members shall be members of a Region based on the geographic location of a mailing address, submitted by the member for purposes of receipt of the journal and other Society correspondence, or an alternative region of their choice. No member may have membership in more than one Region.

Section 2. Boundaries

Region boundaries shall be established along State and/or county (or their equivalent) boundary lines. Foreign areas may be allocated to Regions to ensure opportunity for all members to participate in Region activities. The Executive Director shall maintain and publish a current file and map of all approved Region boundaries and list of members of each region.

Section 3. Establishing Regions

Modification of existing Region boundaries to establish a new or different Region, or to change the geographical areas of two or more existing Regions, shall be requested by the Region Officers Council, require approval of the Board of Directors by a two-thirds majority, and shall be compliant with the laws of the Commonwealth of Virginia. A request for a Charter for a new or modified Region shall be presented to the Board of Directors by the Region Officers Council and must be approved by a plurality of the Council members voting. The number of those voting to request a new or modified region must be at least 20% of the affected Regions' membership. The Charter request shall include proposed boundary lines, along with written approvals of the Regions whose boundaries would be affected and shall be presented to the ASPRS Board of Directors by the Region Officers Council.

Section 4. Dissolution

Dissolution of a Region shall be initiated by the Regions Officers Council. Regions shall be dissolved and their charters rescinded by a two-thirds vote of the Board of Directors. Members of dissolved regions shall become members of a newly formed Region or by selection of an alternative Region, as described above.

Section 5. Financing

Funds required for Region activities shall be part of the annual budget submission by the Region Officers Council to the Executive Director for the annual budget planning cycle. That submission shall include the input from each Region. Regions' requests shall be reviewed by the Board of Directors. Funding approved shall be provided from the Society budget. Regions shall not act in the name of the Society without the prior consent of the Society, nor incur financial obligations for the Society. Regions may conduct meetings, symposia, and collect registration fees to support such activities.

Section 6. Operations

Regions shall adopt bylaws, policies and procedures as necessary to carry out the objectives of the Society in accordance with these Bylaws and the Society's policies. Each Region shall elect Region Officers, appoint committees and form and supervise Chapters, as defined in Article VI, as needed. Regions shall report to the Executive Director and the Region Officers Council, within three weeks of their elections, the names of all elected officials and appointed committee chairs. Region elected officials shall be members of both the Society and the Region of membership as determined by Section 1 of this Article.

Section 7. Functions

Regions shall provide a forum for their members to consider technical and professional matters of Region concern. This may include cooperation with regional entities of related scientific, technical, or professional associations or organizations, or with educational institutions. A Region may establish formal operating relationships with such entities subject to approval of the Board of Directors, but shall not incur any financial obligations in the name of the Society.

Section 8. Support to the Society

a. Regions shall provide support to the Society by:

(1) Electing the Region president and vice president to administer the Region;

(2) Selecting two Region members (typically, but not necessarily, the president and vice president) to serve on the Region Officers Council of the Society.

(3) Developing regional position statements and preparing recommendations relating to Society policies, technical matters, education, legislation and other pertinent matters, and actively participating in the Society planning process. Regions shall not, however, issue resolutions or statements of policy for the Soci-

ety, or act on matters of national importance without specific approval of the Board of Directors.

(4) Developing concepts for Society technical meetings, workshops and seminars within the Region.

(5) Proposing, preparing and sponsoring preparation of technical articles and other publications for the Society publications program.

b. The Region officers shall assure coordination of Region activities with Society's Operating Procedures.

ARTICLE VI. CHAPTERS

Section 1. Definition

Chapters shall be sub-elements of Regions, established as necessary by the Regions to improve Society support to their members and to encourage local participation in Society activities. All Chapter members shall be members in good standing of the Society and members of the Region hosting the Chapter.

Section 2. Establishing Chapters

Regions shall determine their need for establishment of Chapters and shall operate them in accordance with Region Bylaws after a charter for each Chapter is issued by the Region's officers. At least five members of the Region, who are students, and one Member Faculty Advisor at a host institution, must indicate their intent to participate in a Student Chapter before a charter can be issued. For other non-student Chapters, at least ten members must indicate intent to participate in a Chapter, based upon some local geography or affinity of interest. The Region shall send the Region Officers Council and the Executive Director a copy of the petition signed by the required number of members and a copy of the Chapter Bylaws. Those Chapter Bylaws shall be approved by the Region's officers prior to the charter being issued.

Student Chapters may also be established at large by direct charter of the Society if support at the Region level is unavailable, in which case a surrogate host region shall be selected by mutual consent of the Student Chapter and the surrogate host region.

Section 3. Dissolution

Chapters shall be dissolved in accordance with the Region Bylaws and their charters rescinded by a two-thirds vote of the Region's officers. Notification of the dissolution should be provided to the Region Officers Council.

ARTICLE VII. TECHNICAL DIVISIONS

Section 1. Definition

Technical Divisions shall be used to organize and direct the technical, scientific and professional activities of the Society.

Section 2. Establishing Technical Divisions

Technical Divisions shall be established by a two-thirds vote of the Board of Directors, based on a proposal and at the recommendation of the Technical Division Directors Council. Evidence shall be included showing that the specified area of interest has been actively pursued by a committee or working group of the Society for a period of at least one year.

Section 3. Dissolution

Dissolution of Technical Divisions shall be initiated by the Technical Divisions' Council. Technical Divisions shall be dissolved upon a two-thirds vote of the Board of Directors if:

a. A desirable level of activity as determined by the Board of Directors is not maintained, and/or

b. The Technical Division no longer represents an area of technical, scientific or professional interest.

Section 4. Officers and their Responsibilities

Each Technical Division shall have, as a minimum, a Technical Division Director and Assistant Technical Division Director elected by the membership of the Society in accordance with Article IV of these Bylaws. The Assistant Technical Division Director shall serve in the capacity of the Technical Division Director in his/her absence. The duties of the Technical Division Director are, as a minimum:

a. Development and maintenance of a strategic plan for the Technical Division, and the supervision of its activation;

b. Preparation and presentation of periodic reports, in oral or written format, to the Board of Directors, which show the status of program activities;

c. Submission of an annual written report to the Technical Divisions Council, which forwards it to the Executive Director and the President for the membership of the Society, to include an assessment of progress within the Technical Division's sphere of interest;

d. Preparation and maintenance of Technical Division operating procedures, for inclusion in the Society's Operating Procedures, providing a current copy for file with the Executive Director;

e. Representation of the Technical Division on the Technical Division Directors Council; and

f. If elected Chair of the Technical Division Directors Council, serve on the Board of Directors.

Section 5. Operations

As needed, Technical Divisions shall organize working groups and other appropriate organizational subdivisions as necessary to carry forward the work of the Society in their sphere of interest. Joint working groups among Technical Divisions may be organized to permit effective action on issues of common interest. The chair of the Technical Division Directors Council shall be apprised of establishing or dissolving these subdivisions for reporting purposes.

Section 6. Membership
All members of the Society shall be given opportunities to indicate and/or to modify their choice of the Technical Divisions in which they wish to participate. A member may affiliate with any or all of the Technical Divisions of interest to the member.

Section 7. Financing
Technical Divisions shall not levy dues. Funds required for Technical Division activities shall be provided from the Society budget as submitted by the Technical Division Directors Council during the annual budget planning cycle. Technical Divisions shall not act in the name of the Society without the prior consent of the Society, nor incur financial obligations.

ARTICLE VIII. COUNCILS

Section 1. Definition
Councils represent a constituency within the Society and are specialty groups with common interests and goals. The Councils shall act as a liaison and provide a communications forum for and between all interested members on issues that are of importance and affect their relationship with the Society.

Section 2. Establishing Councils
New Councils shall be established by a three-quarters vote of the Board of Directors after considering a written petition by a collection of no fewer than 10 members presented to the Board of Directors. The petition shall include clearly stated objectives, the sphere of interest for the proposed Council, and a charter that defines responsibilities, policies, and procedures as necessary, in accordance with these Bylaws and the Society's policies.

Section 3. Membership
Membership in a Council shall be determined by the Council's charter and operating rules documented in the Society's Operating Procedures.

Section 4. Dissolution
Councils shall be dissolved upon a three-quarters vote of the Board of Directors.

Section 5. Operations
Councils may organize working groups as necessary to carry forward the work of the Society in their sphere of interest. Councils shall adopt a charter to define responsibilities, policies, and procedures as necessary, in accordance with these Bylaws and the Society's policies. The chair of the Governance Committee shall be apprised of establishing or dissolving these working groups for reporting purposes.

Section 6. Officers of the Councils and their Responsibilities
Councils shall have, at a minimum, a Chair and a Vice-Chair elected by the voting members of the Council. Both the Chair and Vice-Chair at the time of election shall be Individual Members or representatives of Corporate Members of the Society. The Vice-Chair shall serve in the capacity of the Chair in his/her absence. The duties of the Chair, at a minimum, are:

a. Organizing and chairing a Council meeting at least as often as the Board of Directors meets in regular session;

b. Development and maintenance of a strategic plan for the Council, and the supervision of its implementation;

c. Preparation and presentation at least bi-annually to the Board of Directors and Executive Director of periodic reports to show the status of the Council activities;

d. Submission of an annual report to Board of Directors, Executive Director, and President for the membership of the Society, to include an assessment of progress within the Council's sphere of interest; and

e. Submission of a budget request for the Council to the Board of Directors and the Executive Director during the annual budget planning process.

Section 7. Financing
Councils shall not levy dues. Councils shall not act in the name of the Society without prior approval of the Board of Directors, nor incur financial obligations. The Regions Officers Council and the Technical Division Directors Council shall review the annual budget plans and requests of their member regions or divisions prior to submission to the Society's annual budget planning process.

Section 8. Corporate Members Council
Membership in the Corporate Members Council shall be open to all Corporate Members of the Society. The Corporate Members Council shall act as a liaison and provide a forum for better communication for and between all Corporate Members in order to address issues of importance that affect their relationship with the Society. Each Corporate Member shall appoint a representative as a member of the Council. The appointed representative shall be considered the Corporate Member of the Society in order to vote in Council elections. The Chair of the Council shall be a full voting member of the Board of Directors.

Section 9. Early-Career Professionals Council
Membership in the Early-Career Professionals Council shall be open to Individual Members of the Society who have not yet completed five career years beyond their most recently completed university degree or are within their first six years of entering the profession. The Early-Career Professionals Council shall engage and mentor early-career professionals; advocate continuing education; foster positive relationships between members transitioning from the member with Student distinction to the member without that distinction; encourage the dissemination of professional and institutional knowledge and standards through education, mentoring and technical opportunities; and work closely with the Society's membership staff and the Student Advisory Council to

strengthen the Society. The Chair of the Council shall be a full voting member of the Board of Directors.

Section 10. Region Officers Council

The Region Officers Council shall consist of two representatives from each Region selected by the Region members based on the Region's Operating Procedures. The Chair of the Council shall be a full voting member of the Board of Directors.

Section 11. Student Advisory Council

Membership in the Student Advisory Council shall be open to all Society members with the Student distinction. The Student Advisory Council shall focus on introducing members with the Student distinction to the mission, goals, activities, and professions represented by the Society. In addition, the Council shall actively develop and promote activities that support these members and give feedback to the Board of Directors on the best way to serve this segment of the membership. The Chair of the Council shall be a full voting member of the Board of Directors.

Section 12. Technical Division Directors Council

The Technical Division Directors Council shall consist of the Directors and Assistant Directors of the Technical Divisions of the Society. The Chair of the Technical Division Directors Council may be a Director, an Assistant Director, and/or a sitting Chair whose term has not yet expired. The Chair of the Council shall be a full voting member of the Board of Directors.

ARTICLE IX. COMMITTEES

Section 1. Appointment

The President, acting for the Board of Directors, shall appoint such Society Permanent Committees, Standing Committees, and Task Forces as may be required by the Bylaws, or as may be necessary. Committees and Task Forces shall report to the Board of Directors through the President.

Section 2. Permanent Committees

Permanent Committees are appointed by the President, acting for the Board of Directors, to address primary Society activities of governance and finance, and insure continuing Society structure for support, development and maintenance for programs. Permanent Committees report to the Board of Directors. There shall be the following Permanent Committees: Audit, Governance.

Section 3. Standing Committees

Standing Committees may be developed as needed and are appointed by the President, acting for the Board of Directors, to address primary Society activities and insure continuing support, development and maintenance for programs . Standing Committees report to the Board of Directors at least annually. They may be created and dissolved by the Board with a two-thirds majority vote.

Section 4. Task Forces

Task Forces of any size may be formed by the President to undertake a single task and are automatically terminated upon completion of that task. Assignment of tasks to Task Forces shall be in the form of a written charge from the President to the Chair with copies to members of the Board of Directors.

Section 5. Joint Committees

When considered to serve the interests of the Society, the President, with the approval of the Board of Directors, may establish Joint Committees with other organizations for treating matters of common interest within the limits of the Bylaws.

Section 6. Audit Committee

The Audit Committee shall consist of a minimum of the Treasurer and two ASPRS Board members appointed by the President. The Treasurer shall serve as the Chair. At least the Chair or one member of the Audit Committee must be generally knowledgeable about accounting and finance matters. The Executive Director shall provide information and support to the Committee but shall not participate in the Committee's decisions.

The Audit Committee shall observe best practice in recommending the change in the independent outside audit team; solicit and review proposals from prospective audit teams; provide a documented recommendation to the Board for selection from among the best candidates; meet with the contracted auditor to review the scope of work for the annual audit; and meet with the auditor at the completion of the audit to review the resulting report including any accompanying management letter. The Committee shall have the authority to engage other advisors as it deems necessary and must approve in advance any non-audit services procured by ASPRS from the outside auditor. The Committee shall provide a report to the Board prior to Board action on the annual audit.

Section 7. Governance Committee

The Governance Committee shall consist of the five most recent and available Past Presidents of the Society. The Immediate Past President, one of the five members of the Governance Committee, shall be the Chair. The next most immediate Past President available shall serve as Chair in the event the Immediate Past President is unable to do so. The Governance Committee shall transact business to ensure that critical management functions of the Society are fulfilled professionally, including, but not limited to, the following:

a. Bylaws
   The Committee shall be responsible for periodically reviewing the Operating Procedures of the Society to determine if they are consistent with these Bylaws and, as appropriate, recommending to the Board of Directors amendment or extension of the Bylaws. The Committee shall advise the officers or directors of Bylaws requirements relative to current or proposed Society actions.

b. Nominations
   The Committee shall nominate candidates for Society offices as required by Article IV of these Bylaws.

c. Professional Conduct
The Committee shall be the custodian of the Society Code of Professional Ethics, responsible for preparing and recommending standards of professional conduct and the procedures to be followed in professional conduct investigations; take responsibility for review and investigation of all questions of professional conduct, to include charges against a member of the Society. The Committee shall inform the Board of Directors of its decisions on all cases considered, including its recommendations for Society action when necessary. The Board of Directors, after review of the report of the Committee concerning a case of violation of the Code of Professional Ethics, shall vote to decide whether formal hearings should be held by the Board of Directors. If the vote is negative, the case is closed. If affirmative, the Board of Directors in formal session shall hear all evidence and decide by secret ballot on appropriate action. A vote of three-quarters of the Board members shall be required for any action.

d. External Relations
The Committee shall identify relationships with external organizations and designate representation or liaison where required.

Section 8. Committee Expenses
Operating expenses for committees shall be included in the Society budget process. Committee chairs shall provide estimates and reports of expenses as required by the Executive Director.

Section 9. Assignment of Responsibilities
Detailed assignments of responsibilities to Permanent Committees, Standing Committees, and Task Forces shall be in the form of a written charter approved by the Board of Directors and published in the Society's Operating Procedures. An annual charge or set of tasks may be added by the President.

ARTICLE X. FINANCES

Section 1. Membership Dues and Fees
Membership dues and other fees shall be determined annually by the Board of Directors after considering the recommendations of the Executive Director. New memberships shall begin in the month dues are received and are subject to renewal 12 months later, i.e., the anniversary date. Dues shall be collected from all categories of membership.

Section 2. Budget
The Executive Director shall prepare an annual budget proposal for the Society showing projected receipts and expenditures for the ensuing fiscal year with recommendations for dues and fees structure, supported with records of receipt and expenditure data for the current and the previous fiscal year. The budget planning process shall include submission of requests from the Council chairs. The budget shall be submitted to the Board of Directors for discussion, recommendation, and approval at its last meeting prior to the beginning of the fiscal year.

ARTICLE XI. ADMINISTRATION

Section 1. Responsibilities of the Board of Directors
The Board of Directors shall have control and direction of the affairs of the Society and shall determine its policies in accordance with the laws under which the Society is organized and within the provisions of the Bylaws. Its powers and responsibilities shall include the following:

a. To have, hold, and administer the property and funds of the Society;

b. To adopt and publish an annual budget for the Society, to review the annual audit of Society accounts, and to review the Society's financial policies;

c. To determine the privileges of members and the dues and fees to be paid by them;

d. To confirm the appointment, contractual arrangements and compensation for the Executive Director, who shall serve at the direction of the Board and who shall be subject to removal from office at any time for cause by a majority vote of the Board;

e. To make appropriations for specific purposes;

f. To authorize public statements on behalf of the Society;

g. To foster and oversee relations with related organizations;

h. To adopt changes to the Bylaws of the Society;

i. To report Board actions to the members of the Society;

j. To take measures to advance the disciplines and interests of the Society and of the profession; and

k. To fill vacancies on the Board of Directors caused by death, disability, or flagrant neglect of performance, after declaring the office vacant.

Section 2. Responsibilities of the Elective Officers
The President shall have supervision of the affairs of the Society, presiding at all Annual and Special Meetings of the Society and meetings of the Board of Directors. In addition to the responsibilities stated in Article IV, the President-Elect and the Vice President shall assist the President as necessary and shall, in the absence of the President, assume the duties of the President, in succession. Detailed guidelines for the responsibilities of the Elective Officers are provided in the Society's Operating Procedures.

Section 3. Responsibilities of the Executive Director
a. The Executive Director shall be responsible for the administration and management of the Society subject to policy guidance of the Board of Directors through the President.

b. The Executive Director shall be responsible for the financial arrangements of the Society subject to policy guidance of the Board of Directors through the President and Treasurer.

c. The Executive Director shall have responsibility for employing, directing, and evaluating the performance of the salaried staff of the Society and for operation of Society office(s).

d. The Executive Director shall develop plans, programs, projects and operating procedures to further the organization and effectiveness of the Society; shall serve as the primary point of contact for the Society with its various components and with other organizational entities and affiliates; and shall insure administrative support for Society Officers, the Board of Directors, Councils, Committee Chairpersons, and Conference Directors.

e. The Executive Director shall arrange for and give timely notice of all Annual and Special Meetings of the Society and the Board of Directors, recording all proceedings and maintaining custody of correspondence and records with the help of the Secretary as defined in Section 5 below. The Executive Director shall prepare:
(1) An annual report for presentation to the Society, and
(2) Other reports as may be requested by the President and the Board of Directors.

Section 4. Responsibilities of the Treasurer

a. The Treasurer shall oversee the financial policies of ASPRS. The Treasurer shall ensure that the accounts of the Society are audited annually by a Certified Public Accountant. The Treasurer shall chair the Audit Committee. The result of the audit shall be reported to the Board of Directors and made available upon request to Society members.

b. The Treasurer shall issue an oral or written report for each Board of Directors Meeting describing the status of Society's finances and make recommendations.

Section 5. Responsibilities of the Secretary

The Secretary shall record the Society's business conducted at all formal meetings and assure preservation of those records for the Executive Director.

Section 6. Absence of Executive Director, Secretary, or Treasurer

During the absence of, or in the event of the disability of, the Executive Director, the Secretary, or the Treasurer, the President with approval of the Board of Directors shall designate a temporary alternate to serve in an acting capacity until a successor is appointed.

ARTICLE XII. MEETINGS

Section 1. Society

a. There shall be an Annual Meeting of the Society, at a time and place approved by the Board of Directors, for installation of Officers, Technical Division Directors and Assistant Technical Division Directors, and the Board of Directors, and the conduct of Society business. Notice of such meeting shall be given by the Executive Director in a publication of the Society to reach the membership no fewer than 60 days prior to the date of the meeting.

b. Special Meetings of the Society may be called by the President with a majority approval of the Board of Directors, or by the President upon the written request of five percent of the voting members of the Society. The Executive Director shall notify members, at least 15 days in advance, of the time, place, and subjects to be considered.

c. A quorum for the transaction of business at an Annual or Special Meeting of the Society shall be 10 percent of the membership eligible to vote. The presiding officer may adjourn the meeting from time to time until a quorum is present.

d. Other meetings of the Society in the form of symposia, conferences, conventions or others for the principal purpose of exchanging information may be held with the approval of the Board of Directors. Such meetings may be cosponsored with other organizations having kindred interests, and shall be widely advertised in Society publications. Normally, an Annual Conference shall be convened at the time of the Society Annual Meeting, and at least one other Society meeting, which may be virtual, shall be held at a location other than that of the Annual Conference.

Section 2. Board of Directors

a. The Board of Directors shall normally meet four times each calendar year. The Board shall also meet upon call of the President or upon demand of a majority of its members. Notice of meetings with the agenda shall be sent to all Board members to be received at least ten days in advance of the meeting.

b. A simple majority of the voting members of the Board of Directors shall constitute a quorum at any meeting of the Board. If fewer than a simple majority are in attendance, the presiding officer may adjourn from time to time until a quorum is present when motions are necessary.

c. In the event of absence of any member of the Board of Directors from two consecutive meetings of the Board, the Executive Director shall call the matter to the attention of the Board for possible action in accordance with Article XI, Section 1(k).

d. Elective Officers and members of the Board of Directors shall not receive any compensation for their services but may be authorized reimbursement for expenses in accordance with Society policies and procedures for such payments.

Section 3. Telephone Conference/Mail Ballot/ Email Ballot

When consideration of any matter by the Board of Directors is required earlier than its next meeting, this may be accomplished by electronic teleconference/video conference, email or mail ballot vote at the discretion of the President. Passage of such votes shall be as specified in the appropriate sections of these Bylaws.

Section 4. Membership Ballots

Whenever, in the judgment of the Board of Directors, any major question shall arise which it believes should be put to a vote of the membership and when it deems it is not expedient to call a Spe-

cial Meeting for such purpose, the Board may, unless otherwise required by these Bylaws, submit such a matter to the membership in writing by mail and/or electronic vote. The question thus presented shall be decided according to a majority of the votes cast by mail and/or electronically within 30 days after its submission to the membership, provided that votes of at least 10% of the Society members eligible to vote shall be received. Action taken as a result of such vote shall be binding upon the Society in the same manner as would action taken at a duly called meeting.

ARTICLE XIII. PUBLICATIONS

Section 1. Purpose
The Society shall have an active publications program to foster and promote the exchange of knowledge, ideas, and information about the sciences, technology, engineering, and operations in photogrammetry, remote sensing, and the related sciences and disciplines of the profession.

Section 2. Society Publications
The Society shall publish an Official Journal and other publications such as a Newsletter, manuals, proceedings of technical meetings, and monographs, as determined by the Board of Directors.

Section 3. Official Journal
All members eligible to vote shall be entitled to receive the Official Journal and Newsletter. Notices and announcements relating to Society affairs published in the Official Journal and/or Newsletter shall be deemed to have been brought to the attention of all members of the Society.

Section 4. Technical Division Publications
Technical Division publications shall be authorized provided that they do not conflict with, or detract from, the Official Journal, and clearly indicate that they are issued by a Technical Division of the Society.

Section 5. Region Publications
Regions shall be authorized to publish newsletters and other technical publications as appropriate to disseminate information of concern to the Region. Those normally shall be financed from Region funds.

ARTICLE XIV. SEAL, INSIGNIA AND LOGO

Section 1. Official Seal and Insignia
The Society shall have an official seal and insignia, with the original on file in the headquarters of the Society.

Section 2. Uses of the Seal, Insignia and Logo
The official seal and insignia (and/or a logo authorized by the Board of Directors) shall appear on correspondence, documents, and publications and on banners, flags, membership pins and other such devices of the Society.

Section 3. Changes
Changes to the official seal and insignia shall require a two-thirds vote of the Board of Directors.

ARTICLE XV. DISSOLUTION

Section 1. Distribution of Assets to Other Organizations
In the event of dissolution of the Society, any assets remaining shall be distributed to one or more regularly organized and qualified educational or scientific non-profit organizations to be selected by the Board of Directors and approved by the membership.

Section 2. Assets in Formation of New Organizations
In the event of dissolution of the Society with intent to form two or more similarly qualified new organizations, and if approved by the Board of Directors and the membership, any assets remaining after payment of all debts and liabilities shall be distributed to the new organizations when formed, in amounts proportional to the distribution of Society members into the new organizations.

Section 3. Dissolution by Subsumption into Another Organization
In the event of dissolution of the Society by subsumption by another organization, and if approved by the Board of Directors and the membership, any assets remaining after payment of all debts and liabilities shall be distributed to the subsuming organization.

ARTICLE XVI. AMENDMENTS

Section 1. Petition for Amendment
Amendment to these Bylaws may be proposed in writing to the Executive Director by petition of at least five members of the Board of Directors or at least fifty members who are qualified to vote.

Section 2. Amendment Procedure
Amendments proposed by the membership shall be considered by the Board of Directors after receipt by the Executive Director. The membership and the Board shall be advised of proposed amendments by notification in writing or in the Society's Official Journal and/or Newsletter. The members shall provide comment within 30 days of notification. The Board shall receive member comments within 15 days after the closing of the member comment period. Proposed amendment(s) shall be considered by the Board at the next Board meeting that is at least 15 days after the Board has received member comments.

Section 3. Adoption
Amendments to these Bylaws shall be adopted by a three-quarters vote of the nine members of the Board of Directors.

Multi-Criteria, Graph-Based Road Centerline Vectorization Using Ordered Weighted Averaging Operators

Fateme Ameri, Mohammad Javad Valadan Zoej, and Mehdi Mokhtarzade

Abstract

In this paper a novel road vectorization methodology based on image space clustering technique and weighted graph theory is presented. The proposed methodology describes a road as a set of optimized points on the centerline which should be connected by defining a number of appropriate criteria. The main contribution of this paper is to design a weighting scheme for combining a small number of road identities using Ordered Weighted Averaging (OWA) operators by defining appropriate decision strategy. In this regard, a novel geometric criterion is introduced. Result of the OWA aggregation specifies weight of each edge in the road network graph. Comparing the proposed approach with two state-of-the-art image space clustering-based road vectorization methods proves its efficiency to deal with roads with different widths, parallel roads with different distances, different types of intersections, and also noise clusters. Obtaining improved quality measures for several high-resolution images, demonstrates the successfulness of the vectorization approach.

Introduction

Identification of digital linear features from remote sensing data in continuous objects such as roads is a complicated procedure. Regarding the significance of vector representation of the roads in many applications, such as automatic vehicle navigation, traffic management, and updating geospatial databases, health care accessibility planning, and even infrastructure management delineation of road centerlines from remote sensing data has been attracted researchers over the last three decades. (Mohammadzadeh *et al.*, 2006)

Linear features have been investigated in various research studies based on different models. The road model describes the appearance of a road in the digital image and makes the task programmable (Gruen and Li, 1995). Some models consider roads as continuous lines (Gruen and Li, 1995; Mena, 2006, Mohammadzadeh *et al.*, 2006; Poullis and You, 2010). Most of researches model the roads using separate line segments which should be connected based on defining an appropriate connection hypothesis (Baumgartner *et al.*, 1999; Hinz and Baumgartner, 2003; Grote *et al.*, 2012). Moreover, a few road extraction methods define the road models based on groups of points on the central axes of roads which should be connected considering radiometric or geometric constrains (Doucette *et al.*, 2001; Ferchichi and Wang, 2005; Mokhtarzade *et al.*, 2010). These point-based road centerline extraction methods provide results with high accuracy defining appropriate geometric and radiometric criteria.

Road extraction researches concentrate on two subjects: (a) Road detection which focuses on identification of raster road segments from other feature classes in the image (Zhu *et al.*, 2004; Mohammadzadeh *et al.*, 2006; Youn *et al.*, 2008; Grote *et al.*, 2012; Matkan *et al.*, 2014; Poullis, 2014), and (b) Road vectorization is related to extraction of road centerline as vector segment (Doucette *et al.*, 2001; Mena, 2006; Mokhtarzade *et al.*, 2010; Karaman *et al.*, 2012; Zarrinpanjeh *et al.*, 2013; Shanmugam and Kaliaperumal, 2015). Among them, some existing road vectorization methods are concentrated on image space clustering techniques to represent the road centerline by connecting initial road candidates (Doucette *et al.*, 2001; Mokhtarzade *et al.*, 2010). There are some problematic issues such as fixed number and uniform distribution of the initial cluster centers in the Doucette *et al.* (2001) method as well as the complexity of computations in Mokhtarzade *et al.* (2010) which have motivated us to establish a novel point-based road centerline vectorization method.

The main contribution of this paper is to design a weighting and fusion scheme for combining the outputs of the various image analysis operators. Although most of the earlier road extraction approaches do the same task by variety of techniques such as artificial intelligence and fuzzy systems (Wiedemann and Hinz, 1999; Hinz and Baumgartner, 2003; Mokhtarzade *et al.*, 2007), segmentation and classification (Bacher and Mayer, 2005; Mohammadzadeh *et al.*, 2006; Poullis and You, 2010; Grote *et al.*, 2012), Dempster-Shafer approaches (Mena and Malpica, 2003; Mena and Malpica, 2005), and Snakes and dynamic programming (Gruen and Li, 1995; Gruen and Li, 1997), this paper uses an adopted weighting and ordering scheme which needs only few parameters and has enough generality to vectorize other linear features. In this regard, a new five-step approach for road centerline vectorization based on image space clustering and weighted graph theory is introduced. An Ordered Weighted Averaging (OWA) based strategy is used to aggregate the road geometric criteria into the cost of each edge in the road network graph. Besides, an innovative road geometric feature is proposed to enhance the results of the aggregation.

OWA operators are defined as a nonlinear combination of the ranked input data which was first proposed by Yager (1988). In the short time since its first appearance, the OWA operators have been used in an amazingly wide range of applications including neural networks (Yager, 1992; Yager, 1995), fuzzy logic controllers (Yager,1991; Yager and Filev, 1992, Chen *et al.*, 2012), group decision-making and multi-criteria decision analysis (Herrera *et al.*, 1996; Liu *et al*, 2013; Jelokhani and Malczewski, 2014), data mining (Torra, 2004), GIS (Rinner and Malczewki, 2002; Malczewski, 2006;Nadi and Delavar, 2011), etc. This various applicability is due to the flexibility of OWA to model variety of aggregators and different

Remote Sensing Department, Geomatics Engineering Faculty, K.N. Toosi University of Technology, No. 1346, ValiAsr Street, Mirdamad cross, Tehran, Iran, Postal code: 19967-15333(fameri@mail.kntu.ac.ir)

Photogrammetric Engineering & Remote Sensing
Vol. 82, No. 2, February 2016, pp. 107–118.
0099-1112/16/107–118

doi: 10.14358/PERS.82.2.107

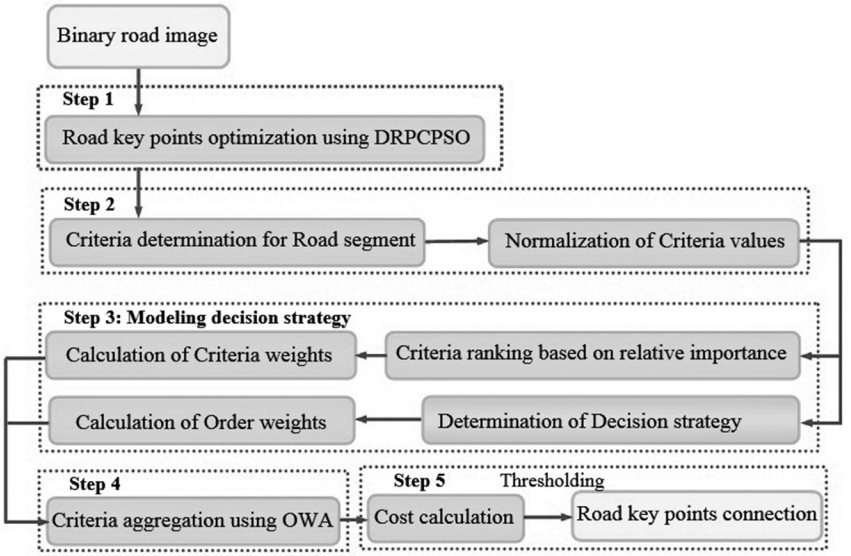

Figure 1. OWA-based road centerline vectorization diagram.

kinds of relations among the criteria selecting an appropriate weighting vector (Ahn, 2008).

By integrating different attributes using the OWA operators in this research, it is intended to provide a more straightforward and satisfactory solution in road vectorization than conventional approaches. In order to evaluate the performance of the proposed approach, several simulated and real high-resolution images were tested.

This paper consists of five sections. Following the introduction, the novel road vectorization methodology using OWA operators and weighted graph theory are presented followed by the experimental results on different simulated and real datasets, then a discussion on the obtained results. Finally, the concluding remarks and future research directions are discussed.

Methodology

The proposed automatic road centerline vectorization approach uses a graph-based model to construct a road network. A graph-based road model consists of a set of nodes some pairs of which are connected by links. Each feasible link is characterized by a cost value indicating the possibility of connection between nodes. In this research, each road key point is represented by a node and each line segment, which is defined between two nodes, is symbolized by a link. The cost of each line segment is calculated based on the aggregation of geometric criteria according to OWA. In this paper, an automatic road centerline vectorization is organized in five steps as follows (Figure 1):

1. Obtaining optimized distribution of road key points in the binary road raster map.
2. Identifying and normalizing effective criteria of road centerline vectorization.
3. Modeling decision strategies of OWA by specifying order weights and criteria weights to establish a true connection between road key points.
4. Aggregating the criteria values based on OWA by means of different decision strategies.
5. Calculation of the cost and selection of suitable line segments defining appropriate threshold to construct the road network topology.

Road Key Point Determination

The procedure of road key point determination is based on the idea of image space clustering (Doucette *et al.*, 2001). In this research, a road network is defined as continuous line segments which are covered by different road patches obtained during clustering process. Each road patch is identified by a point (road key point) which is the centroid of each cluster.

Based on this model, road patch determination (road key point determination) is done by means of Dynamic Road Pixels Clustering using Particle Swarm Optimization (DRPCPSO) algorithm. The DRPCPSO algorithm is a modification of dynamic clustering using PSO algorithm (Omran *et al.*, 2006) to optimize the number and distribution of road patches in the binary road raster map. The DRPCPSO algorithm is a hybrid clustering algorithm composed of a binary PSO to automatically determine the optimum number and distribution of road key points and a traditional K-medians to adjust the chosen road key points. In the DRPCPSO algorithm the partitioning procedures of the spatial positions of road pixels are repeated until the best set (the lowest cost function) of road key points is obtained. In this way an appropriate pattern of road key points which guarantees the optimality of road centerline extraction is achieved. The proposed DRPCPSO algorithm is summarized in Figure 2.

Road Segment Criteria Definition

Following the image space clustering method, road patches are represented by optimized distribution of road key points. The adjacent road key points are to be connected to construct the road network topology. In order to make true connections, a combination of several criteria or prior information about the roads and their appearance should be used. The connection criteria should present fundamental attributes of roads including radiometric and geometric characteristics. Since the connection strategy is defined on the binary road image, no radiometric criteria are used. For the road key point connection in this paper, the compliance of each road segment with three criteria is checked. The summarized criteria are as follows:

- *Distance (d)*

  This criterion is defined as the Euclidean distance of the connecting line between two road key points. It is identical to the line segment length.

- *Direction Difference (DD)*

  The direction difference is measured by the angle between the direction vectors of the two line segments. The direction of one line segment is defined by the direction of the vector which connects its two end points (see

Input: Z, N_{MRKP}

Output: The positions of optimum road key points

$//Z = \{z_j \mid j = 1, 2, ..., N_p\}$: A data set containing the positions of detected road pixels.

$//M = \{m_k \mid k = 1, 2, ..., N_{MRKP}\}$: The set of cluster centers representing possible road key points.

$//S = \{X_i \mid i = 1, 2, ..., s\}$: The swarm of s particles where X_i is a chain of binary values $x_{i,k} \in \{0, 1\}$, $k = 1, 2, ..., N_{MRKP}$

1. Select random number of road key points from M.
2. Initialize the swarm S.
3. Initialize each particle's velocity ($v_{i,k}$) .
4. **For** each particle in S
   4.1. Partition Z using minimum distance (in terms of the Euclidean distance) clustering according to the selected road key points in M.
   4.2. Evaluate the optimality of road key points configuration using a cost function.
   4.3. Update the personal best (y_i) and global best ($\hat{y}$) positions of the particles using minimum cost value.
5. **End For**
6. Apply the binary PSO velocity and position update equations on all particles in S.
7. Repeat step 4 through 6 until the first termination criterion (TC_1) is met.
8. Refine the chosen road key points positions applying K-medians clustering algorithm.
9. Combine the selected set of optimum road key points with a new random set of road key points from Z.
10. Repeat step 2 through 9 until the second termination criterion (TC_2) is met.

Figure 2. DRPCPSO algorithm to obtain optimized road key points.

Figure 3). The direction difference should be lower than a threshold for the two road segments to be connected.

- *Circular Intersection (*CI*)*

  Based on this criterion, which is proposed in this research, a circle of radius R with center at each road key point is considered. Circular intersection is defined as the intersection area between two circles of corresponding road key points. The distance (d) between the centers of the circles (distance between two road key points) affects the size of the intersection area. Considering two circles with the same radius (R) and different values for d, these three situations are introduced:

1. If $d = 0$: two circles are completely overlapped.
2. If $d \geq 2R$: two circles are tangential or may not intersect at all, so the area of intersection is 0.
3. If $d < 2R$: two circles intersect in two distinct points.

In this paper circular intersection in the case $d < 2R$ is selected to investigate the connection condition between different road key points. In that, overlapping of the intersection area between two circles centered at two road key points with the corresponding road patches in the binary road image is considered as a fundamental connection criterion. Based on this criterion, as the number of road pixels in the circular intersection area increases (higher CI), the connection probability of the corresponding road key points is raised (Figure 4).

In general, the distance and the direction difference values should be low and the circular intersection value should be high to correctly connect the road key points.

All the defined criteria are categorized into quantitative variables. To make various criteria of different alternatives comparable, they are normalized using the *maximum score* procedure (Malczewski, 1999). Table 1 summarizes the range of criteria values and their corresponding normalization functions. Among the criteria, d and DD are cost criteria. CI is a benefit criterion which is subtracted from one to be comparable to other cost criteria. In Table 1, d_{max} is the maximum of road key points distance in the data set, DD_{max} corresponds to the maximum of direction difference, and CI_{max} represents the maximum sum of the number of road pixels in two corresponding road patches.

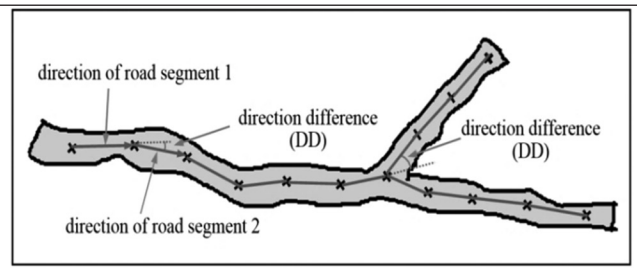

Figure 3. Definition of direction difference.

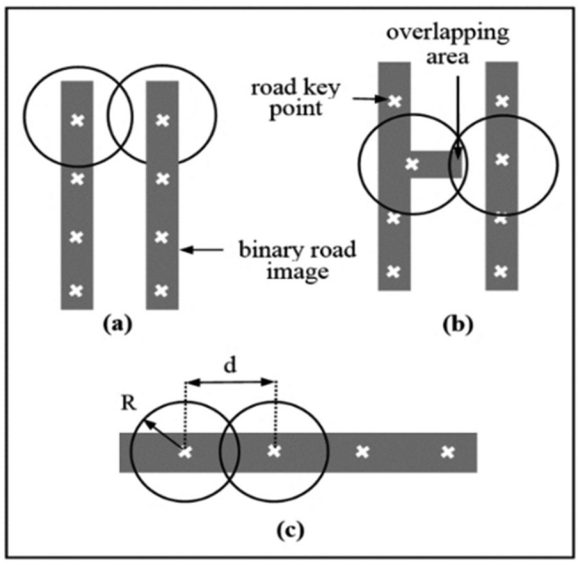

Figure 4. Circular Intersection with binary road image: (a) CI = 0, (b) Small CI, and (c) Large CI.

TABLE 1. RANGE OF CRITERIA VALUES AND THEIR NORMALIZATION FUNCTIONS

Criteria	Range of values	Normalization function
Distance(d)	$[0\ \infty)$	$N(D) = d/d_{max}$
Direction Difference (DD)	$[0\ \pi/2]$	$N(DD) = DD/D_{Dmax}$
Circular intersection (CI)	$[0\ \infty)$	$N(CI) = 1 - CI/CI_{max}$

Modeling Decision Strategies

In order to connect two road key points, the values of each connection criteria are aggregated, considering the importance weight of each criterion. The decision strategy is a primary feature in selecting an aggregation function. One extreme is the situation in which all the criteria are satisfied, and the other extreme is the state where any of the criteria is met. Different decision strategies are located between the mentioned two extreme strategies. In the following section an OWA based aggregation operators is presented.

Ordered Weighted Averaging Operators

The OWA operator was introduced by Yager (1988) and it provides a parameterized family of aggregation operators that include the maximum, the minimum and the arithmetic mean. The *n*-dimensional OWA is a mapping OWA*:* $R^n \rightarrow R$ with an associated weighting vector $W= [w_1, w_2, \ldots, w_n]$ in which $w_j \in [0, 1]$ and $\sum_{j=1}^{n} w_j = 1$. Using this operator a sequence A of *n* scalar values for each alternative in the data set are ordered decreasingly and then weighted according to their ordered position by the weighting vector. If c_j represents the j^{th} largest value in A, Equation 1 is defined:

$$OWA(A) = \sum_{j=1}^{n} w_j c_j \, . \tag{1}$$

The main characteristic of the OWA operator is its flexibility to model a wide range of aggregation strategies (Cornelis *et al.*, 2010). The main goal of reordering step is distinguishing between situations where the highest argument is the best result and situation where the lowest argument is the best result (Merigo and Gil-Lafuente, 2008). For example, the Minimum, the Average, and the Maximum can be modeled by means of OWA operators as follows:

a. *Minimum:* $W_{min}=\{w_j\}$, *where* $w_n=1$, $w_j=0$, $j \neq n$
b. *Average:* $W_{avg}=\{w_j\}$, *where* $w_j=1/n$, $j= 1, \ldots, n$
c. *Maximum:* $W_{max}=\{w_j\}$, *where* $w_1=1$, $w_j=0$, $j \neq 1$

The Maximum operator provides the type of "ANDing" aggregation implemented by the "all" requirement. Similarly, "ORing" aggregation operator is a representative of Minimum operator which fulfill an "at least one" type of condition (Yager, 1988).

In this research the weight vector represents two groups of weights including order weights and criteria weights.

Determination of Order Weights

Assume we want to calculate the cost of each road segment using three criteria $C= \{C_1, C_2, C_3\}$. The relative importance of each criterion is denoted by a weighting vector $W = \{w_1, w_2, w_3\}$. By selecting the appropriate weights in *W*, different arguments can be emphasized based upon their position within the ordered matrix of criteria. For example, if most of the weights were placed near the top of *W*, the criteria with higher scores are emphasized, and if the weights were placed near the bottom of *W*, then the criteria with lower scores in the aggregation process are highlighted. Yager (1988) introduced "ORness" as a measure to describe the behavior of an OWA operator. This operator indicates the degree in which an OWA operator behaves like an OR operator and is defined in Equation 2:

$$Orness(W) = (1/n-1)\sum_{j=1}^{n}((n-j).w_j) \, . \tag{2}$$

As the behavior of an aggregation operator goes from minimum to maximum, the ORness degree will range from 0 to 1. From Equation 2 it is inferred:

a. ORness (0, … , 0,1) = 0 →Min operator
b. ORness (1,0, … , 0) =1 →Max operator
c. ORness (1/*n*,1/*n*, … , 1/*n*)½ →Weighted Linear Combination (WLC) operator.

It is clear that the actual type of aggregation performed by an OWA operator depends upon the form of the weighting vector. Based on the extensive study on the methods of determining the weighting vector, three categories are recognized: Some approaches determine the weights based on the measures which describe the OWA behavior like ORness (Fuller and Majlender, 2001; Amin and Emrouznejad, 2006). A number of approaches have been suggested for obtaining the associated weights by means of linguistic quantifiers (Yager, 1988; Emrouznejad, 2008; Nadi and Delavar, 2011). Other approaches employ the decision attitude of the decision-maker to obtain the associated weights through an objective function (Yager and Filev, 1994; Ahn, 2008). This study utilizes the first category to determine the OWA weights, which is more intuitive for the application in hand.

Determining Order Weights Using ORness

In this paper, a decision strategy is defined using appropriate ORness values which indicates the portion of the criteria necessary for a good solution. Based on Yager (1996) the OWA order weights are computed using Equation 3:

$$w_j = \left(\frac{j}{n}\right)^{\alpha} - \left(\frac{j-1}{n}\right)^{\alpha} \tag{3}$$

where α is the degree of optimism which indicates the decision strategy. The value of α is related to the ORness as follows (Equation 4):

$$\text{ORness} = \frac{1}{1+\alpha} \quad \alpha \geq 0 \, . \tag{4}$$

Changes of α represent a continuum of different decision strategies between the two extreme cases of logic AND or OR. The *ORness=0* ($\alpha \rightarrow \infty$) represents the strategy corresponding to the MIN operator. On the other hand, the ORness=1 (α=0) represents the strategy corresponding to the MAX operator. If *ORness = 0.5* (α = 1), then the strategy corresponds to the conventional WLC, which is situated at the mid-point of the continuum between MIN and MAX operators.

The strategy associated with the *ORness* = 0 is referred to as the extremely pessimistic strategy (see Table 2); Thus, only the lowest criterion value is considered in the evaluation process. Conversely, the extremely optimistic strategy corresponds to *ORness* = 1 (Jelokhani and Malczewski, 2014).

Table 2. The Aggregation/Decision Strategies Corresponding to Specific ORness Value (α Parameter)

α	ORness	Aggregation strategy	Decision strategy
0	1	Logic OR (Max)	Extremely optimistic
0.1	0.9	—	Very optimistic
0.4	0.7	—	optimistic
1	0.5	WLC	Neutral
2	0.3	—	Pessimistic
10	0.1	—	Very pessimistic
∞	0	Logic AND (Min)	Extremely pessimistic

Determination of Criteria Weights

In many applications of multiple criteria aggregation, in addition to the ordered weights of the criteria (w_j), another weight (v_j) is required to reflect the relative significance or the priority of the criteria. The former term reflects the decision strategy and the latter indicates the criteria preferences regarding the decision-maker attitude (Nadi and Delavar, 2011).

To combine these two types of weights, Yager (1997) proposed a criteria weight modification approach for generating the order weight (w_j) based on the inclusion of criterion weight (v_j) according to the reordered criterion value as Equation 5:

$$w_j = \left(\frac{\sum_{k=1}^{j} v_k}{\sum_{k=1}^{n} v_k}\right)^{\alpha} - \left(\frac{\sum_{k=1}^{j-1} v_k}{\sum_{k=1}^{n} v_k}\right)^{\alpha}. \quad (5)$$

The criteria weights typically have the following property (Equation 6):

$$\sum_{j=1}^{n} v_j = 1. \quad (6)$$

So, for alternative i in the data set the OWA operator can be defined as Equations 7 and 8:

$$w_j = \left(\sum_{k=1}^{j} v_k\right)^{\alpha} - \left(\sum_{k=1}^{j-1} v_k\right)^{\alpha} \quad (7)$$

$$\mathrm{OWA}_i = \sum_{j=1}^{n}\left(\left(\sum_{k=1}^{j} v_k\right)^{\alpha} - \left(\sum_{k=1}^{j-1} v_k\right)^{\alpha}\right) c_j. \quad (8)$$

where α indicates the decision strategy based on Equation 4.

In the case of road vectorization, the criteria weights should be determined considering the relative importance of the road segment criteria. A simple and reliable method for estimating criteria weights is based on a ranking of evaluation criteria according to their preference (Stillwell *et al.*, 1981). Referring to this method, the j^{th} criterion weight can be calculated as Equation 9:

$$v_j = \frac{n - r_j + 1}{\sum_{k=1}^{n}(n - r_k + 1)} \quad (9)$$

where j is the rank position of the j^{th} preferable criterion. The most important criterion ranks first ($r_j = 1$), the second most important criterion ranks second ($r_j = 2$), and so on; a rank of $r_j = n$ is assigned to the least important criterion; n is the number of criteria. Referring to Equation 9, the more preferable the criterion is, the higher weight is assigned.

Calculation of Cost for Each Line Segment

Following the determination of normalized criteria values, criteria weights, and aggregation strategy (ORness value), one can calculate the overall aggregation value of each alternative (line segment) utilizing the OWA based decision operator. The OWA aggregation operators are used to transform the predefined properties (criteria) of road segments into normalized values in the range of [0,1]. The cost value of i^{th} line segment is calculated using Equation 10:

$$Cost(i) = \mathrm{OWA}_i \,.\, d_i/Cl_i, \quad (10)$$

It is obvious in Equation 10, the value of cost is directly proportional to the length of the line segment. In that, the cost value is raised by increasing the distance between road key points. Conversely, the cost value is indirectly proportional to the CI value. By increasing the number of road pixels in the circular intersection area of corresponding road key points, the cost value is decreased which leads to selection of the assumed line segment as a road segment. On the whole, this cost function is a decision criterion to accept a line segment as a road segment or reject it. The procedure of cost calculation for each line segment is summarized in Figure 5.

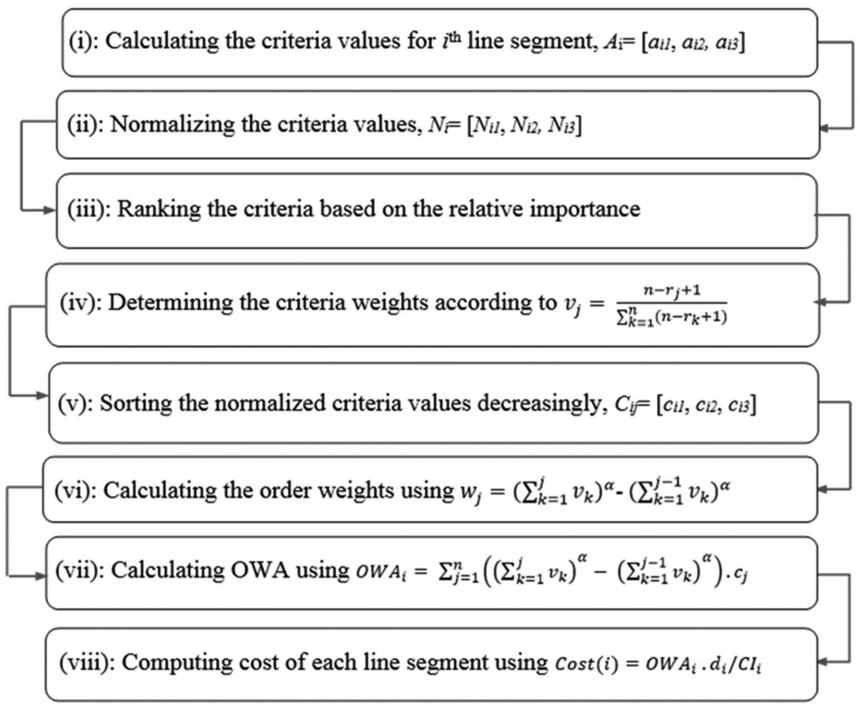

Figure 5. Computing cost of i^{th} line segment based on OWA.

Road Key Point Connection Algorithm

To make true connections between predetermined road key points and to construct road network topology, this section describes a novel road vectorization algorithm. This algorithm relies on the weighted graph theory to introduce geometrical road characteristics to the vectorization strategy. The nodes of the graph correspond to the road key points and the edges are characterized by possible road segments. An OWA aggregation strategy is used to transform the road geometric properties into cost values previously defined .

Before the explanation of the proposed road connection algorithm, it is necessary to specify the appropriate candidate pairs of road key points. For each point in the matrix of predefined positions of road key points (ORKP), the possible line segments around each road key point are considered. The number of possible line segments should be restricted due to two reasons: (a) Calculation of the cost values for all possible line segments from the start road key point computationally has a very poor efficiency, and (b) By increasing the length of the line segments from the start road key point, the possibility of assigning them to the road segment set decreases. In this paper, *K-Nearest Neighbor* (Cover and Hart, 1967) algorithm is used to find the *K* nearest points to each road key point. In this way only the *K* least cost line segments are investigated instead of all the possible line segments. The value of *K* is determined according to the maximum number of road legs involved in the road junction in the image. Based on Garber and Hoel's intersections classification method (2010), there are three major types of intersections: (a) three-leg intersection (like *T* and *Y* junctions), (b) four-leg or cross intersections, and (c) multi-leg intersections, which consist of five or more approaches. In general, multi-leg intersections are less common in order to remove the conflicting movements from the major intersection and thereby increase driving safety (Garber and Hoel, 2010).

The proposed road vectorization algorithm is considered as follows (Figure 6):

- For each road key point in the ORKP matrix, *K*-nearest least cost line segments are specified:
- The cost value for each of the *K* least cost line segments -not included in the road segments set (M_{RS})- is calculated based on the OWA aggregation algorithm (Figure 5).
- If the cost value is within an acceptable range (smaller than predefined threshold, T_{cost}) the line segment is added to the M_{RS}. Otherwise, another nearest line segment is examined.
- This procedure should be repeated until the entire road key points are examined and all the true road segments have been assigned to the M_{RS}.

```
Inputs : Matrix of positions of N Optimum Road Key Points (ORKP), K.

Output: Road segments set (MRS).

1.  For each road key point in ORKP (RKPi);
2.    Determine the K adjacent road key points using KNN algorithm ;
3.    For each line segment (LSj) starting from RKPi ;
4.       If LSj not belonging to MRS ;
5.          Calculate the Cost according to OWA aggragation (Fig. 5);
6.          If  Cost (j) < Tcost
7.             Add LSj to MRS ;
8.          End;
9.       Elseif LSj belonging to MRS ;
10.             Check another LSj ;
11.      End;
12.   End;
13. End;
```

Figure 6. The proposed road key point connection pseudo-code to construct road topology.

The final result of the proposed road vectorization technique is a road network consisting of road centerlines and junctions.

Implementation and Experimental Results

The proposed road vectorization approach was implemented on a PC environment using the professional MATLAB R2012a computer language. The proposed method was implemented on a simulated binary road image along with several different high resolution images.

The quality measures as defined in Wiedemann (2003) were determined based on comparing the vectorized road network with a reference road image, which was manually generated, by means of the "Buffer method in consideration of direction differences." The average width of five pixels on each side of the roads, 10 m for the Ikonos, was selected as buffer width to calculate the quality measures including RMS Error, completeness, and correctness. Besides, the junction RMS Error was calculated as another quality measure to investigate the robustness of the proposed method in junction vectorization. The junction evaluation buffer was set to ten pixels on each road side. The junction evaluation buffer was considered larger than the road evaluation buffer because the inaccuracy in the road centerline is usually largest at the end of the roads (Grote *et al.*, 2012).

Evaluation of Line Segment Alternatives Using OWA

Table 3 illustrates the criteria weights and the order weights by selecting different decision strategies for the three criteria previously defined. As it is shown in the table, the criteria weights are the same as the order weights in the case of OWA aggregation with ORness = 0.5 ($\alpha = 1$). In this situation the conventional WLC is performed on the values of the criteria.

Table 3. Criteria Weights and Order Weights for Three Road Segment Criteria Based on Different ORness

Criteria weights (vj) $N = 3$	Order weights (wj)	ORness						
		0	0.1	0.3	0.5	0.7	0.9	1
0.500	w1	0.000	0.000	0.250	0.500	0.758	0.895	1.000
0.333	w2	0.000	0.001	0.439	0.333	0.170	0.038	0.000
0.167	w3	1.000	0.999	0.311	0.167	0.072	0.067	0.000

Figure 7 shows an example of the cost calculation procedure (see Figure 5) for a set of criteria values of A_i = [15, 10, 80] at the i^{th} line segment in the case of WLC.

In this research, different decision strategies (ORness values) were considered to calculate the OWA values for each line

Road segment criteria: $D = a_{i1} = 15$, $DD = a_{i2} = 10°$, $CI = a_{i3} = 80$

Step i : $A_i = [15, 10, 80]$

Step ii : $N_i = [0.02, 0.11, 0.84]$

Step iii : $r = [1, 3, 2]$

Step iv : $v = [0.50, 0.33, 0.17]$

Step v : $C = [0.84, 0.11, 0.02]$

Step vi : $w = [0.50, 0.33, 0.17]$

Step vii : $OWA_i = 0.46$

Step vii : $Cost = 0.09$

Figure 7. An example of the OWA computation for the i^{th} line segment in the case of WLC.

segment. A higher degree of ORness results in a more optimistic decision strategy. Conversely, a lower degree of ORness leads to a more pessimistic solution. Being either optimistic or pessimistic could be appropriate depending on the problem.

However, in the context of road network topology construction, selection of higher ORness values makes the OWA aggregation values become larger. This effect increases the cost value; therefore, lower number of line segments may belong to the road segment set. On the contrary, if a lower ORness value is assigned, the value of cost is decreased which results in a higher number of line segments being considered as potentially suitable road segments. In such a decision context, identifying appropriate decision strategies is of great significance.

In order to evaluate the performance of the proposed algorithm, a simulated road binary image (Figure 8a) is generated which contains roads with different widths, parallel roads with different distances, and some three and four-leg intersections. In addition, several non-road objects are added to simulate a real detected road image. Results of determining optimized road patches and their corresponding road key points by means of DRPCPSO algorithm is demonstrated in Figure 8b. In this figure, road patches are depicted in grayscale. To correctly determine the appropriate decision strategy, the proposed road key point connection methodology was implemented on the simulated road image regarding different ORness values. The results are depicted in Figure 8c through 8g.

In the case of lower ORness values, there are some falsely extracted road segments (see Figure 8c through 8e) which indicate reduction in the cost values. Therefore, more line segments are accepted as road segment by the proposed algorithm. Alternatively, selecting higher ORness values leads to increase in the cost value raising the missed road segments (see Figure 8f and 8g). The cost of each line segment was finally calculated using Equation 1) by substituting the average of OWA values obtained by selecting different decision strategies. As depicted in Figure 8h the most complete road network is obtained using average OWA value. The isolated road key points in Figure 8h are not connected to the road

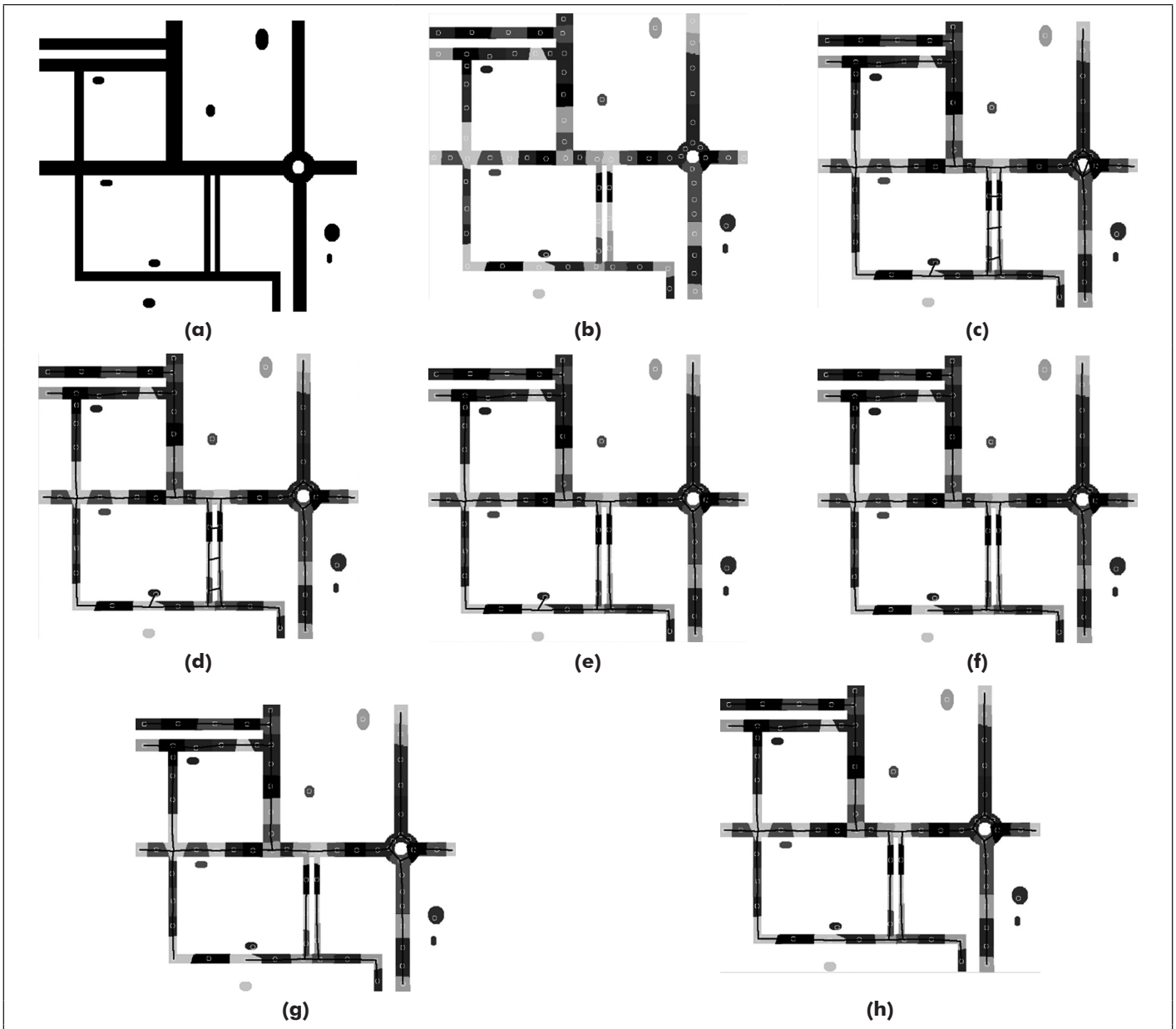

Figure 8. Results with the simulated image: (a) original image, (b) Road key points determination using DRPCPSO, (c) to (g) the proposed road key point connection using ORness of 0, 0.3, 0.5,0.7, and 1, respectively, (h) the proposed algorithm using average OWA value.

network which shows the robustness of the proposed algorithm against noise clusters.

The cost calculation procedure for the suggested line segment in Figure 7 by selecting different ORness values is depicted in Table 4. It is obvious from the Table 4 that the cost value considering the average OWA value has become lower compared to WLC in Figure 7. However, the value of cost is acceptable regarding to the selected cost threshold (T_{cost} = 1).

Table 4. Cost Calculation for the Line Segment Defined in Figure 7 Selecting Different ORness Values

ORness	0	0.1	0.3	0.5	o.7	0.9	1
OWA	0.020	0.027	0.260	0.460	0.660	0.790	0.840
Ave (OWA)= 0.41							
Cost (Ave (OWA))= 0.077							

Figure 9a demonstrates how the OWA values were modified by selecting different decision strategies for ten different line segments in the simulated road image of Figure 8. Regarding Figure 9a, the higher the ORness value is, the higher is the OWA value. The increasing rate is different for each line segment. The average range of OWA values for these ten line segments are depicted in Figure 9b.

Experiment with Imagery

The road centerline vectorization algorithm proposed in this paper can be used on any binary road image regardless of the road detection methodology applied. In the following experiments, the detected binary road image achieved by the combination of fuzzy C-means clustering (Ameri *et al.* 2008), along with the hole-filling and area-based filtering methods (Chaudhuri *et al.*, 2012). To verify the performance of the proposed vectorization algorithm on the real road images, several experiments with high resolution images were carried out. For different input binary road images T_{cost} =1 and R=0.7d were considered. The only parameter that needs to be defined for each image is K. This parameter is selected according to the maximum number of possible road legs in the places of road junction on the image. For all data sets the K value was considered as K = 4, and the cost function was calculated using the average OWA value.

Figure 10a presents a pan-sharpened Ikonos image of Hobart City of Tasmania in an urban area (750 × 650 pixels), and Figure 10b illustrates the detected binary road image. The proposed road key point connection algorithm was applied on the road binary image, and the vectorization results were shown in Figure 10c. Besides, the results were compared with Minimum Spanning Tree (MST) algorithm for road centerline extraction (Ameri *et al.*, 2008), which its outcomes is presented in Figure 10d. As expected the proposed algorithm vectorized the road centerlines more accurately and completely comparing with the MST (see Figure 11).

Figure 12 shows the same procedure on the Ikonos image of Hobart in a non-urban area (700 × 700 pixels). Figure12c and 12d illustrate the results of the centerline vectorization using the proposed methodology and MST, respectively, on the binary road image (Figure 12b). The proposed algorithm extracts most of the roads perfectly with a few false alarms. However, the vectorized road centerline by means of MST contains several false extractions specifically at place of nearby parallel roads in the middle of the image (Figure 12d).

As another experiment, Figure 13a depicts a pan-sharpened Ikonos image of Shiraz, Iran. The proposed vectorization methodology was implemented on the detected road image (Figure 13b) and the extracted road centerlines are shown in Figure 13c. There are some missed connections (depicted by dotted lines) and false extraction (depicted by light solid lines) where the road detection methodology has failed. On the whole, the number of false alarms in MST results (Figure 13d) are more prominent than the proposed method.

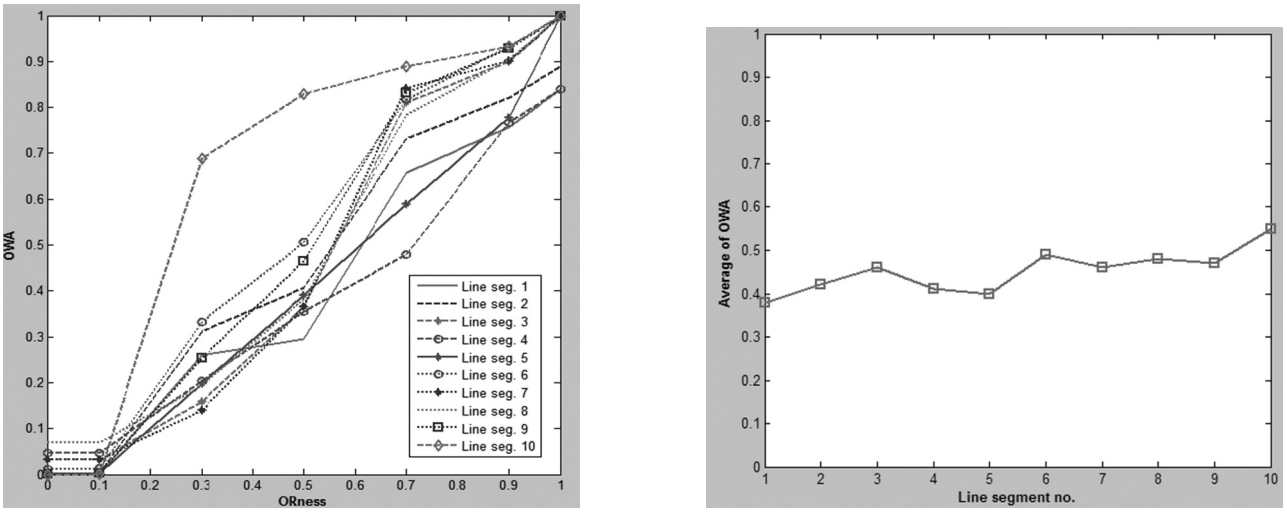

Figure 9. Results for ten different line segments of Figure 8: (a) OWA values based on different decision strategies, and (b) average range of OWA values.

Table 5. Comparison of the Proposed Method with MST for Both Hobart Images

Quality measure	Urban Hobart		Non-urban Hobart		Shiraz	
	Proposed method	MST method	Proposed method	MST method	Proposed method	MST method
RMSE (m)	0.97	1.04	1.1	1.3	0.67	0.73
Completeness (%)	95	89	98	94	88	79
Correctness (%)	96	94	97	93	93	86
Junction RMSE (m)	5.24	5.31	3.11	3.35	7.95	8.23

Table 5 compares the results of the proposed methodology with that of MST for the three tested images. Furthermore, Since the MST is a single-linkage tree structure, closed loops are not possible. In comparison with the proposed methodology, this limitation arises as more missed road segments in the MST results which reduce the completeness value. In addition, in contrast to the proposed methodology, MST is not effective in the vectorization of very close parallel roads which are depicted in enlarged portions of Figures 12 and 13 (c and d). Evidently, a close comparison indicates that our methodology is able to extract a larger accurate road network than the MST.

In all of the experiments, missed road segments are partly caused by context objects like rows of trees, buildings, or their shadows were found at places along the roads in the image (see Figure 11). As a result of road detection failure in this situation, the distance between two road key points becomes too large to be bridged during the road key point connection stage.

Incorrectly extracted road segments particularly occurred at three or four-leg junctions where some nearby road key points existed. Therefore, an enclosed area is created in the

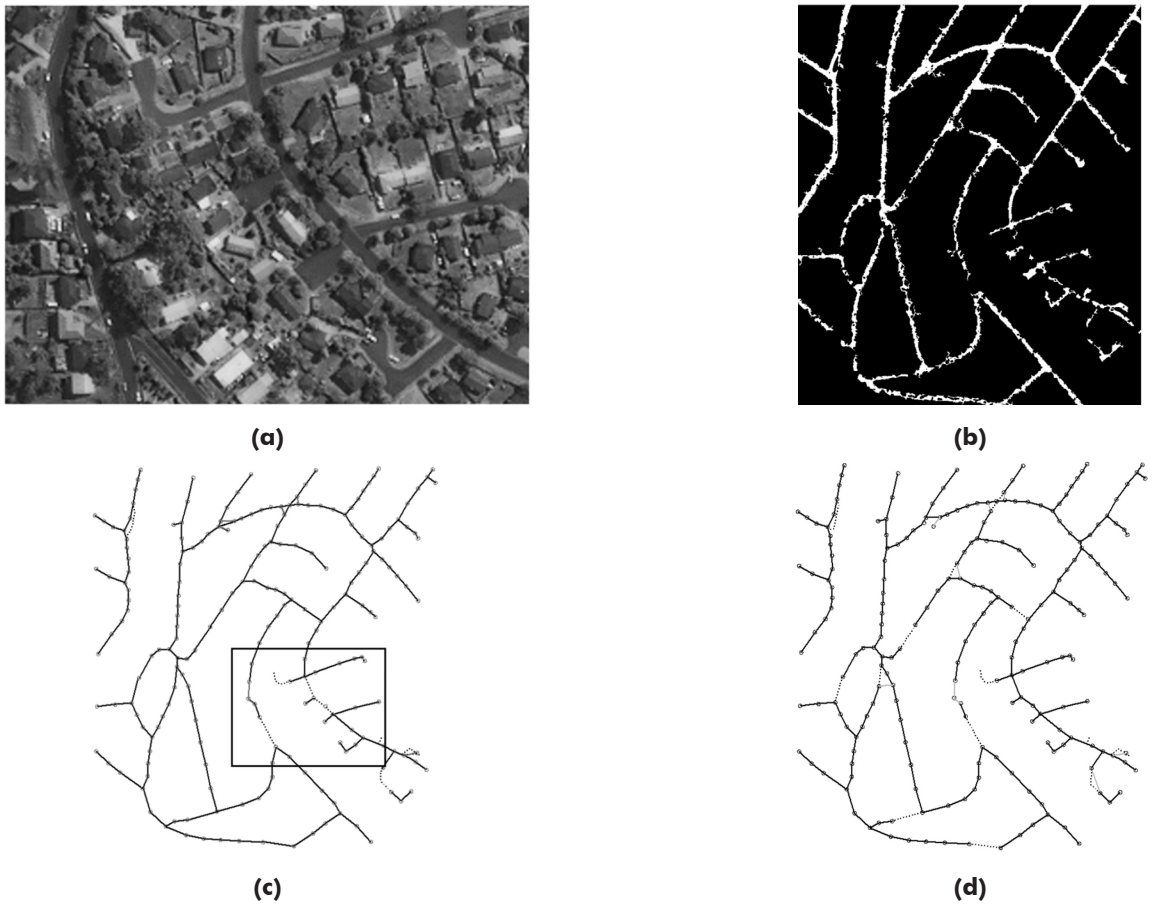

Figure 10. Results of urban Hobart: (a) original image, (b) detected road image, (c) results of the proposed methodology, (d) results of MST. Correctly extracted roads are given in dark solid lines, incorrectly extracted roads in light solid lines, and missing roads in dotted lines.

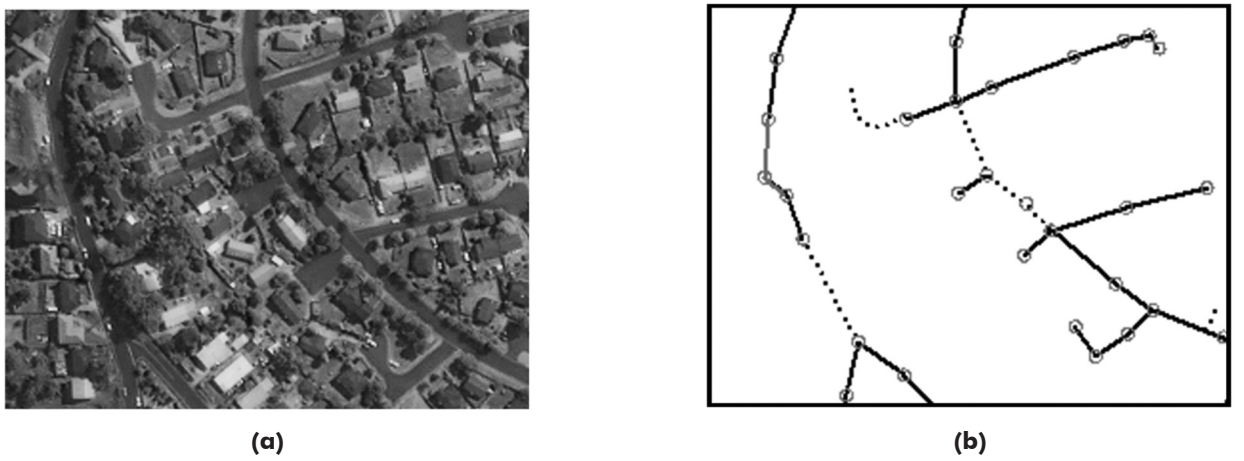

Figure 11. (a) Enlarged cut-out from the original image in Figure 10a, and (b) result of the proposed methodology for the same cut-out in Figure 10c.

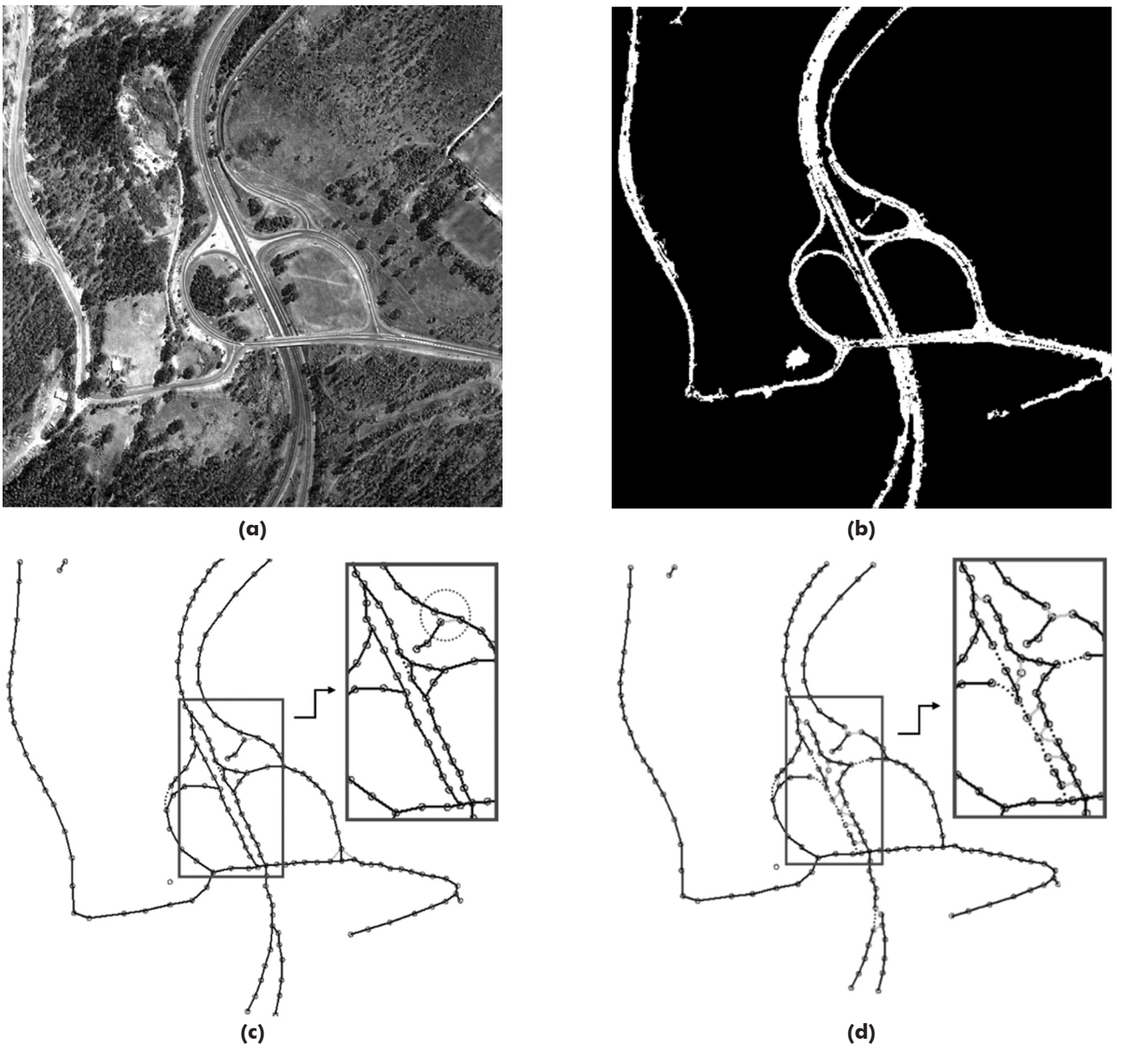

Figure 12. Results of non-urban Hobart: (a) original image, (b) detected road image, (c) results of the proposed methodology, and (d) results of MST: Correctly extracted roads are given in dark solid lines, incorrectly extracted roads in light solid lines, and missing roads in dotted lines.

road network graph instead of multi-leg intersections (like the one shown by dotted circle in the cut-out of Figure 12c).

The RMSE values in the Table 5 are approximately 1-meter in all the experiments which are acceptable for the images used. However, the values of junction RMS errors are far from the desirable values. Since finding the corresponding position of the junction point in both the reference and the vectorized result is not expected; the junction geometrical accuracy is less accurate than that of roads.

Comparison with Other State-of-the-Art Approaches

In this section, the evaluation of the proposed vectorization approach compared with two different approaches for road network vectorization is presented. The first approach uses a Self-Organizing Road Map (SORM) algorithm which combines a K-medians spatial clustering approach with a post-convergence node linking MST algorithm (Doucette *et al.*, 2001). The second one uses a combination of a novel Increasing Ellipse Clustering (IEC) methodology and the fuzzy ellipse-shaped clustering (Mokhtarzade *et al.*, 2010).These two approaches employ the idea of image space clustering for road vectorization similar to the proposed methodology.

In the following a pan-sharpened Ikonos image, an urban aerial image, and a pan-sharpened QuickBird image are depicted in Figure 14a through 14c, respectively. These data sets contain roads with different shapes and widths and also numerous three and four-leg intersections. The outputs of different road detection methodologies including an object-oriented classification methodology (Nghi and Mai, 2008), an object-oriented classification by means of eCognition® software (Mokhtarzade *et al.*, 2010), and an artificial neural networks (Mokhtarzade *et al.*, 2007) were used for Figure 14a through 14c, respectively. The variety of different road detection methodologies were applied to evaluate the capability of the proposed algorithm to deal with different road binary images.

The results of applying the proposed vectorization methodology, the SORM algorithm, and the IEC and fuzzy

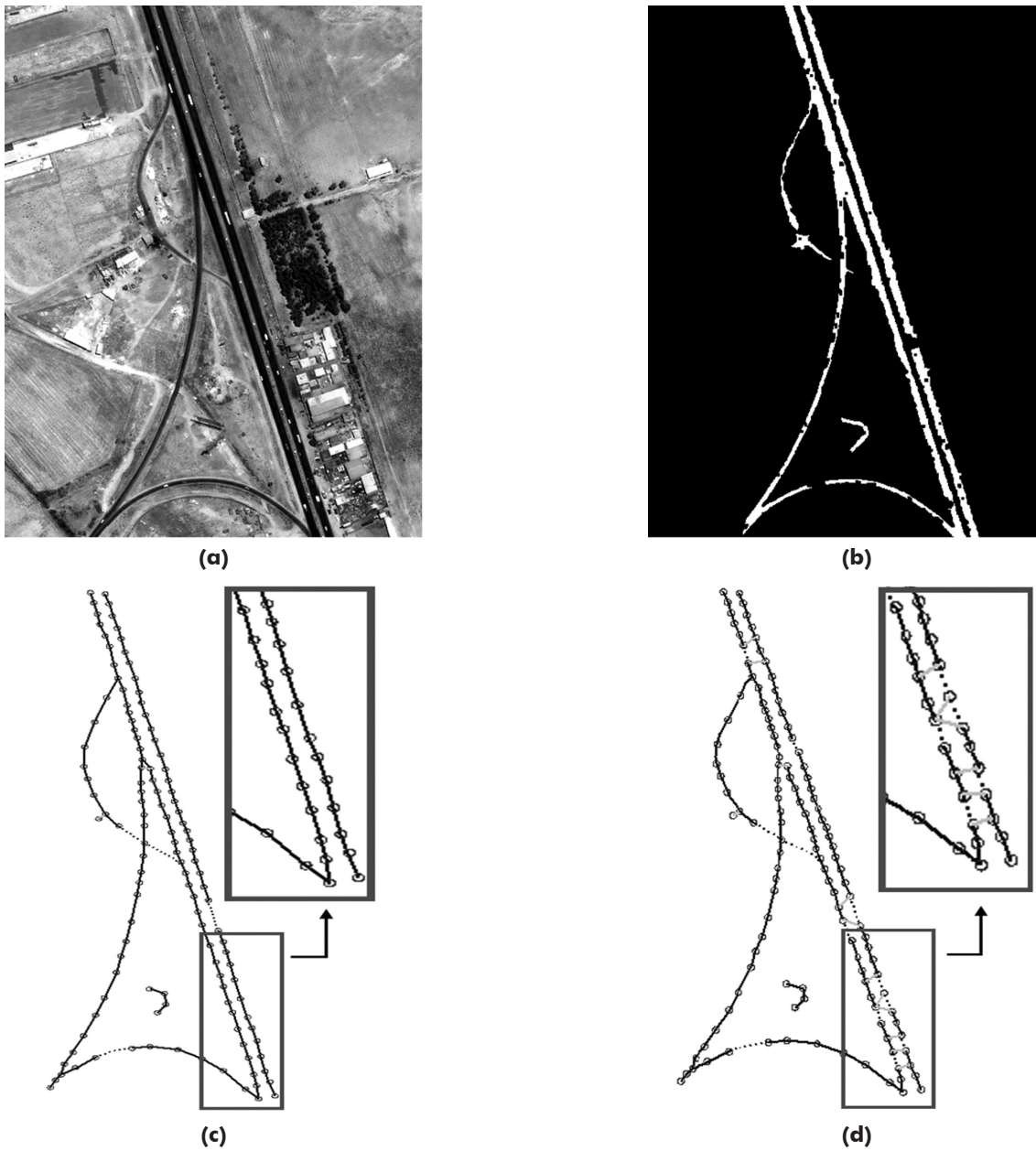

Figure 13. Results of an Ikonos image of Shiraz: (a) original image, (b) detected road image, (c) result of the proposed methodology, and (d) results of MST.

ellipse-shaped clustering technique on the three data sets are presented in Figure 15a through 15c, 15d through 15f, and Figure 15g through 15i, respectively.

The results of the evaluation are summarized in Table 6. The evaluation shows that the vectorization results of different approaches are almost similar with respect to sub-pixel RMSE values. On the other hand, the proposed methodology is able to extract a larger road network and to achieve a higher completeness values in comparison with the other methods. The first reason is the success of the proposed centerline extraction method in presence of missing information on the detected roads. The second reason is that the proposed method is able to vectorize closed shapes in the road network (depicted by dotted rectangles in Figure 15a and 15b). In contrast, since the SORM uses the MST algorithm in the node linking stage, it has some deficiencies in extracting a complete road network.

Concerning the junction RMSE in Table 6, the IEC and fuzzy clustering method outperforms the other two approaches at road junctions; they are able to extract the road junction's position by means of the controlling fuzzy parameters (Mokhtarzade *et al.*, 2010). Falsely extracted junctions by the proposed method most frequently happened where the width of connecting roads are high at the junction's intersection area. In this situation some nearby road key points exist at the intersection which forms an enclosed area (shown by dotted circles in Figure 15c). Generally, the performance of the proposed method is superior to others in both completeness and correctness.

Discussion

The main objective of this research is to investigate the ability of OWA based aggregation strategy to solve a problem with a unique solution (a true road network). In this context, different decision strategies between being extremely pessimistic and extremely optimistic were tested and the strategy

Figure 14. Image data set.

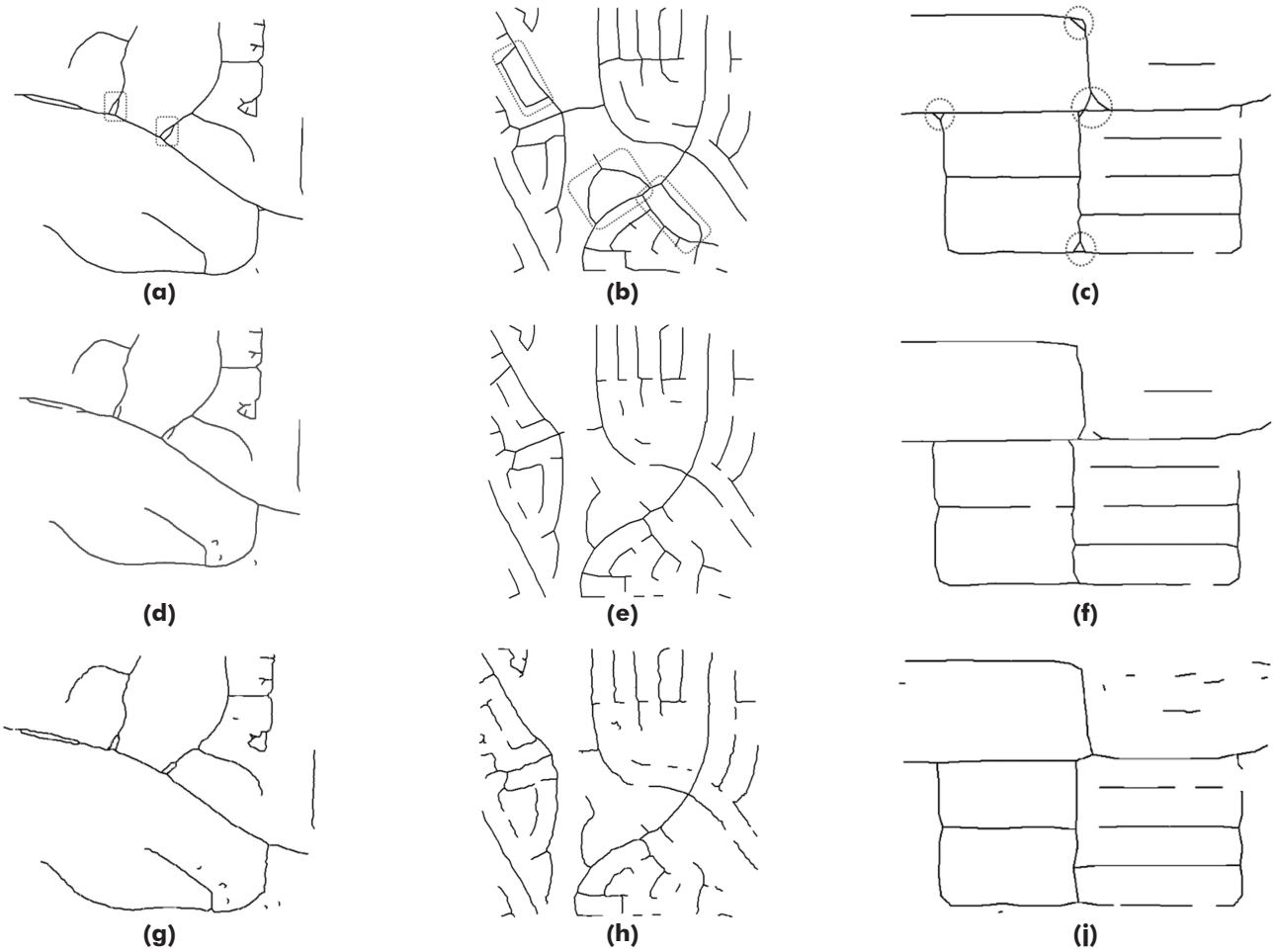

Figure 15. (a) through (c) results of the proposed vectorization methodology on the three data sets, (d) through (f) results of the SORM on the three data sets, and (g) through (i) results of the IEC and fuzzy ellipse-shaped clustering on the three data sets

Table 6. Comparison of the Proposed Method with Two Other Image Space Clustering Methods for Road Vectorization with Respect to Quality Measures

Data sets	Method	RMSE	Completeness	Correctness	Junction RMSE
Ikonos image	Proposed method	0.53	91	89	2.65
	SORM	0.61	72	80	2.50
	IEC & fuzzy clustering	0.54	89	86	2.11
Aerial image	Proposed method	0.50	90	97	3.53
	SORM	0.76	75	87	3.56
	IEC & fuzzy clustering	0.56	81	89	2.94
QuickBird image	Proposed method	0.38	92	93	4.20
	SORM	0.67	86	89	4.07
	IEC & fuzzy clustering	0.55	88	91	3.25

corresponding to OWA average value was found to be appropriate. This strategy proved to balance the effect of being optimistic and pessimistic in constructing a complete road network. It appears that being optimistic leads more gaps to arise in the extracted roads, and thus network completeness is reduced. Alternatively, selection of pessimistic strategy will overestimate the extracted line segments which are not necessarily correct. In none of these situations the accurate assessment parameters are obtained.

One of the advantages of the proposed method is considering knowledge about the appearance of the roads with a small number of geometric criteria, without using any radiometric features, in the road key point connection stage. In this framework, an innovative road geometric feature (CI) was proposed to decide which road key points are inclined to be connected to construct the true road network topology.

The proposed methodology is capable of vectorizing roads in presence of small disturbances on the road surface. Besides, this methodology is efficient in the case of roads with different widths, closed shapes in the road network, and also nearby parallel roads comparing with SORM and IEC and fuzzy clustering method. These advantages improve the quality measures prominently. Another achievement of the research is the robustness of the proposed algorithm against noise clusters. The robustness of the algorithm in presence of small non-road objects decreases the falsely extracted road segments.

By the way, it is obvious that the outcome of the vectorization stage is highly affected by the road detection output. The better is the result of the detection stage, the more complete and accurate vectorized road network is attained. In this research different road detection techniques were employed. The evaluation results justify the robustness of the proposed vectorization approach applying different detection methodologies.

Another important aspect is using a few parameters including K, R, and T_{cost} by the algorithm. The parameters R and T_{cost} are quite stable, as shown by the fact that they were tested on multiple images from different scenes and different sensors. It is necessary to select the radius of the overlapping circles (R), higher than half of the distance between two road key points. In all the experiments parameter R between [0.6d , 0.7d] was appeared to be appropriate. R >0.7d results in wrong connection especially in place of nearby parallel roads. Values in the range of [0.5d , 0.6d] reduce CI, which leads to higher cost values and missed road segments. In selection of the cost threshold value, If $d_i \leq CI_i$, then the cost will be in the range of [0,1]. On the other hand, if $d_i > CI_i$, then the cost will become larger than "0" (Cost ≥0). Eventually, the value of T_{cost} was experimentally defined as "1" to ensure the most complete and accurate road network. Only one parameter (K) had to be changed regarding the types of intersections in the images. Although, selecting the same maximum number of K for all the images does not have a considerable effect on the results; selecting smaller values only restricts the searching space for the road key points around.

However, our experimental results indicate a number of limitations. It is often not possible to extract a whole road completely in the case of disturbances in the appearance of roads that results in a large gaps in the detected road. Another deficiency of the proposed connection method is construction of enclosed area at place of junction where the width of connecting roads is high. To overcome this disadvantage a precise intersection modeling should be considered.

Conclusions

This paper proposed and verified a novel road vectorization methodology using image space clustering technique and weighted graph theory. According to the experimental results, the proposed road vectorization method is efficient and accurate in road network topology construction at different types of intersections, roads with dissimilar widths, parallel roads, and also images containing isolated non-road clusters. Furthermore, it shows robustness in vectorizing a road network regardless of the detection methodology. This method has also enough generality to include appropriate connection criteria to vectorize other types of linear cartographic features. The results are acceptable enough to be used in GIS databases with negligible operator interferences. Precise modeling of the context objects and intersections can improve the topological and geometrical quality of the results, which can be considered as the primary direction for the future research.

Acknowledgment

The authors would like to gratefully acknowledge the many valuable suggestions made by Najmeh Neisani Samani, assistant professor at Tehran University.

References

Ahn, B.S., 2008. Preference relation approach for obtaining OWA operators weights, *International Journal of Approximate Reasoning*, 4:166–178.

Ameri, F., A.M. Mobaraki, and M.J. Valadanzoej, 2008. Semi-automatic extraction of different-shaped road centerlines from MS and pan-sharped Ikonos images, *International Archives of Photogrammetry, Remote Sensing and Spatial Information Sciences*, Vol. XXXVII, Part B3b, Beijing, China..

Amin, G.R., and A. Emrouznejad, 2006. An extended minimax disparity to determine the OWA operator weights, *Computers & Industrial Engineering*, 50:312–316.

Bacher, U., and H. Mayer, 2005. Automatic road extraction from multispectral high resolution satellite images, *CMRT05*, *International Archives of Photogrammetry and Remote Sensing*, Vol. XXXVI, Part 3/W24.

Baumgartner, A., C. Steger, H. Mayer, W. Eckstein, and H. Ebner, 1999. Automatic road extraction based on multi-scale, grouping and context, *Photogrammetric Engineering & Remote* Sensing 65:777–786.

Chaudhuri, D., N.K. Kushwaha, and A. Samal, 2012. Semi-automated road detection from high resolution satellite images by directional morphological enhancement and segmentation techniques, *IEEE Journal of Selected Topics in Applied Earth Observation and Remote Sensing*, Vol. 5.

Chen, L.H., C.C. Hung, and C.C. Tu, 2012. Considering the decision maker's attitudinal character to solve multi-criteria decision-making problems in an intuitionistic fuzzy environment, *Knowledge-Based Systems*, (36)129–138.

Cornelis, C., N. Verbiest, and J. Jensen, 2010. Ordered weighted average based fuzzy rough sets, *Proceedings of the 5th International Conference on Rough Sets and Knowledge Technology (RSKT 2010)*, pp. 78–85.

Cover, T.M., and P.E. Hart, 1967. Nearest neighbor pattern classification, *IEEE Transactions on Information Theory*, 13:21–27.

Doucette, P., P. Agouris, A. Stefanidis, and M. Musavi, 2001. Self-organised clustering for road extraction in classified imagery, *ISPRS Journal of Photogrammetry and Remote Sensing*, 55:347-358.

Emrouznejad, A., 2008. MP-OWA: The most preferred OWA operator, *Knowledge-Based Systems*, 21:847–851.

Ferchichi, S., and S. Wang, 2005. Optimization of cluster coverage for road center-line extraction in high resolution satellite images, *Proceedings of the IEEE International Conference on Image Processing*, pp. 201–204

Fuller, R., and P. Majlender, 2001. An analytic approach for obtaining maximal entropy OWA operator weights, *Fuzzy Sets and Systems*, 124:53-57.

Garber, N., and L. Hoel, 2010. *Traffic & Highway Engineering*, Cengage Learning Publishing, Fourth edition, ISBN:0495438537.

Grote, A., C. Heipke, and F. Rottensteiner, 2012. Road network extraction in suburban areas, *The Photogrammetric Record*, 27(137):8–28.

Gruen, A., and H. Li, 1995. Road extraction from aerial and satellite images by dynamic programming, *ISPRS Journal of Photogrammetry and Remote Sensing*, 50(4):H-20.

Gruen, A., and H. Li, 1997. Semi-automatic linear feature extraction by dynamic programming and LSB snakes. *Photogrammetric Engineering & Remote Sensing*, 63(8):985–995.

Herrera, F., E. Herrera-Viedma, and J.L. Verdegay, 1996. Model of consensus in group decision making under linguistic assessments, *Fuzzy Sets and Systems*, 78:73–87.

Hinz, S., and A. Baumgartner, 2003. Automatic extraction of urban road networks from multi-view aerial imagery, *ISPRS Journal of Photogrammetry & Remote Sensing*, 58:83– 98.

Jelokhani-Niaraki, M., and J. Malczewski, 2014. A group multicriteria spatial decision support system for parking site selection problem: A case study, *Land Use Policy*, (42):492–508.

Karaman, E., U. Çinar, E. Gedik, Y. Yardimci, and U. Halici, 2012. A new algorithm for automatic road network extraction in multispectral satellite images, *Proceedings of the 4th GEOBIA*, 07-09 May, Rio de Janeiro, Brazil, p.455.

Liu, H., J. Cai, and L. Martínez, 2013. The importance weighted continuous generalized ordered weighted averaging operator and its application to group decision making, *Knowledge-Based Systems*, 48:24–36.

Malczewski, J., 1999. *GIS and Multicriteria Decision Analysis*, Wiley, New York.

Malczewski, J., 2006. Ordered weighted averaging with fuzzy quantifiers: GIS based multi criteria evaluation for land-use suitability analysis, *International Journal on Applied Earth Observation and Geoinform*ation, 8(4):270–277.

Matkan, A.A., M. Hajeb, and S. Sadeghian, 2014. Road extraction from lidar data using support vector machine classification, *Photogrammetric Engineering & Remote Sensing*, 80(5):409-422.

Mena, J.B., 2006. Automatic vectorization of segmented road networks by geometrical and topological analysis of high resolution binary images, *Knowledge-Based Systems*, 19:704–718.

Mena, J., and J. Malpica, 2003. Color image segmentation using the Dempster-Shafer theory of evidence for the fusion of texture, *International Archives of the Photogrammetry, Remote Sensing and Spatial Information Sciences*, Vol. 34-3/W8, pp. 139–144.

Mena, J., and J. Malpica, 2005. An automatic method for road extraction in rural and semi-urban areas starting from high resolution satellite imagery, *Pattern Recognition Letters*, 26:1201–1220.

Merigo, J.M., and A.M. Gil-Lafuente, 2008. Using the OWA operator in the Minkowski distance, *World Academy of Science, Engineering And Technology*, Vol. 2-2008:09–29.

Mohammadzadeh, A., A, Tavakoli, and M.J. ValadanZoej, 2006. Road extraction based on fuzzy logic and mathematical morphology from pan-sharpened Ikonos images, *The Photogrammetric Record*, 21(113):44-60.

Mokhtarzade, M., and M.J. Valadan Zoej, 2007. Road detection from high resolution satellite images using artificial neural networks, *International Journal of Applied Earth Observation and Geoinformation*, 9(1):32–40.

Mokhtarzade, M., M.J. Valadan Zoej, H. Ebadi, and M.R. Sahebi, 2010. An innovative image space clustering technique for automatic road network vectorization, *Photogrammetric Engineering & Remote Sensing*, 76(7):841–852.

Nadi, S., and M.R. Delavar, 2011. Multi-criteria, personalized route planning using quantifier-guided ordered weighted averaging operators, *International Journal of Applied Earth Observation and Geoinformation*, pp. 322–335.

Nghi, D.H., and L.C. Mai, 2008. An object-oriented classification technique for high resolution satellite imagery, *Proceedings of the International Symposium on Geoinformatics for Spatial Infrastructure Development in Earth and Allied Sciences*, Hanoi, Vietnam.

Omran, M.G., A.P. Engelbrecht, and A. Salman, 2006. A Dynamic clustering using particle swarm optimization with application in image classification, *Pattern Analysis and Application*, pp. 332-344.

Poullis, C., 2014. Tensor-Cuts: A simultaneous multi-type feature extractor and classifier and its application to road extraction from satellite images, *ISPRS Journal of Photogrammetry and Remote Sensing*, (95):93–108.

Poullis, C., and S. You, 2010. Delineation and geometric modeling of road networks, *ISPRS Journal of Photogrammetry and Remote sensing* 65(2):165-181.

Rinner, C., and J. Malczewki, 2002. Web-enabled spatial decision analysis using ordered weighted averaging (OWA), *Journal of Geographical Systems*, (4):385–403.

Shanmugam, L., and V. Kaliaperumal, 2015. Water flow based geometric active deformable model for road network, *ISPRS Journal of Photogrammetry and Remote Sensing*, (102):140–147.

Stillwell, W.G., D.A. Seaver, and W. Edwards, 1981. A comparison of weight approximation techniques in multi-attribute utility decision making, *Organizational Behavior and Human Performance*, 28(1):62–77.

Torra, V., 2004. OWA operators in data modeling and reidentification, *IEEE Transactions on Fuzzy Systems*, 12:652–660.

Wiedemann, C., 2003. External evaluation of road networks, *ISPRS Archives*, Vol. XXXIV, Part 3/W8, 17-19 September, Munich.

Wiedemann, C., and S. Hinz, 1999. Automatic extraction and evaluation of road networks from satellite imagery, *International Archives of Photogrammetry and Remote Sensing*, Vol. 32(3-2W5):95–100.

Yager, R.R., 1988. On ordered weighted averaging aggregation operators in multicriteria decision making, *IEEE Transactions on Systems, Man, and Cybernetics*, 18 (1):183–190.

Yager, R.R., 1991. Connectives and quantifiers in fuzzy sets, *Fuzzy Sets and Systems*, 40:39–75.

Yager, R.R., 1992. On a semantics for neural networks based on fuzzy quantifiers, *International Journal of Intelligent Systems*, 7:765–786.

Yager, R.R., 1995. Fuzzy aggregation of modular neural networks with ordered weighted averaging operators, *International Journal of Approximate Reasoning*, 13:359–375.

Yager, R.R., 1996. Quantifier guided aggregation using OWA, *International Journal of Intelligent Systems*, 11:49–73.

Yager, R.R., 1997. On the inclusion of importances in OWA aggregations, *The Ordered Weighted Averaging Operators* (R.R. Yager and J. Kacprzyk, editors), *Kluwer Academic Publishers*, Boston, Massachusetts, pp. 41–59.

Yager, R.R., and D.P. Filev, 1992. Fuzzy logic controllers with flexible structures, *Proceedings of the Second International Conference on Fuzzy Sets and Neural Networks*, pp. 317–320.

Yager, R.R., and D. Filev, 1994. Parameterized "andlike" and "orlike" OWA operators, *International Journal Of General Systems*, 22:297–316.

Youn, J., J.S. Bethel, E.M. Mikhail, and C. Lee, 2008. Extracting urban road networks from high-resolution true orthoimage and lidar, *Photogrammetric Engineering & Remote Sensing*, 74(2):227–238.

Zarrinpanjeh, N., F. Samadzadegan, and T., Schenk, 2013. A new ant based distributed framework for urban road map updating from high resolution satellite imagery, *Computers & Geosciences*, 54:337-350. Zhu, P., Z. Lu, X. Chen, K. Honda, and A. Eiumnoh, 2004. Extraction of city roads through shadow path reconstruction using laser data, *Photogrammetric Engineering & Remote Sensing*, 70(12):1433-1440.

(Received 24 February 2015; accepted 04 June 2015; final version 31 July 2015)

Seamline Determination for High Resolution Orthoimage Mosaicking Using Watershed Segmentation

Mi Wang, Shenggu Yuan, Jun Pan, Liuyang Fang, Qinghua Zhou, and Guopeng Yang

Abstract

Image mosaicking is a process during which multiple orthoimages are combined into a single seamless composite orthoimage. One of the most difficult steps in the automatic mosaicking of orthoimages is the seamline determination. This paper presents a novel algorithm that selects seamlines based on marker-based watershed segmentation. A representative seamline is extracted at the object level and the pixel level as follows. First, a watershed segmentation is performed to obtain the objects. To avoid over-segmentation, a regional adaptive marker-based watershed segmentation is proposed. Second, the object difference estimated by the correlation coefficient of each object is calculated, and the region adjacency matrix is built. Third, a technique for minimizing the maximum object cost is adopted to determine the objects through which the seamlines pass. Finally, pixel-level optimization is performed using Dijkstra's algorithm with a binary min-heap to determine the final seamlines. The experimental results on digital aerial orthoimages in different areas demonstrate the feasibility and effectiveness of the proposed method compared with other algorithms.

Introduction

Orthoimages integrate the rich information content of images and the geometric properties of maps (ground projection) and can be easily combined with additional information from geographic information systems (GIS) to create an orthoimage map. Thus, they have become a popular visualization product and planning instrument (Kerschner, 2001).

Image mosaicking is defined as a necessary process in which multiple orthoimages are combined into a single seamless composite orthoimage for many applications, such as environmental monitoring and disaster management (Pan and Wang, 2011). When mosaicking orthoimages, seamline determination is one of the key steps and has an important impact on the quality of the final mosaic. It is the process of finding a path with the least difference in the overlapping area of the images to be merged. The purpose of seamline determination is to minimize as much as possible the discontinuity in the final mosaic of the path. In an orthoimage, objects not included in the Digital Terrain Model (DTM), or wrongly modeled, would appear at different locations in various orthoimages because of the variation in viewing angles (Kerschner, 2001). Particularly for high-resolution aerial orthoimages of urban areas, different facets of an object, e.g., a building, may appear in different images.

In previous studies, scientists attempted to develop methods to determine an optimal seamline to improve the quality of orthoimage mosaicking. Milgram (1975) defined the "best" seamlines by minimizing the amount of artificial edge in a certain width in terms of pixel value difference between two overlapping images to determine the lowest cost path. Fernandez *et al.* (1998) defined seamlines by bottleneck shortest paths. Fernandez and Marti (1999) developed a Greedy Randomized Adaptive Search Procedure (GRASP) to optimize the bottleneck shortest paths. Afek and Brand (1998) determined seamlines based on a matching algorithm and local transformation. Kerschner (2001) proposed a "two snake" method to find seamlines in areas with high color and texture similarity. The two snakes approach the desired line in the image from opposite sides. During their evolution, the two snakes attract one another and the optimal seamlines are determined when the two snakes merge into one. Soille (2006) proposed a morphological image compositing algorithm. The main idea of the algorithm was to allow for the automatic positioning of the mosaic seamlines along salient image structures to diminish their visibility. Chon *et al.* (2010) used Dijkstra's algorithm (Dijkstra, 1959) based on the Normalized Cross Correlation (NCC) cost function, and limited the maximum difference in seamline selection. This method enabled the search to possibly find a longer seamline with less highly mismatched pairs. Ma and Sun (2011) proposed an improved A* algorithm combining lidar point clouds for orthoimage seamlines optimization. This method was able to intelligently bypass the obstacle areas smartly, and the resulting path could get close enough to the initial seamlines. Yu *et al.* (2012) presented an automatic seamlines location algorithm which used image appearance (i.e., color, edge, and texture), image saliency and location constraints for mosaicking optical remote sensing images. Wang *et al.* (2012), Wan *et al.* (2012) and Wan *et al.* (2013) suggested an approach using vector roads to aid in generating seamlines for aerial image mosaicking. Pan *et al.* (2014b) put forward a method of seamline determination by mean shift segmentation for orthoimage mosaicking in an urban area.

In this paper, we present a new method of seamline determination based on marker-based watershed segmentation for high-resolution orthoimage mosaicking. It determines the optimal seamlines at both the object and pixel level. First, the

Mi Wang and Jun Pan are with the State Key Laboratory of Information Engineering in Surveying, Mapping and Remote Sensing, Wuhan University, 129 Luoyu Road, Wuhan, Hubei 430079, China; and the Collaborative Innovation Center of Geospatial Technology, 129 Luoyu Road, Wuhan, Hubei 430079, China (panjun1215@whu.edu.cn).

Shenggu Yuan, Liuyang Fang, and Guppeng Yang are with the State Key Laboratory of Information Engineering in Surveying, Mapping and Remote Sensing, Wuhan University, 129 Luoyu Road, Wuhan, Hubei 430079, China.

Qinghua Zhou is with the China Railway Engineering Consulting Group Co., Ltd, 15 Guangan Road, Beijing100055, China.

Photogrammetric Engineering & Remote Sensing
Vol. 82, No. 2, February 2016, pp. 121–133.
0099-1112/16/121–133

doi: 10.14358/PERS.82.2.121

regional adaptive marker-based watershed segmentation algorithm is used to obtain the objects of the overlapping area in the left image. Then, the overlapping area of the right image is overlaid with the objects' boundaries of the overlapping area of the left image. Second, the correlation coefficient is used to estimate the degree of the objects' differences between the left image and the right image. The region adjacency matrix (a detailed definition is shown in Equation 5) is built in the correlation coefficient object map. A connectivity analysis algorithm with minimized maximum difference is used to determine the preferred objects areas (hereafter referred to as POAs). The POAs are areas through which it is preferred that the seamlines pass. Finally, pixel-level optimization is performed using Dijkstra's shortest-path searching algorithm to find the final seamlines (Fredman and Tarjan, 1987; Cherkassky *et al.*, 1996; Cormen *et al.*, 2001; Chen *et al.*, 2007).

This work has several significant improvements and extensions in contrast to the publication of Pan (Pan *et al.*, 2014b) on this topic:

1. A regional adaptive marker-based watershed segmentation is used to obtain the objects of the overlapping area, which improves the efficiency.
2. A one-to-one correlation between the left image and the right image is established by overlaying the overlapping area of the right image with the objects' boundaries of the left image to estimate the difference based on objects.
3. A connectivity analysis algorithm with minimized maximum difference is used to determine the POAs, which we call a seamline determination at the object level in this paper.
4. Dijkstra's shortest-path searching algorithm with a binary min-heap is used to improve the efficiency of Dijkstra's shortest-path searching algorithm.

Data Preparation

Two Data Sets of digital color aerial orthoimages were used to test the proposed algorithm in this study. All images were provided by the Heilongjiang Institute of Geomatics Engineering and Seasky Geomatics Technologies, Inc., China. The ground resolution of Data Set 1 is 0.5 m and the overlapping area size is 3,030 pixels by 2,067 pixels, which covers a downtown area of a big city with a large number of high-rise buildings. The ground resolution of Data Set 2 is 0.2 m and the overlapping area size is 2,438 pixels by 4,824 pixels, covering the suburban district.

Methodology

To minimize visual discontinuities, the seamline should avoid crossing obvious objects, e.g., buildings and high bridges. Relief displacement mainly occurs because a DTM does not contain elevations for these obvious objects. A differential expression is used to evaluate the difference of the overlapping area between the left and right images. A differential expression is a major difficulty in seamline determination. The differential expression generally uses a cost matrix to store the difference of the overlapping area. Common differential expression methods based on pixels and local regular subimages cannot evaluate the difference exactly. If object-based recognition were performed, the differential expression would be improved. The seamlines can be guaranteed to avoid crossing objects such as buildings and high bridges by setting the areas of those stand-alone objects to the highest difference. However, object-based recognition is a very difficult task. Therefore, the proposed algorithm adopts the segmentation algorithm to improve the differential expression.

Figure 1 shows the flowchart of the proposed method. Seamlines are extracted through a three-step operation: (a) segmentation by regional adaptive marker-based watershed; (b) seamline determination at the object level; and (c) seamline determination at the pixel level. Specifically, the second step includes three sub-operations: calculating the object correlation coefficients, building the region adjacency matrix and POAs determination. In addition, if the left and right image are in the RGB color space, our method will transfer them into

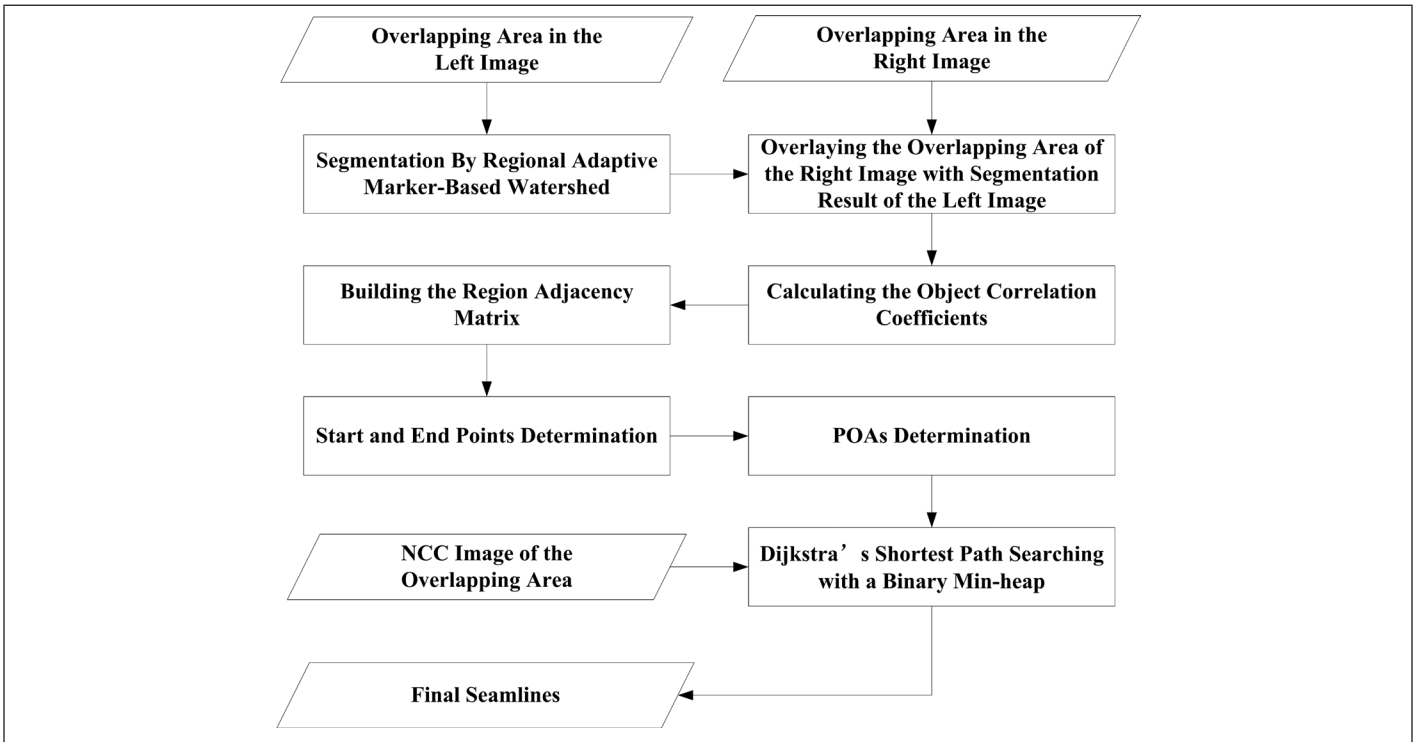

Figure 1. The flowchart of the proposed seamline determination method.

the hue, saturation and intensity (HSI) color spaces and then process them by using the intensity vector.

Regional Adaptive Marker-Based Watershed Segmentation

Regional adaptive marker-based watershed segmentation is an improvement on base watershed segmentation. The watershed segmentation algorithm is based on visualizing an image in three dimensions: two spatial coordinates versus intensity. It is usually applied to the gradient image. Suppose that a hole is punched in each regional minimum and that the entire topography is flooded from below by letting water rise through the holes at a uniform rate. When the rising water levels in distinct catchment basins are about to merge, a dam is built to prevent the merging. The flooding will eventually reach a stage when only the tops of the dams are visible above the water line. These dam boundaries correspond to the dividing lines of the watersheds. Therefore, they are the (connected) boundaries extracted by a watershed segmentation algorithm (Meyer and Beucher, 1990; Vincent and Soille, 1991; Meyer, 1992; Gonzalez and Woods, 2002; Li *et al.*, 2010; Zhang *et al.*, 2010).

However, direct application of the above watershed segmentation algorithm generally leads to over-segmentation due to noise and other local irregularities of the gradient. A solution is to control over-segmentation based on the concept of markers; in other words, marker-based watershed segmentation (Gonzalez and Woods, 2002). Marker-based watershed segmentation is a two-stage process: including the extraction of marker image and the labeling of pixels (flooding). There are various land cover objects with different texture granulations in a high spatial resolution remote sensing image. The gradient magnitudes of the pixels are intricately distributed. The gradient magnitudes within the homogenous object are commonly lower than that of the boundary pixels. However, the gradient magnitudes of pixels in objects with complex texture may be comparable or ever higher than that of the boundary pixels. It will fail to extract correct marker image with a single threshold for binarization (Li *et al.*, 2010). Therefore, when applying the method to high spatial resolution remote sensing image segmentation, the noises or textures of the image are usually labeled as pseudo-local minimum regions, resulting in over-segmentation.

To reduce over-segmentation, in this paper we adopt a regional adaptive marker-based watershed segmentation algorithm similar to that proposed by Li *et al.* (2010), but with minor modifications. First, a regional adaptive marker extraction method is adopted to obtain the marker image by using a threshold image (TI). Let GI represent the gradient image; then the marker image is defined as a binary image (BW) that is the result of the logical operation: BW = GI < TI. The low-pass component of the gradient image (LCG) calculated by the Butterworth low-pass filter corresponds to the main contents of the gradient image (GI). Therefore, the LCG can be used to set the TI. Multiplying the LCG with an appropriate scale factor (T, [0–1]) is useful for the marker extraction of objects with textures. It is suggested that T be set in the range between 0.6 and 0.7. However, for a homogenous object, the scaled LCG may be too low and lead to over-segmentation. For such objects, an empirical statistic threshold (EST) is used as the threshold. The EST value for a certain image is defined as the α fractile of the gradient level probability distribution; α ranges from [0 - 1]. For each pixel in TI, the corresponding scaled LCG value is compared with the EST value; the maximum between them is defined as the pixel value. Then, markers in the BW with insufficient spatial support are rejected because these markers are usually caused by noise. An appropriate area threshold (A), which is equal to the area of the smallest discernible object, is set to remove these markers. Second, the image labeling scheme in Meyer's algorithm is implemented by using a one queue and one stack data structure (Li *et al.*, 2010).

To estimate the value of α adaptively, we use the Otsu method (Otsu, 1975; Sahoo *et al.*, 1988) to estimate the value of α.

Seamline Determination at the Object Level

In this section, we propose a differential expression method based on objects. The overlapping area of the right image is overlaid with the objects' boundaries of the overlapping area of the left image obtained in the previous step. Overlaying the overlapping area of the right image with the objects' boundaries of the left image not only establishes a one-to-one correlation between the left image and the right image, but also provides a method to estimate the difference based on objects. Because of the relief displacement, the same objects that cover the obvious objects, e.g., buildings and high bridges, of the overlapping area of the left image may not cover the same terrestrial features of the overlapping area of the right image. When calculating the difference of the objects, the objects belonging to the obvious objects, such as buildings and high bridges, will have low correlation coefficients. The objects with small relief displacements, such as roads, grass, squares, and rivers will have high correlation coefficients.

After obtaining a one-to-one correlation of the objects, the correlation coefficient is used to estimate the degree of differences at the object level. The correlation coefficient $\rho(\kappa)$ for the k^{th} object is computed with Equation 1 and Equation 2, where the "Object" is the set of pixels belong to an object; $f(i,j)$ and $g(i,j)$ are the pixel values at coordinates (i,j) in the left and right image, respectively; i and j are row and column coordinates; $\bar{f}_k$ and $\bar{g}_k$ are the average of the N pixel values of the k^{th} object in the left and right image. To improve the efficiency, $\rho(\kappa)$ is computed by Equation 3; $\rho(\kappa)$ has a range between -1.0 and 1.0. The cost (degree of difference) at the k^{th} object, cost (k), is defined in Equation 4. The cost value approaches 0.0 for objects with small differences and 1.0 for objects with large differences.

$$\rho(k) = \frac{\sum_{i,j\in Object}[(f(i,j)-\bar{f}_k)(g(i,j)-\bar{g}_k)]}{\sqrt{\sum_{i,j\in Object}(f(i,j)-\bar{f}_k)^2 \sum_{i,j\in Object}(g(i,j)-\bar{g}_k)^2}} \quad (1)$$

$$\bar{f}_k = \frac{1}{N}\sum_{i,j\in Object} f(i,j),\ \bar{g}_k = \frac{1}{N}\sum_{i,j\in Object} g(i,j) \quad (2)$$

$$\rho(k) = \frac{\sum_{i,j\in Object} f(i,j)g(i,j) - \frac{1}{N}\sum_{i,j\in Object} f(i,j)\sum_{i,j\in Object} g(i,j)}{\sqrt{[\sum_{i,j\in Object} f(i,j)^2 - \frac{1}{N}(\sum_{i,j\in Object} f(i,j))^2][\sum_{i,j\in Object} g(i,j)^2 - \frac{1}{N}(\sum_{i,j\in Object} g(i,j))^2]}} \quad (3)$$

$$\text{cost}(k) = [1.0 - \rho(\kappa)]/2.0 \quad (4)$$

After estimating the cost of the objects (the object cost map), the POAs determination is based on the object cost map and the adjacency relationships of the objects. Figure 2 shows a demonstration of POAs determination. Figure 2 a shows the object cost map; Figure 2b shows the POAs (white objects) of the object cost map. The white and black circles represent the start and end pixels, respectively. The darker color of the object denotes higher difference. To determine the POAs, the region adjacency matrix is built based on the object cost map. The object cost map can be described as a graph in which the objects are vertexes. If two objects are adjacent, there is an edge between the two objects. The region adjacency matrix is a way of representing a N vertex graph, $G = (V, E)$, by a $N \times N$ matrix whose entries are Boolean values. The region adjacency matrix $a[i][j]$ is defined by Equation 5 (Cormen, *et al.*, 2001):

$$a[i][j] = \begin{cases} true & if\ (i,j) \in E \\ false & otherwise \end{cases} \quad (5)$$

Similar to Chon *et al.* (2010), minimizing the maximum difference is used to determine the POAs. To improve the efficiency, instead of using Dijkstra's algorithm to determine the POAs, the proposed method uses the connectivity analysis algorithm and binary search to determine the POAs gradually. The proposed algorithm is summarized as below:

1. Determine the start object and end object. The start and end objects are the objects to which the start and end points of the seamline belong, respectively. The intersection points of image boundaries are determined as the start and end points (Chon *et al.*, 2010). In Figure 2, the start object and end objects are object I and object D.
2. Sort the cost of the objects in excluding the start and end objects ascending. As shown in Figure 2, the sorting cost array SortCost[] is [0.22, 0.24, 0.34, 0.35, 0.42, 0.45, 0.56, 0.65, 0.80, 0.85]. Set L to 0 and R to $N-3$, where N is the number of objects.
3. Set the threshold: TH = SortCost [$(L+R)/2$]. An object with a cost that is not larger than TH could be passed. A connectivity algorithm is used to find if there exists a way between the start object and the end object.
4. If a path between the start object and the end object exists, set $R = (L+R)/2$; if not, set $L = (L+R)/2$.
5. If $R-L>1$, repeat Step 3 and Step 4 until $R\text{-}L<=1$. Then, the minimized maximum difference value *MinMaxDiff* is equal to SortCost[R]. The objects whose costs are not larger than the *MinMaxDiff* together constitute the POAs.

Seamline Determination at the Pixel Level

The seamline optimization at the pixel level is to optimize the seamlines in the POAs. Intersection points of image boundaries are determined as the start and end points (Chon *et al.*, 2010).

$$NCC(x,y)=\frac{\sum_{i=x-2}^{x+2}\sum_{j=y-2}^{y+2}[(f(i,j)-\bar{f}_{x,y})(g(i,j)-\bar{g}_{x,y})]}{\sqrt{\sum_{i=x-2}^{x+2}\sum_{j=y-2}^{y+2}(f(i,j)-\bar{f}_{x,y})^2\sum_{i=x-2}^{x+2}\sum_{j=y-2}^{y+2}(g(i,j)-\bar{g}_{x,y})^2}} \quad (6)$$

$$\bar{f}_{x,y}=\frac{1}{25}\sum_{i=x-2}^{x+2}\sum_{j=y-2}^{y+2}f(i,j),\bar{g}_{x,y}=\frac{1}{25}\sum_{i=x-2}^{x+2}\sum_{j=y-2}^{y+2}g(i,j) \quad (7)$$

$$NCC(x,y)=\frac{\sum_{i=x-2}^{x+2}\sum_{j=y-2}^{y+2}f(i,j)g(i,j)-\frac{1}{25}\sum_{i=x-2}^{x+2}\sum_{j=y-2}^{y+2}f(i,j)\sum_{i=x-2}^{x+2}\sum_{j=y-2}^{y+2}g(i,j)}{\sqrt{[\sum_{i=x-2}^{x+2}\sum_{j=y-2}^{y+2}f(i,j)^2-\frac{1}{25}(\sum_{i=x-2}^{x+2}\sum_{j=y-2}^{y+2}f(i,j))^2][\sum_{i=x-2}^{x+2}\sum_{j=y-2}^{y+2}g(i,j)^2-\frac{1}{25}(\sum_{i=x-2}^{x+2}\sum_{j=y-2}^{y+2}g(i,j))^2]}} \quad (8)$$

A quantity called the normalized cross correlation (NCC) between the overlapping area of two images is used to estimate the degree of difference (Chon *et al.*, 2010). The NCC for a pixel (x, y) is computed using 5×5 sub-images as expressed in Equation 6 and Equation 7, where $\bar{f}_{x,y}$ and $\bar{g}_{x,y}$ are the average of the 25 pixel values of the left and right image; $f(i,j)$ and $g(i,j)$ are the pixel values at coordinates (i,j) in the left and right image, respectively; i and j are row and column coordinates. To improve the efficiency, the NCC is computed with Equation 8. The NCC has a range between −1.0 and 1.0. The cost (degree of difference) at pixel (x, y), $cost(x, y)$, is defined in Equation 9. The cost value approaches 0.0 for pixels with small differences and 1.0 for pixels with large differences.

$$cost(x, y) = [1.0 - NCC(x, y)]/2.0 \quad (9)$$

The cost of pixel (x,y) in the overlapping area is defined as:

$$D(x, y) = \begin{cases} cost(x, y) & f(x, y)\in POAs \\ +\infty & otherwise \end{cases}. \quad (10)$$

Instead of using the defined cost of pixels directly, the proposed method uses the differential cost to calculate the local cost between neighboring pixels when applying Dijkstra's algorithm to search for the final seamlines (Pan *et al.*, 2014b). The local cost between two neighboring pixels is defined as:

$$d_{uv,kl} = | D(u,v) - D(k,l) | \quad (11)$$

where (u,v) and (k,l) are two neighboring pixels; $D(u,v)$ and $D(k,l)$ are the costs of pixels (u,v) and (k,l), respectively, which are defined in Equation 10. Let $NBR(u,v)$ be the set of neighboring nodes of (u,v), $cost(u,v)$, and $cost(k,l)$ be the global minimum costs from the start pixel to (u,v) and (k,l), respectively. Then,

$$cost(u,v) = \min\{d_{uv,kl} + cost(k,l);(k,l)\in NBR(u,v)\} \quad (12)$$

Dijkstra's Shortest-Path Searching Algorithm with a Binary Min-heap

Dijkstra's algorithm is a global optimization technique that solves the single-source shortest-path problem on a weighted, directed graph $G = (V, E)$ for the case in which all edge weights are nonnegative (Dijkstra, 1959; Cormen *et al.*, 2001). Given a source vertex s in a weighted directed graph $G = (V, E)$ where all edges are non-negative, the pseudo-code for Dijkstra's algorithm is presented in Algorithm 1. Dijkstra's algorithm maintains the vertices of the graph V in two disjoint and complementary sets of vertices $S \subseteq V$ and $Q \subseteq V$. S includes all vertices whose shortest path from s has been determined. Q is a priority queue initialized for all $x\in V$. Q is keyed by dist[x], which is the length of the current shortest known path from s to $x\in Q$. $w(u, v)$ is the length of the two neighbor nodes u and v (Cormen *et al.*, 2001). The upper bound of the

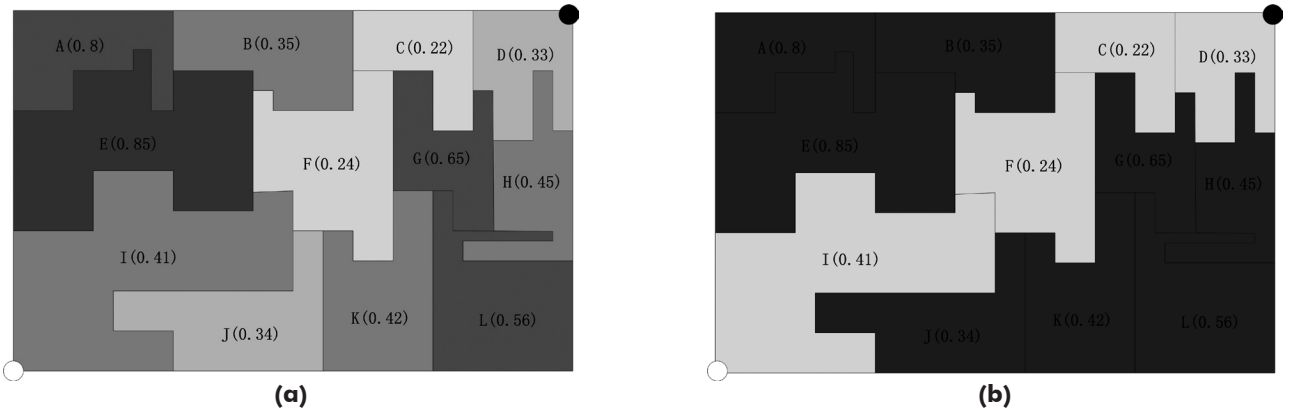

Figure 2. The demonstration of POAs determination: (a) the object cost map, and (b) the POAs (white objects) of the object cost map

running time of Dijkstra's algorithm on a graph with edges E and vertices V can be expressed as a function of $|E|$ and $|V|$ using big-O notation (Cormen *et al.*, 2001). The running time of Dijkstra's algorithm depends on how the min-priority queue is implemented. The simplest implementation of the Dijkstra's algorithm stores the vertices of set Q in an ordinary linked list or array, and each extract_min(Q) (line 10) operation is simply a linear search through all vertices in Q. In this case, the running time is $\Theta(|V|*|V|+|E|)$.

For a sparse graph, i.e., graphs with far fewer than $\Theta(|V|*|V|)$ edges, Dijkstra's algorithm can be improved by implementing the min-priority queue with a binary min-heap. The pseudo-code for Dijkstra's algorithm with a binary min-heap is presented in Algorithm 2. Each extract_min_with_ min- priority(Q) (line 11) operation then takes time $\Theta(\lg|V|)$. As before, there are $|V|$ such operations. The time to build the binary min-heap is $\Theta(\lg|V|)$. Each Q.decrease_min-priority(v, dist[v]) operation (line 16) takes time $\Theta(\lg|V|)$, and there are still at most $|E|$ such operations. Therefore, the algorithm requires $\Theta((|V|+|E|)\lg|V|)$ time (Fredman and Tarjan, 1987; Cherkassky *et al.*, 1996; Cormen *et al.*, 2001; Chen *et al.*, 2007). To apply Dijkstra's algorithm to seamline determination, each node has eight neighboring nodes. The graph is sufficiently sparse where the number of the edges is $8*|V|$. Therefore, we use the min-priority queue with a binary min-heap to improve the efficiency of Dijkstra's algorithm.

Algorithm 1: Dijkstra's Algorithm

```
1  Dijkstra(G, s)
2  dist[s] = 0
3  for each vertex v∈V
4  if v ≠ s
5  dist[v] = ∞
6  pre [v] = undefined
7  S = Ø
8  Q = V
9  while Q ≠ Ø do
10 u = extract_min(Q)
11 S = S∪{u}
12 for each vertex v∈Adj(u) do
13 dist[v] = min(dist[v], dist[u]+w(u, v))
14 pre[v] = u
```

Algorithm 2: Dijkstra's Algorithm with Binary Min-heap

```
1  Dijkstra_Binary_Min-heap(G, s)
2  dist[s] = 0
3  for each vertex v∈V
4  if v ≠ s
5  dist[v] = ∞
6  pre [v] = undefined
7  Q.add_with_min-priority(v, dist[v])
8  S = Ø
9  Q = V
10 while Q ≠ Ø do
11 u = extract_min_with_min- priority(Q)
12 S = S∪{u}
13 for each vertex v∈Adj(u) do
14 dist[v] = min(dist[v], dist[u]+w(u, v))
15 pre[v] = u
16 Q.decrease_min-priority(v, dist[v])
```

Experimental Results and Discussion

The proposed method has been implemented in C++ in Microsoft Visual C++ 6.0. The Geospatial Data Abstraction Library (GDAL) is used to read and write image files. A desktop computer with an Intel(R) Core(TM) i3-540 M 3.07 GHz processor, 6 GB of internal memory and a hard disk with a 500 GB capacity, a 16 MB cache and 7200 r/min speed was used for data processing. The proposed method was performed with T =0.65 and A = 15, where T is the scale factor for the marker extraction and A is the area of the smallest discernible object.

The results of the proposed method were compared with Dijkstra's (Dijkstra, 1959), Chon's (Chon *et al.*, 2010) and Pan's (Pan *et al.*, 2014b) algorithms. The experiment of Data Set 1 is shown in Figure 3 to Figure 6; and the experiment of Data Set 2 is shown in Figure 7 to Figure 10. All of the methods were performed without an image pyramid except Pan's method. Pan's method builds one pyramid level with a 3×3 average filter (Pan *et al.*, 2014b). In Figure 3 and Figure 7, (a) and (b) show the overlapping area of the left and right image, respectively; (c) shows the POAs (white areas) overlaid on the overlapping area of the left image. In Figure 3c and Figure 7c, a technique for minimizing the maximum object cost is adopted to determine the POAs. The technique is to find a connected region between the start object and the end object for which the maximum object cost in the region is a minimum. Therefore, obvious objects, especially the buildings and high bridges, are excluded as much as possible from the determined POAs. In Figure 4 and Figure 8, (a) compares the seamlines determined by Dijkstra's algorithm with those of the proposed method, (b) shows the details of the marked rectangles in (a), (c) compares the seamlines determined by Chon's algorithm and those determined by the proposed method, (d) shows the details of the marked rectangles in (c), (e) compares the seamlines determined by Pan's algorithm and those determined by the proposed method, and (f) shows the details of the marked rectangles in (e). The reasonable seamline should avoid crossing obvious objects as much as possible, e.g., buildings and high bridges. Relief displacement mainly occurs because a DTM does not contain elevations for these obvious objects (Pan *et al.*, 2014b; Chen *et al.*, 2014). In Figure 4, the proposed method successfully avoided crossing most of the obvious objects, and the seamlines were mainly along the roads or low bridges. The seamline only crossed one end of the bridge, which was shown in Figure 4b. Dijkstra's algorithm crossed several bridges. Chon's method went across one bridge and two buildings, which was shown in Figure 4d. Pan's method had a good result in Data Set 1. In Figure 8, the proposed method also successfully avoided crossing most of the obvious objects, and the seamlines were mainly along the road. Dijkstra's algorithm crossed several buildings, which was shown in Figure 8b. Chon's method went across several buildings, which was shown in Figure 8d. Pan's method went across several buildings, which was shown in Figure 8f. According to the Figure 4 and Figure 8, compared with the other three methods, the seamlines determined by the proposed method were more reasonable and successfully avoided crossing most of the obvious objects, and the seamlines were mainly along the roads or low bridges. The final resultant mosaicked images using different seamline determination

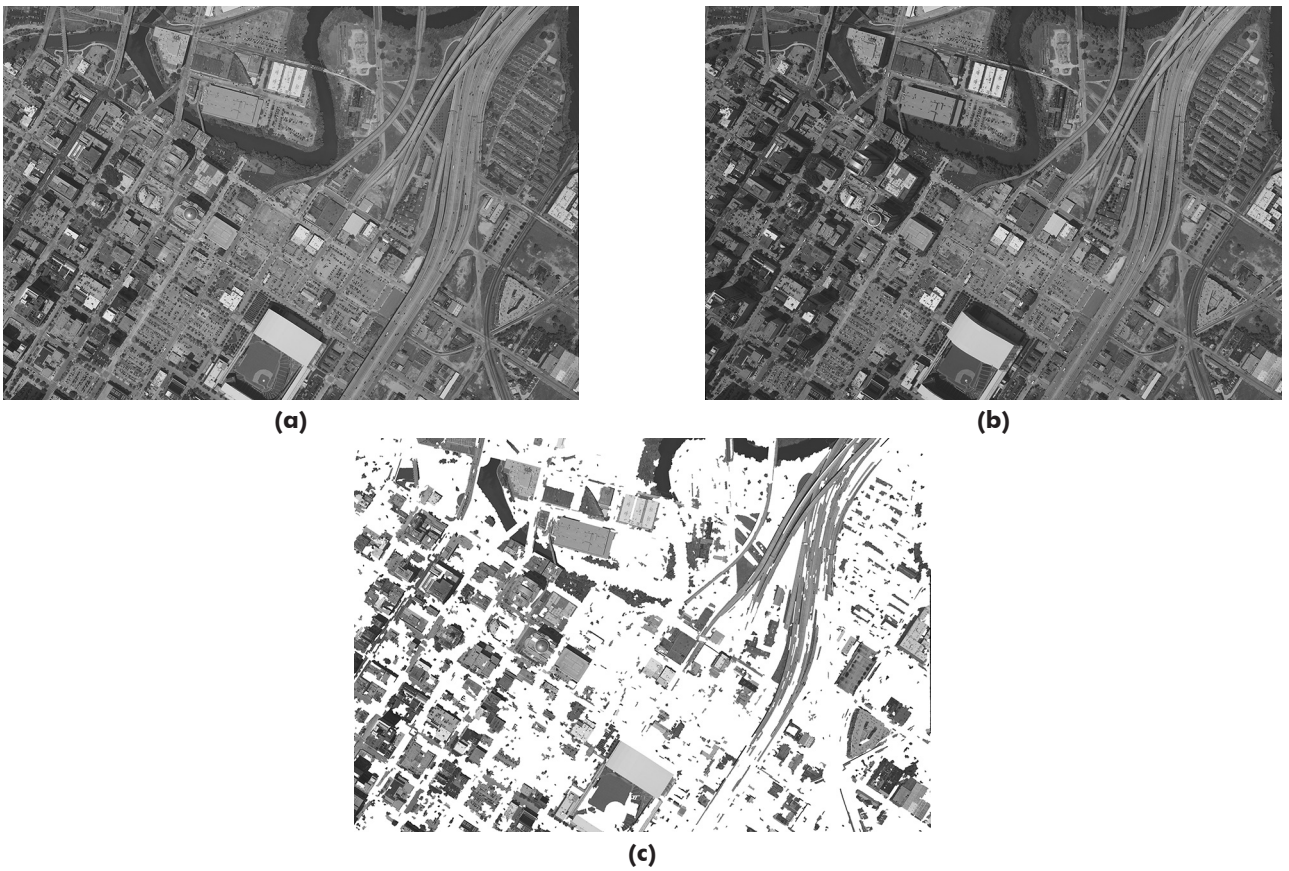

Figure 3. POAs determination for Data Set 1: (a) the overlapping area of left image, (b) the overlapping area of right image, and (c) POAs (white areas) overlaid on the overlapping area of the left image.

methods without feathering are demonstrated in Figure 5 and Figure 9. In order to achieve high-quality image mosaicking results, the feathering is applied along the seamlines to achieve a seamless mosaic (Kerschner, 2001; Pan *et al.*, 2009; Wan *et al.*, 2012; Wang *et al.*, 2012; Wan *et al.*, 2013; Pan *et al.*, 2014a), but this paper focuses on the automatic seamline determination. In order to show possible visual discontinuities appeared in the mosaicked images using different seamline determination methods, the final resultant mosaicked images are mosaicked using different seamline determination methods without feathering (Pan *et al.*, 2014b). Figure 6 and Figure 10 further show the selected regions in Figure 5 and Figure 9 without feathering, using different seamline determination methods. To compare the final resultant mosaicked images using different seamline determination methods directly, the same selected regions are considered for the previous methods and the proposed method. In order to show visual discontinuities, we added marked ellipse to show the visual discontinuities appeared in the mosaicked images in the Figure 6 and Figure 10. They show that visual discontinuities appear in the mosaicked images using the other three methods.

In many related studies, seamline quality is not generally evaluated through accuracy assessment (Chen *et al.*, 2014). Therefore, similar to the evaluation method in other relevant studies (Ma and Sun, 2011; Pan *et al.*, 2014b; Chen *et al.*, 2014), the quantitative index applied in the proposed method is the number of times that seamlines pass through obvious objects. To evaluate the performance of the different methods fairly, all of the four methods were tested in a single thread. The processing time for seamline determination was recorded for comparison. A quantitative comparison of Data Set 1 and Data Set 2 was made as shown in Table 1. It can be seen that the seamlines determined by Dijkstra's algorithm passed through five bridges in Data Set 1 and six buildings in Data Set 2. Chon's method was much better, but the seamlines went across one bridge and two buildings in Data Set 1 and twenty-two buildings in Data Set 2, and used the most processing time. Pan's method had a good result in Data Set 1, but it went across three buildings in Data Sets 2. Although Pan's method used the image pyramid to improve the efficiency, it still used more processing time than the proposed method. The seamlines determined by the proposed method passed through one bridge in Data Set 1, which is shown in Figure 4(b), and no obvious objects in Data Set 2. By comparison, our method obtained the best outcome and bypassed most obvious objects successfully. By using regional adaptive marker-based watershed segmentation and Dijkstra's shortest-path searching algorithm with a binary min-heap, the run

Table 1. Comparison of Previous Methods with the Proposed Method

Data set	Method	Number of obvious objects passed through	Processing time(s)
1	Dijkstra's	5 bridges	349.160
	Chon's	1 bridge and 2 building	13766.832
	Pan's	none	166.578
	Proposed	1 bridge	12.012
2	Dijkstra's	6 building	1173.606
	Chon's	22 building	91566.173
	Pan's	3 building	176.202
	Proposed	none	36.551

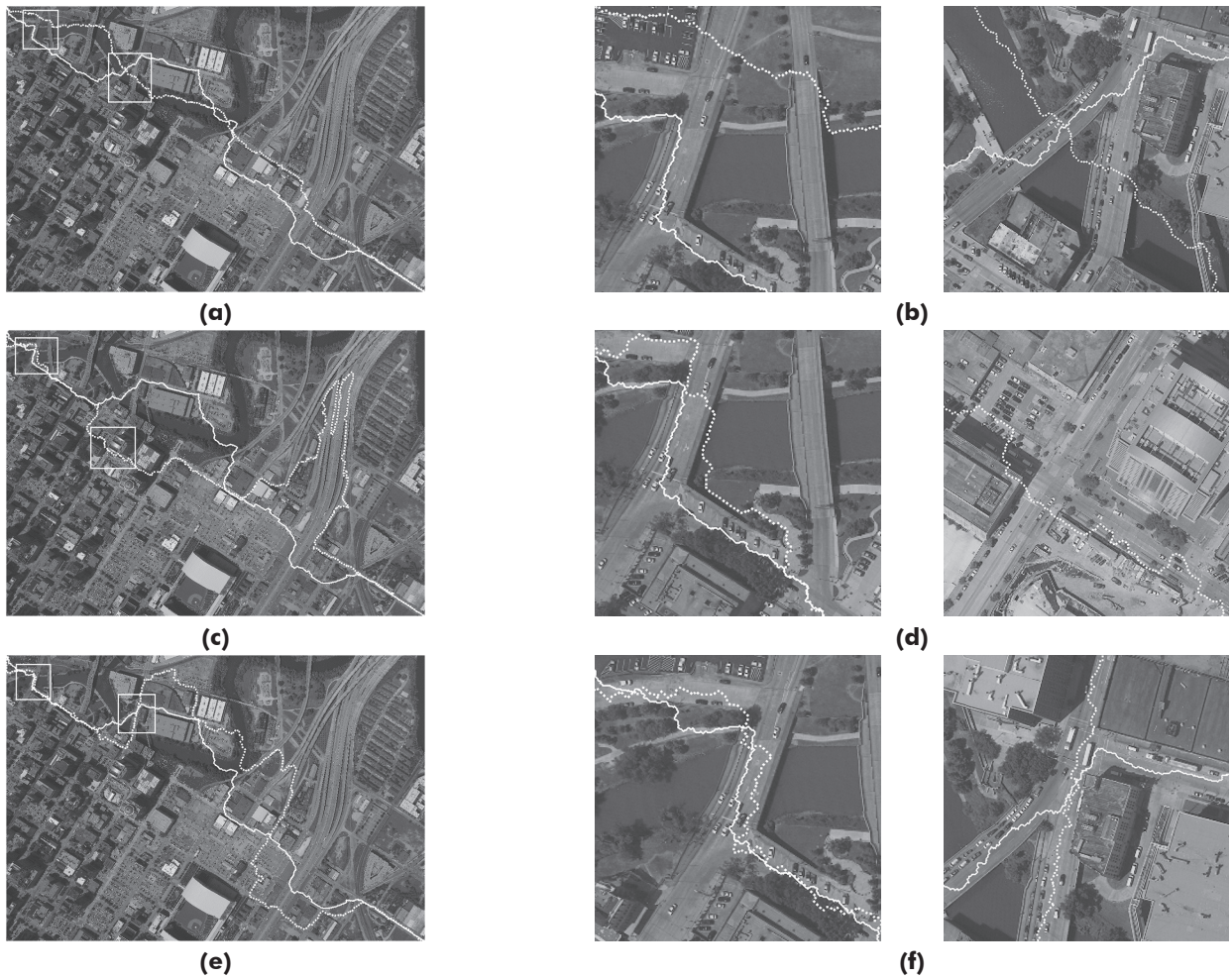

Figure 4. Seamline determination for Data Set 1: (a) seamlines determined by Dijkstra's algorithm (dotted line) and the proposed method (solid line), (b) details of marked rectangles in (a), (c) seamlines determined by Chon's method (dotted line) and the proposed method (solid line), (d) details of marked rectangles in (c), (e) seamlines determined by Pan's method (dotted line) and the proposed method (solid line), (f) details of marked rectangles in (e).

time of the proposed method takes 12.012 sec and 36.551 sec for Data Set 1 and 2, respectively.

It is suggested that a value of T in the range between 0.6 and 0.7 be chosen (Li *et al.*, 2010). In our experiment, T was set to 0.65 and A was set to 15 in Figure 3 to Figure 10. Here, we set T to 0.6, 0.65, and 0.7, while setting A to 15, for the segmentation of the overlapping area and compare the results. The three seamlines with different values of T for the two Data Sets are almost the same. This experiment demonstrates that the proposed algorithm is robust and is not sensitive to the segmentation parameter T in the range between 0.6 and 0.7 for the two Data Sets.

However, it should be noted that the effect of the proposed method is determined by the result of the segmentation. There are two tunable parameters in the segmentation method: the area A of the smallest discernible object and the scale factor T for the marker extraction. The area threshold A can be set as the area of smallest discernible object on the image, but there is still no automatic solution to selecting the scale factor T at present. In actual production, what we did was to choose certain typical images and test which parameters would produce suitable segmentation results. Then, the selected parameters were applied to other images for seamline determination in mosaicking. The change of parameter T induces different marker extraction results for different types of objects. For the textured objects, the lower the value of T is, the less the object inner pixels are marked and the more the markers are extracted, which leads to their over-segmentation, and vice versa; however, for the homogenous objects, the lower the value T is, the more the object inner pixels are marked and the less the markers are extracted, which may lead to their under-segmentation, and vice versa (Li *et al.*, 2010). Figure 11 shows seamlines determined in the proposed method of Data Set 1 with different values of T, where A is set to 15. A quantitative comparison of seamlines determined by the proposed method for Data Set 1 with different values of T is made as shown in Table 2. Although Li *et al.* (2010) suggested setting T to a value in the range between 0.6 and 0.7 in the regional adaptive marker-based watershed segmentation, it can be seen that the seamlines determined results in the proposed method are much different for different values of T. According to Table 2, an acceptable seamlines determination result is obtained by setting T to 0.5 for Data Set 1. It is suggested that a value of T in the range between 0 and 1 be chosen in the proposed method.

Conclusions

In this paper, we proposed a novel method for seamline determination based on marker-based watershed segmentation. The segmentation is used to improve the seamline determination. It determines the optimal seamlines at two different

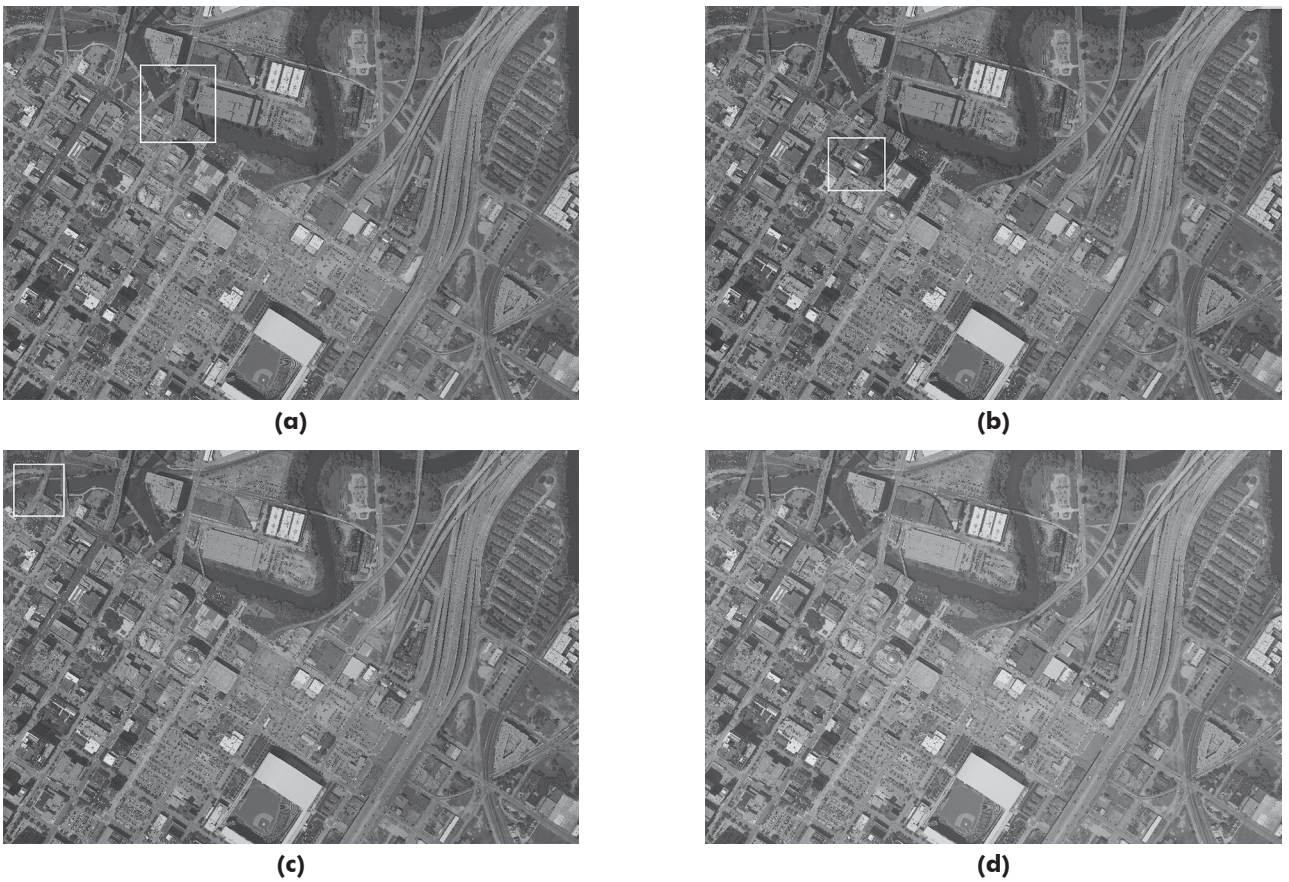

Figure 5. Mosaicked image for Data Set 1: (a) Dijkstra's algorithm, (b) Chon's method, (c) Pan's method, (d) the proposed method.

TABLE 2. COMPARISON OF THE PROPOSED METHOD WITH DIFFERENT VALUES OF T FOR DATA SET 1

The Values of T	Number of obvious objects passed through	Processing time(s)
0.4	none	11.669
0.5	none	11.809
0.8	1 bridge	11.965
0.9	1 bridge	11.918

levels: the object and pixel level. At the object level, most of the obvious objects, especially the buildings and high bridges, will be excluded from the POAs. At the pixel level, Dijkstra's shortest-path searching algorithm with a binary min-heap is used to find the final seamlines. Two Data Sets of digital aerial orthoimages with different ground resolution are adopted to validate our algorithm. The results demonstrate the potential of the proposed method. Compared with Dijkstra's algorithm, Chon's algorithm and Pan's algorithm, seamline determined by the proposed method successfully bypass most of the obvious objects and fellow roads or rivers. Moreover, our method has a higher efficiency and can also be integrated into the seamlines network optimization framework easily (Pan *et al.*, 2009; Mills and McLeod, 2013; Pan *et al.*, 2014a).

Nevertheless, there is still room for improvement in the proposed method. First, the effect of the proposed method is determined by the result of the segmentation, and there is no way to select the optimal parameter for segmentation automatically. Second, when determining the POAs, our method only used the correlation coefficient to assess the degree of differences between objects. According to object-oriented thinking, the attribute of the objects, such as shape, geometry, texture, and contextual semantic information, can be used to estimate the degree of difference between objects. These issues will be addressed in the future.

Acknowledgments

The work was supported by the National Basic Research Program of China (973 Program, No. 2014CB744201, 2012CB719901), a Foundation for the Author of National Excellent Doctoral Dissertation of PR China (FANEDD, No. 201249), and the National Natural Science Foundation of China (No. 91438203, 41371430, 91438112). The authors also thank the anonymous reviews for their constructive comments and suggestions.

References

Afek, Y., and A. Brand, 1998. Mosaicking of orthorectified aerial images, *Photogrammetric Engineering & Remote Sensing*, 64(2):115–124.

Chen, M., R.A. Chowdhury, V. Ramachandran, D.L. Roche, and L. Tong, 2007. *Priority Queues and Dijkstra's Algorithm*, Computer Science Department, University of Texas at Austin, 1–25 p.

Chen, Q., M. Sun, X., Hu, and Z. Zhang, 2014. Automatic seamline network generation for urban orthophoto mosaicking with the use of a digital surface model, *Remote Sensing*, 6(1):12334–12359.

Cherkassky, B.V., A.V. Goldberg, and T. Radzik, 1996. Shortest paths algorithms: Theory and experimental evaluation, *Mathematical Programming*, 73(2):129–174.

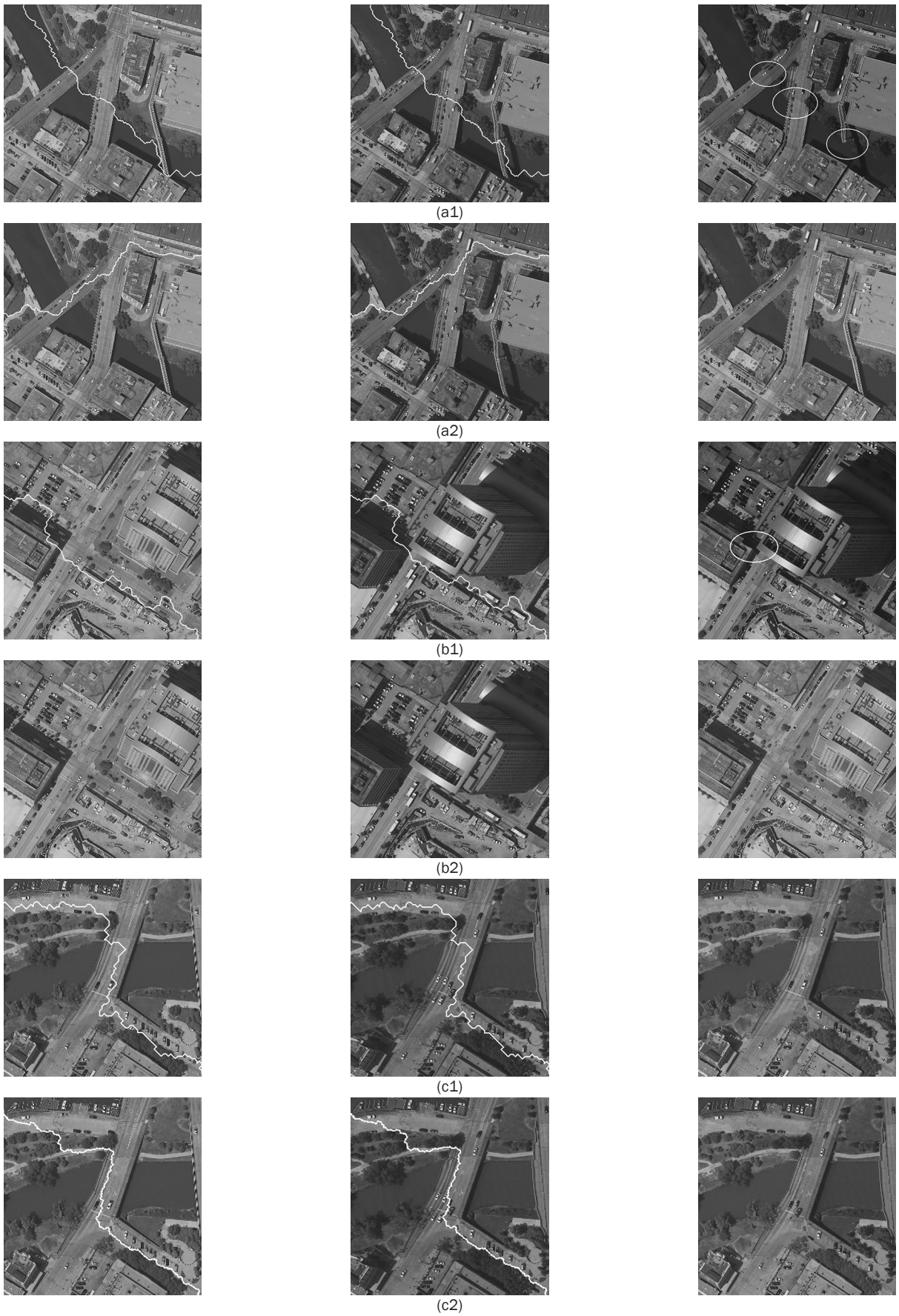

Figure 6. Selected regions of (from left to right) left image with seamline (solid line), right image with seamline (solid line) and mosaicked image for Data Set 1: (a1) Dijkstra's algorithm, (a2) the proposed method, (b1) Chon's method, (b2) the proposed method, (c1) Pan's method, (c2) the proposed method.

Figure 7. POAs determination for Data Set 2: (a) the overlapping area of left image, (b) the overlapping area of right image, and (c) POAs (white areas) overlaid on the overlapping area of left image.

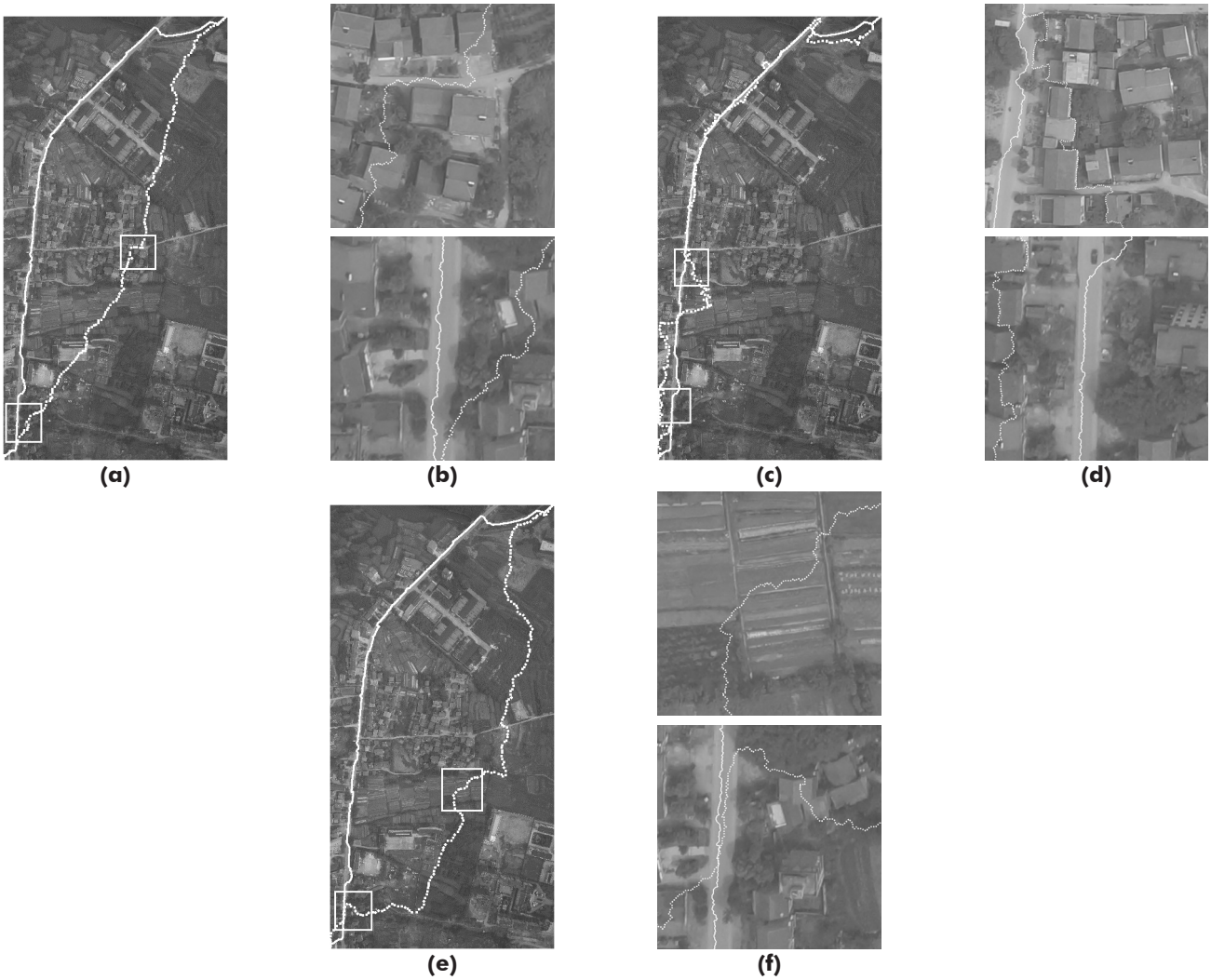

Figure 8. Seamline determination for Data Set 2: (a) seamlines determined by Dijkstra's algorithm (dotted line) and the proposed method (solid line), (b) details of marked rectangles in (a) and (c) seamlines determined by Chon's method (dotted line) and the proposed method (solid line), (d) details of marked rectangles in (c) , (e) seamlines determined by Pan's method (dotted line) and the proposed method (solid line), (f) details of marked rectangles in (e).

Chon, J., H. Kim, and C.S. Lin, 2010. Seam-line determination for image mosaicking: A technique minimizing the maximum local mismatch and the global cost, *ISPRS Journal of Photogrammetry and Remote Sensing*, 65(1):86–92.

Cormen, T.H., C.E. Leiserson, R.L. Rivest, and C. Stein, 2001. *Introduction to Algorithms*, MIT Press, Cambridge, Massachusetts, 507:661–662 p.

Dijkstra, E.W., 1959. A note on two problems in connexion with graphs, *Numerische Mathematik*, 1(1):269–271.

Fernandez, E., R. Garfinkel, and R. Arbiol, 1998. Mosaicking of aerial photographic maps via seams defined by bottleneck shortest paths, *Operations Research*, 46(3):293–304.

Fernandez, E., and R. Marti, 1999. GRASP for seam drawing in mosaicking of aerial photographic maps, *Journal of Heuristics*, 5(2):181–197.

Fredman, M.L., and R.E. Tarjan, 1987. Fibonacci heaps and their uses in improved network optimization algorithms, *Journal of the ACM (JACM)*, 34(3):596–615.

Gonzalez, R.C., and R.E. Woods, 2002. *Digital Image Processing*, Prentice-Hall, Upper Saddle River, New Jersey, 791-792, 798–800 p.

Kerschner, M., 2001. Seamline detection in colour orthoimage mosaicking by use of twin snakes, *ISPRS Journal of Photogrammetry and Remote Sensing*, 56(1):53–64.

Li, D., G. Zhang, Z. Wu, and L. Yi, 2010. An edge embedded marker-based watershed algorithm for high spatial resolution remote sensing image segmentation, *IEEE Transactions on Image Processing*, 19(10):2781–2787.

Ma, H.C., and J. Sun, 2011. Intelligent optimization of seam-line finding for orthophoto mosaicking with LiDAR point clouds, *Journal of Zhejiang University-Science C-Computers & Electronics*, 12(5):417–429.

Meyer, F., and S. Beucher, 1990. Morphological segmentation, *Journal of Visual Communication and Image Representation*, 1(1):21–46.

Meyer, F., 1992. Color image segmentation, *Proceedings of the International Conference on Image Processing and its Applications*, *1992*, pp. 303–306.

Milgram, D.L., 1975. Computer methods for creating photomosaics, *IEEE Transactions on Computers*, 24(11):1113–1119.

Mills, S., and P. McLeod, 2013. Global seamline networks for orthomosaic generation via local search, *ISPRS Journal of Photogrammetry and Remote Sensing*, 75:101–111.

Otsu, N., 1975. A threshold selection method from gray-level histograms, *Automatica*, 11(285-296):23–27.

Pan, J., M. Wang, D. Li, and J. Li, 2009. Automatic generation of seamline network using area Voronoi diagrams with overlap, *IEEE Transactions on Geoscience and Remote Sensing*, 47(6):1737–1744.

Pan, J., and M. Wang, 2011. A seam-line optimized method based on difference image and gradient image, *Proceedings of the 19th International Conference on Geoinformatics 2011*, Shanghai, China, pp. 1–6.

Pan, J., M. Wang, D. Ma, Q. Zhou, and J. Li, 2014a. Seamline network refinement based on area Voronoi diagrams with overlap, *IEEE Transactions on Geoscience and Remote Sensing*, 52(3):1658–1666.

Pan, J., Q. Zhou, and M. Wang, 2014b. Seamline determination based on segmentation for urban image mosaicking, *IEEE Geoscience and Remote Sensing Letters*, 11(8):1335–1339.

Sahoo, P.K., S. Soltani, and A.K.C. Wong, 1988. A survey of thresholding techniques, *Computer Vision, Graphics, and Image Processing*, 41(2):233–260.

Soille, P., 2006. Morphological image compositing, *IEEE Transactions on Pattern Analysis and Machine Intelligence*, 28(5):673–683.

Vincent, L., and P. Soille, 1991. Watersheds in digital spaces: An efficient algorithm based on immersion simulations, *IEEE Transactions on Pattern Analysis and Machine Intelligence*, 13(6):583–598.

Wan, Y., D. Wang, J. Xiao, X. Lai, and J. Xu, 2013. Automatic determination of seamlines for aerial image mosaicking based on vector roads alone, *ISPRS Journal of Photogrammetry and Remote Sensing*, 76:1–10.

Wan, Y., D. Wang, J. Xiao, X. Wang, Y. Yu, and J. Xu, 2012. Tracking of vector roads for the determination of seams in aerial image mosaics, *IEEE Geoscience and Remote Sensing Letters*, 9(3):328–332.

Wang, D., Y. Wan, J. Xiao, X. Lai, W. Huang, and J. Xu, 2012. Aerial image mosaicking with the aid of vector roads, *Photogrammetric Engineering & Remote Sensing*, 78(11):1141–1150.

Yu, L., E.J. Holden, M.C. Dentith, and H. Zhang, 2012. Towards the automatic selection of optimal seam line locations when merging optical remote-sensing images, *International Journal of Remote Sensing*, 33(4):1000–1014.

Zhang, G., Z. Wu, and L. Yi, 2010. Marker-based watershed segmentation embedded with edge information, *Proceedings of the International Conference on Image Analysis and Signal Processing (IASP)*, Zhejiang, China, pp. 375–380.

(Received 26 November 2014; accepted 22 July 2015; final version 19 August 2015)

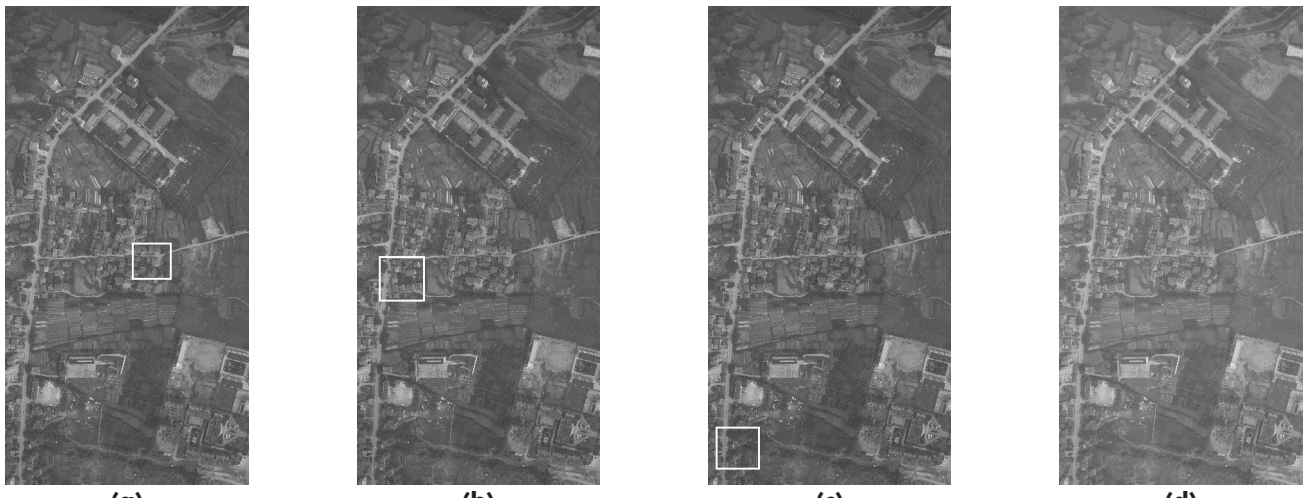

Figure 9. Mosaicked image for Data Set 2: (a) Dijkstra's algorithm, (b) Chon's method, (c) Pan's method, (d) the proposed method.

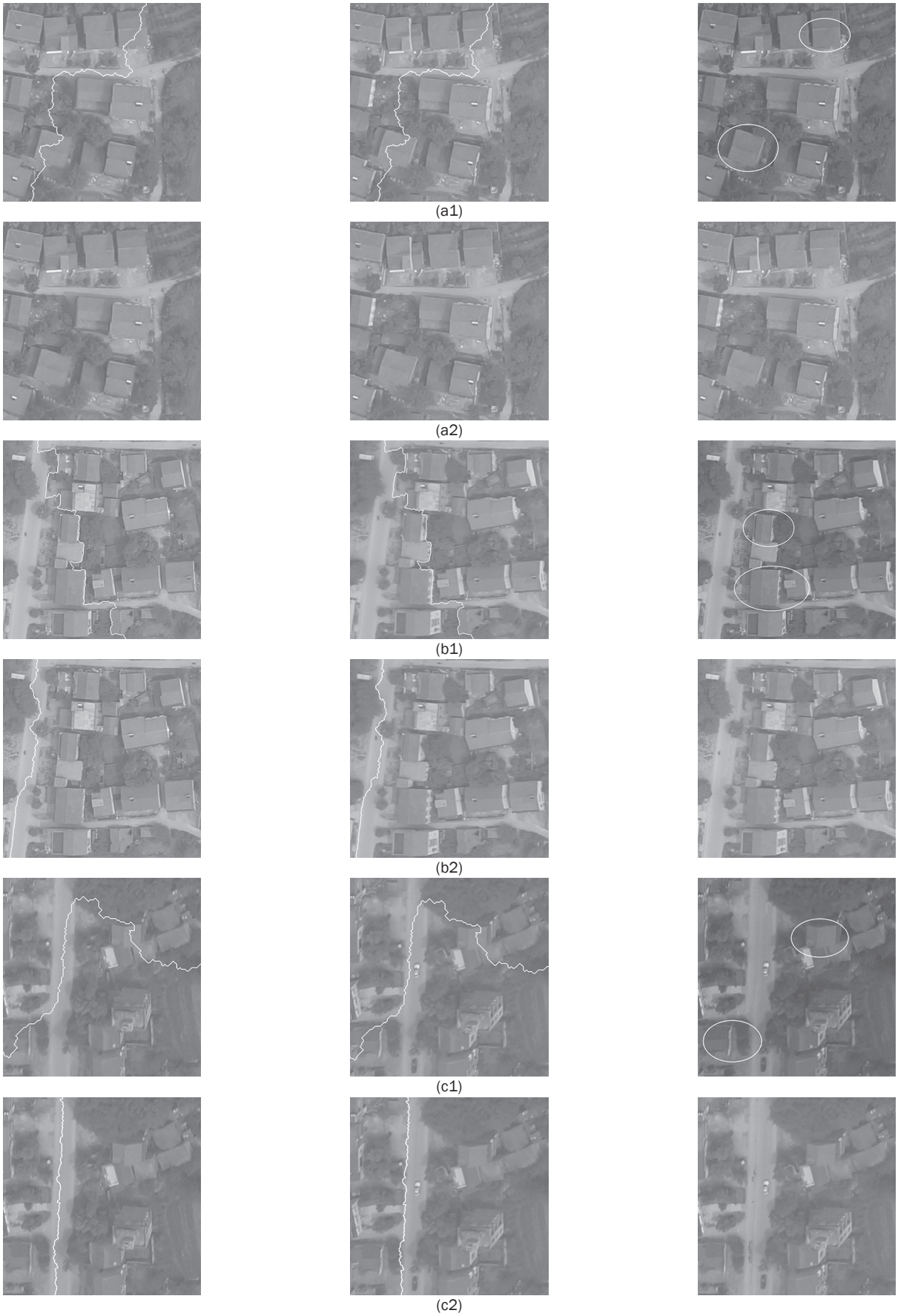

Figure 10. Selected regions of (from left to right) left image with seamline (solid line), right image with seamline (solid line) and mosaicked image for Data Set 2: (a1) Dijkstra's algorithm, (a2) the proposed method, (b1) Chon's method, (b2) the proposed method, (c1) Pan's method, (c2) the proposed method.

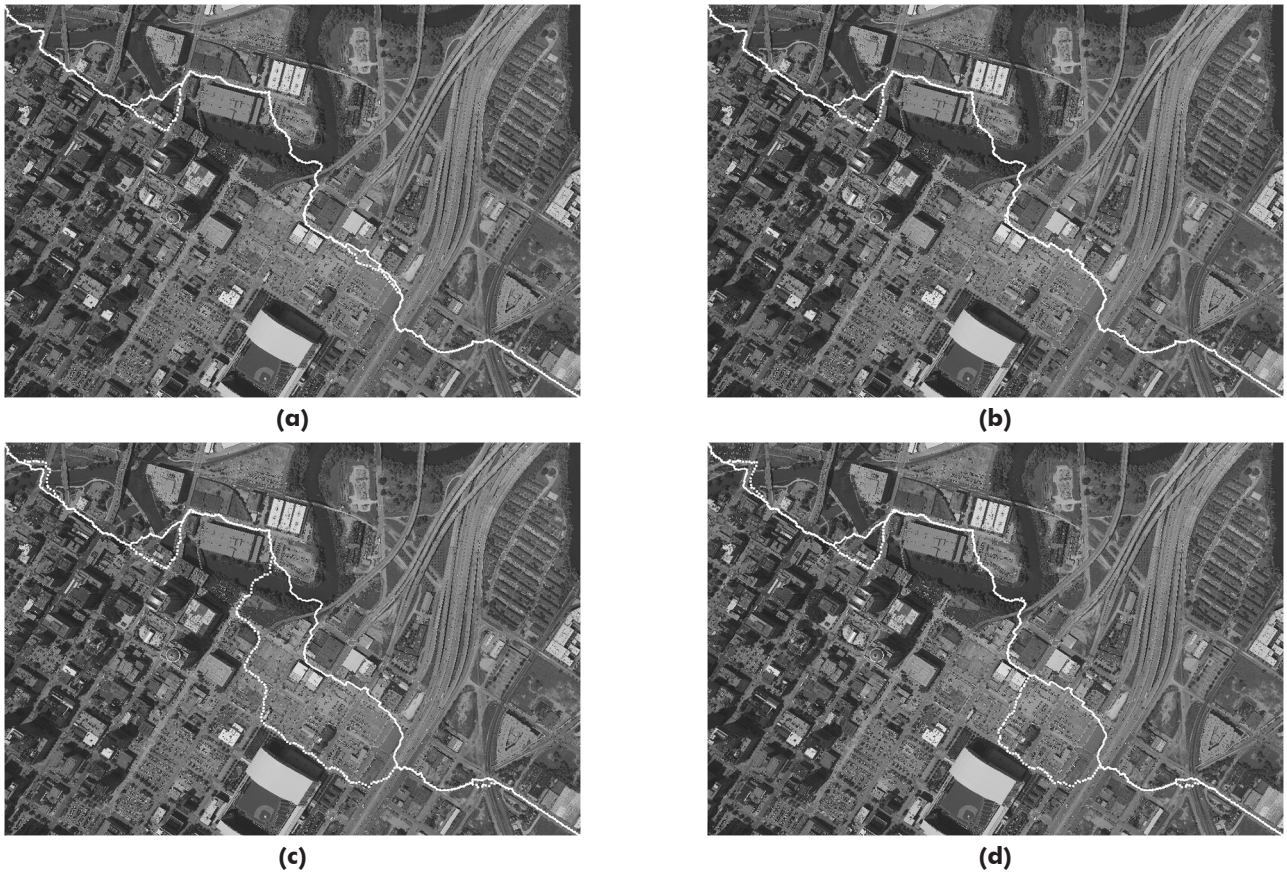

Figure 11. Seamlines determined by the proposed method for Data Set 1 with different values of *T*: (a) *T* is 0.65 (solid line) and *T* is 0.4 (dotted line), (b) *T* is 0.65 (solid line) and *T* is 0.5 (dotted line), (c) *T* is 0.65 (solid line) and *T* is 0.8 (dotted line), and (d) *T* is 0.65 (solid line) and *T* is 0.9 (dotted line).

CALENDAR

FEBRUARY

26, GeoByte—Beyond NDVI … 2016. For more information, visit http://www.asprs.org/GISD-Division/Online-Seminars.html.

MARCH

25, GeoByte—A Geospatial Approach to Mapping Environmental Sound Levels Across the United States. For more information, visit http://www.asprs.org/GISD-Division/Online-Seminars.html.

APRIL

11-15, IGTF 2016, Ft. Worth, Texas, For more information, visit http://conferences.asprs.org/Fort-Worth-2016/blog.

29, GeoByte—Designing National Park Service Visitor Maps. For more information, visit http://www.asprs.org/GISD-Division/Online-Seminars.html.

To have your special event published in *PE&RS*, contact Rae Kelley, rkelley@asprs.org.

MAY

24-25, GEO Business 2016, London, United Kingdom. For more information, visit http://geobusinessshow.com/.

27, GeoByte—CyberGIS: Foundations and Principles. For more information, visit http://www.asprs.org/GISD-Division/Online-Seminars.html.

JULY

22, GeoByte—Getting More From Remote Sensing Data Using OGC Standards. For more information, visit http://www.asprs.org/GISD-Division/Online-Seminars.html.

30–August 7, "COSPAR 2016"—41st Scientific Assembly of the Committee on Space Research (COSPAR), Istanbul, Turkey. For more information, visit http://www.cospar-assembly.org.

AUGUST

5, GeoByte—Aqueduct Global Flood Analyzer – A Web Tool To Estimate Global Flood Risks For Current and Future Scenarios. For more information, visit http://www.asprs.org/GISD-Division/Online-Seminars.html.

FORTHCOMING ARTICLES

Ting On Chan, *Derek D. Lichti*, *David Belton*, and *Hoang Long Nguyen*, Automatic Point Cloud Registration Using a single Octagonal Lamp Pole.

John W. Coulston, *Christine E. Blinn*, *Valerie A. Thomas*, and *Randolph H. Wynne*, Approximation Prediction Uncertainty for Random Forest Regression Models.

Bonnie Ruefenacht, Comparison of Three Landsat-TM Compositing Methods: A Case Study Using Modeled Tree Canopy Cover.

Ahmed Izadipour, *Behzad Akbari*, and *Barat Mojaradi*, A Feature Selection Approach for Segmentation of Very High-Resolution Satellite Images.

Zhuoting Wu, *Dennis Dye*, *John Vogel*, and *Barry Middleton*, Estimating Forest and Woodland Aboveground Biomass Using Active and Passive Remote Sensing.

Robyn A. Barbato, *Karen L. Foley*, *Adam LeWinter*, *David Finnegan*, *Sergey Vecherin*, *John E. Anderson*, *Kennrth Yamamoto*, *Christian Borden*, *Eathan Fahy*, *Nathan Calandra*, and *Charles M. Reynolds*, The Attenuation of Retroreflective Signatures on Surface Soils.

Dan Liu, *Xuejun Liu*, and *Meizhen Wang*, Camera Self-Calibration with Lens Distortion from a Single Image.

Taoyang Wang, *Guo Zhang*, *Yonghua Jiang*, *Siyue Wang*, *Wenchao Huang*, and *Litao Li*, Combined Calibration Method Based on Rational Function Model for the Chinese GF-1 Wide-Field-of-View Imagery

Cai Cai, *Peijun Li*, and *Huiran Jin*, Extraction of Urban Impervious Surface Using Two-Season Worldview-2 Images: A Comparison.

Craig Mahoney, *Chris Hopkinson*, *Alex Held*, *Natascha Kljun*, and *Eva van Gorsel*, ICESat/GLAS Canopy Height Sensitivity Inferred from Airborne Lidar.

Somayeh Yavari, *Mohammad Javad Valadan Zoej*, *Mahmod Reza Sahebi*, and *Mehdi Mokhtarzade*, A Novel Automatic Structural Linear Feature-Based Matching Method Based on New Concepts of Mathematically-Generated Points and Lines.

Aaron E. Maxwell, *Timothy A. Warner*, and *Michael P. Strager*, Predicting Palustrine Wetland Probability Using Random Forest Machine Learning and Digital Elevation Data- Derived Terrain Models.

Pramod Kumar Konugurthi, *Raghavendra Kune*, *Ravi Nooka*, and *Venkataraman Sarma*, Autonomous Ortho-Rectification of Very High Resolution Imagery Using SIFT and Generic Algorithm.

SRTM Error Distribution and its Associations with Landscapes across China

Quan Zhang, Qinke Yang, and Chunmei Wang

Abstract

In this paper the distribution of 3-second elevation error in the data from the Shuttle Radar Topography Mission (SRTM) over the whole of China and its associations with topographic and land cover factors were systematically evaluated. The landscape features extracted from different datasets at more than 500,000 sites were used to determine the variation pattern in the errors by the method of single factor analysis. The results showed that the topographic attributes derived from SRTM data could adequately represent the terrain of China. However, there were extended and observable areas with abnormalities in a small proportion of the data. Slope was the dominant factor affecting elevation error compared with other landscape features (aspect, vegetation, etc.). The mean errors in glaciers, deserts and wetlands were -1.05 m, -2.03 m and -2.43 m, and 1.05 m in built-up areas. In general the elevation errors in the SRTM data formed a complex pattern of variation across China.

Introduction

Land surface elevation datasets are important foundations for studying topography, land surface processes, and global environmental change. With technological advances, remote sensing platforms (satellites, space shuttles, etc.) are increasingly being used to acquire high-quality surface elevation data (Nelson *et al.*, 2009). The Shuttle Radar Topography Mission (SRTM) C-band data is a near-global digital elevation dataset collected and released through collaboration between the National Aeronautics and Space Administration (NASA) and the National Geospatial-Intelligence Agency (NGA). The SRTM data has been released in two formats: one with a resolution of 1-second and the other with a resolution of 3-seconds (Rabus *et al.*, 2003; Farr *et al.*, 2007). Although the SRTM 1-second global dataset is now being released worldwide in phases, starting September 2014, the 3-second dataset, which has been released to the public since 2003, has gained a great deal of attention and has been applied extensively in geoscience studies worldwide (Zandbergen, 2008; Yang *et al.*, 2011). For that reason, the 3-second product has been used for the current study. Since its initial release, the SRTM 3-second dataset has been continuously upgraded by a number of groups of which one example is the Consultative Group on International Agricultural Research (CGIAR) version 4 (Jarvis *et al.*, 2008). However, despite the improvements, SRTM still suffers from certain issues in representing the geomorphology of the land surface. In some cases, these issues can significantly affect the accuracy of research outcomes.

Quan Zhang is with the College of Urban and Environmental Sciences, Northwest University, No.1 Xufu Street, Chang'an District, Xi'an, Shaanxi Province 710127, P.R. China

Qinke Yang (corresponding author) and Chunmei Wang are with the College of Urban and Environmental Sciences, Northwest University, No.1 Xufu Street, Chang'an District, Xi'an, Shaanxi Province 710127, P.R. China (qkyang@nwu.edu.cn).

The quality of the basic released SRTM data is closely related to the properties of the remote sensing devices, the interaction between the land surface and radar signals, and the base data processing. Among these factors, the effect of the device on the quality of SRTM data is usually the result of changes in the attitude of the space shuttle and signal transmission anomalies from the sensors. Rodríguez *et al.* (2006) provided a detailed explanation of the data error characteristics caused by the properties of platforms and sensors. The land surface features which interact with radar signals and result in elevation data errors, include topographic attributes and land-cover. In regard to SRTM data, the elevation error in areas with steep terrain is larger whereas in flat areas the elevation error is smaller but includes striping noise (Carabajal and Harding, 2006). The pixel values of the SRTM data provide effective height information for an area of the Earth's surface, but in many areas the STRM elevation value can be different from that of the bare surface (Gallant and Read, 2009; Nelson *et al.*, 2009). Currently, most discussions of the effects of surface objects on the quality of SRTM data have focused on increased effective elevation due to vegetation (Weydahl *et al.*, 2007; Baugh *et al.*, 2013; Su and Guo, 2014). Man-made objects, such as urban built-up, can also affect the quality of the SRTM data, but only a few studies to date have focused on this effect (Gamba *et al.*, 2002). In other situations, the SRTM radar signal can penetrate the actual ground surface, including snow-covered surfaces, ice, deserts, etc., and yield elevation values that are lower than the actual bare surface. The radar signal can also penetrate vegetation crowns, so vegetation height information in SRTM data is normally also an underestimate of the height to the vegetation crowns (Carabajal and Harding, 2006; Kenyi *et al.*, 2009). Because of the impact of the device properties and land surface features, there were many voids in the preliminary SRTM products. Although many of these problems have been effectively fixed in later versions through spatial interpolation and multi-source data fusion (Delaney *et al.*, 2005; Kuuskivi *et al.*, 2005; Grohman *et al.*, 2006; Reuter *et al.*, 2007), the processing that corrected these problems can also introduce new errors to the SRTM data.

The SRTM data incorporating the effects of land-cover height (vegetation, buildings, etc.) essentially provide estimates for a Digital Surface Model (DSM) (Nelson *et al.*, 2009) whereas the elevation of the bare ground surface is the objective of a Digital Elevation Model (DEM). Although there are previous studies focusing on the elimination of land-cover height effects and particularly of vegetation height effects (Gallant and Read, 2009; Baugh *et al.*, 2013; Su and Guo, 2014), no fully satisfactory and universal methods are yet available for the large scale conversion of the SRTM DSM to a DEM. In a number of studies where a high-accuracy DEM at large scale is not available, SRTM

Photogrammetric Engineering & Remote Sensing
Vol. 82, No. 2, February 2016, pp. 135–148.
0099-1112/16/135–148

doi: 10.14358/PERS.83.2.135

data has been used as a substitute and used along with simple filter processes or even no conversion (Sesnie *et al.*, 2008; Barr and Clark, 2009; Li *et al.*, 2013b). This could certainly bring adverse effects into the research results. Therefore, to establish the magnitude of these effects, it is important to assess the quality of SRTM data in relation to the land surface. Such a study is also a precondition for any attempt to strip the height of land -cover from SRTM to reach a DEM.

Elevation errors in SRTM data are usually studied by employing high-accuracy elevation datasets to represent the actual elevation and comparing them with SRTM data. The high-accuracy elevation datasets primarily include two types: one is elevation data obtained from ground measurements using a global positioning system (GPS) receiver and the other is a digital elevation model (DEM) that is known to be more accurate than SRTM data. Ground-measured GPS elevation data are of high accuracy; the error can be controlled to within 0.5 m (Rodríguez *et al.*, 2006) and the GPS value derived error can be regarded as an absolute error (Gesch *et al.*, 2012). However, a DEM data with high accuracy that provides continuous and complete coverage over a large area is often more suitable as reference data. Accurate DEM data have been used here for studying the associations of SRTM elevation error and landscape features, because it overcomes some defects of the GPS method in diverse landscapes. For example, rugged mountainous terrain and dense forests are unreachable for GPS devices which results in a less than comprehensive evaluation of error (Gorokhovich and Voustianiouk, 2006). Usually, DEM datasets provide the most suitable data for a country or region. Examples of previous application include the National Elevation Dataset (NED) with resolution of 1-second used by Shortridge and Messina (2011) and the high-accuracy DEM data with resolution of 3-seconds generated from 1:250 000 scale topographic maps used by Miliaresis and Paraschou (2005). Because the error obtained is not the actual bias of SRTM data to the bare land surface, it may be more appropriate to regard the error derived from the reference DEM as a relative error, however, the reference Hc-DEM (see the Data Section) used in this study is believed to be precise enough to closely characterize the SRTM error (NASMG, 2008). Over larger areas (e.g., continental scale), a method typically used to assess the accuracy of SRTM data is sample survey. For example, Guth (2006) used hundreds of thousands of regular-grid sample points to study elevation errors in SRTM data over the United States.

There are many studies that have identified land-cover issues with SRTM data (Shortridge, 2006; Castel and Oettli, 2008; Miliaresis, 2008; LaLonde *et al.*, 2010), but most of them take a local area as a case study. Current systematic studies of SRTM data quality over large areas have primarily focused on the Amazon basin, Australia, and the United States, and the SRTM data error exhibits different characteristics due to variations in the topography and land-cover in these areas. The Amazon Basin is primarily covered by tropical rainforests, so the SRTM data quality is largely affected by vegetation effects. In the regions of umbrageous forest SRTM shows a vertical offset of around 30 meters (Blitzkow *et al.*, 2007). Australia is dominated by desert and has generally low topographic relief, so the SRTM data clearly exhibit stripes in low relief areas with a wavelength of about 800 m and amplitude of about 0.2 to 4 m (Gallant and Read, 2009). The United States consists of mountains in the west and east with plains in the center with relatively large variations of elevation error in the east and west and small error variations at the center, with the mean error being just over 2 m (Shortridge and Messina, 2011). Compared with these areas, the topography and land covers of China are more complex. Among the different regions there are many diverse landforms and significant variations in topographic relief, hydrology, and vegetation types as well as other land coverages. In addition, glaciers, deserts, and wetlands are also widely distributed (Li *et al.*, 2013a). Therefore, the distribution of SRTM data errors is relatively complex, and has been briefly explored in the preliminary study of the quality of global SRTM data by Rodríguez *et al.* (2006). However, although SRTM data have been widely used in studies of China (Yang *et al.*, 2012; Pieczonka *et al.*, 2013; Sun *et al.*, 2013; Neckel *et al.*, 2014), a detailed evaluation of SRTM data across the whole of China is still lacking.

The objective of this study is to present the diversities of effects associated with different land surface features in China on the quality of SRTM data and to provide information about the applicability and background of uncertainty in the SRTM 3-second datasets to its users. In this way, the reliability of their research results can be improved. Because the topography and land-cover types in China are complex, an elevation error in one position may be subjected to the effect of a combination of different factors, and the dominant factor that effects elevation error may vary across different areas. For SRTM data in China, this study initially endeavored to employ the whole sample method (all sample points without classification are included in the analysis of the associations between SRTM error and factors). This has been used in prior estimations of SRTM error (Gorokhovich and Voustianiouk, 2006; Shortridge and Messina, 2011). However, its use did not lead to suitable results that were consistent with the previous findings. These findings included SRTM elevation error increasing with increasing slope and vegetation coverage, and the errors in vegetation-covered areas being usually positive. As a consequence, the single factor method (in which sub-samples are separated conditionally to ensure they are dominated by single factor) was adopted for this study to explore the characteristics of SRTM error in complex landscapes and eliminate interference between the various factors.

Data and Methods

Data

The SRTM data used in this study was the CGIAR Version 4 dataset obtained from the CGIAR-CSI website (*http://*SRTM.*csi.*CGIAR.*org/*) (Jarvis *et al.*, 2008). The data covers the landscapes of the whole of China and uses the WGS84 horizontal datum and the EGM96 vertical datum and the resolution is 3-seconds. The reference DEM data was the hydrologically correct DEM (Hc-DEM) data generated from 1:50 000 topographic maps from the National Geomatics Center of China (NASMG, 2002). The resolution of the DEM data was 25 m, and used the Gauss Kruger Projection in 6° wide zones based on the Xian80 Geographical Coordinate System and the 1985 National Height Datum. The reference data was generated from the map sheets using ANUDEM software (Hutchinson, 2004) in which the Hutchinson algorithm (Hutchinson, 1989) is an internationally popular DEM interpolation algorithm that can specifically incorporate the hydrological correctness of the product. Of the elevation datasets that cover the whole of China, the 1:50 000 topographic map has been established as the most accurate (NASMG, 2008) with vertical errors controlled within 3 m for the flat areas, 5 m for hills, 8 m for mountain areas, and 14 m for the steep mountain areas. The ANUDEM-generated DEM data includes topographic feature lines (terrain shape, streamlines, and ridge lines) (Clarke and Burnett, 2003) and derived topographic attributes (slope and aspect, etc.) having high accuracy (Yang *et al.*, 2007).

To investigate the relationships between the SRTM elevation error, the topographic attributes and the land-cover types, other ancillary datasets were also introduced into this study. The topographic attributes include two parameters of slope and aspect that were derived from both the Hc-DEM and SRTM data for a comparative analysis in the consideration of the SRTM data quality assessment and the internal relationship

between the elevation error and slope and aspect. The annual composite forest cover data (DiMiceli *et al.*, 2001) of 2000, obtained from the Global Land Use Database of the University of Maryland, display the distribution of vegetation types and coverage in China relatively accurately (Figure 1). These data have been used in other analyses of SRTM errors (Hansen *et al.*, 2003; Carabajal and Harding, 2006; Van Niel *et al.*, 2008, Shortridge and Messina, 2011). The North China Plain and the plains in the lower reaches of the Yangtze River are topographically flat and include widely distributed densely urbanized areas. The SRTM data of these regions contains information that includes the height of the urban built-up areas, so the areas with dense urbanization were located from Google Earth™ image maps. Furthermore, distribution maps of glaciers (Wu and Li, 2014), deserts (Wang *et al.*, 2005b), and wetlands (NIGA, 2000) were obtained from the Cold and Arid Regions Science Data Center of the Chinese Academy of Sciences. Glaciers, deserts, and wetlands, which are concentrated in western and northern China, are active subjects in climate change research (Shi *et al.*, 2007). The radar signals show different characteristics in these areas compared with bare land and land covered by vegetation, so it is necessary to study the characteristics of the elevation error in these land types (Figure 2) separately.

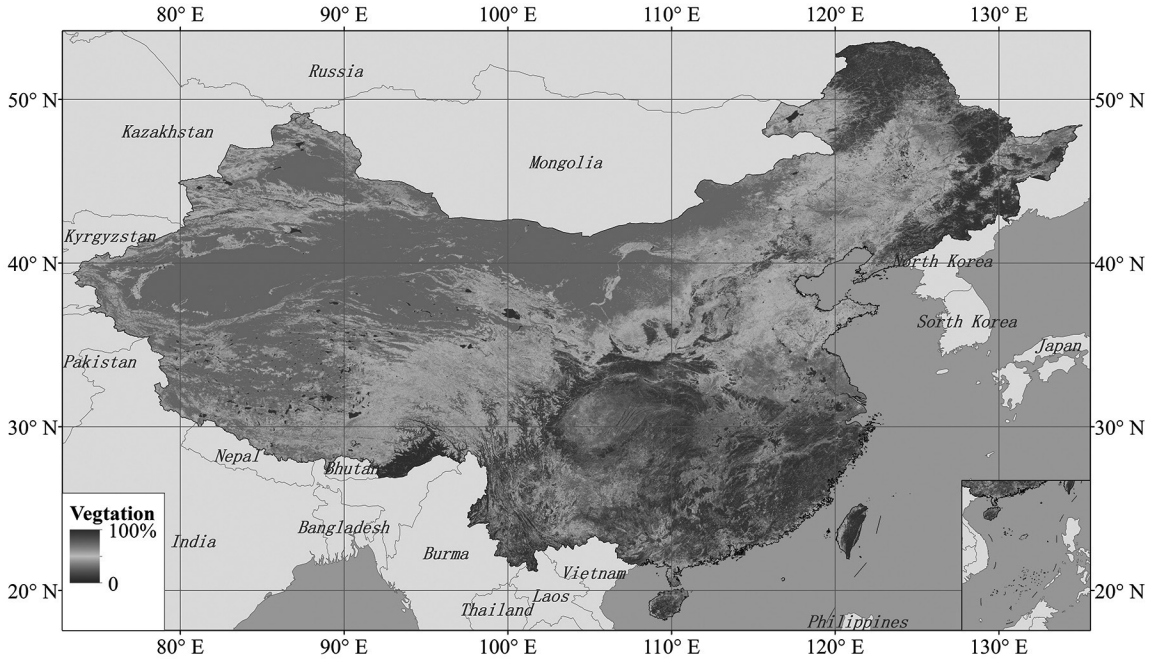

Figure 1. Vegetation cover in China.

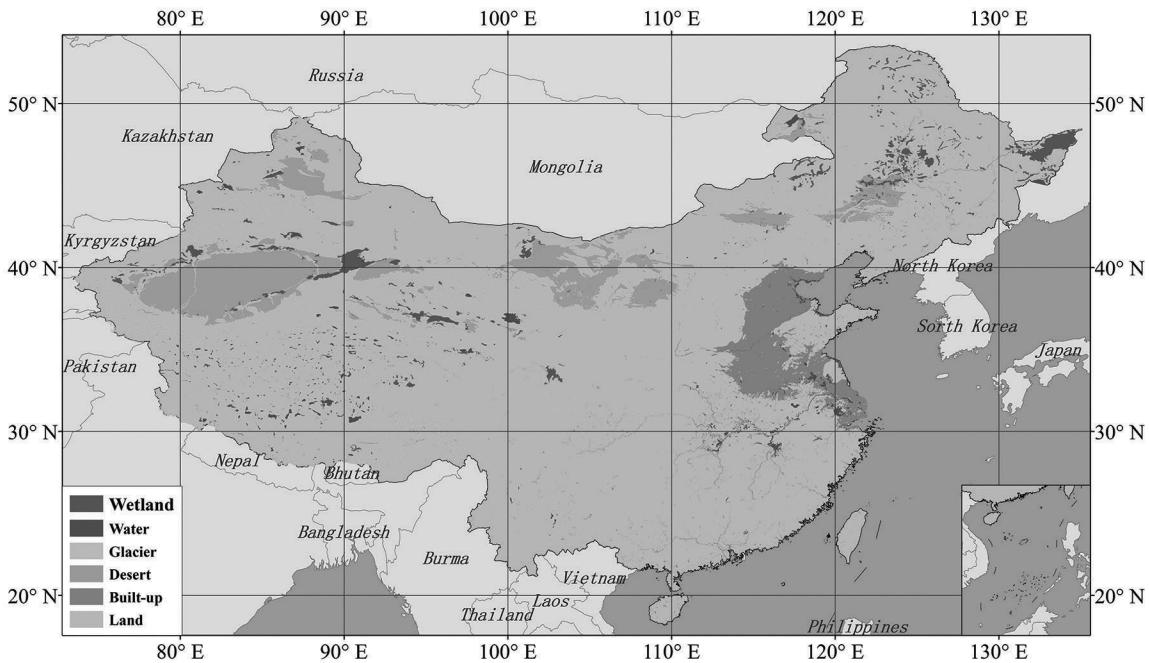

Figure 2. Different land-cover types in China.

Methods

The bias between the EGM96 Height Datum used by SRTM data and the 1985 National Height Datum used by the Hc-DEM has a mean value of 0.357 m and increases gradually from east to west and south to north (Guo *et al.*, 2004).This bias was first corrected in this study. The SRTM data error includes both positioning error and the elevation error. Van Niel *et al.* (2008) demonstrated that the positioning error has a large impact on the assessment of the differences between SRTM data and other DEM data. Some studies have quantified the mis-registration between SRTM data and high-resolution DEMs (Hofton *et al.*, 2006; Rodríguez *et al.*, 2006; Smith and Sandwell, 2003) and others have assessed the impact that the mis-registration has on applications (Dai and Khorram, 1998; Townshend *et al.*, 1992; Verbyla and Boles, 2000; Wang and Ellis, 2005). Eliminating the positioning error is a prerequisite for exploring the characteristics of elevation error on SRTM data applications. It is sufficient that the relative positioning precision is guaranteed in most applications of the SRTM data with other datasets. In order to avoid change of SRTM elevation values due to the resampling process during the spatial registration, basing the alignment on SRTM data, the spatial registration was conducted on Hc-DEM data and had two steps: preliminary registration and accurate registration. As the preprocessing step, the original Hc-DEM was resampled to 1-second resolution before the conduct of spatial registration. The method for preliminary registration was described by Van Niel *et al.* (2008). To improve the local precision of this step, the SRTM data and resampled Hc-DEM data were segmented into 1.5° × 1° tiles first. Accurate registration was then conducted to reduce any local positioning errors that occur during preliminary registration, and the method used in this step was described by Shortridge and Messina (2011). The SRTM elevation error is defined as the bias between Hc-DEM and SRTM elevation values for the same position so the registration accuracy is critical. The SRTM data had a mean error of –0.81 m with a standard deviation of 27.36 after preliminary registration and a mean error of –0.35 m with a standard deviation of 14.96 m after accurate registration. Thus, the elevation error was significantly reduced by the accurate registration leading to more reliable estimates of the elevation error.

The topographic attributes of slope and aspect used in this study were derived from the SRTM data and the registered Hc-DEM, which were both based on the WGS84 horizontal datum and a geographic coordinate system with the unit of cell size being degrees. The conventional algorithms for slope and aspect require that the unit of elevation should be in accordance with cell size (usually meters).The algorithm was refined so as to estimate slope and aspect directly in the geographic coordinate system. Zhou and Liu (2004) have evaluated the errors of conventional grid based algorithms of slope and aspect, among which the method of third-order finite difference weighted by reciprocal of squared distance was evaluated as accurate and so was adopted in this study. Compared with algorithms in projected coordinate systems, the difference in geographic coordinate systems is that the unit of cell size is degrees, which need to be converted to the units of length. Supposing that the Earth is a perfect sphere (the difference of equatorial radius and polar radius can be ignored in the calculation of slope and aspect in this study), the length of cell size is a constant in north-south direction (Y_d) but varies with latitude in the east-west direction (X_d), which can be expressed as:

$$X_d = Y_d \cos \alpha \quad (1)$$

where α represents the latitude of the center cell in the unit of radians. The radius of the earth was set to 6,371,393 m in this study, thus Y_d is 92.662,437 m. The slope and aspect values in geographic coordinate system can be derived by combining the parameters of Y_d, the latitude value of each cell in SRTM data, and Equation 1 with the algorithms of slope and aspect.

Although the Hc-DEM dataset is the best elevation dataset for China, some areas, primarily in the Taklimakan Desert and southeastern Tibet, are still problematic. In both datasets, the elevations of the inland waters were obtained using a special data processing algorithm and were not based on the radar signals. Therefore, the water bodies in both datasets and the problematic areas in the Hc-DEM datasets were excluded from the analysis of the SRTM errors. One thing to note here is that there exist overlaps between water bodies and wetlands which spread over the middle and lower reaches of the Yangtze River and the Qinghai-Tibet Plateau, so the remaining wetlands involved in this study are mainly concentrated in northwest and northeast China.

The sample survey method was adopted in this study. To ensure the number of sample points meets the statistical requirements at the continental level, and for the different zoning and classification systems, as well as to ensure that the data redundancy is as low as possible, a total number of 518,587 independent sample points were obtained. The samples are spread across the whole of China and distributed on a regular grid. The interval value of the sample points was set by reference to the study of SRTM error in the US by Shortridge and Messina (2011), in which the value used was 0.055833°. Considering the more complex landscape in China, the interval value was reduced to 0.0425° (51-pixel distance, or about 4.7 km in the north-south direction and 2.8 to 4.5 km in the east-west direction) in this study. The variation pattern of the SRTM elevation error and its associations with the influencing factors were then explored using basic statistical analysis of sub-samples, which, conversely, had been separated according to the attributes of various factors. The sub-samples based on slope and aspect were separated using the SRTM data and considering the internal relationship between the elevation error and the SRTM slope and aspect.

The design specification of the SRTM mission is for an absolute elevation error of less than 16 m for 90 percent of the entire region (Rabus *et al.*, 2003), and is one of the most critical indicators describing the quality of SRTM data. In previous local evaluations of SRTM data quality, most regions have met the specification (Rabus *et al.*, 2003; Van Zyl, 2001), although in global evaluations, some regions have had absolute errors exceeding 16 m. Therefore, the original 90 percent error specification for SRTM is used for this study as well.

Results, Analysis, and Discussion

Basic Topographic Attributes

Within China, the distribution of the SRTM sample points with elevations greater than 0 is shown in Figure 3a. The mean elevation of the entire sample was 1,787.56 m, and the number of sample points tended to decrease with increasing elevation. Specifically, the proportion of sample points in lower altitude areas was the largest. Peak percentages of points occurred around 0 to 50 m, 1000 to 1050 m, and 4900 to 4950 m, and the minimum percentages of points fell between 700 to 750 m and 2600 to 2650 m, above 6,000 m, the percentage of sample points tended to be 0. The same pattern was also present in the Hc-DEM elevation distribution curves.

The three very large terrain zones separated by the elevation values of two minimum percentages of points are generally similar to the widely accepted three main terrain terraces in the geomorphology of China (Zhao *et al.*, 1995) (Figure 4). The low-elevation sample points are primarily distributed in the eastern part of China, the medium-elevation sample points distributed in the middle part of China and northwest China, and the high-elevation sample points distributed in the Qinghai-Tibet Plateau.

The proportion of points with an SRTM elevation less than 0 m was 0.11 percent, the majority of which were located in the Turpan Basin and scattered in the southeastern coastal areas.

Among the sample points, the lowest elevation of –154 m was located at Aiding Lake in the Turpan Basin, and the highest elevation of 8,186 m was located in the Himalayan Mountains.

The frequency distribution of the SRTM slope sample points is shown in Figure 3b. The peak near to 0° indicates a large proportion of low-slope sample points. The number of sample points decreased with increasing slope and specifically decreased rapidly within the range of 0 to 5° and more slowly above 5°. The number of points with a slope greater than 45° approached 0. Figure 5 shows the spatial distribution of these three slope levels. The proportion of sample points with slope less than 5° was 52.4 percent, and these points were mainly located in northeast China, northwest China and part of the Qinghai-Tibet Plateau. Sample points with slope greater than 45° only accounted for 0.3 percent and were primarily distributed in the Tianshan Mountains, the western Kunlun Mountains, and the boundary between the second terrain terrace and the southeastern Qinghai-Tibet Plateau. Sample points with slope between 5° and 45° were widely distributed in the hilly and mountainous regions nationwide. The mean slope of the entire sample was 9.06°.

Considering that the 3-second SRTM data were aggregated from the 1-second data, the derived slope data were attenuated as the spatial resolution reduced, which meant an overall trend to gentler topography and smaller average slope, it was therefore necessary to account for the influence of the attenuation (Yang *et al.*, 2008). In this study, the average slope of Hc-DEM and SRTM data were 9.85° and 9.02°, respectively, which indicated that the slope of SRTM data reduced on average by 0.83° compared with the Hc-DEM. This reduction produced little effect on the following analysis of the SRTM elevation error over the entire sample but should be corrected in practical applications to local areas.

The distribution of the SRTM aspect sample points is shown in Figure 6a. The aspect showed a significant pattern of concentration in the four main directions (north, east, south, and west) and four secondary directions (northeast, southeast, southwest, and northwest). Furthermore, the proportion of points in the secondary directions was greater than that in the main directions. Among the main directions, the proportion of points in the north and south direction was greater than that in the east and west direction. This pattern was significantly different from the reference Hc-DEM (Figure 6b), which demonstrated that the SRTM data had a significant problem in the representation of aspect.

Previous studies have noted that the tracking direction of the remote sensing platforms has a great impact on SRTM

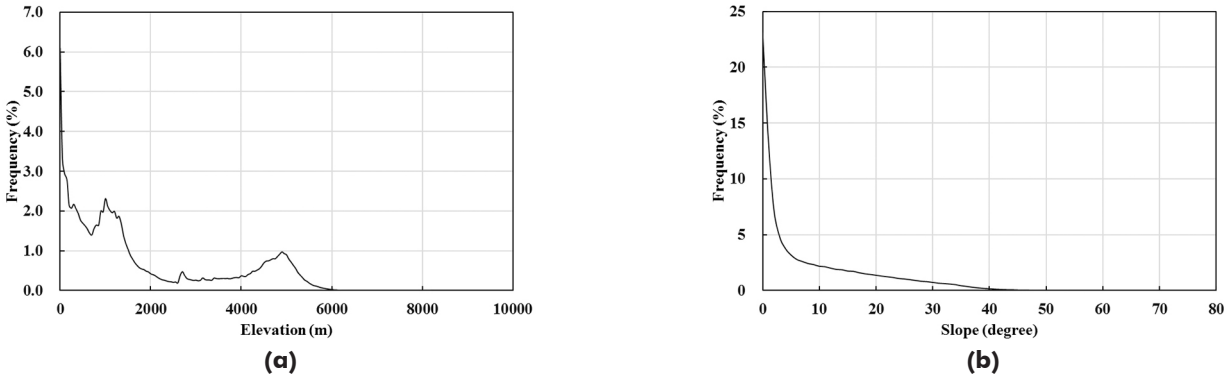

Figure 3. Frequency distribution of (a) Elevation, and (b) Slope of SRTM data.

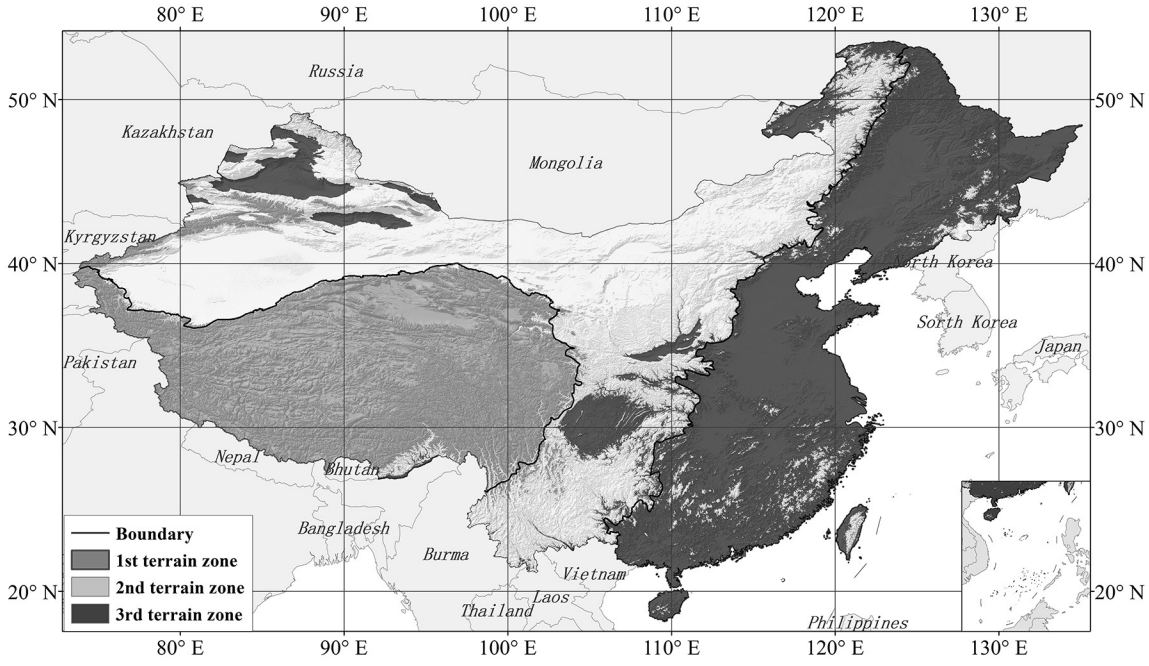

Figure 4. The three terrain zones in China.

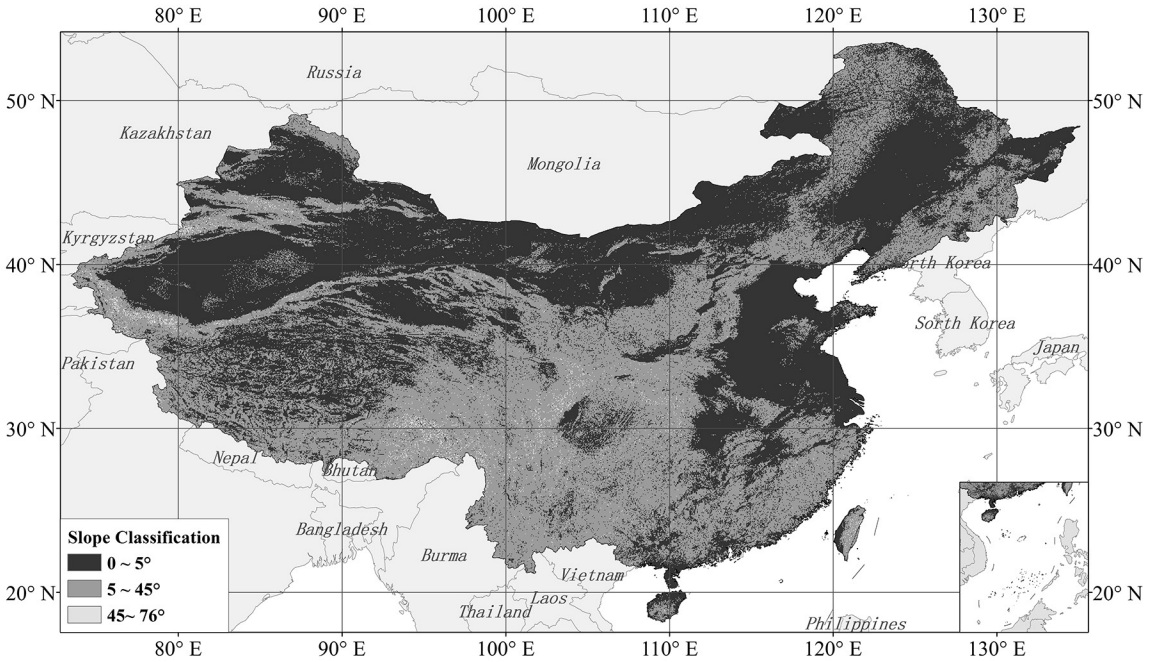

Figure 5. Spatial distribution of three slope levels in China.

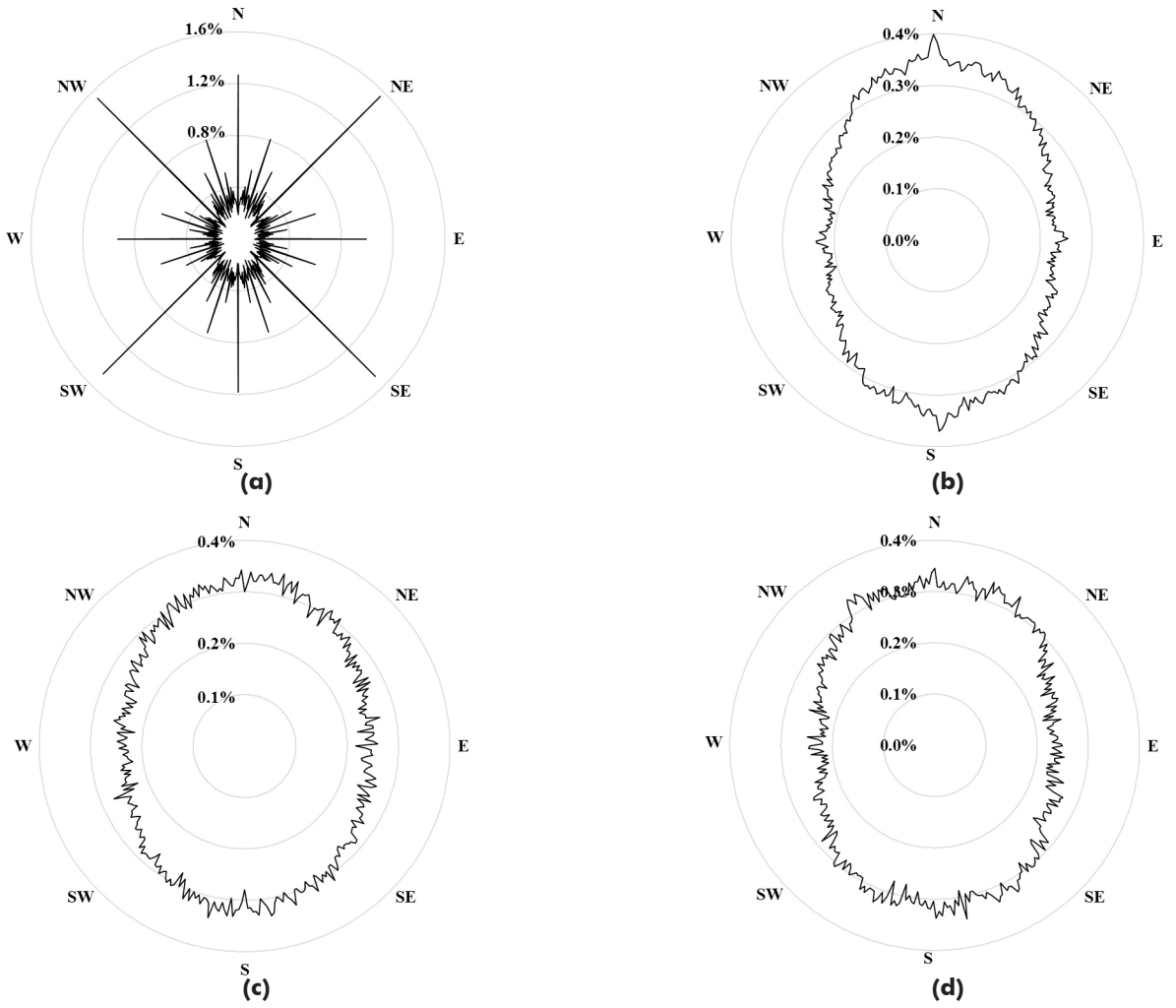

Figure 6. Frequency distribution of aspect of SRTM data and Hc-DEM: (a) Aspect of SRTM data (all sample points), (b) Aspect of Hc-DEM (all sample points), (c) Aspect of SRTM data (sample points with slopes greater than 5°, and (d) Aspect of Hc-DEM (sample points with slopes greater than 5°)

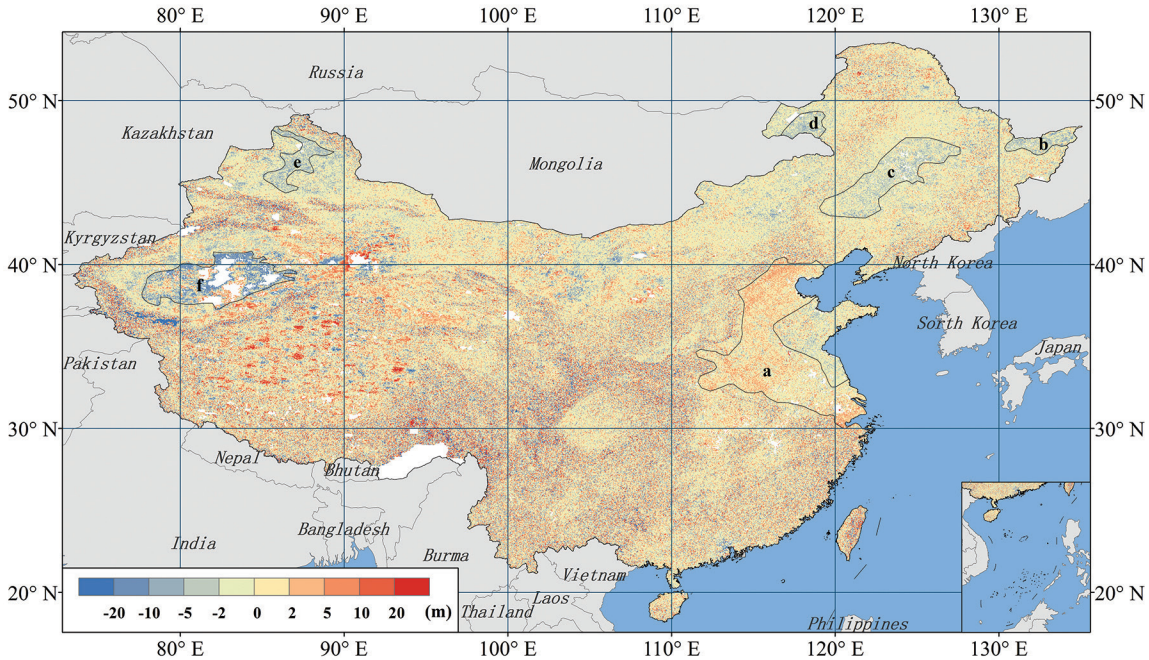

Plate 1. Spatial distribution of SRTM error in China. Positive errors are concentrated in the region labeled with 'a', while negative errors are concentrated in the regions labeled with “b”, “c”, “d”,“e”, and “f”.

data, and an obvious example is the emergence of northeast to southwest and northwest to southeast stripes in flat areas (Gallant and Read, 2009; Miliaresis and Paraschou, 2005). In Figure 6c, the distribution curve of the aspect in rolling terrain (with slope greater than 5°) tended to be smooth. The frequency in the main and secondary directions were significantly reduced, and the proportion of sample points in north and south directions were more than in the east and west directions. These patterns were as same as those in the aspect distribution of Hc-DEM data with slope greater than 5° (Figure 6d). Therefore, the majority of samples with aspects in the eight directions belonged to flat areas with slope less than 5°. It is reasonable to suppose that the properties of the platforms directly affected the aspect distribution in the generated SRTM data. The trait of relatively more north and south facing slopes in the aspect curve from the SRTM data with slopes greater than 5° also reflected a fact that the major mountains and valleys in China trend from east to west (Wang *et al.*, 2004).

Distribution of SRTM Error

The spatial distribution of the SRTM elevation error across China is shown in Plate 1, in which positive errors indicated that the SRTM elevation was greater than that in Hc-DEM for the same position, and negative errors indicated that the SRTM elevation was lower than that in Hc-DEM. Larger errors primarily occurred in the mountainous areas with complex terrains whereas smaller errors primarily occurred in the flat areas.

The positive errors were concentrated in the North China Plain and the plains in the mid-and lower-reaches of the Yangtze River (region labeled with an “a” in Plate 1), where the land is flat and urban areas are densely distributed, so the main source of error was the height of buildings. The negative errors were concentrated in the Northeast Plain (region labeled with a “b” in Plate 1), the Sanjiang Plain (region labeled with a “c” in Plate 1), and the Horqin region (region labeled with a “d” in Plate 1) in northeast China, the Junggar Basin (region labeled with an “e” in Plate 1), and the Tarim Basin (region labeled with a “f” in Plate 1) in Xinjiang province. These areas are dominated by desert and wetland landscapes, and the wetlands are normally frozen in February (the month that the shuttle flew the SRTM mission) with the land surface covered by ice. It is therefore very likely that the main source of elevation error was the penetration of the radar signals into the ground. In other widely spread mountain-dominated areas, the variation of SRTM data error was much greater.

The SRTM error for the entire sample ranged from −1,224.0 m to 1,195.2 m. For the whole of China, the number of points whose absolute error was greater than 16 m accounted oly for 1.75 percent of the sample. Figure 7 shows the frequency distribution of the elevation error of 90 percent of the sample points, which indicated a clearly symmetrical distribution with errors concentrated in the vicinity of 0 m and ranging from −7.4 m to 7.4 m, which was significantly better than that originally specified for the SRTM error. The mean error using 90 percent of the sample points was −0.023 m.

The Obvious Abnormalities

There were some areas with clearly abnormal elevation information in the SRTM data. These were almost certainly caused by the impact of the land surface on radar signals and the data processing. The characteristics of these areas differed greatly from the surrounding normal areas, and these differences could be observed directly. The cell values in these areas were not only greatly different from the true elevation, but also failed to present the structure of the land surface as measured (for example) by slope and aspect. Figure 8 shows one example of an abnormality expressed in the form of elevation, slope and aspect compared with surrounding normal data.

For the whole of China, the obvious abnormalities in the SRTM data included large continuous areas of “vague topography” and local “elevation anomalies”. The regions suffering from the issue of “vague topography” were larger with areas approximately from 25.6 km² to 2045.8 km². The topographic relief in these areas was lower than the surrounding areas and displayed missing details, and the topographic attributes appeared vague or even false (Figure 9a). The regions suffering from the issue of “elevation anomalies” were smaller with areas approximately from 0.08 km² to 0.71 km², and they appeared as non-existent “isolated peaks” or “deep sinks” (Figure 9b).

Table 1 shows that the total number of sample points with

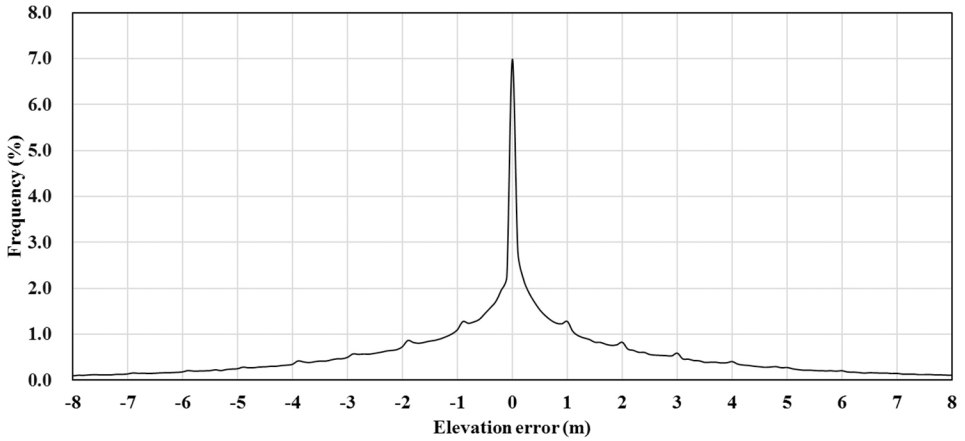

Figure 7. Frequency distribution of SRTM error (90 percent sample points).

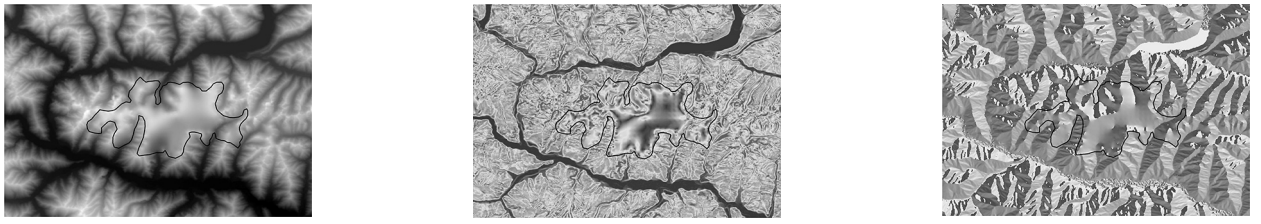

Figure 8. Abnormalities expressed in the form of (a) elevation, (b) slope, and (c) aspect.

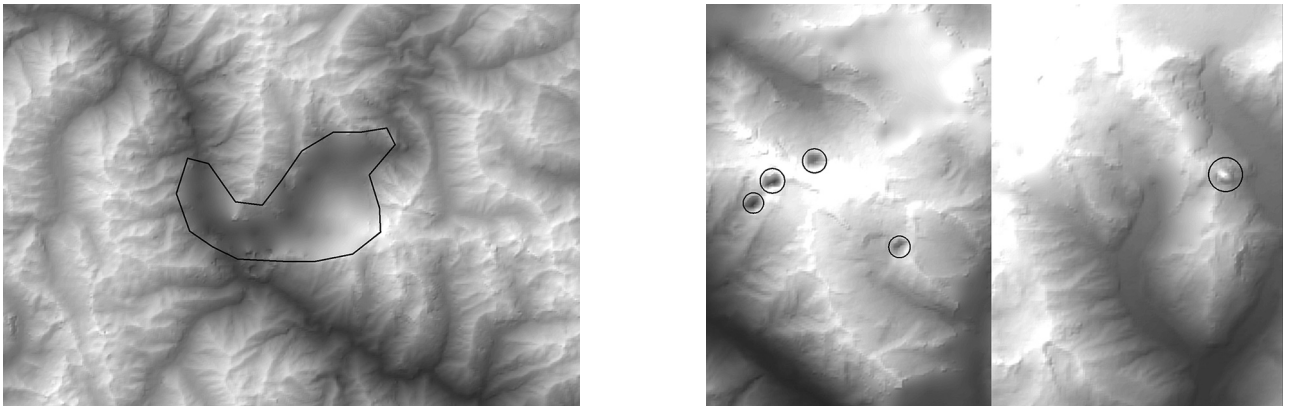

Figure 9. Obvious abnormality types: (a) "Vague topography" issue, and (b) "Elevation anomalies" issue.

obvious abnormalities was 4,646, which accounted for 0.90 percent of the entire sample. In particular, the largest positive and negative errors were 1,195.22 m and –1223.99 m, respectively, which were significantly higher and lower than the SRTM mission's specifications. The mean error of the abnormal areas was -35.52 m with an error standard deviation of 141.08. The mean error of the areas with elevation anomalies exceeded that of the areas with vague topography by as much as 14 fold. However, the number of points in the areas with elevation anomalies was 1,450, which was less than 3,169, the number of points in the areas with vague topography.

Figure 10 shows the distribution of these data abnormalities, which are primarily located in the western part and the northeast part of China. As seen from the background of SRTM hillshade data, areas with elevation abnormalities were primarily distributed in the mountains, glacier-covered areas and deserts. Because of the large elevation errors in these regions and serious problems with topographic expression, the impact of the abnormalities in the SRTM data on the applications and analysis should not be neglected. Although the number of sample points in abnormal areas only accounted for 0.90 percent of the entire sample, the number of sample points with larger error (assuming an error of more than 50 m as indicating large) located in the abnormal area accounted for 68.59 percent of the entire sample of large errors. To avoid

Table 1. Statistical Characteristics of the Obvious Abnormalities in SRTM Data

Sample type	Min(m)	Max(m)	Mean(m)	STD	Size (m^2)
All	-1223.99	1195.22	-35.52	141.08	4,646
Vague topography	-1223.99	1195.22	-6.71	97.37	3,196
Elevation anomaly	-769.84	231.36	-99.04	192.38	1,450

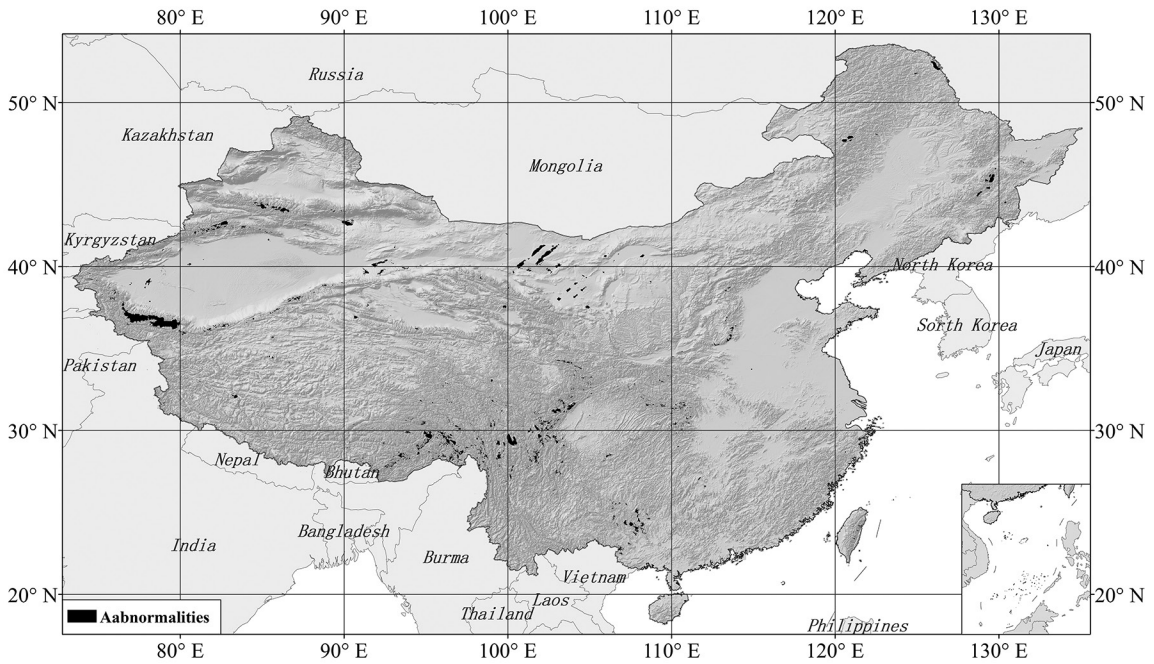

Figure 10. Spatial distribution of obvious abnormalities in China.

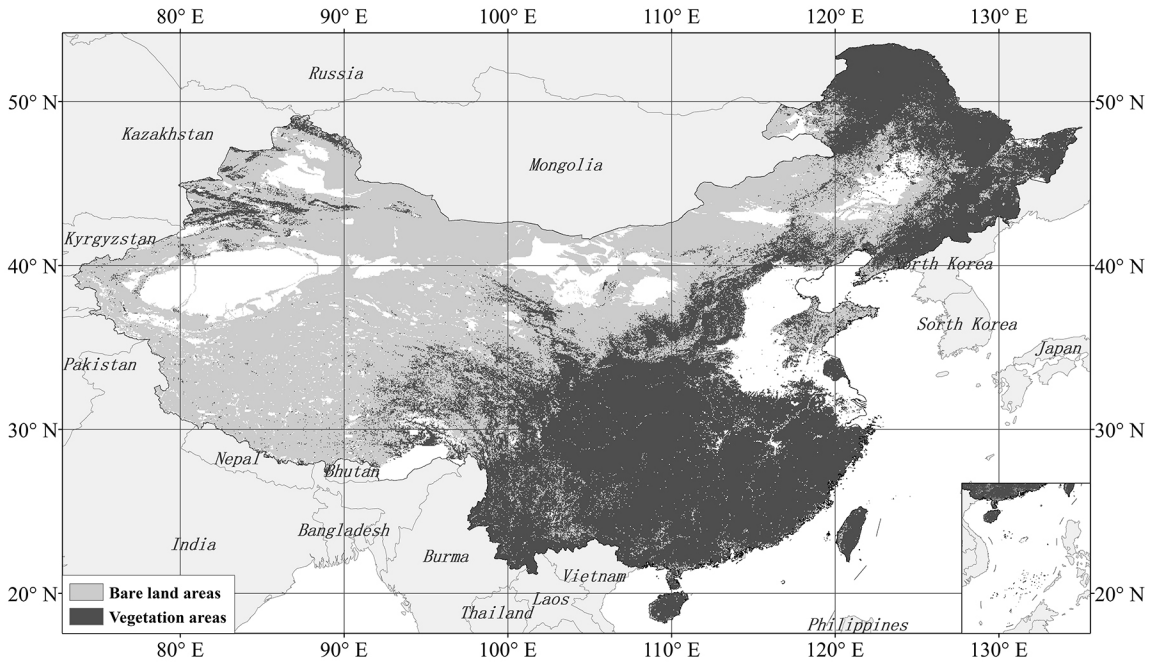

Figure 11. Regions for topography and vegetation factors.

interference from these abnormal areas on the subsequent analysis of the elevation errors, the sample points in these abnormal areas were excluded so that the statistical results would be more widely applicable.

Relation between Terrain and Land Cover Factors and SRTM Errors

SRTM Errors and Topography

The topographic factors that affected the SRTM elevation error included slope and aspect. For this part, the sample points located in built-up urban areas, deserts, glaciers, and wetlands were excluded. Additionally, to reduce the impact of variations in vegetation coverage, the sampling points with vegetation coverage less than 5 percent were selected from the remaining sample points. This assumes that the impact of the vegetation in these areas on the SRTM data could be ignored due to the low vegetation density and height. Finally, the sample points selected for topographic factors were primarily distributed in the west part and the northern middle part of China as seen in Figure 11 labeled as bare land areas. The total number of samples was 237,083, which accounted for 46.13 percent of the entire sample without SRTM data abnormalities, and had a mean error of 0.18 m with a standard deviation of 5.48.

Table 2 lists the basic statistics for the elevation errors of SRTM data for different slope levels. The mean errors showed

a decreasing trend and changed from positive to negative as the slope increased, except that the value for the 25° to 35° slope level was slightly greater than that for the 15° to 25° level. Mean errors in the 0° to 2° level were positive but negative in the other levels. The smallest elevation error was 0.05 m for the 0° to 2° level, while the largest error was -0.86 m at the >35° level. In terms of the standard deviation, the overall variation in the errors increased with increasing slope, but the minimum variation in the errors occurred at the slope level of 2° to 5°, the standard deviation range from 3.98 to 17.51. Although the maximum positive and negative errors were relatively large and at a magnitude of hundreds, the large errors made up a small proportion of the entire sample with the 90 percent error exceeding 16 m only in the >35° level.

Table 3 presents the basic statistics for the SRTM elevation errors for different aspects. The mean errors were smaller in southwestern directions than that in northeastern directions. The errors in most directions were negative while the positive errors only distributed in the northern directions of 0° to 45° and 315° to 360°. The largest negative error was -0.44 m and located in the direction of 225° to 270°, the largest positive error was 0.08 m and located in the direction of 0° to 45°. The variations in the standard deviation and 90 percent errors were not obvious in different directions (5.5 ±1 and 6.8 ±0.2 m, respectively), which meant a slight variation of errors in different aspects.

Further statistics revealed that the same pattern of smaller mean errors in the southwestern directions and larger mean errors in the northeastern directions was observed for various aspects at different slope levels. Meanwhile, the mean errors showed a smaller proportion of positive errors for higher slope levels. In most aspects, the elevation errors in different slope levels also tended to decrease numerically with increasing slope.

The mean errors of the different slope levels varied within a range from -0.86 m to 0.05 m with an interval of 0.91 m, and the standard deviation varied from 3.98 to 17.51. The mean error for various aspects varied from −0.44 m to 0.08 m with an interval of 0.52 m, and the standard deviation fluctuated around a value of 5. All of the above indicates that among the topographic factors, slope has a larger impact on the SRTM errors than aspect.

Table 2. Statistical Characteristics of the Elevation Error Variation in the Slope Sample Type

Slope(°)	Min(m)	Max(m)	Mean(m)	STD	90% Error(m)	Size (m²)
0 to 2	-220.38	153.71	0.05	4.29	5.9	98,603
2 to 5	-174.51	283.48	-0.19	3.98	4.5	45,082
5 to 15	-232.15	315.64	-0.36	4.13	5.0	50,940
15 to 25	-464.12	287.72	-0.48	7.48	8.5	24,670
25 to 35	-208.62	174.36	-0.45	9.29	12.9	14,137
>35	-201.92	406.30	-0.86	17.51	18.6	3,651

Table 3. Statistical Characteristics of the Elevation Error Variation in the Aspect Sample Type; Flat Terrain with Slope of 0 was Excluded

Aspect(°)	Min(m)	Max(m)	Mean(m)	STD	90% Error(m)	Size (m²)
0 to 45	-177.86	315.64	0.08	5.16	6.6	35,498
45 to 90	-464.12	182.41	-0.03	6.17	6.7	26,064
90 to 135	-174.51	188.94	-0.13	5.37	6.8	23,915
135 to 180	-166.77	130.04	-0.37	4.98	6.8	34,975
180 to 225	-284.23	287.72	-0.43	6.04	7.0	35,868
225 to 270	-208.62	119.21	-0.44	5.41	6.9	24,689
270 to 315	-106.45	119.45	-0.21	5.03	6.8	22,001
315 to 360	-162.90	406.30	0.04	5.65	6.7	33,439

SRTM Errors and Vegetation

Rules similar to those used for the topographic factors were followed in the analysis of the relationship between the SRTM elevation errors and vegetation cover. First, the sample points in the deserts, glaciers, built-up urban areas, and wetlands were ruled out, but the difference in this part was that only the sample points with vegetation coverage greater than 5 percent were included. The sample points for the vegetation factor defined in this way were primarily distributed in the hilly areas and low mountains in northeastern China and most parts of central and southern China. The area can be seen in Figure 10 labeled as vegetation areas. The total number of samples was 213,449 that accounted for 41.53 percent of the entire sample set with SRTM data abnormalities excluded and had a mean error of 0.02 m with a standard deviation of 10.46.

The SRTM elevation errors in these areas were influenced by the joint effects of variations in vegetation cover and topographic attributes. The previous analysis indicated that slope had a greater impact on the errors than aspect. Thus, only the impact of the slope was also considered when analyzing the characteristics of SRTM elevation error for areas with vegetation coverage greater than 5 percent.

Figure 12 demonstrates the change in mean elevation errors of the SRTM data with vegetation coverage at different slope levels. At all slope levels, the value of the errors increased monotonically with increasing vegetation coverage. However, only the mean error at 0° to 2° slope level was positive for all the levels of vegetation coverage and varied from 0.15 m to 1.67 m. For other higher slope levels, the mean errors were small for all levels of vegetation coverage due to the impact of slope, which could be negative in the low levels of vegetation coverage indeed. The >35° slope level contained the smallest error

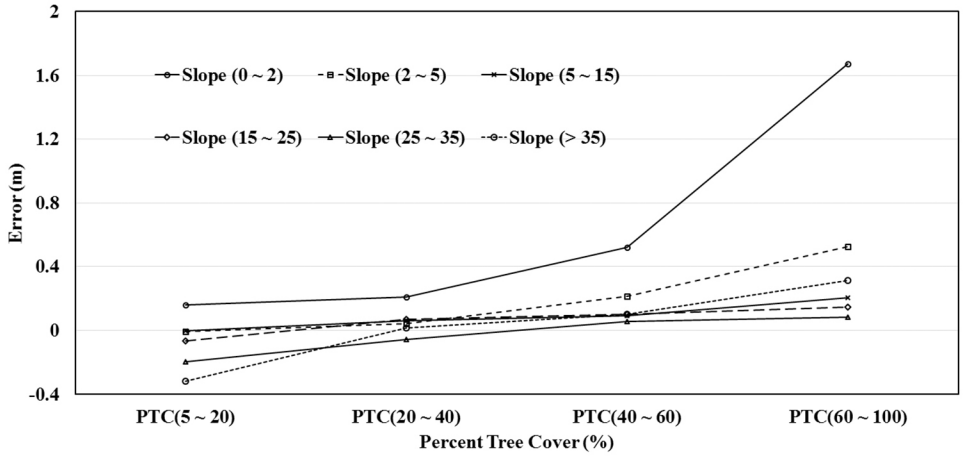

Figure 12. Relationship of SRTM error and vegetation coverage in different slope levels; PTC represents Percent Tree Cover.

Table 4. Statistical Characteristics of the Relationship between the SRTM Elevation Error and Vegetation Coverage in the Slope Range of 0° to 2°; PTC represents Percent Tree Cover

PTC(%)	Min(m)	Max(m)	Mean(m)	STD	90% Error(m)	Size (m^2)
5 to 20	-43.91	88.72	0.15	3.54	4.8	29,353
20 to 40	-31.60	67.94	0.22	3.55	4.9	6,423
40 to 60	-19.80	35.20	0.52	3.76	5.5	1,613
60 to 100	-13.01	17.57	1.67	4.39	8.1	341

Table 5. Statistical Characteristics of the SRTM Errors in Glaciers, Deserts, Urban Built-up Areas and Wetlands without Data Anomalies

Sample type	Min(m)	Max(m)	Mean(m)	STD	90% Error(m)	Size (m^2)
Glacier	-346.71	275.50	-1.05	19.97	19.6	4,335
Desert	-95.47	42.12	-2.03	5.16	9.6	37,804
Wetland	-14.10	8.87	-2.43	2.30	5.0	5,598
Urban Built-up	-11.02	17.17	1.05	2.23	4.0	17,697

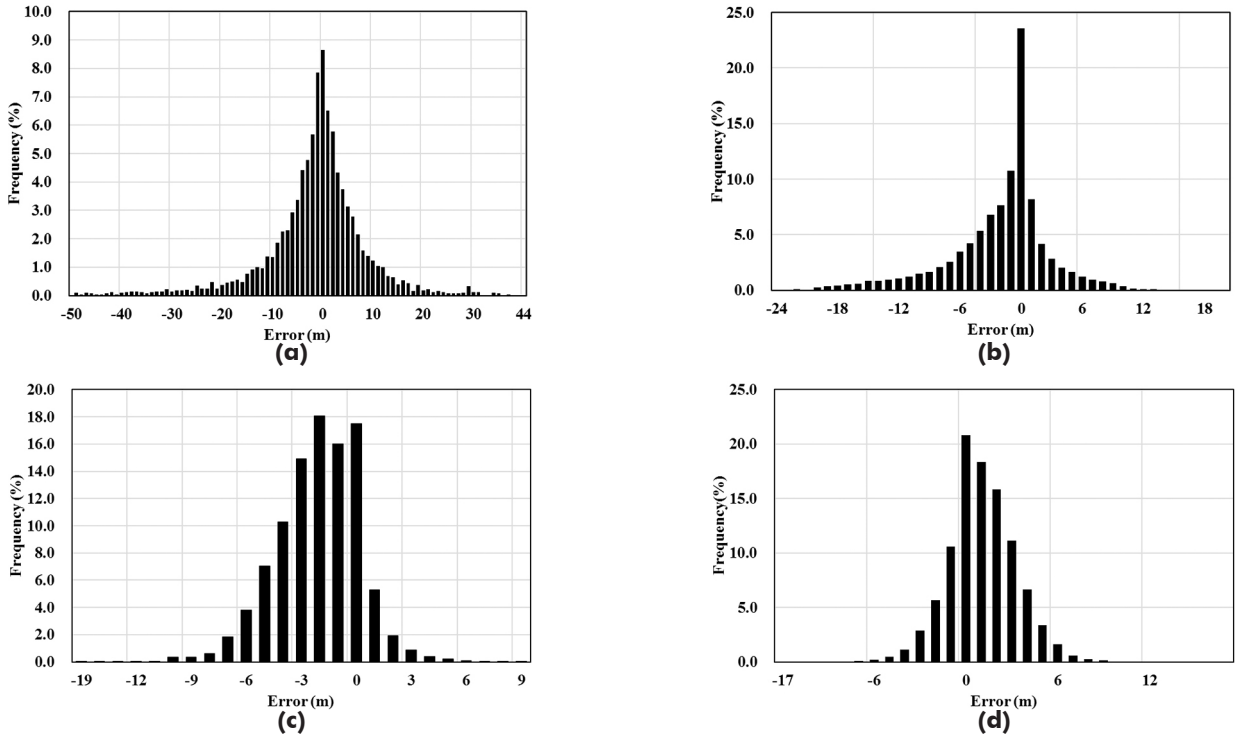

Figure 11. Frequency distribution of the SRTM error in areas with different landscape features: (a) Glaciers, (b) Deserts, (c) Wetlands, and (d) Built-up areas.

of −0.32 m. It can be concluded that variations in slope have a greater impact on the elevation error than vegetation coverage.

Changes in the elevation error of the SRTM data with respect to the vegetation coverage at different slope levels indicated that the elevation error was rarely affected by slopes between 0° and 2°. This could be taken to reflect the general pattern of changes in errors with respect to vegetation coverage; and the basic statistics are listed in Table 4. The mean elevation errors increased with increasing vegetation coverage, and the standard deviation of the errors also showed a slightly increasing trend. Furthermore, the 90 percent errors varied only slightly with the vegetation coverage.

SRTM Errors and Land Covers

Figure 2 shows the spatial distribution of different land cover types in China. Glacier-covered areas are primarily located in the mountains where they create large areas in SRTM having data abnormalities giving a maximum negative error of −1,223.99 m and a maximum positive error of 524.91 m. Similarly, there were large areas of SRTM with anomalies in the deserts, which led to a maximum positive error of 58.81 m and a maximum negative error of −95.47 m. In the wetlands that were sensed during a freezing winter in February, both the maximum positive and negative errors were relatively small. The error of only one sample point exceeded the specification and reached −19.40 m. Although densely built-up areas were topographically flat, the maximum positive and negative error reached ±17 m because of the presence of high buildings and deep open pits. The statistics for the sample points in the glaciers, deserts, and urban areas that exclude the data abnormalities are presented in Table 5.

Among these four land-cover types, the proportion of sample points in Desert and Built-up areas was much higher than that in the Glacier and Wetland areas. The statistics indicated that the mean errors in glaciers, deserts and wetlands were negative at −1.05 m, −2.03 m, and −2.43 m, respectively, while the mean error of the building-covered areas was positive at 1.05 m. This observation supported the suggestion that penetration of radar signals in glaciers, deserts and wetlands (in freezing winters) can cause an underestimation of the SRTM elevation of the actual surface. The overestimation of the actual surface SRTM elevation in the building-dense areas is also consistent with the height measurement of SRTM being above the bare ground. These characteristics were also reflected in histograms of the error in these four surface cover types (Figure 13). The error associated with glaciers, deserts, and wetlands showed a slightly negatively skewed distribution, and that associated with building-covered areas was positively skewed. The standard deviation of the errors revealed that the magnitude of the change in elevation errors was smallest for wetlands and built-up urban areas, in the middle for the deserts and highest for the glaciers. Wetlands and built-up

urban areas are located in plains, whereas glaciers are located in steep mountains and deserts have rolling surfaces. These differences in topographic relief among the four landscapes meant that changes in the standard deviation of the elevation error were also primarily affected by the slope.

Conclusions

The distribution of SRTM error and its associations with various influencing factors within China has been analyzed in this study. The main conclusions are summarized as follows:

1. The spatial and statistical distributions of the main topographic attributes derived from SRTM data accurately represent the actual topographic characteristics of China. The elevation distribution reflects the three basic terrain terraces in China. The peak in the frequency curve of slope was located near to 0° and an inflection point occurred near 5°, which separated the landscape into flat plains and rolling mountains. SRTM data was, however, found to have a significant problem in the estimation of aspect in flat areas. On the other hand, the aspect frequency distribution curves of the areas with slopes greater than 5° were consistent with independently derived and accurate DEM data and indicated correctly that the mountains in China mostly trend from east to west.
2. Most of the elevation errors were close to 0, and the 90 percent error for the entire sample was only 7.4 m, which met the original 16 m specification for the SRTM mission within the sub-samples of the different factors. Only the steep slope samples and the glacier samples failed to fully meet this specification. While the magnitudes of both the maximum positive and negative errors of the entire sample exceeded 1,000 m, there were only a small number of sample points with an absolute error greater than 50 m. In areas with large errors, SRTM data had some obvious issues with "elevation anomalies" and "vague topography" where it does not properly represent the structure of the land surface. Although these areas accounted for only a small proportion of the land in China, some special attention should be paid to them.
3. The elevation error of the SRTM data was closely related to the topography and land-cover. Different factors had distinct impacts on the SRTM errors and caused distinct error variation patterns. Slope had the strongest impact on the errors, and it also affected the variation patterns of error in the other factors. The spatial distribution of the errors indicated that flat areas generally exhibited small errors whereas mountains generally displayed larger errors. The land cover type with greatest concentration of positive errors was the urban built-up type, with a mean error of 1.05 m, whereas the negative errors were concentrated in deserts and wetlands (freezing winter) with mean errors below −2 m. Because the glacier-covered areas were dominated by mountains, no concentration of positive or negative errors occurred, but the mean error of the entire glacier area was −1.05 m. The statistical results for the various factors indicated that the elevation errors changed from positive to negative between plains and high mountains and that the magnitude of the errors gradually increased as the slope increased, with mean errors in the range from 0.05 m to −0.86 m. For the different aspects, the positive errors were concentrated in northern directions, while the negative errors occurred more often in southwestern directions. In flat areas (slopes within the range of 0° to 2°) with vegetation, the elevation errors increased with increasing vegetation coverage and had a mean error that varied within the range of 0.15 m to 1.67 m. In terms of standard deviation, the variation of elevation errors increased with increasing slope and vegetation coverage, but did not diverge greatly among different aspects.

Contrary to other studies that concluded the SRTM error usually showed an overall positive bias, mainly caused by vegetation and artifacts on the bare ground, the overall mean error of the SRTM data in China is negative. One reason for this could be the presence of widespread deserts, freezing wetlands, and glaciers where the radar signal can penetrate to depths below the surface, and also to the abundant rugged mountains with high slopes where the errors trend to negative.

For the users of SRTM data in China, the information summarized above can lead to a better understanding of the characteristics of elevation errors and how they may affect their research. Although SRTM data have relatively good quality taken over the full extent of China, users should take notice of the errors and issues that exist locally in the data when employing it in their applications. For example, the stripes in flat areas; the obvious abnormalities in mountains, glacier-covered areas and deserts; overestimation of elevation in built-up areas and areas covered by vegetation; underestimation of elevation in desert, wetland and glacier areas; and large negative errors in steeply sloping areas and their predominance in southwest facing aspect areas. To use the SRTM data appropriately, users should first avoid employing the data located around the obvious abnormalities and (if possible) refer to an alternative (e.g., topographic map-derived DEM) source of data. Second, users are recommended to adopt already widely-used methods of regression algorithms to correct the remaining errors in SRTM data. There are already methods for addressing the problems of striping, built-up areas, and vegetation covered areas (Gallant and Read, 2009; Baugh *et al.*, 2013), so the SRTM data should be updated to meet the accuracy requirements of the applications.

It is reasonable to measure the quality of SRTM data by elevation error, but the relationship between SRTM morphology and the actual surface morphology is another important indicator of the quality of the data and has a significant impact on numerous topographic analyses. There are already some publications which have addressed these issues, including river networks (Da Paz *et al.*, 2007; Li and Wong, 2009; Hancock *et al.*, 2006; Liu 2008), and how the slope shape affects the prediction of soil erosion (Verstraeten, 2006), but most have only been studied at the local scale. In one important case, however, the Hydro SHEDS (Lehner *et al.*, 2008) Project used SRTM data to provide hydrographic information for global-scale applications, although there was no systematic evaluation of the final data quality. Thus, there is still no complete assessment of effect of SRTM quality on surface morphology at the large scale, which, of course, includes the extent of China and therefore needs further studies in the future.

Acknowledgments

This study was funded by the National Natural Science Foundation of China (41371274, 41301284), the Ministry of Water Resources industry-specific appropriation (201201081) and the Natural Science Basic Research Plan in Shaanxi Province of China (Program No.2013JQ5002). We thank the Institute of Soil and Water Conservation of the Chinese Academy of Sciences and Ministry of Water Resources (CAS / MWR ISWC), the Spatial Information Department of the Consultative Group of International Agricultural Research, the Global Land Use Database of the University of Maryland, and the Cold and

Arid Regions Scientific Data Center of the Chinese Academy of Sciences for providing data. Special thanks to the anonymous reviews and Professor David Jupp of CSIRO for providing constructive suggestions.

References

Barr, I.D., and C.D. Clark, 2009. Distribution and pattern of moraines in far NE Russia reveal former glacial extent, *Journal of Maps*, 5(1):186–193.

Baugh, C.A., P.D. Bates, G. Schumann, and M.A. Trigg, 2013. SRTM vegetation removal and hydrodynamic modeling accuracy, *Water Resources Research*, 49(9):5276–5289.

Blitzkow, D., A.C.O.C. de Matos, and J.P. Cintra, 2007. SRTM evaluation in Brazil and Argentina with emphasis on the Amazion region, *Dynamic Planet* (P. Tregoning and C. Rizos, editors), Springer, Berlin Heidelberg, pp. 266–271.

Castel, T., and P. Oettli, 2008. Sensitivity of the C-band SRTM DEM vertical accuracy to terrain characteristics and spatial resolution, *Headway in Spatial Data Handling: 13th International Symposium on Spatial Data Handling, Lecture Notes in Geoinformation and Cartography* (A. Ruas and C. Gold, editors), Springer, Berlin, pp. 163–176.

Carabajal, C.C., and D.J. Harding, 2006. SRTM C-Band and ICESat laser altimetry elevation comparisons as a function of tree cover and relief, *Photogrammetric Engineering & Remote Sensing*, 72(3):287–298.

Clarke, B., and K. Burnett, 2003. Comparison of digital elevation models for aquatic data development, *Photogrammetric Engineering & Remote Sensing*, 69(12):1367–1375.

Da Paz, A.R., W. Collischonn, A. Risso, and C.A.B. Mendes, 2007. Errors in river lengths derived from raster digital elevation models, *Computers & Geosciences*, 34(11):1584–1596.

Dai, X., and S. Khorram, 1998. The effects of image misregistration on the accuracy of remotely sensed change detection, *IEEE Transactions on Geoscience and Remote Sensing*, 36(5):1566–1577.

Delaney, M., T. Kuuskivi, and X. Li, 2005. Evaluation of different solutions to fill voids in SRTM elevation datasets, *Global Priorities in Land Remote Sensing*, 23-27 October, Sioux Falls, South Dakota.

DiMiceli, C.M., M.L. Carroll, R.A. Sohlberg, C. Huang, M.C. Hansen, and J.R.G.Townshend, 2001. Vegetation continuous fields MOD44B, *2000 Percent Tree Cover, Collection 5*, University of Maryland, College Park, Maryland, URL: *http://www.landcover.org/data/vcf/index.shtml* (last date accessed: 11 November 2015).

Farr, T.G., P.A. Rosen, E. Caro, R. Crippen, R. Duren, S. Hensley, M. Kobrick, M., Paller, E. Rodriguez, L. Roth, D. Seal, S. Shaffer, J. Shimada, M. Werner, M. Oskin, D. Burbank, and D. Alsdorf, 2007. The shuttle radar topography mission, *Review of Geophysics*, 45(2):RG2004.

Gallant, J.C., and A. Read, 2009. Enhancing the SRTM data for Australia, *Proceedings of Geomorphometry, 2009*, 31:149–154.

Gamba, P., F. Dell Acqua, and B. Houshmand, 2002. SRTM data characterization in urban areas, *International Archives of Photogrammetry Remote Sensing and Spatial Information Sciences*, 34(3/B):55–58.

Gesch, D., M. Oimoen, Z. Zhang, D. Meyer, and J. Danielson, 2012. Validation of the ASTER global digital elevation model version 2 over the conterminous United States, *International Archives of the Photogrammetry, Remote Sensing and Spatial Information Sciences*, XXXIX-B4:281–286.

Gorokhovich, Y., and A. Voustianiouk, 2006. Accuracy assessment of the processed SRTM-based elevation data by CGIAR using field data from USA and Thailand and its relation to the terrain characteristics, *Remote Sensing of Environmen*t, 104:409–415.

Grohman, G., G. Kroenung, and J. Strebeck, 2006. Filling SRTM voids: The delta surface fill method, *Phtogrammetric Engineering & Remote Sensing*, 72(3):213–216.

Guo, H., W. Jiao, and X. Yang, 2004. The systematic difference and its distribution between the 1985 national height datum and the global quasigeoid, *Acta Geodaetica et Cartographica Sinica*, 33(2):100–104 (in Chinese).

Guth, P.L., 2006. Geomorphometry from SRTM: Comparison to NED, *Photogrammetric Engineering & Remote Sensing*, 72(3):269–277.

Hancock, G.R., C. Martnez, K.G. Evans, D.R. and Moliere, 2006. A comparison of SRTM and high-resolution digital elevation models and their use in catchment geomorphology and hydrology: Australian examples, *Earth Surface Processes and Landforms*, 31(11):1394–1412.

Hansen, M., R.S. DeFries, J.R. Townshend, M. Caroll, C. Dimiceli, and R. Sohlberg, 2003. Global percent tree cover at a spatial resolution of 500 meters: First results of the MODIS vegetation continuous fields algorithm, *Earth Interactions*, 7(10):1–5.

Hofton, M.A., R. Dubayah, J.B. Blair, and D. Rabine, 2006. Validation of SRTM Elevations over vegetated and non-vegetated terrain using medium footprint lidar, *Photogrammetric Engineering & Remote Sensing*, 72(3):279–285.

Hutchinson, M.F., 1989. A new procedure for gridding elevation and stream line data with automatic removal of spurious pits, *Journal of Hydrology*, 106(3):211–232.

Hutchinson, M.F., 2004. ANUDEM, version 5.1, *User Guide*, The Australian National University, Centre for Resource and Environmental Studies, Canberra, URL: *http://fennerschool.anu.edu.au/files/usedem53_pdf_16552.pdf* (last date accessed: 11 November 2015).

Jarvis, A., H.I. Reuter, A. Nelson, and E. Guevara, 2008. Hole-filled SRTM for the globe, version 4, available from the CGIAR-CSI SRTM 90m Database, URL: *http://srtm.csi.cgiar.org* (last date accessed: 11 November 2015).

Kenyi, L.W., R. Dubayah, M. Hofton, and M. Schardt, 2009. Comparative analysis of SRTM-NED vegetation canopy height to LIDAR-derived vegetation canopy metrics, *International Journal of Remote Sensing*, 30(11):2797–2811.

Kuuskivi, T., J. Lock, X. Li, S. Dowding, and Mercer, B., 2005. Void fill of SRTM elevation data: Performance evaluations, *Proceedings of the ASPRS 2005 Annual Conference*, *Geospatial Goes Global: From Your Neiborhood to the Whole Planet*, 07-11 March, Baltimore, Maryland, pp.7–11.

LaLonde, T., A. Shortridge, and J. Messina, 2010. The influence of land cover on Shuttle Radar Topography Mission (SRTM) elevations in low-relief areas, *Transactions in GIS*, 14(4):461–479.

Lehner, B., K. Verdin, and A. Jarvis, 2008. New global hydrography derived from spaceborne elevation data, *Eos Transactions*, AGU, 89(10):93–94.

Li, B., B. Pan, W. Cheng, J. Han, D. Qi, and C. Zhu, 2013a. Research on geomorphological regionalization of China, *Acta Geggraphica Sinica*, 68(3):291–306 (in Chinese).

Li, J., and D.W.S. Wong, 2009. Effects of DEM sources on hydrologic applications, *Computers, Environment and Urban Systems*, 34(3):251–261.

Li, S., D. Sun, M. Goldberg, and A. Stefanidis, 2013b. Derivation of 30-m resolution water maps from TERRA/MODIS and SRTM, *Remote Sensing of Environment*, 134:417–430.

Liu, Y., 2008. An evaluation on the data quality of SRTM DEM at the alpine and plateau area, north-western of China, *The International Archives of the Photogrammetry, Remote Sensing and Spatial Information Sciences*, XXXVII:1123–1127.

Miliaresis, G.C., and C.V. Paraschou, 2005. Vertical accuracy of the SRTM DTED level 1 of Crete, *International Journal of Applied Earth Observation and Geoinformation*, 7(1):49-59.

Miliaresis, G.C., 2008. The landcover impact on the aspect/slope accuracy dependence of the SRTM-1 elevation data for the Humbolt Range, *Sensors*, 8(5):3137–3149.

NASMG, 2002. *Industry Standard of the People's Republic of China CH/T1008-2001*, Foundational digital geographic information products: 1:10,000 and 1:50,000 digital elevation model, Standards Press of China, Beijing.

NASMG, 2008. *The National Standard of the People's Republic of China GB/18316-2008*, The examination rules and acceptance of digital surveying and mapping product, Standards Press of China, Beijing.

Neckel, N., J. Kropacek, T. Bolch, and V. Hochschild, 2014. Glacier mass changes on the Tibetan Plateau 2003-2009 derived from ICESat laser altimetry measurements, *Environmental Research Letters*, 9(1):014009.

Nelson, A., H.I. Reuter, and P. Gessler, 2009. DEM Production Methods and Sources, *Developments in Soil Science* (H. Tomislav and I.R. Hannes, editors), Elsevier, pp. 65–85.

NIGA, 2000. 1:1,000,000 *Wetland datasets of China, Environmental and Ecological Science Data Center for West China, Lanzhou*, URL: *http://westdc.westgis.ac.cn/data/447de2a9-7b95-4231-a9af-2aa3351e5cc8* (last date accessed: 11 November 2015)

Pieczonka, T., T. Bolch, J. Wei, and S. Liu, 2013. Heterogeneous mass loss of glaciers in the Aksu-Tarim Catchment (Central Tien Shan) revealed by 1976 KH-9 Hexagon and 2009 SPOT-5 stereo imagery, *Remote Sensing of Environment*, 130:233–244.

Rabus, B., M. Eineder, A. Roth, and R. Bamler, 2003. The shuttle radar topography mission - A new class of digital elevation models acquired by spaceborne radar, *ISPRS Journal of Photogrammetry and Remote Sensing*, 57(4):241–262.

Reuter, H.I., A. Nelson, and A. Jarvis, 2007. An evaluation of void filling interpolation methods for SRTM data, *International Journal of Geographical Information Science*, 21(9):983–1008.

Rodríguez, E., C.S. Morris, and J.E. Belz, 2006. A global assessment of the SRTM performance, *Photogrammetric Engineering & Remote Sensing*, 72(3):249–260.

Sesnie, S.E., P.E. Gessler, B. Finegan, and S. Thessler, 2008. Integrating Landsat TM and SRTM-DEM derived variables with decision trees for habitat classification and change detection in complex neotropical environments, *Remote Sensing of Environment*, 112(5):2145–2159.

Shi, Y., Y. Shen, E. Kang, D. Li, Y. Ding, G. Zhang, and R. Hu, 2007. Recent and future climate change in northwest China, *Climatic Change*, 80(3-4):379–393.

Shortridge, A., 2006. Shuttle Radar Topography Mission elevation data error and its relationship to land cover, *Cartography and Geographic Information Science*, 33(1):65–75.

Shortridge, A., and J. Messina, 2011. Spatial structure and landscape associations of SRTM error, *Remote Sensing of Environment*, 115:1576–1587.

Smith, B., and D. Sandwell, 2003. Accuracy and resolution of shuttle radar topography, *Geophysical Research Letters*, 30(9):1467.

Su, Y., and Q. Guo, 2014. A practical method for SRTM DEM correction over vegetated mountain areas, *ISPRS Journal of Photogrammetry and Remote Sensing*, 87:216–228.

Sun, W., Q. Shao, and J. Liu, J., 2013. Soil erosion and its response to the changes of precipitation and vegetation cover on the Loess Plateau, *Journal of Geographical Sciences*, 23(6):1091–1106.

Townshend, J.R.G.,C.O. Justice, C. Gurney, and J. McManus, 1992. The impact of misregistration on change detection, *IEEE Transactions on Geoscience and Remote Sensing*, 30(5):1054–1060.

Van Niel, T.G., T.R. McVicar, L. Li, J.C. Gallant, and Q. Yang, 2008. The impact of misregistration on SRTM and DEM image differences, *Remote Sensing of Environment*, 112:2430–2442.

Van Zyl, J.J., 2001. The Shuttle Radar Topography Mission (SRTM): A breakthrough in remote sensing of topography, *Acta Astronautica*, 48(5):559–565.

Verbyla, D.L., and S.H. Boles, 2000. Bias in land cover change estimates due to misregistration, *International Journal of Remote Sensing*, 21(18):3553–3560.

Verstraeten, G., 2006. Regional scale modelling of hillslope sediment delivery with SRTM elevation data, *Geomorphology*, 81(1):128–140.

Wang, H., and E.C. Ellis, 2005. Image misregistration error in change measurements, *Photogrammetric Engineering & Remote Sensing*, 71(9):1037–1044.

Wang, X., Z. Wang, and J. Fang, 2004. Mountain ranges and peaks in China, *Biodiversity Science*, 12(1):206–212 (in Chinese).

Wang, Y., J. Wang, Y. Qi, and C. Yan, 2005. *The Map of Desert Distribution in 1:100,000 in China*, Cold and Arid Regions Science Data Center, Lanzhou, URL: *http://dx.doi.org/10.3972/westdc.006.2013.db* (last date accessed: 11 November 2015).

Weydahl, D.J., J. Sagstuen, Ø.B. Dick, and H. Rønning, 2007. SRTM DEM accuracy assessment over vegetated areas in Norway, *International Journal of Remote Sensing*, 28(16):3513–3527.

Wu, L., and X. Li, 2004. *Dataset of the First Glacier Inventory in China*, Cold and Arid Regions Science Data Center, Lanzhou, URL: *http://dx.doi.org/10.3972/westdc.011.2013.db* (last date accessed: 11 November 2015).

Yang, L., X. Meng, and X. Zhang, 2011. SRTM DEM and its application advances, *International Journal of Remote Sensing*, 32(14):3875–3896.

Yang, Q., T.R. McVicar, T.G. Van Niel, M.F. Hutchinson, L. Li, and X. Zhang, 2007. Improving a digital elevation model by reducing source data errors and optimising interpolation algo-rithm parameters: an example in the Loess Plateau, China, *International Journal of Applied Earth Observation and Geoinformation*, 9(3):235–246.

Yang, Q., D. Jupp, R. Li, and W. Liang, 2008. Re-scaling lower resolution slope by histogram matching, *Advances in Digital Terrain Analysis* (Q. Zhou, B. Lees, and G. Tang, editors), Springer, Berlin Heidelberg, pp. 193–210.

Yang, Y., S. Shang, and L. Jiang, 2012. Remote sensing temporal and spatial patterns of evapotranspiration and the responses to water management in a large irrigation district of North China, *Agricultural and Forest Meteorology*, 164:112–122.

Zandbergen, P., 2008. Applications of Shuttle Radar Topography Mission elevation data, *Geography Compass*, 2(5):1404–1431.

Zhao, J., Y. Chen, Y. Han, Z. Li, Y. Liu, and W. Li, 2003. *Physical Geography of China*, Higher Education Press, Beijing (in Chinese).

Zhou Q., and X. Liu, 2004. Error analysis on grid-based slope and aspect algorithms, *Photogrammetric Engineering & Remote Sensing*, 70(8):957–962.

(Received 01 November 2014; accepted 05 June 2015; final version 28 July 2015)

A Region-Line Primitive Association Framework for Object-Based Remote Sensing Image Analysis

Min Wang and Jie Wang

Abstract

In this study, we propose a novel region-line primitive association framework (RLPAF) for OBIA. In this framework, segments (region primitive) and straight lines (line primitive) are obtained by image segmentation and straight line detection, respectively, before their corresponding intra-primitive features are extracted. An association model is built on inter-primitive topology and direction relationships. Several region-line collaborative features are also derived. Image analysis is then performed based on both region and line primitives. The advantage of RLPAF is the collaborative utilization of complementary information between regions and lines throughout the entire OBIA process: from image segmentation, to feature extraction, and finally, object recognition. To validate this framework, RLPAF is applied on road network extraction from high spatial resolution (HSR) remote sensing images. Experiments show that the proposed framework and methods refine primitive shape and spatial relationship analyses, as well as obtain higher method accuracy, than OBIAs based on only regions.

Introduction

Object-based image analysis (OBIA) has become a routine technique for extracting information from HSR images. Representative commercial OBIA software systems include Trimble Worldwide's eCognition and the ENVI Feature Extraction module. Compared with traditional pixel-based image analysis (PBIA), the minimum analyzing units in OBIA are generally regions (or segments from the viewpoint of image segmentation) that are composed of mutually related pixels. In this study, we mainly use the term "region" because the analyzing units in the proposed technical framework can also be obtained using other methods aside from image segmentation, e.g., by utilizing geographic information system data. Compared with PBIA, OBIA utilizes more abundant features (e.g., texture, shape, and spatial relationship) among objects. In addition, it facilitates the fusion of knowledge rules in image processing and analysis. Thus, OBIA may be a better choice than PBIA for extracting information from HSR images (Benz *et al.*, 2001; Benz *et al.*, 2004; Blaschke, 2010; Blaschke *et al.*, 2014).

Image segmentation plays a critical role in OBIA because high-quality segments serve as the foundation for succeeding analyses. Meinel and Neubert (2004) compared segmentation methods used in several OBIA software systems and found that the best among them is multi-resolution segmentation (MRS) (Baatz and Shäpe, 2000). Moreover, many studies have been conducted to improve the performance of MRS. Typical schemes include applying automatic approaches to a best-scale selection (Drăguţ *et al.*, 2010 and 2014; Tullis *et al.*, 2010; Tong *et al.*, 2012) or using several auxiliary data sources, including geographic information system databases, digital maps, and LiDAR data (Smith and Morton, 2010; Anders *et al.*, 2011). Furthermore, different kinds of segmentation methods (e.g., combining edge and region information) have also been suggested (Kermad and Chehdi, 2002; Li *et al.*, 2010; Lin and Chen, 2010; Chen *et al.*, 2012; Yu *et al.*, 2012). Thus, we proposed the hard-boundary constrained image segmentation (HBC-SEG) method, which exhibited many advantages over MRS, particularly in region boundary precision (Wang and Li, 2014). We further reduced the over-segmentation errors of HBC-SEG through a novel collinear and ipsilateral neighborhood (IPSL-neighborhood) model based on region and straight line relationship modeling (Wang *et al.*, 2015).

Abundant features can be obtained based on regions after image segmentation. Commonly used features include region spectra, shapes, textures, and spatial relationships at the same scale or at different scales. Based on these features and flexible classification rules, OBIA can potentially achieve more accurate classification than traditional PBIA for HSR images. OBIA generally uses supervised or rule-based classification schemes to classify images. Common tools include nearest neighbors, support vector machines (SVMs), and fuzzy rule-based classifiers.

Numerous studies on OBIA applications have been conducted based on the aforementioned technical framework. Typical cases include image classification (Gao *et al.*, 2011; Laliberte *et al.*, 2012; Salehi *et al.*, 2012; Du *et al.*, 2013; Rasi *et al.*, 2013), thematic information extraction or object recognition (Walter 2004; Huang and Zhang, 2008; Hu and Weng, 2011; Sebari and He, 2013; Benarchid and Raissouni, 2013; d'Oleire-Oltmanns *et al.*, 2014), and change detection (Johansen *et al.*, 2010; Lu *et al.*, 2011; Hebel *et al.*, 2013). Man-made object classification or recognition is common when HSR images are used. This phenomenon is jointly decided by the booming of HSR images, which changes application requirements, and the technical features of OBIA, which are suitable for such kinds of application. High-quality image segmentation, robust classification rules, and minimum algorithm parameter dependency are important issues that should be solved to promote the practicability of these methods.

Despite their diverse technical details, common OBIA applications generally follow the "segment and then classify" framework. In this framework, the minimum analyzing unit (region) is determined after an image is segmented. Then, subsequent analyses are implemented in regions. Several OBIA studies have combined image segmentation and classification in flexible schemes, which weakens the role of initial segmentation. For example, in Tiede *et al.* (2010 and 2011), segmentations were also tailored at a later stage for specific classes or regions in the image when required in the classification process. However, the region-based analysis framework has been completely adopted in the aforementioned studies. Although

Key Laboratory of Virtual Geographic Environment (Nanjing Normal University), Ministry of Education, Nanjing, Jiangsu, P.R. China, 210023; and the Jiangsu Center for Collaborative Innovation in Geographical Information Resource Development and Application, Nanjing, Jiangsu, P.R. China, 210023 (sysj0918@126.com; wangjieyl@sina.com).

Photogrammetric Engineering & Remote Sensing
Vol. 82, No. 2, February 2016, pp. 149–159.
0099-1112/16/149–159

doi: 10.14358/PERS.82.2.149

regions are superior to pixels in many aspects, regions remain limited in other aspects. For example, image edges, which are critical in spatial information, are not considered during common OBIAs. Image edge lines generally denote object boundaries or borders and exhibit strong semantic connotations. However, region boundaries obtained by image segmentation do not necessarily match image edge lines in quantity and location. Thus, the use of image edges in OBIA should be enhanced to improve the performance of this technique.

In general, man-made objects are important targets when extracting information from HSR images. Compared with natural objects, man-made objects frequently have distinctive shapes, e.g., straight line-shaped boundaries. Thus, straight edge lines are used in this study. The information integration of edges and regions is not a new concept in the field of image processing. Several studies have combined these two elements to improve segmentation. However, the current study presents a distinctive scheme of "region and line integration" for OBIA. To improve performance, regions and lines are used collaboratively throughout the entire technical chain of OBIA, i.e., from low-level image processing (segmentation) and feature extraction to high-level image analysis (classification and recognition). Under this framework, several new analysis techniques for object shapes and relationships have been designed. In addition, we have designed a scheme for road network extraction from HSR images to validate the framework. In our experiments, these techniques have exhibited superiority over common OBIAs, which demonstrates the application values of the proposed framework.

The rest of this paper is organized as follows. The next Section presents the proposed technical model, including region and line primitive extraction, feature calculation, and relationship modeling, followed by a discussion of a case study of the framework, which proposes the road extraction scheme. The framework and the methods are also validated through several experiments in this section. The final Section provides a summary of the study.

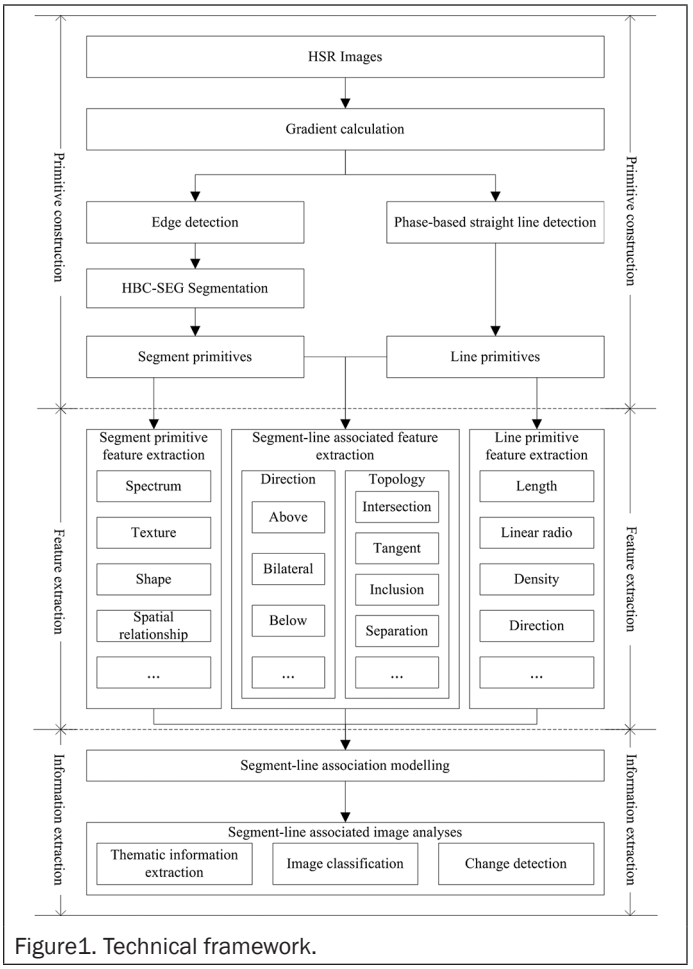

Figure1. Technical framework.

Methods

In a previous study (Wang *et al.*, 2015), we proposed a novel IPSL-neighborhood model based on region and line relationship modeling, which further refined HBC-SEG and reduced its over -segmentation errors. In the current study, region and line relationship modeling is systemically extended and improved. Several new concepts, indices, and operators are derived, which facilitate subsequent OBIA steps, including feature extraction and classification. Thus, the extended technical model is called region-line primitive association framework (RLPAF) for OBIA. We call region and line "primitive" because both are utilized as the basic analyzing units for subsequent image analyses. Then, we apply RLPAF on road network extraction from HSR images to validate the ideas and techniques.

Technical Framework of RLPAF

The region-line primitive association framework (RLPAF) is presented in Figure 1. First, region primitives are obtained from HBC-SEG, which also produces image gradients (Wang *et al.*, 2015). The gradient map is regrouped into line support regions through Burn's phase-grouping method (Burns *et al.*, 1986), and straight lines are then detected. Multiple region and line features, including the spectra and shapes of the regions as well the lengths and directions of the lines, are calculated. Region and line topologies as well as their orientation relationships are then calculated to build the association model. Several kinds of OBIAs, including thematic information extraction, image classification, or change detection can be conducted by using the aforementioned two kinds of primitives. In the proposed framework, regions and lines are highly integrated across the entire OBIA process through image segmentation, feature extraction, and high-level image analysis.

Region and Line Primitive Extraction

In this technique, the Canny edge detection method (Canny, 1986) initially extracts image edges. Then, the edges are embedded into watershed segmentation (Vincent and Soille, 1991) for initial image segmentation. The initial sub-regions (i.e., the bases of subsequent merging) are obtained after edge allocation. Subsequently, edge-constrained merging iteratively combines the sub-regions until all merging costs exceed a maximum threshold, which produces the initial regions. Non-constrained merging that is controlled by a significantly small threshold converts the initial regions into final regions. First-stage merging allows the growth of regions but is limited by image edges. In the second stage, trivial regions are removed by merging them with one another or into large regions. HBC-SEG exhibits good segmentation accuracy, including over- and under-segmentation accuracies. The region boundary obtained using this method is highly consistent with the actual boundaries (edges) of spatial objects, which facilitates the modeling of region and line relationships.

Based on the gradient map obtained using HBC-SEG, straight edge lines are detected using the phase-grouping method. This method is based on phase (gradient orientation) and is different from the edge-based straight line detection method. Pixels with the same phases are grouped into regions, and the center straight lines of the regions are obtained by least squares fitting. This method can extract the so-called weak-contrast straight lines from images because phase is used for line detection instead of gradient. In principle, this method is fast and concise. Straight line features, including lengths, directions, and densities, are calculated for use in subsequent analyses.

Region-Line Association Modeling

We classify the direction relationships of a region to a line as "above," "bilateral," and "below." These classifications indicate that the region is located above the line, on the two sides of the line, and below the line, respectively. In particular, if the line is vertical, then "above" denotes the right side of the line. The topology of a region to a line includes separation, intersection, tangent, and inclusion. The last is regarded as a special case of intersection. The combination of different direction and topology relationships creates several region-line relationships. Relationships, in which regions and lines are in contact (including the topologies of intersection, tangent, and inclusion), are more important than cases where they are separated. Thus, the following model is mainly built for cases in contact.

Let regions Q and R be two subpixel sets within image I. $Q = \{q_i = (x_i,y_i) \mid i \in [1,k],\ k = |Q|\}$ and, $R = \{r_i = (x_i,y_i) \mid i \in [1,k],\ k = |R|\}$where x and y are the pixel coordinates, and $|\cdot|$ is the potential of a set. Let straight line segment L be a pixel set in I: $L = \{l_i = (x_i,y_i) \mid i \in [1,k],\ k = |L|\}$. L fits the following straight line equation where a and b are the coefficients:

$$Z_L = y - ax - b = 0, \tag{1}$$

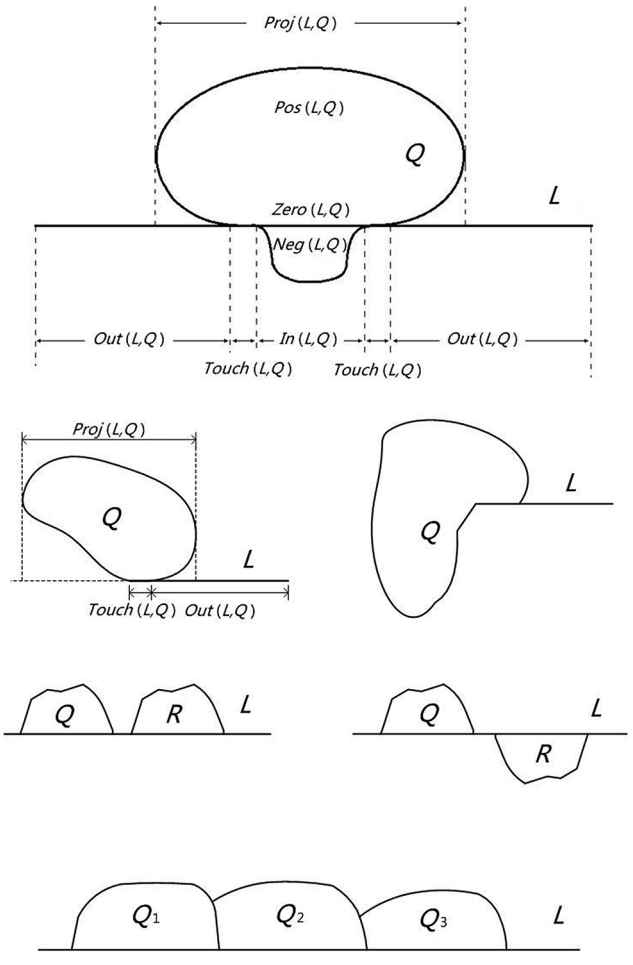

Figure 2. Region–line relationship modeling. (a) A pair of touching region and line. (b) A unilateral case that does not satisfy Equation 7. (c) A tangent relationship that is not unilateral. (d) An IPSL-neighborhood relationship. (e) Regions that are not IPSL-neighbors because they are located bilaterally to line L, and (f) An IPSL chain.

Regions Q and R need to intersect line L as follows:

$$Q \cap L \neq \emptyset,\ R \cap L \neq \emptyset \tag{2}$$

As shown in Figure 2a, we define the direction and topology operator sets, which work on regions and straight lines and produce their subsets. The direction operator set is defined as follows:

$$Dir(Q,L) = \{Neg(Q,L),\ Zero(Q,L),\ Pos(Q,L)\} \tag{3}$$

which denotes a subset extracted from Q that is located above, on, or below line L. For example, operator $Neg(Q,L)$ is defined as follows:

$$Neg(Q,L) = \{q_i = (x_i,y_i) \mid y_i - ax_i - b < 0\} \tag{4}$$

The other two operators exhibit similar forms. Let B_Q be the boundary pixels of Q defined by four connected neighborhoods. We define the topology operator set as follows:

$$Top(L,Q) = \{In(L,Q),\ Touch(L,Q),\ Out(L,Q),\ Proj(L,Q)\}. \tag{5}$$

The first three operators denote a subset extracted from L, which is contained by, touched by, or outside Q. For example, operator $Touch(L,Q)$ is defined as follows:

$$Touch(L,Q) = \{l_i \mid l_i \in B_Q, l_i \in L\}. \tag{6}$$

Operator $Proj(L,Q)$ denotes the straight line segment obtained by vertically projecting Q onto L, as shown in Figure 2a and 2b.

Concepts based on Region-Line Association Model

A set of line-based concepts is proposed and used in subsequent OBIAs. In general, the line should be long and the projected length of the intersecting region should not considerably exceed those of the parts of the line that fall within and intersect the region to investigate only meaningful relationships between a pair of region and line. That is,

$$|L| \geq T_a \tag{7-1}$$

$$\text{and } \frac{|Proj(L,Q)|}{|In(L,Q)| + |Touch(L,Q)|} \leq T_b, \tag{7-2}$$

where T_a and T_b are two user defined thresholds. Based on Equation 7, the following concepts or indices are defined by considering the topology and directional relationships among regions and lines.

1. Unilateral and Tangent Relationship

Region Q is unilateral to line L if it satisfies Equation 8, as follows:

$$|Pos(Q,L)| + |Zero(Q,L)| = |Q| \text{ or } |Neg(Q,L)| + |Zero(Q,L)| = |Q|. \tag{8}$$

The combination of Equations 2 and 8 indicate that $|Zero(Q,L)|$ is not zero. In this case, region Q is also tangent to line L in topology. Thus, region Q is called unilateral and tangent to L. Considering the possible errors in image segmentation and straight line extraction, the aforementioned conditions are relaxed. Q is unilateral and tangent to L when threshold T_c is close to 1.0, that is,

$$\frac{\left|Pos(Q,L)\right|+\left|Zero(Q,L)\right|}{|Q|}\geq T_c \quad (9\text{-}1)$$

$$\text{or } \frac{\left|Neg(Q,L)\right|+\left|Zero(Q,L)\right|}{|Q|}\geq T_c. \quad (9\text{-}2)$$

A tangent topology does not guarantee the unilateral relationship of a region to a line, as shown in Figure 2c.

2. Ipsilateral Neighbors

If both regions Q and R satisfy Equation 9 and are located along the same side of line L, then they are named ipsilateral neighbors with respect to L (IPSL-neighbors), as illustrated in Figure 2d. Regions Q and R are not necessarily direct neighbors, i.e., they share a common boundary. Multiple IPSL-neighborhood relationships between regions Q and R are possible, with respect to multiple correlated straight lines. Intuitively, spatial objects are highly related with one another, i.e., semantically homogeneous, if they are arranged in a semantically meaningful configuration (e.g., a straight line). In this case, the regions should be located on the same side of a straight line, which is a powerful and meaningful spatial constraint.

3. Ipsilateral and Homogeneous Chain

Suppose a chain is composed by a set of regions, which is formed as Q_1, Q_2, …, Q_n, in which each region in the chain is a direct neighbor of the previous region, as illustrated in Figure 2f. If these regions exhibit some form of homogeneity and are all IPSL-neighbors with respect to line L, then the chain is labeled as an ipsilateral and homogeneous chain (IPSL-H chain). Q_1 and Q_n are two nodes in this chain. The regions in the IPSL-H chain are apparently highly related with one another because the chain is constrained by similar attributes, a specific shape, and an unbroken structure.

4. Line-Based Length-to-Width Ratio

The shape feature of the length-to-width ratio (*LW*) is defined as the length (l) versus the width (w) of the minimum bound rectangle (MBR) of an object, i.e.,

$$LW = l/w. \quad (10)$$

Linear objects can be extracted when they have large *LW* values. However, measuring *LW* may not yield precise results for linear but irregularly shaped objects. Thus, the line-based length-to-width ratio (LBLW) is defined as follows. Suppose we have a line L tangent to region Q, as illustrated in Figure 3. We move line L stepwise along its perpendicular direction and record the position where $|In(L,Q)|$ declines dramatically. The moving steps w_2 is the line-based width (*LBW*) of Q with respect to line L, $|Proj(L,Q)|$ is the line-based length (*LBL*), and LBLW is defined as *LBL* versus *LBW*, as follows:

$$\text{LBLW} = |Proj(L,Q)|/w_2. \quad (11)$$

Similar to an IPSL-neighborhood relationship, a region can have multiple LBLW measures based on its multiple tangent straight lines. Thus, irregular shapes can be described in objective and precise manners.

5. Region and Line Mutual Conversions

The following operations on region-and-line mutual conversion are defined to extend spatial relationship analyses between regions and lines.

Region-to-Line Conversion

Given a region Q and its contacting line set $\{L\}$, region-to-line conversion is defined as the operation that extracts a subset from $\{L\}$ with respect to specific constraints. Typically, extracting a subset of $\{L\}$, which is tangent to region Q and parallel to the main axis of Q (if Q has one), may be a useful region-to-line conversion, which is applied in the case study.

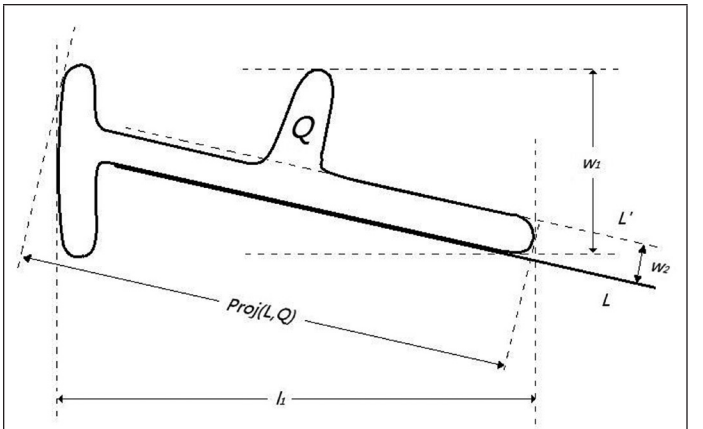

Figure 3. Line-based length-to-width ratio.

Line-to-Region Conversion

Given a straight line L and its contacting region set $\{Q\}$, line-to-region conversion is defined as the operation that extracts a subset from $\{Q\}$ with respect to specific constraints. For example, regions in the subset may be constrained to be located on the same side of and tangent to line L, which indicates that only the IPSL–neighbors within $\{Q\}$ are retrieved.

Line-to-Line Conversion

Given a straight line L and its neighboring straight lines $\{L^*\}$, line-to-line conversion is defined as the operation that extracts a subset from $\{L^*\}$ with respect to specific constraints. The neighboring relationship between two straight lines is defined based on they both intersect the same region. As a typical case, the extraction of straight lines parallel to L is applied in the case study.

Case Study of RLPAF

Region and line primitives, as well as their mutual relationships in image classification or information extraction, can be comprehensively applied based on RLPAF. In this study, an example on a road network extracted from HSR images is provided. In impervious surface classification from HSR images, roads and buildings are sometimes difficult to distinguish between each other when they are composed of similar materials. However, roads exhibit typical linear features, and thus, road regions obtained by image segmentation frequently have high *LW*s. In the OBIA framework, shape features (typically measured in *LW*), along with the spectral signature, serve as important clues in extracting linear features such as roads. In image segmentation, however, roads are not always segmented into ideal, high *LW* regions because of over-segmentation errors and road appearance changes. A significant number of true road regions are lost if judging is only based on high *LW*s. In addition, MBR-based *LW* is limited when linear features are irregularly shaped (e.g., with high curvatures or many forks).

Thus, we designed an RLPAF-based road-extraction method (Figure 4). The method combines two processes, namely, first-level supervised classification and second-level rule analysis. To separate an impervious surface from other ground features, coarse-grained supervised classification based on region spectral signatures was initially performed. Only three classes were specified: water body, vegetation and others, and impervious surface. First-level classification helps distinguish roads from other linear features in second-level rule-based classification, e.g., rivers and channels. Additional features, including region textures, shapes, or statistics on straight lines, may

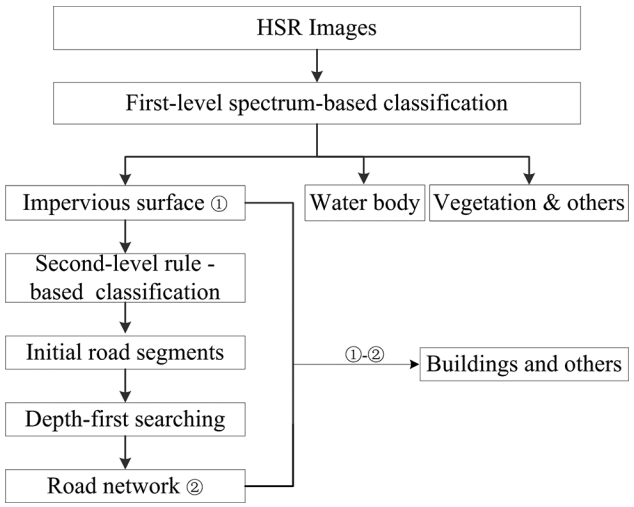

Figure 4. Impervious surface classification and road extraction.

Algorithm 1. Pseudo-codes of the Depth Searching Road Network Algorithm.

Input: Thresholds of LBLW (T_1), *LBW* (T_2), and straight line length (T_3)
For each region, P_1 in the impervious surface with an LBLW that is larger than T_1 (with respect to straight line L_1) and an *LBW* that is smaller than T_2
  Mark P_1 as road;
Set all straight lines parallel to L_1 (including L_1) as {*L*}, which are tangent to P_1 and are longer than T_3; *//region-to-line conversion; use these lines to search neighboring road regions.*
 For each straight line L_2 in {*L*}
  Within the impervious surface, get the IPSL–neighbors of P_1 with respect to L_2 with *LBW*s less than T_2 and form set {*P*}; *// line-to-region conversion; search possible road regions with small* LBLW*s but suitable LBWs.*
  For each P_2 in {*P*}
   Mark P_2 as road;
Get all straight lines parallel to L_2 that are tangent to P_2 and longer than T_3, and add these lines to {*L*}; *//line-to-line conversion; depth searching along L_1, L_2, and succeeding lines can continue…*
  End For
 End For
End For

Table 1. Experimental data

Experimental area	Image type	Image resolution	Image size (pixels)	Data description
Area 1	ALOS multi-spectral image with four bands	10 m	576 × 493	Collected in February 2007 in Jiangning, Nanjing, China
Area 2	China's GF-1 multi-spectral image with four bands	8 m	1013 × 1032	Collected in 2014 in Jiajiang, Nanjing, China

be considered for first-level classification. However, classification accuracy was not increased significantly by these features in our experimental areas. In addition, the proposed scheme was mainly designed for validating RLPAF on road extraction, and classification accuracy on impervious surfaces was not the main focus. Thus, the most simple classification scheme was designed for first-level impervious surface extraction.

Second-level rule-based classification extracts high LBLW segments within an impervious surface as roads. The proposed method utilizes spectra and shape features comprehensively through the two-level classification scheme and exhibits better performance than OBIA that uses a common *LW* feature. However, the aforementioned procedure cannot extract road regions with low LBLWs. Road borders can be extracted or fitted piecewise as straight lines because roads are generally man-made linear features with even widths and directions. Moreover, these lines possibly span several regions (called IPS-neighbors in this study). Straight lines can serve as direction guides for searching road regions with low LBLWs. Thus, a straight line-guided depth-searching step was designed to extend initial, broken road regions into a road network. This searching step involves several region-to-line, line-to-line, and line-to-region conversions, which are mainly based on IPSL-neighborhood relationships. Road regions with low LBLWs and sufficient *LBW*s are appended and formed the final road network. The pseudo-codes of the road searching step are presented in Algorithm 1.

Experiments

Experimental Data

The proposed technical framework and algorithm was implemented with Visual C++ 2010. The operating system used was Windows-7 with an Intel(R) Xeon(R) E5620 2.40 GHz CPU and 3.48 GB RAM. The methods were applied in different HSR images for validation. Two experimental areas were selected for method illustration. Table 1 shows the image type, resolution, size, imaging date, and location of the two test areas.

Experimental Procedure

Commonly used measures, including *Recall*, *Precision*, and *F-measure*, were employed to evaluate road-extraction accuracy.

$$Recall = \frac{TP}{TP + FN}$$
$$Precision = \frac{TP}{TP + FP} \quad , \qquad (12)$$
$$F - measure = \frac{2 \times Precision \times Recall}{Precision + Recall}$$

where *TP* is the number of true positives; *FP* is the number of false positives; *FN* is the number of false negatives; and *F-measure* is a combination of precision and recall, which is a harmonic mean of the two measures. An ideal road extraction method should have high precision and recall ratios. In practice, however, *Precision* and *Recall* measures are generally in conflict with each other. Thus, *F-measure* was used as the comprehensive index to evaluate method performance in our experiments. After segmentation, we first screened out "real" road segments by visual interpretation and compared the machine-extracted roads with their visual counterpart to evaluate method accuracy. In visual interpretation, if a segment has over 50 percent road pixels, then the segment is marked as a road. This scheme excludes the influence of segmentation on evaluating road extraction accuracy.

After image segmentation and straight line extraction, segment-and-line relationships were built, which involved three inputs. T_a is equal to 15, which indicates that straight lines shorter than 15 pixels are not considered. T_b is equal to 3.0, which indicates that the projected lengths of segments should be less than thrice their contained and intersected straight lines. T_c is equal to 0.90 for the unilateral and tangent relationships of segments. These inputs were specified by sample testing and were used as uniform default inputs in all experimental analyses.

We designed the following experimental procedure to validate the proposed method on road extraction. An impervious surface was first extracted from HSR images by first-level supervised classification using region spectral features. Then, three road extraction schema, i.e., using common *LW* measure (the LW method), LBLW measure (the LBLW method), and LBLW measure combined with depth searching (the LBLW&DS method), were applied on the impervious surface to select road regions with *LW*s or LBLWs that exceeded a threshold (*T*). For all three methods, a high threshold *T* excluded many false roads (i.e., *Precision* measure increases) than a low *T*, whereas the chance of omitting real roads increases (i.e., *Recall* measure decreases). Thus, threshold *T* was adjusted from low to high, and the *precision-recall* and *F-measure* curves of the three methods were drawn to evaluate their robustness during threshold changes.

In HBC-SEG method, regions are generally merged to their extreme sizes (the edge position) under small scales. The smallest default scale of 10 was used for all image segmentations in our experiments. Regions were then classified using an SVM classifier with Gaussian radial basis function (RBF) kernels. The Gaussian RBF kernels had a penalty factor *C* of 25 and a kernel width σ of 40. The region spectral mean values of all image bands were used in classification. A minimum amount of training samples were selected for SVM classification if the impervious surfaces were extracted totally. The classification results were not edited and possible errors were left. Second-level road extraction was conducted directly on the extracted impervious surfaces for an objective method evaluation.

The inputs for second-level road extraction were as follows: threshold *T* ranging from 2.5 to 4.5, with a step of 0.5. For the LBLW method, a region was extracted as roads if its *LW* or LBLW was larger than *T*. Thus, the result obtained by the LBLW method was a superset of the results obtained by the LW method. The results of the LBLW&DS method, which integrated a depth-searching step into the LBLW method, formed a superset of the LBLW results. The road width threshold T_2 was 16 pixels. All inputs were fixed in all experiments.

For each of the experimental areas, training samples were selected thrice, the corresponding first- and second-level classifications were performed, average accuracy measures were obtained, and accuracy curves were drawn. The regions obtained in image segmentation could have different sizes, and thus, method accuracy was evaluated in two ways, namely, by counting the road region number and by summing up the road region areas, for a comprehensive comparison.

Experimental Analyses

The quantitative results of road extraction are prsesented in Table 2 and Figure 5. Accuracy in the two experimental areas was evaluated by region number and area, and the results exhibited slight differences, which led to the same conclusion. Given a threshold *T*, the recall ratios of the three methods were LBLW&DS > LBLW > LW, whereas their precision measures were reversed as LW > LBLW > LBLW&DS. These results were reasonable because the region sets obtained by the three methods were LW⊆LBLW⊆LBLW&DS. For the LBLW and LBLW&DS methods, the risk of including false road regions increased as the number of included true road regions rose. Errors resulted because some false roads might have large LBLWs. In addition, the depth-searching step of the LBLW&DS method was mainly based on road ductility along several straight lines, which unavoidably included some false road regions with small LBLWs that were attached to these straight lines. These errors were more apparent in urban areas than in rural areas. However, the LBLW and LBLW&DS methods obviously performed better than the LW method on the *F-measure,* given the same threshold *T.* The compensation on *recall ratio* far exceeded that on *precision* loss when the LBLW and LBLW&DS methods were compared with the LW method. In addition, the LBLW&DS method had flat *F-measure* curves in all the experiments. Along with the increase in *T*, an increasing number of road regions were abandoned by the LBLW and LW methods, which caused the *F-measure* curves to decline. However, the LBLW method restored a significant number of regions through the depth-searching step, and thus, maintained high *F-measure* accuracy. In this scenario, the depth-searching process reduced algorithm parameter dependency and increased method robustness.

The *precision-recall* curves also verified the aforementioned conclusions. Given the same threshold *T,* the LBLW&DS method exhibited the lowest *precision* and the highest *recall*

Table 2. Accuracy of Road Extraction

Areas	Evaluation schemes	T	LW Method			LBLW Method			LBLW&DS Method		
			Precision	Recall	F-Measure	Precision	Recall	F-Measure	Precision	Recall	F-Measure
Area 1	Region number	2.5	0.587	0.442	0.504	0.576	0.624	0.599	0.542	0.696	0.609
		3.0	0.665	0.367	0.473	0.655	0.555	0.601	0.599	0.648	0.623
		3.5	0.739	0.304	0.431	0.718	0.472	0.569	0.643	0.591	0.616
		4.0	0.768	0.218	0.340	0.760	0.388	0.514	0.662	0.555	0.604
		4.5	0.831	0.161	0.270	0.833	0.313	0.456	0.690	0.519	0.593
	Region area	2.5	0.618	0.416	0.497	0.605	0.629	0.617	0.569	0.699	0.627
		3.0	0.692	0.350	0.465	0.676	0.565	0.616	0.625	0.652	0.638
		3.5	0.752	0.295	0.424	0.736	0.490	0.588	0.668	0.600	0.632
		4.0	0.763	0.222	0.344	0.765	0.417	0.540	0.684	0.571	0.622
		4.5	0.821	0.173	0.286	0.835	0.348	0.492	0.712	0.534	0.610
Area 2	Region number	2.5	0.536	0.425	0.474	0.510	0.542	0.525	0.495	0.671	0.569
		3.0	0.597	0.329	0.424	0.562	0.425	0.484	0.539	0.614	0.574
		3.5	0.643	0.255	0.365	0.617	0.342	0.440	0.565	0.566	0.565
		4.0	0.653	0.183	0.286	0.647	0.284	0.395	0.581	0.549	0.565
		4.5	0.694	0.134	0.224	0.674	0.214	0.325	0.594	0.512	0.550
	Region area	2.5	0.528	0.426	0.472	0.497	0.561	0.527	0.477	0.681	0.561
		3.0	0.589	0.337	0.429	0.553	0.450	0.496	0.521	0.623	0.567
		3.5	0.637	0.264	0.374	0.605	0.374	0.462	0.549	0.577	0.563
		4.0	0.659	0.198	0.305	0.638	0.319	0.425	0.569	0.564	0.566
		4.5	0.697	0.151	0.248	0.670	0.247	0.362	0.584	0.529	0.555

ratio among the three methods, which caused its curves to be positioned in the upper left, as shown in Figure 5a, 5c, 5e, and 5g. The left-shift of the LBLW curves was smaller than that of the LBLW&DS curves, but exhibited an obvious up-shift compared with the LW curves. This finding denotes that the LBLW method exhibited a slight decrease in *precision* and an obvious increase in *recall ratio* compared with the LW method. Furthermore, if the *precision* measure was fixed, then the *recall ratio*s of the three methods were ranked as LBLW&DS > LBLW > LW. Meanwhile, if the *recall ratio* was fixed, then the *precision* measure was ranked in the same order. Analyses of the *recall-precision* curves also showed that both the LBLW&DS and LBLW methods were significantly superior to the LW method. The conclusions coincide with the results of the analyses of the *F-measure* curves.

In Table 2, *F-measure* was the highest when the LBLW threshold was 3.0. The corresponding classification results were selected for further visual interpretation and analysis. In the two experimental areas, impervious surfaces were extracted totally although several misclassifications with other classes were included. For example, the sands (bare lands) in the upper left corner of Plate 2a were misclassified as an impervious surface because they produced similar spectra as an impervious surface. First-level classification errors were also transmitted to second-level road extraction. Several false impervious surfaces in this corner were misclassified as roads by the LW and LBLW

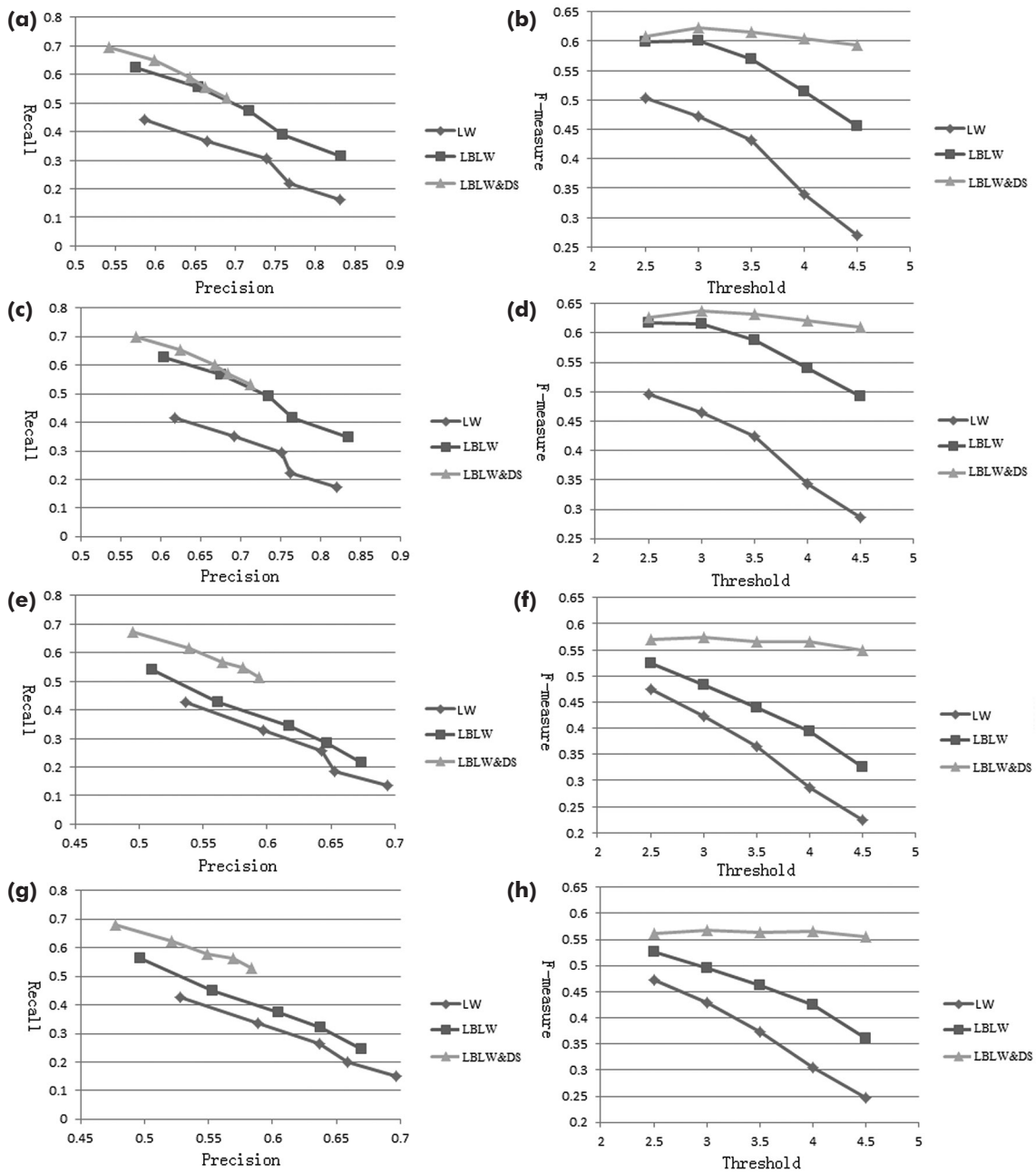

Figure 5. Accuracy analyses of the two experimental areas. (a) and (e) *Precision–recall* curves of areas 1 and 2, respectively, obtained by counting region number; (b) and (f) *F-measure* curves of areas 1 and 2, respectively, obtained by counting region number; (c) and (g) *Precision–recall* curves of areas 1 and 2, respectively, obtained by counting region area; and (d) and (h) *F-measure* curves of areas 1 and 2, respectively, obtained by counting region area.

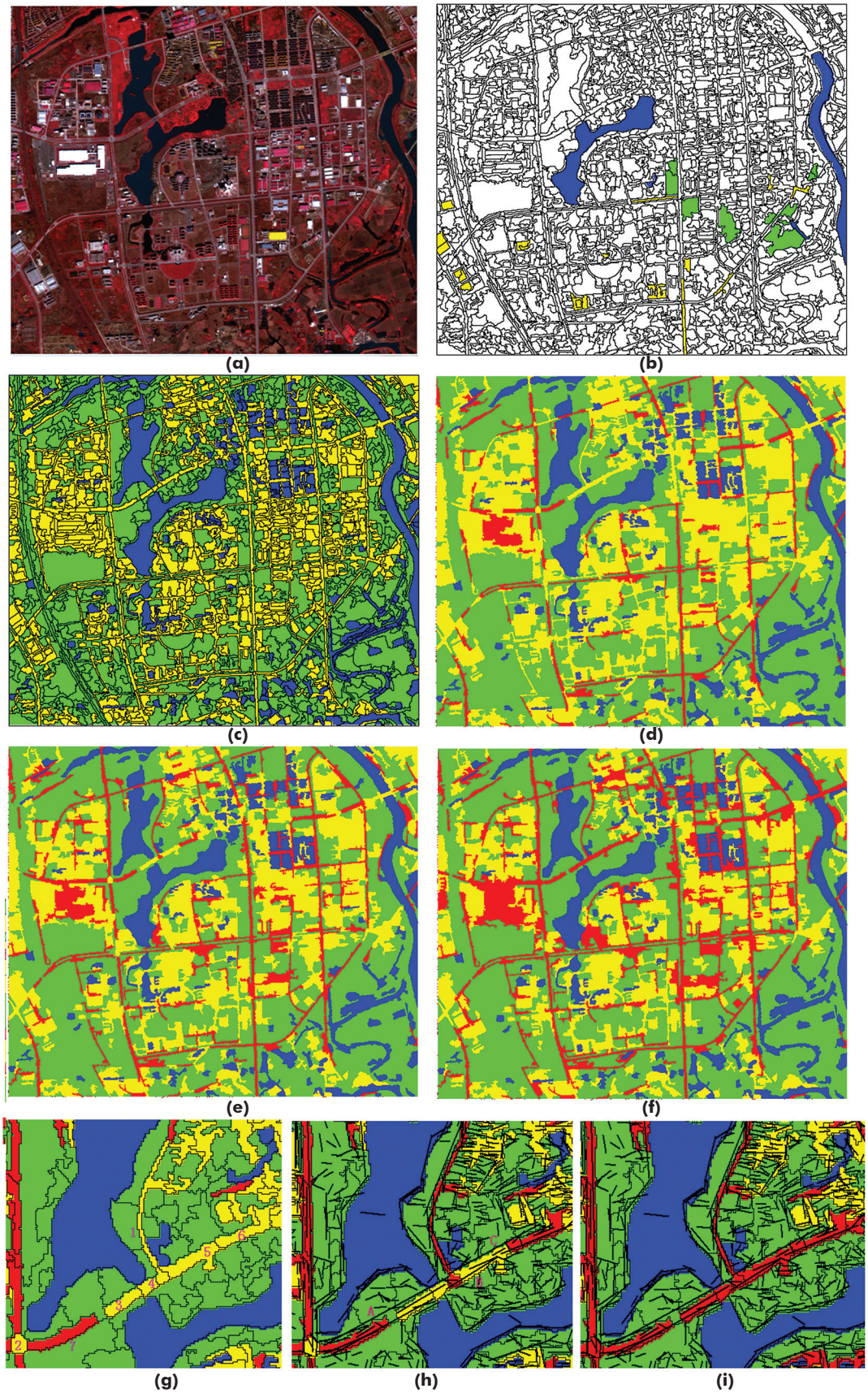

Plate 1. Experimental area 1: (a) Original data, (b) Segmentation results and training samples; (c) First-level spectrum-based classification, (d), (e), and (f). The red regions are roads extracted by the LW, LBLW, and LBLW&DS methods, respectively, (g), (h), and (i). The zoomed-in images of (d), (e), and (f), respectively.

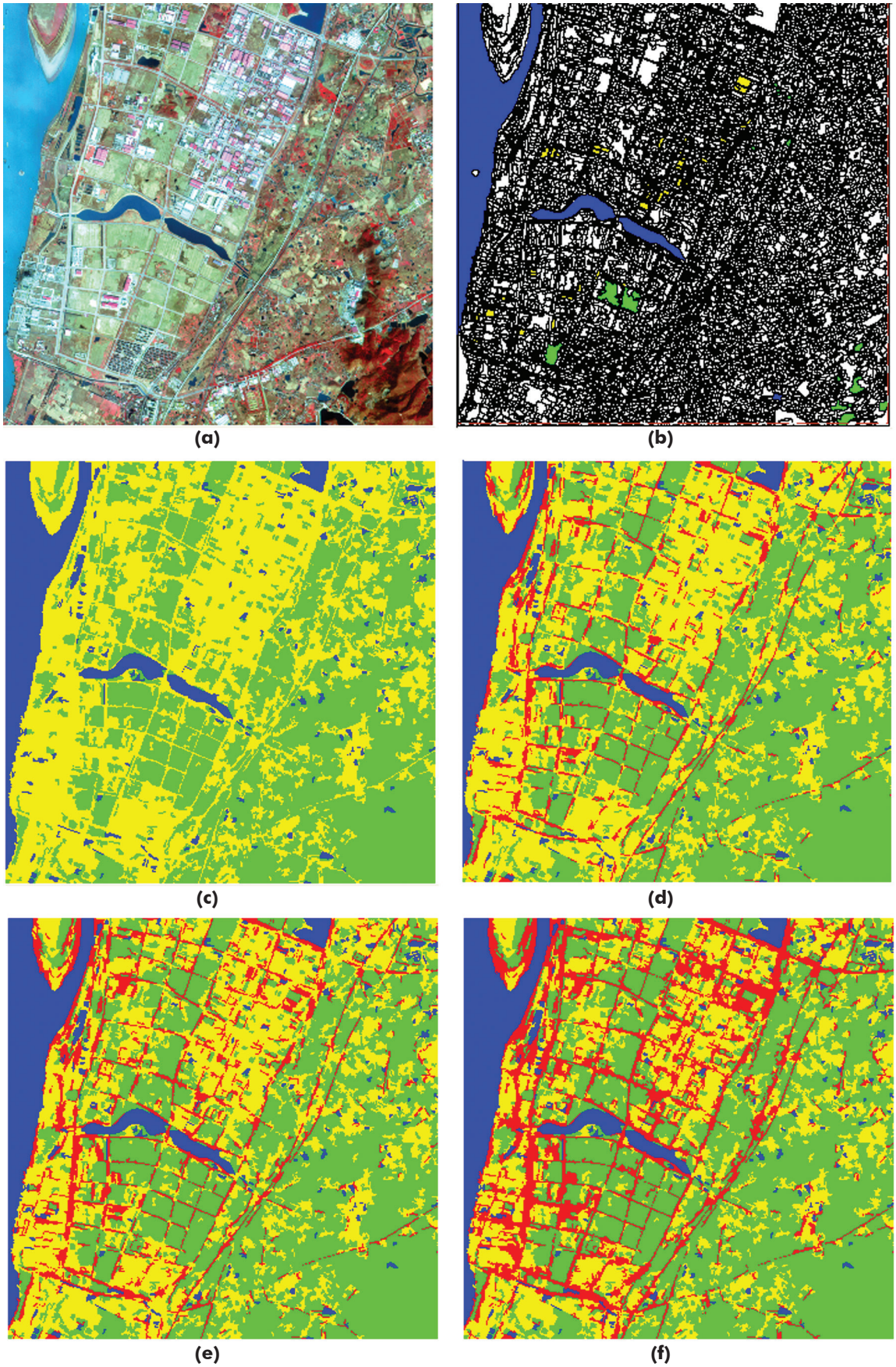

Plate 2. Experimental area 2: (a) Original data, (b) Segmentation results and training samples, (c) First-level spectral classification, (d), (e), and (f). The red regions are the roads extracted by the LW, LBLW, and LBLW&DS methods, respectively.

methods. After introducing the depth-searching process, these errors were magnified in the LBLW&DS method, as shown in Plate 2f. In the two experimental areas, the LW method retrieved the minimum road regions and formed a broken road network. The LBLW and LBLW&DS methods obtained significantly denser road regions and formed continuous road networks while inducing additional errors. Visual interpretation was completely coherent for the aforementioned quantitative analyses.

An enlarged section of experimental area 1 is shown in Plate 1g to 1i. In Plate 1g, a road intersection (region 2), parts of a horizontal road (regions 3 to 6), and an arc-formed road (region 1) were not extracted as roads because their *LW*s were less than 3.0. In Plate 1h, which illustrates the LBLW method, straight lines overlap onto regions. The LBLW of region 1 was larger than 3.0 based on the straight lines fitted on the edge lines. Similarly, the LBLW of region 6 was larger than 3.0, which was calculated based on the below tangent straight line. Thus, regions 1 and 6 were classified as roads by the LBLW method. However, road regions 3, 4, and 5 were not extracted as roads by the LBLW method because neither their *LW* nor their LBLW reached 3.0.

Such defects of a broken road were solved by the depth-searching process. For example, region 7, which was extracted as road by the LBLW method, acted as the starting point of depth searching for neighboring road regions in the LBLW&DS method. First, a tangent straight line (A) of region 7 was fetched (region-to-line conversion). This line served as the direction guide for the next possible road regions, and thus, regions 3 and 4 were found. Region 3 did not share a common boundary with region 7 because of some segmentation errors, which would fail in common neighborhood searching. However, the depth-searching process successfully overrode the gap and fetched regions 3 and 4 (line-to-region conversion) because these regions were located on the same negative side of straight line A and were IPSL-neighbors. These regions were accepted as members of the road network because they were classified as impervious surface in the first-level classification and had suitable LBLWs.

By contrast, neighboring parallel lines B and C were fetched from line A (line-to-line conversion). Based on the IPSL-neighborhood relationships with respect to lines B and C, the impervious surface region 5 was retrieved and extracted as road (line-to-region conversion). The depth-searching process, which involved the aforementioned conversions between regions and lines, were iteratively performed from the left and right sides of region 7 along the straight line direction until no IPSL-neighbor was found, which resulted in a complete road. Region 2 was also extracted as a road by another depth-searching process that was conducted from the vertical direction. In the experiments, straight lines played at least two important roles. (a) Region shape analysis became more accurate than that in common region only-based OBIA, and (b) The line-based, depth-searching process offered precise directions and the capability to override gaps. These advantages exhibited the feasibility and superiority of the proposed technical schemes.

However, the road network obtained by the proposed method remained imperfect. For example, defects such as broken roads and burrs, as shown in Plates 1f and 2f, were commonly found in urban areas with complex backgrounds. These defects were comprehensively caused by possible segmentation and classification errors, as well as the simplicity of current road-extraction rules. Sophisticated OBIA rules or processing are necessary to improve the accuracy of road extraction, particularly in urban areas. Nevertheless, the proposed scheme can serve as an initial step for road extraction because of its simplicity and effectiveness. A more precise road extraction technique may be achieved based on this scheme and by including additional optimization steps. In particular, a set of continuous road regions may form a homogeneous IPSL-H chain. Short chains can be trimmed by calculating the chain length because roads are generally long. Furthermore, by checking whether the nodes of a chain touch other roads, dangle chains can also be trimmed because roads are generally connected. In addition, the IPSL-H chain may also be used to smoothen road regions and remove blurs because roads generally have a fixed width, and thus, a set of regions provides more optical clues than a single region when estimating road width. In addition to these extensions, factors that include occlusions by other ground objects (e.g., high and large buildings, trees, and shadows) and highly complex road shapes (e.g., multiple overpassed road intersections), may also be considered to improve road extraction. Considering that this study mainly focused on validating RLPAF, particularly several of its derived concepts and operators, complex spatial constraints and rules were not investigated comprehensively. The extracted road network still exhibited many defects and might only serve as an initial extracted result for subsequent refinement. In the future, the aforementioned spatial relationships should be considered for a mature OBIA-based road extraction system.

Conclusions

In this study, we propose RLPAF to extract information from remote sensing images. This framework comprehensively utilizes line and region primitives in OBIA by image segmentation, straight line detection, and region-line relationship modeling. The proposed framework is then applied and validated in extracting road networks from HSR images. In this framework, regions and lines are closely integrated throughout the entire OBIA process. During image segmentation, lines (edges) are first embedded into sub-region merging as spatial constraints, which outputs regions with precise boundaries. During feature extraction, the direction and topology features of regions and lines are used to build the association model. Then, several newly formed region-line associated features are derived. During the information extraction stage, region and line primitives are collaboratively used for rule-based object discrimination. Such a highly systematic technical framework of line and region integration has not yet been reported in state-of-the-art OBIA studies and software systems, and thus, is the main contribution of our study.

In the road extraction task, RLPAF improves region shape analysis and spatial relationship reasoning. It can also be utilized in many other forms. For example, regions may be classified using the "line-based texture" by calculating the orientation, length, and density of their intersecting straight lines. In addition, IPSL-neighborhood relationships may screen out highly homogeneous neighbors in context-based image classifications. Extending the applications of the proposed framework and methods, as well as optimizing their performance, will be the focus of our future investigation.

Acknowledgments

This work is jointly supported by the National Natural Science Foundation of China (41171321), the Natural Science Foundation of Jiangsu Province, China (BK20140042), the Natural Science Foundation of the Jiangsu Higher Education Institutions of China (11KJA420001), the Jiangsu Surveying, Mapping and Geoinformation Project (JSCHKY201503), the Qing Lan Project, and the Priority Academic Program Development of Jiangsu Higher Education Institutions.

References

Anders, N.S., A.C. Seijmonsbergen, and W. Bouten, 2011. Segmentation optimization and stratified object-based analysis for semi-automated geomorphological mapping, *Remote Sensing of Environment*, 115(12):2976–2985.

Baatz, M., and A. Shäpe, 2000. Multiresolution segmentation: an optimization approach for high quality multi-scale image segmentation, *Angewandte Geographische Informationsverarbeitung XI* (J. Strobl, T. Blaschke, and G. Griesebner, editors). Salzburg: Herbert Wichmann Verlag, Heidelberg, pp. 12–23.

Benarchid, O., and N. Raissouni, 2013. Support vector machines for object based building extraction in suburban area using very high resolution satellite images, A case study: Tetuan, Morocco, *International Journal of Artificial Intelligence*, 2(1):43–50.

Benz, U., M. Baatz, and G. Schreier, 2001. Oscar - object oriented segmentation and classification of advanced radar allow automated information extraction, *Proceedings of the International Geoscience and Remote Sensing Symposium (IGARSS)*, 4:1913–1915.

Benz, U.C., P. Hofmann, G. Willhauck, I. Lingenfelder, and M. Heynen, 2004. Multiresolution,object-oriented fuzzy analysis of remote sensing data for GIS-ready information, *ISPRS Journal of Photogrammetry and Remote Sensing*, 58(3-4):239–258.

Blaschke, T., 2010. Object-based image analysis for remote sensing, *ISPRS Journal of Photogrammetry and Remote Sensing*, 65(1): 2–16.

Blaschke, T., G.J. Hay, M. Kelley, S. Lang, P. Hofmann, E. Addink, R.-Q. Feitosa, F. nan der Meer, H. van der Werff, F. van Coillie, and D. Tiede, 2014. Geographic Object-Based Image Analysis - Towards a new paradigm, *ISPRS Journal of Photogrammetry and Remote Sensing*, 87(2014):180–191.

Burns, J.B., A.R. Hanson, and E.M. Riseman, 1986. Extracting straight lines, IEEE *Transactions on* Pattern *Analysis and Machine Intelligence*, 8(4):425–456.

Canny, J.F., 1986. A computational approach to edge detection, IEEE *Transactions on* Pattern *Analysis and Machine Intelligence*, PAMI-8(6):679–698.

Chen, J., J. Li, D. Pan, Q. Zhu, and Z. Mao, 2012. Edge-guided multiscale segmentation of satellite multispectral imagery, *IEEE Transactions on Geoscience Remote Sensing*, 50(11):4513–4520.

d'Oleire-Oltmanns, S., I. Marzolff, D. Tiede, and T. Blaschke, 2014. Detection of gully-affected areas by applying Object-Based Image Analysis (OBIA) in the Region of Taroudannt, Morocco, *Remote Sensing*, 6(9):8287–8309.

Drăguţ, L., D. Tiede, and S.R. Levick, 2010. ESP: A tool to estimate scale parameter for multiresolution image segmentation of remotely sensed data, *International Journal of Geographical Information Science*, 24(6):859–871.

Drăguţ, L., O. Csillik, C. Eisank, and D. Tiede, 2014. Automated parameterization for multi-scale image segmentation on multiple layers, *ISPRS Journal for Photogrammetry and Remote Sensing*, 88:119–127.

Du, Y., D. Wu, F. Liang, and C. Li, 2013. Integration of case-based reasoning and object-based image classification to classify SPOT images: A case study of aquaculture land use mapping in coastal areas of Guangdong Province, China, *GIScience & Remote Sensing*, 50(5):574-589.

Gao, Y., P. Marpu, I. Niemeyer, and D. Runfola, 2011. Object-based classification with features extracted by a semi-automatic feature extraction algorithm - SEaTH, *Geocarto International*, 26(3):211–226.

Hebel, M., M. Arens, and U. Stilla, 2013. Change detection in urban areas by object-based analysis and on-the-fly comparison of multi-view ALS data, *ISPRS Journal on Photogrammetry and Remote Sensing*, 86:52–64.

Hu, X., and Q. Weng, 2011. Impervious surface area extraction from IKONOS imagery using an object-based fuzzy method, *Geocarto International*, 26(1):3–20.

Huang, X., and L. Zhang, 2008. An adaptive mean-shift analysis approach for object extraction and classification from urban hyperspectral imagery, *IEEE Transactions on Geoscience and Remote Sensing*, 46(12):4173–4184.

Johansen, K., L.A. Arroyo, S. Phinn, and C. Witte, 2010. Comparison of geo-object based and pixel-based change detection of riparian environments using high spatial resolution multi-spectral imagery, *Photogrammetric Engineering & Remote Sensing*, 76(2):123–136.

Kermad, C.D., and K. Chehdi, 2002. Automatic image segmentation system through iterative edge-region co-operation, *Image and Vision Computing*, 20(8):541–555.

Laliberte, A.S., D.M. Browning, and A. Rango, 2012. A comparison of three feature selection methods for object-based classification of sub-decimeter resolution UltraCam-L imagery, *International Journal of Applied Earth Observation and Geoinformation*, 15:70–78.

Li, D., G. Zhang, Z. Wu, and L. Yi, 2010. An edge embedded marker-based watershed algorithm for high spatial resolution remote sensing image segmentation, *IEEE Transactions on Image Processing*, 19(10):2781–2787.

Lin, C.H., and C.C. Chen, 2010. Image segmentation based on edge detection and region growing for thinprep-cervical smear, *International Journal of Pattern Recognition*, 24(7):1061–1089.

Lu, P., A. Stumpf, and N. Kerle, 2011. Object-oriented change detection for landslide rapid mapping, *IEEE Geoscience and Remote Sensing Letters*, 8(4):701–705.

Meinel, G., and M. Neubert, 2004. A comparison of segmentation programs for high resolution remote sensing data, *International Archives of Photogrammetry*, 35:1097–1105.

Rasi, R., R. Beuchle, C. Bodart, and M. Vollmar, 2013. Automatic updating of an object-based tropical forest cover classification and change assessment, *IEEE Journal of Selected Topics in Applied Earth Observations and Remote Sensing*, 6(1):66–73.

Salehi, B., Y. Zhang, and M. Zhong, 2012. Object-based classification of urban areas using VHR imagery and height points ancillary data, *Remote Sensing*, 4(8):2256–2276.

Sebari, I., and D.C. He, 2013. Automatic fuzzy object-based analysis of VHSR images for urban objects extraction, *ISPRS Journal Photogrammetry Remote Sensing*, 79:171–184.

Smith, G.M., and R.D. Morton, 2010. Real world objects in Geographic Object-Based Image Analysis through the exploitation of existing digital cartography and image segmentation, *Photogrammetric Engineering & Remote Sensing*, 76(2):163–171.

Tiede, D., S. Lang, F. Albrecht, and D. Holbling, 2010. Object-based class modeling for cadastre constrained delineation of geo-objects, *Photogrammetric Engineering & Remote Sensing*, 76(2):193–202.

Tiede, D., S. Lang, P. Fureder, D. Holbling, C. Hoffmann, and P. Zeil, 2011. Automated damage indication for rapid geospatial reporting, *Photogrammetric Engineering & Remote Sensing*, 77(9): 933–942.

Tong, H., T. Maxwell, Y. Zhang, and V. Dey, 2012. A supervised and fuzzy-based approach to determine optimal multi-resolution image segmentation parameters, *Photogrammetric Engineering & Remote Sensing*, 78(10):1029–1044.

Tullis, J.A., J.R. Jensen, G.T. Raber, and A.M. Filippi, 2010. Spatial scale management experiments using optical aerial imagery and LIDAR data synergy, *GIScience & Remote Sensing*, 47(3):338–359.

Vincent, L., and P. Soille, 1991. Watershed in digital spaces: an efficient algorithm based on immersion simulations, IEEE *Transactions on* Pattern *Analysis and Machine Intelligence*, 13(6):583–598.

Walter, V., 2004. Object-based classification of remote sensing data for change detection, *ISPRS Journal Photogrammetry Remote Sensing*, 58(3):225–238.

Wang, M., and R. Li, 2014. Segmentation of high spatial resolution remote sensing imagery based on hard-boundary constraint and two-stage merging, *IEEE Transactions on Geoscience and Remote Sensing*, 52(9):5712–5725.

Wang, M., Y. Sun, and G. Chen, 2015. Refining high spatial resolution remote sensing image segmentation for man-made objects through a collinear and ipsilateral neighborhood model, *Photogrammetric engineering & Remote sensing*, 81(5):397–406.

Yu, P., A.K. Qin, and D.A. Clausi, 2012. Unsupervised polarimetric SAR image segmentation and classification using region growing with edge penalty, *IEEE Transactions on Geoscience and Remote Sensing*, 50(4):1302–1317.

(Received 18 June 2015; accepted 31 August 2015; final version 07 September 2015)

Sliver Removal in Object-Based Change Detection from VHR Satellite Images

Luigi Barazzetti

Abstract

This paper presents a novel strategy for object-based change detection using very high spatial resolution (VHR) satellite images captured under variable off-nadir view angles. The variable off-nadir angle, along with weak absolute orientation, generates spurious slivers during the multitemporal comparison of classification results. The proposed solution for accurate object-to-object comparison is based on an intermediate registration of object-based classification results with a piecewise affine transformation followed by robust, geometry-based techniques for sliver removal. Although different remote sensing applications require different strategies and methods for object-based change detection, the approach developed in this paper can overcome the overall limitation introduced by the slivers generated by weak geo-localization, variable off-nadir angles, and image segmentation.

Introduction

Object-based Change Detection from VHR Images

Over the last decade, the availability of very high spatial resolution satellite images has opened new opportunities in the fields of photogrammetry and remote sensing (Rogan and Chen, 2004). Nowadays, multispectral images with sub-meter spatial resolution can be captured by numerous platforms characterized by short revisit time (see Belward and Skøien, 2015). Metric accuracy has recently reached 30 cm with the launch of WorldView-3 in August 2014. Although the metric resolution is still not comparable with aerial images (VVHR, i.e., very, very high resolution), the continuous acquisition of VHR images is more straightforward than an aerial block (Barazzetti *et al.*, 2014), which is expensive and requires a flight plan. Some actual information on aerial cameras and rules for image acquisition can be found in Kraus (2007).

Traditional pixel-based data processing (Lu *et al.*, 2004; Radke *et al.*, 2005) is based on the use of the spectral information encapsulated into the digital numbers of the image pixels. In the case of VHR images, pixels are significantly smaller than real objects (buildings, tree crowns, roads, etc.) and data processing may evolve from a basic pixel-to-pixel approach toward a new object-to-object concept defined as Geographic Object-Based Image Analysis (GEOBIA; Hay and Castilla, 2008).

GEOBIA is based on segmentation of an image to generate objects (i.e., groups of pixels that are consistent for geometry, texture, or context). Objects have not only spectral information but also spectral statistics (min-max values, mean, standard deviation, median, etc.), position information (distance to, center coordinates, etc.) geometric characterization (area, perimeter, width, height, elliptic fit, etc.), and relationships with other objects (close to, far from, etc.). GEOBIA tools are already available in several commercial software packages for remote sensing image analysis, such as eCognition® (Definiens Imaging GmbH, Munich, Germany), ENVI EX module (ITT Visual Information Solutions, Colorado), ERDAS Imagine® Objective module (ERDAS, Inc., Norcross, Georgia), PCI FeatureObjeX (PCI Geomatics, Ontario, Canada), and IDRISI Selva (Clark Labs, Massachusetts).

The advent of high spatial resolution remote-sensing imagery has also provided new opportunities for Object-Based Change Detection (OBCD, see Löw *et al.*, 2015). In OBCD, objects extracted and classified from satellite time series are compared by using not only spectral information but also object geometry (Löw *et al.*, 2015). OBIA has a strong connection to GIS data processing. However, one of the fundamental challenges in OBCD concerns the lack of spatial correspondence between objects detected in multi-temporal time series, due to both geometric and spectral variability. In other words, objects independently extracted from time series can have different boundaries (Blaschke, 2010) for the reasons illustrated in the next section.

Main Factors Affecting Object-to-Object Correspondence

Given two VHR satellite images, the main factors that affect object-to-object correspondence are (a) the variable off-nadir angle, (b) the overall geo-localization accuracy estimated with (or without) a bias-compensated Rational Polynomial Coefficient (RPC) camera model (Poli and Toutin, 2012), (c) the resolution of the Digital Elevation Model (DEM) used in orthorectification, and (d) the segmentation approach for object generation in OBIA.

Shown in Figure 1 is the effect of a variable off-nadir angle in two QuickBird images. Large off-nadir angles reduce revisit time, but images lack geometric consistency with terrain-corrected satellite images and other geo-products (maps, spatial databases, etc.; see Kapnias *et al.*, 2008). In Figure 1b, the sub-vertical wall exhibits a non-constant spatial displacement of about 9 m, whereas image spatial resolution is 0.6 m.

Overall geo-localization is another issue of primary importance in which map or geodetic coordinates are related to the pixels of the image (Oh and Lee, 2015). Orientation parameters of VHR satellite images are provided with a set of Rational Polynomial Coefficients (RPC) derived by the image data provider from the rigorous model using navigation data. RPCs comprise 80 coefficients and allow sensor and camera model data to remain unrevealed (Fraser *et al.*, 2006; Poli, 2007). However, the direct use of RPCs for image orientation has limitations in determining the true spatial orientation of every scan line, errors within the direct measurement of sensor orientation (especially attitude), and position and velocity (Fraser and Hanley, 2003). Sensor orbit and data acquisition characteristics lead to errors in direct geo-localization significantly larger than ground resolution (ground sampling distance, GSD) and require a correction as a bias in image space. The narrow field-of-view of the satellite line scanner (approaching a parallel projection for practical purposes) and the

Department of Architecture, Built Environment and Construction Engineering, Politecnico di Milano, via Ponzio 31, 20133 Milan, Italy (luigi.barazzetti@polimi.it).

Photogrammetric Engineering & Remote Sensing
Vol. 82, No. 2, February 2016, pp. 161–168.
0099-1112/16/161–168

doi: 10.14358/PERS.82.2.161

nature of the error signals (small attitude or ephemeris errors, gyro systems, and in-scan velocity, etc.) can be modeled with an affine transformation estimated from a set of ground control points (GCPs), obtaining sub-pixel accuracy also for long strips (Fraser and Hanley, 2005; Xiong and Zhang, 2009; Fraser and Ravanbakhsh, 2011). Accurate estimation of correction coefficients also requires an accurate DEM, especially in the case of hilly and mountainous areas (Rogan and Chen, 2004).

Object-based change detection with VHR time series is affected by slivers generated during the segmentation phase. This means that multitemporal boundaries do not always match precisely. In the example shown in Figure 2, the same algorithm for object-based classification was used on two satellite images acquired at different dates. The extracted polygonal features (black line and grey areas visualized on the same image) do not match for (a) the variable off-nadir angle during image acquisition, and (b) effects during the segmentation phase. This means that polygon overlay for change detection (e.g., union, intersection, symmetrical difference, etc.) will provide some small, spurious polygons.

According to Burrough and McDonnell (1998), the number of slivers between two polygons can be empirically estimated as $S = \frac{2e_1e_2}{(e_1+e_2)} - 3$, where e_1 and e_2 are the number of nodes of input polygons. Although this empirical relationship was developed for GIS datasets created with manual measurements, it highlights a significant issue: the more vertices, the more slivers. For this reason, automated segmentation for small-object identification will be more affected by slivers, which must be detected and removed. Although GIS packages have tools for sliver removal, mainly based on surface analysis (extension, number of nodes, etc.), it is difficult to set a valid single-value threshold for complex and large datasets.

This paper presents a novel technique for sliver detection and removal in object-based change detection. The method is robust for the problems previously outlined, including the lack of accurate georeferencing (large mismatches) and variable off-nadir angles or segmentation issues (lack of edge-to-edge correspondence resulting in slivers).

The Developed Solution for Sliver Detection and Removal

The Proposed Workflow

The proposed solution is a two-step methodology where (a) classification segments are registered with local geometric transformations, and (b) the remaining spurious slivers are removed with additional geometric constraints. The method is fully automated but requires some initial thresholds that depend on the local characteristics of the geographic location, the phenomena under investigation, the available images, and the main error sources outlined in the previous section (weak orientation parameters, the resolution of the DEM used in orthorectification, variable off-nadir angles).

The input for the proposed methodology is comprised of images and classification maps (polygonal shapefiles). Images can be previously geo-corrected with the bias-compensated camera model to improve overall geo-localization accuracy. However, the method can handle images with weak absolute orientation, including raw images (without correction of the

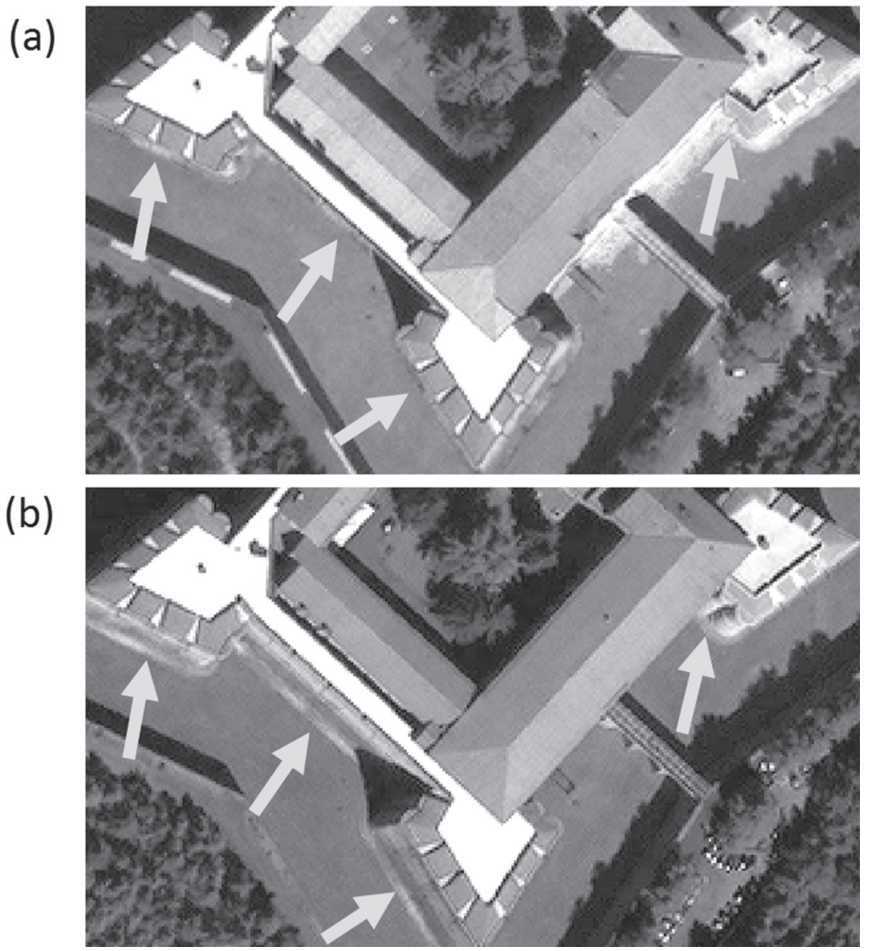

Figure 1. Two QuickBird images acquired with different off-nadir angles: (a) 5.60°, and (b) 10.65°. The spatial displacement due to sub-vertical objects is about 9 m in (b); ground sampling distance is 0.6 m.

relief) or orthorectified images with the direct use of RPC coefficients (without bias-compensation).

In the case of a multitemporal image sequence, the user is required to generate classification polygons for the different images, which can be independently segmented and classified with different solutions available on the commercial market (Figure 3, top). The aim of this work is not the implementation of a new solution for object-based classification. The main aim is the development of a general procedure able to handle the spatial inconsistency in the comparison of classification maps (Figure 3, bottom). The proposed solution offers a large flexibility for the choice of the software and the procedure for classification, which is strictly dependent on project requirements.

Detection of Corresponding Points from Images with Weak Geo-localization

Given two images, $\boldsymbol{I}_1$ and $\boldsymbol{I}_2$, from which classifications $\boldsymbol{c}_1$ and $\boldsymbol{c}_2$ are derived using object-based image analysis, rigorous comparison for change detection needs an exact overlap of object edges extracted at different epochs.

The proposed solution is based on a registration approach by means of piecewise affine transformation functions automatically estimated from a set of homologous points. Because input images could be affected by different geometric issues, an approach based on image tiling was developed. The subdivision of images into smaller tiles allows one to reduce the lack of rigorous image orientation and terrain correction (raw images), since geometric deformation should be less within small image subsets. The method uses a default tile size of 1,280 × 1,280 pixels, which can be adjusted after checking the final point distribution. The tiles of both images are independently matched by using initial georeferencing parameters as approximate values. The implementation is derived from a solution for close-range image orientation described in Barazzetti *et al.* (2013), which was adapted to handle medium-resolution satellite images (Barazzetti *et al.*, 2014).

The matching of images $\boldsymbol{I}_1$ and $\boldsymbol{I}_2$ is carried out with an additional, robust check based on an affine transformation limited to tile extension. Given a set of corresponding image points $\boldsymbol{x}_1 = (x_1, y_1, 1)^T \longleftrightarrow \boldsymbol{x}_2 = (x_2, y_2, 1)^T$ (written in homogeneous coordinates) between two generic tiles, the condition

$$\boldsymbol{x}_1 = \begin{bmatrix} x_1 \\ y_1 \\ 1 \end{bmatrix} = \begin{bmatrix} a & b & c \\ d & e & f \\ 0 & 0 & 1 \end{bmatrix} \begin{bmatrix} x_2 \\ y_2 \\ 1 \end{bmatrix} = \mathbf{H}\ \boldsymbol{x}_2 \tag{1}$$

must be checked. The estimation of transformation parameters (encapsulated in matrix **H**) needs to be coupled with robust techniques, as robust methods allow the detection of possible outliers in the observations. The proposed method is based on the analysis of several sets of image coordinates randomly extracted from the whole dataset. A solution for **H** can be identified and removed with an iterative process where several **H** matrices are estimated. A minimum number of trials m is given by:

$$m = \frac{log(1-P)}{\log\left(1-(1-e)\right)^s} \tag{2}$$

where P is the probability from a given size of sample s, with a percentage of outliers e. The goal is the extraction of a good subset of m corresponding points $[\boldsymbol{x}_1 \longleftrightarrow \boldsymbol{x}_2]$ where outliers are rejected and the transfer error

$$d_r^2 = d(\boldsymbol{x}_2, \mathbf{H}^{-1}\ \boldsymbol{x}_1)^2 + d(\boldsymbol{x}_1, \mathbf{H}\ \boldsymbol{x}_2)^2 \tag{3}$$

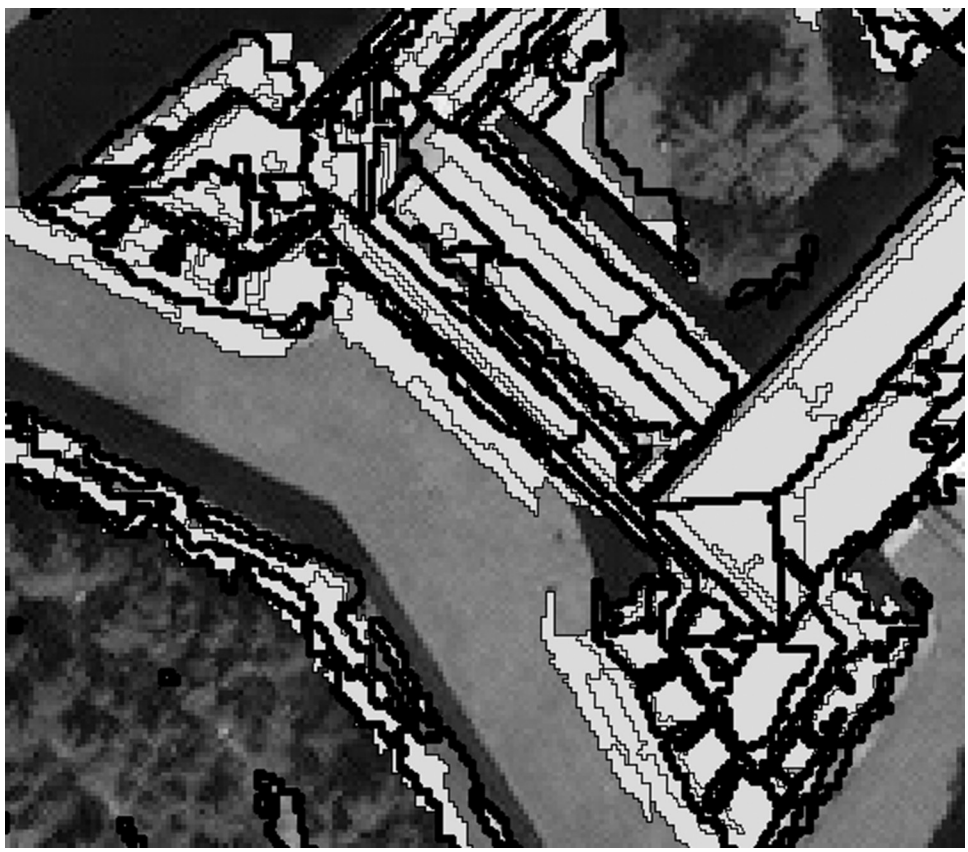

Figure 2. The same objects (grey polygons and black, thick lines) extracted from two satellite images do not match precisely match : accurate object-to-object comparison is not feasible.

is minimum. The random selection of points is carried out by considering their distribution in the images because the computed affinity is extended to the whole tile. A grid of 128 × 128 pixels is used to obtain a uniform distribution. The threshold for transfer error is another input datum that depends on the expected geo-localization accuracy. This varies from 1 to 2 pixels (terrain corrected data with bias-compensated RPCs) up to several pixels depending on the CE90% for raw images without terrain correction.

Two-Step Sliver Removal

Points extracted from different tiles are numerically reassembled to obtain a dataset extended to the overlapping area between $\boldsymbol{I}_1$ and $\boldsymbol{I}_2$. The full dataset is used to warp classification

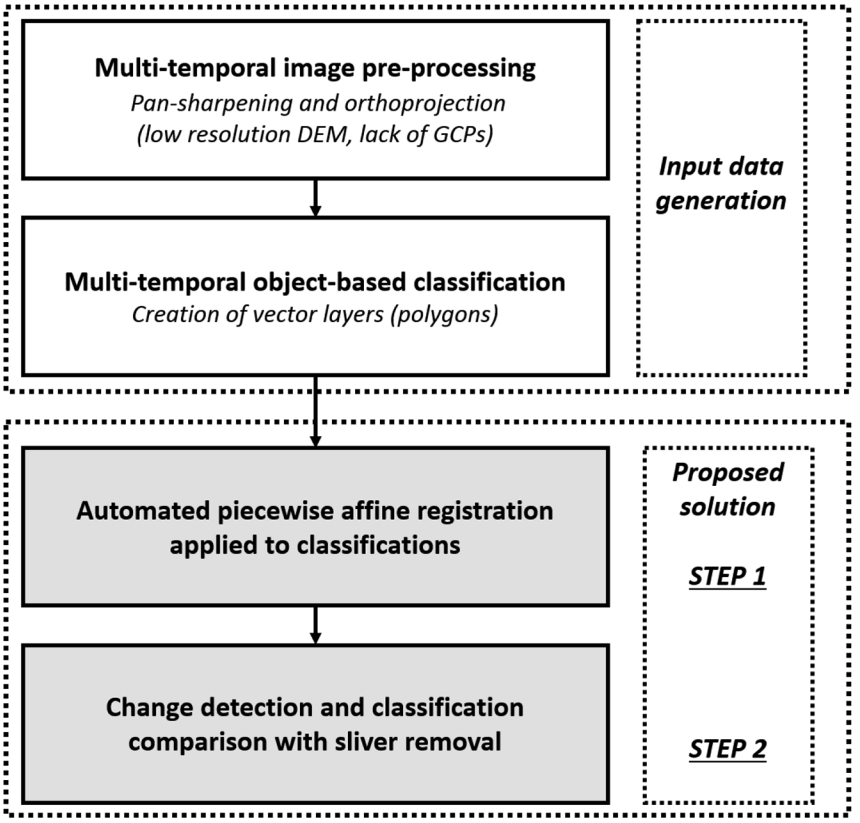

Figure 3. The developed solution for sliver removal in object-based change detection.

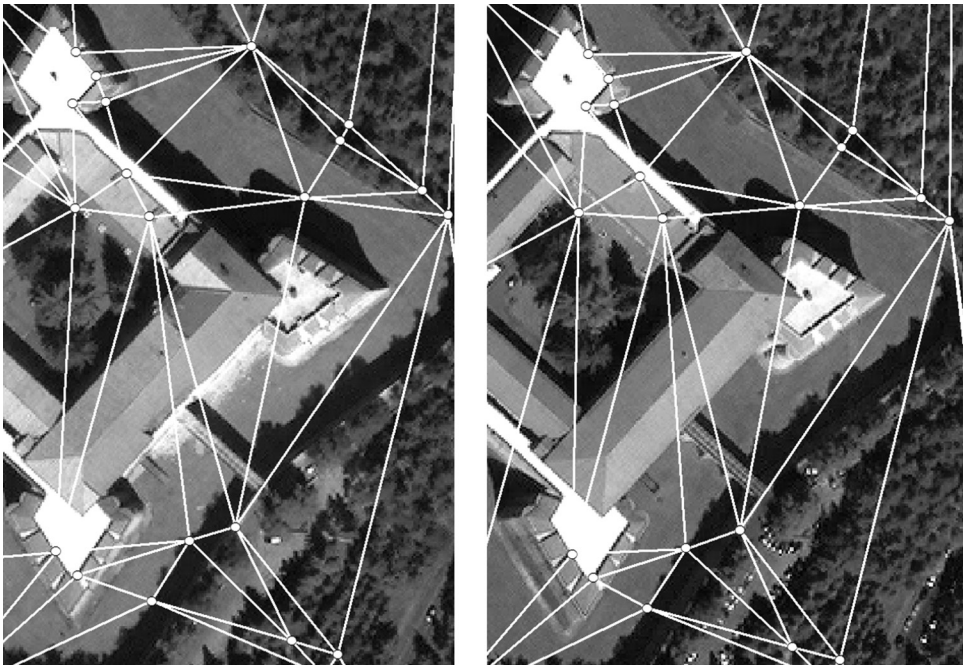

Figure 4. Example of automatically generated triangulation scheme for classification registration with piecewise affine function.

$\boldsymbol{c}_1$ on $\boldsymbol{c}_2$ with multiple piecewise affine functions estimated on a Delaunay triangulation (Figure 4) given by the corresponding points (Step 1). Indeed, the affine transformation (for the single tile used in the previous section) is only an approximation for images with weak geo-localization accuracy.

The choice of an affine transformation on a triangulated network ensures that the union of interpolated functions is continuous. In addition, the transformation can be efficiently evaluated by numerically stable methods. Let $\boldsymbol{x}_{2i}$ and $\boldsymbol{x}_{1i}$ (i = 1, 2, 3) be the un-deformed and deformed vertices of a generic triangle by means of an affine mapping $\boldsymbol{x}_{2i} = \boldsymbol{L}(\boldsymbol{x}_{1i})$; a corresponding point $\boldsymbol{x}_{2P} \longleftrightarrow \boldsymbol{x}_{1P}$ inside the triangle can be written as a unique combination of vertex points:

$$\boldsymbol{x}_{2P}=\mu_1\boldsymbol{x}_{21}+\mu_2\boldsymbol{x}_{22}+\mu_3\boldsymbol{x}_{23}=\mu_1\boldsymbol{L}(\boldsymbol{x}_{11})+\mu_2\boldsymbol{L}(\boldsymbol{x}_{12})+\mu_3\boldsymbol{L}(\boldsymbol{x}_{13})=\boldsymbol{L}(\boldsymbol{x}_{1P}) \tag{4}$$

where the numerical coefficients can be evaluated as:

$$\begin{aligned}
\mu_1 &= det\begin{bmatrix} \boldsymbol{x}_{2P} & 1 \\ \boldsymbol{x}_{22} & 1 \\ \boldsymbol{x}_{23} & 1 \end{bmatrix} / det\begin{bmatrix} \boldsymbol{x}_{21} & 1 \\ \boldsymbol{x}_{22} & 1 \\ \boldsymbol{x}_{23} & 1 \end{bmatrix} = det\begin{bmatrix} \boldsymbol{x}_{1P} & 1 \\ \boldsymbol{x}_{12} & 1 \\ \boldsymbol{x}_{13} & 1 \end{bmatrix} / det\begin{bmatrix} \boldsymbol{x}_{11} & 1 \\ \boldsymbol{x}_{12} & 1 \\ \boldsymbol{x}_{13} & 1 \end{bmatrix} \\
\mu_2 &= det\begin{bmatrix} \boldsymbol{x}_{21} & 1 \\ \boldsymbol{x}_{2P} & 1 \\ \boldsymbol{x}_{23} & 1 \end{bmatrix} / det\begin{bmatrix} \boldsymbol{x}_{21} & 1 \\ \boldsymbol{x}_{22} & 1 \\ \boldsymbol{x}_{23} & 1 \end{bmatrix} = det\begin{bmatrix} \boldsymbol{x}_{11} & 1 \\ \boldsymbol{x}_{1P} & 1 \\ \boldsymbol{x}_{13} & 1 \end{bmatrix} / det\begin{bmatrix} \boldsymbol{x}_{11} & 1 \\ \boldsymbol{x}_{12} & 1 \\ \boldsymbol{x}_{13} & 1 \end{bmatrix} \\
\mu_3 &= det\begin{bmatrix} \boldsymbol{x}_{21} & 1 \\ \boldsymbol{x}_{22} & 1 \\ \boldsymbol{x}_{2P} & 1 \end{bmatrix} / det\begin{bmatrix} \boldsymbol{x}_{21} & 1 \\ \boldsymbol{x}_{22} & 1 \\ \boldsymbol{x}_{23} & 1 \end{bmatrix} = det\begin{bmatrix} \boldsymbol{x}_{11} & 1 \\ \boldsymbol{x}_{12} & 1 \\ \boldsymbol{x}_{1P} & 1 \end{bmatrix} / det\begin{bmatrix} \boldsymbol{x}_{11} & 1 \\ \boldsymbol{x}_{12} & 1 \\ \boldsymbol{x}_{13} & 1 \end{bmatrix}
\end{aligned} \tag{5}$$

and $\mu_1+\mu_2+\mu_3=1$, with $\mu_i>0$. This means that mapping can be efficiently evaluated in the reference layer ($\boldsymbol{c}_2$) and applied to the other one ($\boldsymbol{c}_1$) with a linear transformation. Coefficients can be estimated for the different triangles of the network (a) to provide an overall improvement of classification overlap (in terms of spatial position), and (b) to reduce the effect of variable off-nadir angles and weak geo-localization accuracy. Resampling is not performed on images to improve CPU time. As mentioned, the reference system is provided by classification $\boldsymbol{c}_2$, whereas $\boldsymbol{c}_1$ is warped using a set of piecewise functions obtaining a new classification $\boldsymbol{c}_{1^*}$ without alterations of topological information. Geometrical constraints in the triangulated networks (e.g., self-intersections) of images $\boldsymbol{I}_1$ and $\boldsymbol{I}_2$ can also be used to remove incorrect matches.

Finally, residual misalignments between segments can be interpreted as spurious slivers visible after polygon intersection with Boolean algebra. Slivers are located close to boundaries and have an elongated shape that can be exploited for automated removal. Given a generic polygon made up of n pixels, a 2 × 2 covariance matrix can be generated by estimating the following geometry-based quantities (variances and covariance):

$$\begin{aligned}
\sigma_x^2 &= \frac{1}{n}\sum_{x,y} x_i^2 - \left[\frac{1}{n}\sum_{x,y} x_i\right]^2 \\
\sigma_y^2 &= \frac{1}{n}\sum_{x,y} y_i^2 - \left[\frac{1}{n}\sum_{x,y} y_i\right]^2 \\
\sigma_{xy} &= \frac{1}{n}\sum_{x,y} x_i y_i - \left[\frac{1}{n}\sum_{x,y} x_i\right]\left[\frac{1}{n}\sum_{x,y} y_i\right]
\end{aligned} \tag{6}$$

The identification of elongated features can be carried out by using the ratio between the variances and the average side of the object in term of pixels, obtaining the following density index:

$$\delta = \frac{\sqrt{n}}{\sqrt{\sigma_x^2 + \sigma_y^2} + 1} \tag{7}$$

where δ is a positive number that assumes small values (close to zero) for very elongated objects, whereas squared elements have a large density. The denominator of Equation 7 can be interpreted as the average radius of the object.

Density can be used to separate slivers from real changes detected from the intersection of variable classes. It is a relative index that does not depend on the spatial extension of the object and can be used for images captured by different platforms, including scale variations.

Case Study

Data Description and Object-Based Classification

This section illustrates the results of the method with a dataset acquired over the city of L'Aquila (Italy). On 06 April 2009, the city was struck by an earthquake. Two hundred ninety-seven people died, while both modern and historical buildings underwent some severe damage. Remote-sensing change detection plays a fundamental role in damage assessment after natural disasters (Alexakis *et al.*, 2014), but a rapid response is achievable only if the post-event image is captured as soon as possible following the disaster, notwithstanding a possible unfavorable acquisition geometry due to the lack of geo-products such as accurate DEMs and on-site measurements

Pre- ($\boldsymbol{I}_1$: 04 September 2006, off-nadir angle 10.65°, GSD 0.63 m) and post-event ($\boldsymbol{I}_2$: 08 April 2009, off-nadir angle 5.60°, GSD 0.62 m) QuickBird images were provided by DigitalGlobe as a standard product, that is, with a geolocation accuracy of 23 m (CE90%). GCPs for accurate orthorectification were not available. Pan-sharpening was used to produce a four-band mosaic starting from panchromatic (0.6 m) and multispectral (2.4 m) data. Overall, the nominal geospatial error is significantly larger than the resolution of the pan-sharpened images (23 m versus 0.6 m). Figure 5 shows the matching and triangulation results for an image.

Object-based change detection was carried out with specific algorithms developed for the city. The goal of this paper is not a detailed description of the specific algorithms developed to identify damaged buildings, which are only briefly presented. The proposed case study is an example used to demonstrate the advantage of the new method for sliver removal.

Object-based classification for $\boldsymbol{I}_1$ and $\boldsymbol{I}_2$ was carried out with three classes: vegetation ($\boldsymbol{V}$), shadows ($\boldsymbol{S}$), and object ($\boldsymbol{O}$). Complete classification results (i.e., for the whole image) are given by the union of different categories: $\boldsymbol{c}_1 = [\boldsymbol{V}_1 \cup \boldsymbol{S}_1 \cup \boldsymbol{O}_1]$ and $\boldsymbol{c}_2 = [\boldsymbol{V}_2 \cup \boldsymbol{S}_2 \cup \boldsymbol{O}_2]$. A preliminary segmentation was used to detect small objects corresponding to vegetated areas. Vegetation was identified by using the average normalized vegetation index (NDVI). Objects classified as vegetation were excluded from data processing. Next, a new segmentation with a larger scale factor was used for the unclassified areas to generate larger elements that include shadows, roads, parking areas, buildings, and so on. Shadows can be extracted by considering their low average brightness. Finally, all the remaining segments were classified as objects.

Figure 6 shows details for three historical buildings in L'Aquila. Large damage (Figure 6a) is visible and casts an additional shadow in the post-event image. It is evident that the spatial error for classes $\boldsymbol{O}_1$ and $\boldsymbol{O}_2$ is very large for the weak orientation parameters encapsulated in the delivered Rational Polynomial Coefficients (Figure 6b).

Object-Based Change Detection with Sliver Removal

To minimize the overall discrepancy from the lack of accurate geo-localization, image matching was carried out by splitting the original images into four rectangular tiles with a small overlapping area. This operation produces eight images that can be matched by considering a threshold for outliers of 23 m, that is, the expected geo-localization accuracy of QuickBird data (CE90%). A final RMS of approximately 8 m was found for the different tiles because the affine model is not suitable for the whole tile. Obviously, the RMS values of least squares estimation are not optimal in terms of metric accuracy. However, the aim of this matching step is only the extraction of corresponding points for the estimation of the piecewise affine functions and classification resampling.

Shown in Figure 6c is the result after classification registration based on the piecewise affine functions estimated on the triangulation from the detected set of corresponding points. The initial poor geo-localization accuracy in classification $\boldsymbol{c}_1 = [\boldsymbol{V}_1 \cup \boldsymbol{S}_1 \cup \boldsymbol{O}_1]$ (Figure 6b) is significantly enhanced, obtaining a new consistent set of polygonal files $\boldsymbol{c}_{1^*} = [\boldsymbol{V}_{1^*} \cup \boldsymbol{S}_{1^*} \cup \boldsymbol{O}_{1^*}]$ (Figure 6c). The spatial modification allows objects in $\boldsymbol{c}_{1^*}$ to be compared with $\boldsymbol{c}_2$, notwithstanding results that are still affected by spurious slivers.

As the goal was the detection of partially collapsed buildings, object-based change detection was carried out with an algorithm developed for the city of L'Aquila. The basic assumption is the use of shadow information, which becomes visible in the post-earthquake image. The intersection between vegetation and shadows in the pre-earthquake image and shadows after the earthquake is estimated as $\boldsymbol{S}_2 \cap (\boldsymbol{V}_{1^*} \cup \boldsymbol{S}_{1^*})$. These areas are removed from data processing. Then, damaged buildings ($\boldsymbol{DB}$) are detected with the relationship $\boldsymbol{DB} = (\boldsymbol{S}_2 \setminus \boldsymbol{S}_2 \cap (\boldsymbol{V}_{1^*} \cup \boldsymbol{S}_{1^*})\ \boldsymbol{O}_{1^*}$. The results still affected by slivers from the lack of edge correspondence of the multi-temporal polygons are shown in Figure 6d.

Finally, the estimation of the density for the different polygons forming layer $\boldsymbol{DB}$ can be used to remove small slivers. A threshold of 1.6 for geometric density was used to separate slivers from real-change polygons. The use of a triangulated, irregular network allows one to obtain a very good correspondence for object boundaries, for which the remaining spurious effect gives objects like filaments. Although the considered case study is very complicated (the medieval city center of L'Aquila has very irregular buildings, monuments, squares, etc.), the method was able to isolate real changes (damaged buildings) from errors generated by mismatching boundaries.

Conclusions

This paper describes a procedure for sliver removal in object-based change detection from VHR images. The method is a two-step solution based on (a) piecewise affine functions for a preliminary spatial registration of classification results, and (b) a sliver removal for the resulting elongated features. The method is robust for effects such as weak geo-localization accuracy (e.g., the case of raw images), scale variations, shadows, and fragmented segmentation.

The proposed case study is the city of L'Aquila. Damaged buildings were detected using object-based image analysis after the earthquake in 2009. However, the method was developed considering a wider use in object-based change detection where slivers are inevitable. The proposed solution can overcome the limitation of Boolean algebra with vector classification layers without perfect edge-to-edge correspondence. The lack of perfect boundary correspondence generates spurious slivers during basic and simple geometric operations on vector layers.

The developed solution offers a large flexibility in the preliminary phases of the work (e.g., image registration, pan-sharpening, and object-based classification). These tasks can be carried out with different commercial software, where the users can modify the parameters of image analysis following

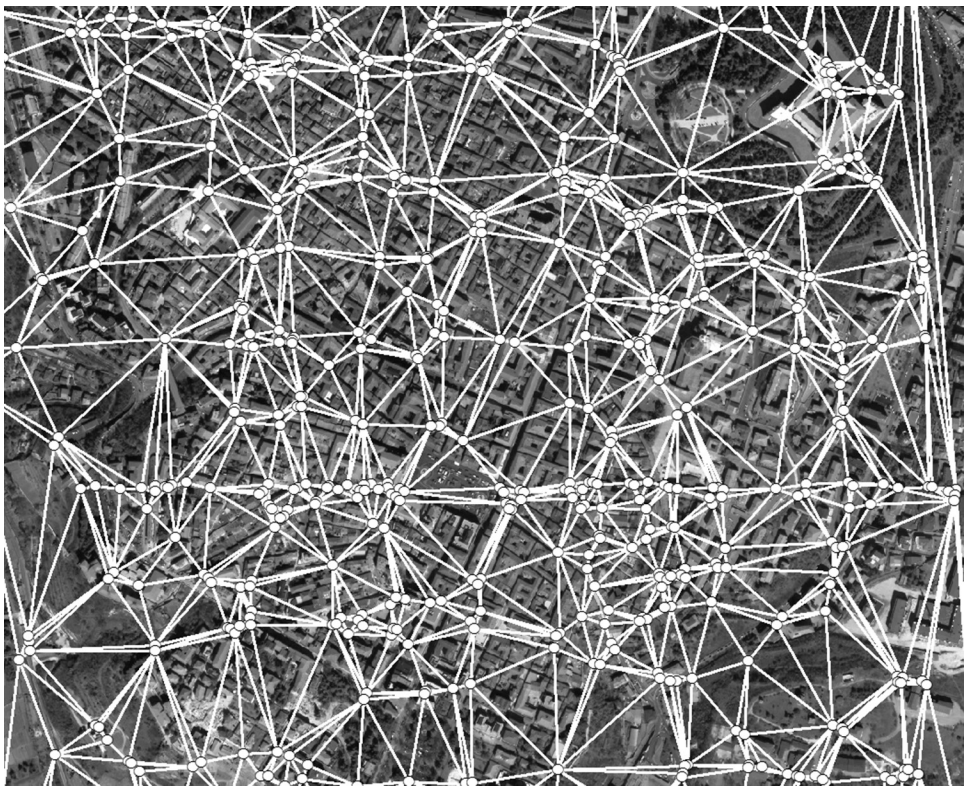

Figure 5. The triangulation for an image of the case study acquired on 08 April 2009.

the requirements of their specific applications. Then, the spatial error in classification polygons is removed with the proposed procedure for a rigorous, multitemporal comparison of classification results in an efficient, object-based change detection framework.

Future work consists of testing the proposed methodology in different environments not only limited to urban areas. Land-cover type can have a significant impact on object-based classification algorithms, starting from the segmentation phase to the choice of procedures for polygon comparison in change detection. In fact, completely different segmentation results are expected for natural environments (e.g., forested environments) or agricultural areas with clear boundaries, resulting in classification polygons with variable shape and size. Future developments are related to the implementation of strategies able to improve the preliminary registration step based on piecewise affine functions. A denser set of corresponding points would result in a better alignment of the classification polygons and a more reliable separation of spurious slivers based on the geometry of elongated features.

References

Alexakis, D.D., E. Gryllakis, A. Koutroulis, A. Agapiou, K. Themistocleous, I. Tsanis, S. Michaelides, S. Pashiardis, C. Demetriou, K. Aristeidou, A. Retalis, F. Tymvios, and D.G. Hadjimitsis, 2014. GIS and remote sensing techniques for the assessment of land use changes impact on flood hydrology: The case study of Yialias Basin in Cyprus, *Natural Hazards and Earth System Sciences*, 14: 413–426.

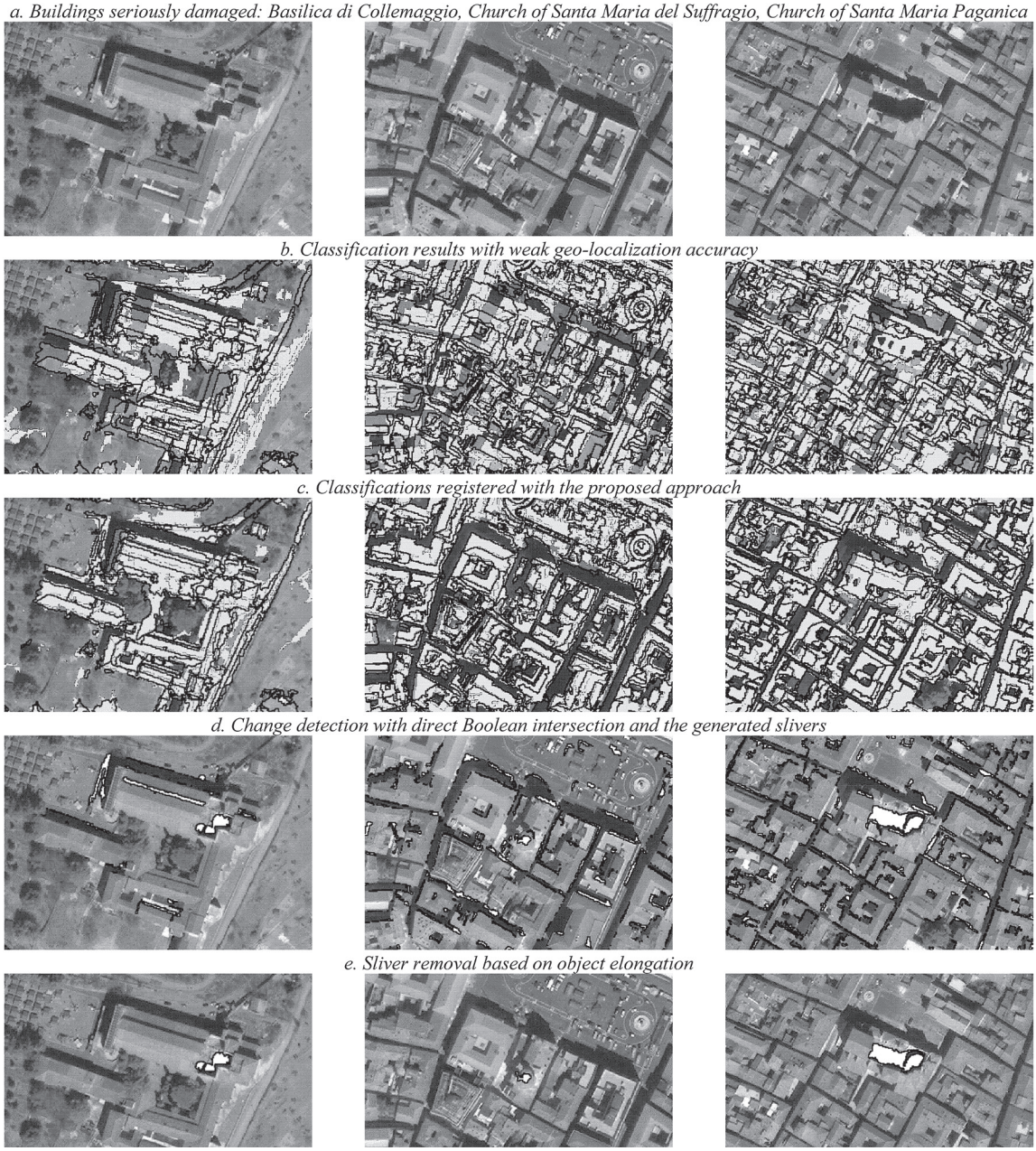

Figure 6. Three representative, damaged buildings and the results with the proposed workflow. Grey areas with thin lines and transparent areas with thick lines (figures (b) and (c)) correspond to classification classes O_{1^*} and O_2, respectively. Figure (d) shows the result affected by slivers after polygon intersection. Figure (e) illustrates the result after sliver removal.

Barazzetti, L., M. Previtali, and M. Scaioni, 2013. Stitching and processing gnomonic projections for close-range photogrammetry, *Photogrammetric Engineering & Remote Sensing*, 79(6):573–582

Barazzetti, L., M. Gianinetto, and M. Scaioni, 2014. Automatic co-registration of satellite time series via Least Squares adjustment, *European Journal of Remote Sensing*, 47:55–74.

Belward, A.S., and J.O. Skøien, 2015. Who launched what, when and why, Trends in global land-satellites, *ISPRS Journal of Photogrammetry and Remote Sensing*, 103, pp. 115–128.

Blaschke, T., 2010. Object based image analysis for remote sensing, *ISPRS Journal of Photogrammetry and Remote Sensing*, 65:2–16.

Burrough, P.A., and R.A. McDonnell, 1998. *Principles of Geographical Information Systems*, *Spatial Information Systems* (P.H.T. Beckett, P.A. Burrough, M. Goodchild, and P. Switzer, editors), pp. 352.

Fisher, P., A. Comber, and R. Wadsworth, 2005. Land use and land cover: Contradiction or complement, *Re-Presenting GIS* (P. Fisher and P. Unwin, editors), Chichester: John Wiley & Sons, Inc., pp. 85–98.

Hall, O., and J.G. Hay, 2003. A multiscale object-specific approach to digital change detection, *International Journal of Applied Earth Observation and Geoinformation*, 4(4):311–327.

Hay, G.J., and G. Castilla, 2008. Geographic object-based image analysis (GEOBIA), *Object-Based Image Analysis - Spatial Concepts for Knowledge-Driven Remote Sensing Applications* (T. Blaschke, S. Lang, and G.J. Hay, editors), Berlin: Springer, pp. 77–92.

Fraser, C.S., and H.B. Hanley, 2003. Bias *Compensation in Rational Functions for Ikonos Satellite Imagery*, *Photogrammetric Engineering & Remote Sensing*, 69(1):53–57.

Fraser, C.S., and H.B. Hanley, 2005. Bias-compensated RPCs for sensor orientation of high-
resolution satellite imagery, *Photogrammetric Engineering & Remote Sensing*, 71(8):909–915.

Fraser, C.S., G. Dial, and J. Grodecki, 2006. Sensor orientation via RPCs, *ISPRS Journal of Photogrammetry and Remote Sensing*, 60(3):182–194.

Fraser, C.S., and M., Ravanbakhsh, 2011. Precise georeferencing of long strips of ALOS imagery, *Photogrammetric Engineering and Remote Sensing*, 77(1):87–100.

Kapnias, D., P. Milenov, and S. Kay, 2008. Guidelines for best practice and quality checking of ortho imagery - Issue 3, *JRC Scientific and Technical Reports*, ISBN 978-92-79-10969-0, ISSN 1018-5593, 45 p.

Kraus, K., 2007. Photogrammetry, *Geometry from Images and Laser Scans*, Second edition, Walter de Gruyter, Berlin - New York, 459 pages.

Löw, F., P. Knöfel, and C. Conrad, 2015. Analysis of uncertainty in multi-temporal object-based classification, *ISPRS Journal of Photogrammetry and Remote Sensing*, 105:91–106.

Lu, D., P. Mausel, E. Brondizio and F. Moran, 2004. Change detection techniques, *International Journal of Remote Sensing*, 25:2365–2407.

Oh, J., and C. Lee, 2015. Automated bias-compensation of rational polynomial coefficients of high resolution satellite imagery based on topographic maps, *ISPRS Journal of Photogrammetry and Remote Sensing*, 100:14–22.

Poli, D., 2007. A rigorous model for spaceborne linear array sensors, *Photogrammetric Engineering and Remote Sensing*, 73(2):187–196.

Poli, D., and T. Toutin, 2012. Review of developments in geometric modelling for high resolution satellite pushbroom sensors, *The Photogrammetric Record*, 27(137):58–73

Radke, R.J., S. Andra, O. Al-Kofahi, and B. Roysam, 2005. Image change detection algorithms: A systematic survey, *IEEE Transactions on Image Processing*, 14:294–307.

Rogan, J., and D. Chen, 2004. Remote sensing technology for mapping and monitoring land-cover and land-use change, *Progress in Planning*, 61(4):301–325.

Xiong, Z., and Y. Zhang, 2009. A generic method for RPC refinement using ground control information, *Photogrammetric Engineering & Remote Sensing*, 75(9):1083–1092.

(Received 20 April 2015; accepted 01 September 2015; final version 09 September 2015)

SUSTAININGMEMBERS

3D Laser Mapping LTD
www.3dlasermapping.com

Acute3D
www.acute3d.com

Aerial Cartographics of America, Inc. (ACA)
www.aca-net.com

Aerial Services, Inc.
www.AerialServicesInc.com

Aero-Graphics, Inc.
www.aero-graphics.com

AeroTech Mapping Inc.
www.atmlv.com

Aerovel Corporation
www.aerovelco.com

Air Photographics, Inc.
www.airphotographics.com

The Airborne Sensing Corporation
www.airsensing.com

Axis GeoSpatial, LLC
www.axisgeospatial.com

Ayres Associates, Inc.
www.AyresAssociates.com

BNP Media, Point of Beginning Magazine
www.bnpmedia.com

Bohannan Huston, Inc.
www.bhinc.com

Cardinal Systems, LLC
www.cardinalsystems.net

Certainty 3D LLC
www.certainty3d.com

CompassData, Inc.
www.compassdatainc.com

DAT/EM Systems International
www.datem.com

Dewberry
www.dewberry.com

DigitalGlobe
www.digitalglobe.com

DMC International Imaging Ltd.
www.dmcii.com

Dynamic Aviation Group, Inc.
www.dynamicaviation.com

Eagle Mapping, Ltd
www.eaglemapping.com

Elecnor Deimos Imaging
www.deimos-imaging.com

Environmental Research Incorporated
www.eri.us.com

Esri Research Institute, Inc.
www.esri.com

EXELIS
www.exelisvis.com

Flatdog Media, Inc./Professional Surveyor Magazine
www.profsurv.com

Fugro EarthData, Inc.
www.earthdata.com

GeoBC
www.geobc.gov.bc.ca

GEOconnexion International
www.geoconnexion.com

GeoCue Group
info@geocue.com

Global Science & Technology, Inc.
www.gst.com

GRW Aerial Surveys, Inc.
www.grwinc.com

Harris Corporation
www.harris.com

Hexagon Geospatial
www.hexagongeospatial.com

HyVista Corporation
www.hyvista.com

ICAROS, Inc.
www.lcaros.us

Intergraph (ERDAS Inc.)
www.intergraph.com/geospatial

Keystone Aerial Surveys, Inc.
www.keystoneaerialsurveys.com

Kucera International
www.kucerainternational.com

Lead'Air, Inc.
www.trackair.com

LizardTech
www.lizardtech.com

Magnolia River Geospatial
www.magnolia-river.com

Mapix Aerial
www.mapixaerial.com

MDA Information Systems LLC
www.mdaus.com

Merrick & Company
www.merrick.com/gis

Michael Baker Jr., Inc.
www.mbakercorp.com

Microsoft UltraCam Team (Vexcel Imaging, GmbH)
www.microsoft.com/ultracam

Miller Creek Aerial Mapping, LLC
www.mcamaps.com/

NGA-National Geospatial-Intelligence Agency
www.nga.mil

NOAA National Geodetc Survey
www.ngs.noaa.gov

North West Group
www.nwgeo.com

NSTec, Remote Sensing Laboratory
www.nstec.com

Observera, Inc.
www.observera.com

PANalytical NIR
www.asdi.com

PCI Geomatics
www.pcigeomatics.com

Pickett & Associates, Inc.
www.pickett-inc.com

Pictometry International Corp.
www.pictometry.com

Pix4D US, Inc.
www.pix4d.com

Riegl USA, Inc.
www.rieglusa.com

Robinson Aerial Survey, Inc. (RAS)
www.robinsonaerial.com

SIIS (SI Imaging Services)
www.si-imaging.com

The Sanborn Map Company
www.sanborn.com

The Sidwell Company
www.sidwellco.com

Spectral Evolution
www.spectralevolution.com

Surveying And Mapping, LLC (SAM)
www.sam.biz

Teledyne Optech
www.teledyneoptech.com

Trimble
www.trimble.com

Towill, Inc.
www.towill.com

University of Twente/Faculty ITC
www.itc.nl

USDA/National Agricultural Statistics Service
www.nass.usda.gov

U.S. Geological Survey
www.usgs.gov

Visual Intelligence Systems, LP
www.visualintelligenceinc.com

Wilson & Company, Inc., Engineers & Architects
www.wilsonco.com

Wiser Company, LLC
www.wiserco.com

Woolpert LLP
www.woolpert.com

XEOS Imaging Inc.
www.xeosimaging.com

By joining ASPRS you too can achieve personal geospatial excellence through participation in and contribution to a professional organization that is shaping and advancing geospatial science and remote sensing technology worldwide.

Achieve Geospatial Excellence

Some of the benefits of membership include the ability to:

- Participate in one of the most influential consortiums of academic, private and public sector geospatial professionals in North America
- Network with a proactive community of contributors to geospatial technology, industry, policy, & education internationally
- Seek guidance in implementing best practices (standards and specifications) and obtaining professional certification for demonstrable competency
- Access and contribute to the official ASPRS publication with the most current and influential papers in the field
- Keep track of global geospatial technology trends by belonging to the U.S. member organization of the International Society for Photogrammetry and Remote Sensing (ISPRS)
- Access continuing education for accredited professional certification
- Acquire scholarships and mentorships as a student member to promote personal professional development and career advancement

asprs THE IMAGING & GEOSPATIAL INFORMATION SOCIETY

www.asprs.org

something

awesome

is coming your way

Over the last year ASPRS has invested in substantial upgrades to our members-only pages, with the aim of facilitating the internal business of regions, committees, and divisions. With these improvements in early 2016, ASPRS will also be rolling out its new engaging and compelling website with striking imagery and visual design!